



HAL
open science

Fast reactor design with enhanced Doppler Effect : Core design, computer scheme design, uncertainty evaluation

Maciej Zajackowski

► To cite this version:

Maciej Zajackowski. Fast reactor design with enhanced Doppler Effect : Core design, computer scheme design, uncertainty evaluation. Accelerator Physics [physics.acc-ph]. Université Grenoble Alpes [2020-..], 2020. English. NNT : 2020GRALI054 . tel-03116415

HAL Id: tel-03116415

<https://theses.hal.science/tel-03116415v1>

Submitted on 20 Jan 2021

HAL is a multi-disciplinary open access archive for the deposit and dissemination of scientific research documents, whether they are published or not. The documents may come from teaching and research institutions in France or abroad, or from public or private research centers.

L'archive ouverte pluridisciplinaire **HAL**, est destinée au dépôt et à la diffusion de documents scientifiques de niveau recherche, publiés ou non, émanant des établissements d'enseignement et de recherche français ou étrangers, des laboratoires publics ou privés.

THÈSE

Pour obtenir le grade de

DOCTEUR DE L'UNIVERSITÉ GRENOBLE ALPES

Spécialité : **Mécanique des fluides, Procédés, Energétique**

Arrêté ministériel : 25 mai 2016

Présentée par

Maciej ZAJĄCZKOWSKI

Thèse dirigée par **Cyrille DE SAINT JEAN**, Expert International,
CEA DAM

et codirigée par **Vincent PASCAL**
et **Jean-Marc PALAU**

préparée au sein du **Laboratoire LEPH au CEA Cadarache**
dans l'**École Doctorale I-MEP2 - Ingénierie - Matériaux,**
Mécanique, Environnement, Energétique, Procédés,
Production

**Fast reactor design with enhanced Doppler
effect: core design, computer scheme
design, uncertainty evaluation**

**Conception de réacteurs à neutrons rapides
à effet Doppler renforcé : conception, mise
au point de schémas numériques, evaluation
des incertitudes**

Thèse soutenue publiquement le **16 octobre 2020**,
devant le jury composé de :

Madame Elsa Merle

Professeur, Université Grenoble Alpes, Président de jury

Monsieur Gilles Ban

Professeur, ENSICAEN, Rapporteur

Monsieur Alain Hébert

Professeur, Polytechnique Montréal, Rapporteur

Monsieur Adrien Bidaud

Professeur, Université Grenoble Alpes, Examineur

Monsieur Sylvain David

Professeur, CNRS, Examineur

Monsieur Cyrille De Saint Jean

Ingénieur de recherche, CEA, Directeur de thèse

Monsieur Jean-Marc Palau

Ingénieur de recherche, CEA, Encadrant (Invité)

Monsieur Vincent Pascal

Ingénieur de recherche, CEA, Encadrant (Invité)



Abstract

In order to improve passive safety of Sodium-cooled Fast Reactors (SFR) in case of unprotected transients such as Unprotected Loss of Flow (ULOF) or Unprotected Transient Overpower (UTOP), The French Alternative Energies and Atomic Energy Commission proposed a CADOR concept — a new design of SFR core with enhanced Doppler effect. One of the most important design features is the addition of moderating materials inside fuel assemblies to decrease the average neutron energy by around 40 %. The solution leads to roughly three times higher Doppler effect due to increase in neutron population in resonance energy range. On the other hand, the softened neutron spectrum changes other core properties. For example, it increases the importance of low-energy neutron scattering and absorption. Moreover, the heterogeneous moderator placement in the assembly may cause an uneven reaction rate distribution and a risk of power peaks not observed in standard SFRs. To demonstrate the safety of CADOR design, it is essential to first evaluate the reliability of calculation tools following a Verification, Validation and Uncertainty Quantification (VVUQ) process. The changes in the neutron balance put into question the applicability of standard neutron transport calculation schemes to the case of CADOR. Therefore, the purpose of this thesis is to establish an accurate neutron transport calculation scheme, in line with VVUQ principles, that takes into account all relevant physical phenomena related to atypical properties of the CADOR core.

A two-step calculation scheme of deterministic neutron transport code APOLLO3[®] was defined as a basis for the analysis. The CADOR cores with two different moderator types, Be and ZrH₂, were used. The elements of the scheme and their possible improvements were studied through direct comparison with the reference Monte Carlo code TRIPOLI-4[®]. The systematic biases of numerical models, such as: different spatial homogenization approaches or resonance upscattering treatment, different energy and spatial mesh definitions, were studied with respect to accuracy of multiplication factor, Doppler effect and reaction rates. The most important sources of uncertainties were identified and quantified. Finally, as a first estimation of the sensitivity of the multiphysics calculation scheme, the impact of the uncertainties on simulations UTOP and ULOF transients was evaluated via coupling with MACARENa, a calculation code for transient analysis in SFRs.

The results indicate that the accuracy of calculation scheme can be improved by applying exact scattering treatment, notably in case of core with ZrH₂ moderator where utilization of simplified scattering kernel leads to underestimation of Doppler effect of up to 5.2 %. With exact scattering treatment the global bias of the calculation scheme of APOLLO3[®] was estimated at approximately 500 pcm for core with Be moderator and 460 pcm for core with ZrH₂ moderator. The biases in case of CADOR are of the same order of magnitude as for conventional SFR designs. By preserving more heterogeneous description of the fissile zone during homogenization process the global bias can be further reduced by 110–280 pcm depending on the studied level of heterogeneity; however this approach has a drawback of significantly higher computational complexity. The sensitivity analysis performed in MACARENa suggests that the uncertainties of neutronic calculations have minor impact on the progression of simulated transients. This work shows that the methods available in APOLLO3[®] provide a good accuracy of calculation of SFRs, even in case of less conventional designs. The low uncertainties

of the calculation scheme indicate robustness of the numerical models used; the calculation scheme provides sufficient accuracy to be applied in fast reactor design and safety studies.

keywords: fast reactors, APOLLO3[®], SFR, CADOR, Doppler effect, V&V, moderation

Résumé

Afin d'améliorer la sûreté passive des réacteurs rapides refroidis au sodium (SFR) en cas de transitoires non protégés, tels que la perte de débit non protégée (ULOF) ou une insertion de réactivité (UTOP), le CEA a proposé le concept CADOR — une nouvelle conception du cœur SFR avec un effet Doppler renforcé. L'une des caractéristiques de conception la plus importante est l'introduction de modérateur dans chaque assemblage combustible pour diminuer l'énergie moyenne des neutrons d'environ 40 %. La solution conduit à un effet Doppler environ trois fois plus élevé en raison de l'augmentation de la population de neutrons dans les résonances. D'autre part, le spectre neutronique adouci modifie d'autres propriétés du cœur. Par exemple, le placement hétérogène du modérateur dans l'assemblage peut entraîner une distribution inégale de la taux de réaction et un risque de pics de puissance non observés dans les SFR standard. Pour démontrer la sûreté du concept CADOR, il est essentiel d'évaluer d'abord la fiabilité des outils de calcul, à la suite d'un processus de vérification, validation et quantification d'incertitude (VVQI). Les modifications du bilan neutronique remettent en question l'applicabilité des schémas de calcul standards du transport neutronique dans le cadre de ce concept CADOR. Par conséquent, le but de cette thèse est d'établir un schéma de calcul de neutronique précis, conforme aux principes de la VVQI, prenant en compte tous les phénomènes physiques pertinents liés aux propriétés atypiques de CADOR.

Un schéma de calcul basé sur le code neutronique déterministe APOLLO3[®] a été défini comme base de l'analyse. Les cœurs CADOR avec deux types de modérateurs différents, beryllium (Be) et hydrure de zirconium (ZrH₂), ont été utilisés. Les éléments du schéma et leurs améliorations possibles ont été étudiés par comparaison directe avec le code Monte Carlo de référence TRIPOLI-4[®]. Les biais systématiques des modèles numériques (différentes approches d'homogénéisation spatiale ou de traitement de l'upscattering résonant, différentes définitions d'énergie et de maillage spatial) ont été étudiés pour la précision de keff, l'effet Doppler et les taux de réactions. Les sources d'incertitudes les plus importantes ont été identifiées et quantifiées. Enfin, comme première estimation de la sensibilité du schéma de calcul multi-physique, l'impact des incertitudes sur les simulations des transitoires UTOP et ULOF a été évaluée par couplage avec MACARENa, un code de calcul pour l'analyse transitoire en SFR.

Les résultats indiquent que la précision du schéma de calcul peut être améliorée en appliquant un traitement de diffusion exact, notamment en cas de cœur avec modérateur ZrH₂ où l'utilisation d'un modèle de diffusion simplifié conduit à une sous-estimation de l'effet Doppler jusqu'à 5.2 %. Avec un traitement de diffusion exact, le biais global du schéma de calcul d'APOLLO3[®] a été estimé à environ 500 pcm pour le cœur avec le modérateur Be et 460 pcm pour le cœur avec le modérateur ZrH₂. Les biais dans le cas de CADOR sont du même ordre de grandeur que pour les cœurs SFR conventionnels. En conservant une description plus hétérogène de la zone fissile pendant le processus d'homogénéisation, le biais global peut être encore réduit de 110–280 pcm en fonction du niveau d'hétérogénéité étudié ; cependant, cette approche présente l'inconvénient d'une complexité de calcul nettement plus élevée. L'analyse de sensibilité réalisée dans MACARENa suggère que les incertitudes des calculs neutroniques ont un impact mineur sur la progression des transitoires simulés. Ce travail montre que les méthodes disponibles dans APOLLO3[®] fournissent une bonne précision de calcul des SFR, même dans le cas de conceptions moins conventionnelles. Les faibles incertitudes du schéma

de calcul indiquent la robustesse des modèles numériques utilisés; le schéma de calcul offre une précision suffisante pour être appliqué dans la conception des réacteurs rapides et leurs études de sûreté.

mots-clés: réacteur à neutrons rapides, APOLLO3[®], RNR-Na, CADOR, effet Doppler, V&V, moderation

Acknowledgments

First of all, I would like to sincerely thank my thesis director Cyrille de Saint Jean and my supervisors Vincent Pascal and Jean-Marc Palau for guiding me through these three years, for all the discussions we had and all helpful comments that made this work better.

I would like to express my gratitude to the Jury members, in particular my Rapporteurs Alain Hébert and Gilles Ban, for finding time to critically evaluate this manuscript and participating in the final defense, despite the difficulties brought by the pandemic.

I would like to thank people from SPRC and SESI for all the help I received, in particular Pascal Archier, Laurent Buiron, , Jean-Baptiste Droin, Bastien Faure, Martin Foissy, Gilles Noguere, Pierre Sciora, Pierre Tamagno and Giorgio Valocchi.

I want to thank my future wife Emilia for her thorough proofreading of this text, for being my personal arbiter elegantiarum and for her support anytime I needed it.

Finally, I wish to thank my parents for support and encouragement throughout my entire educational journey.

Table of Contents

Abstract	i
Résumé	iii
Acknowledgments	v
List of Figures	xi
List of Tables	xv
List of Acronyms	xviii
1 Introduction	1
1.1 Nuclear power and global energy needs	1
1.2 Generation IV reactors	2
1.3 Advantages of fast neutron reactors	3
1.4 Sodium-cooled fast reactors	5
1.5 Criticality and delayed neutrons	6
1.5.1 Neutron multiplication via chain reaction	6
1.5.2 Impact of delayed neutrons	6
1.6 Transients in SFRs	8
1.7 Reactivity feedback in SFR	8
1.8 The CADOR core	10
1.9 CADOR design features	11
1.10 Numerical calculations and APOLLO3 [®]	14
1.11 VVUQ process	15
1.12 Aim of the thesis	15
2 Neutron transport theory and calculation methods	16
2.1 Neutron as a point particle	16
2.2 Neutron cross-section	16
2.3 Resonance in cross-section	17
2.4 Neutron transport equation	19
2.4.1 Definitions	19
2.4.2 Neutron transport equation — integro-differential form	20

2.4.3	NTE at steady state	23
2.4.4	Integral form of NTE at steady state	23
2.5	Solving NTE — the criticality problem	24
2.6	Deterministic methods	25
2.6.1	Energy discretization	25
2.6.2	Power iteration method, external and internal iterations	27
2.6.3	Expansion of the scattering cross-section	28
2.6.4	Angular and spatial discretization methods	29
2.6.4.1	Discrete ordinates method (S_n)	29
2.6.4.2	Method of Spherical harmonics (P_n)	30
2.6.4.3	Collision probability method	30
2.6.4.4	Method of Characteristics	31
2.6.4.5	Discontinuous Galerkin Finite Element Method and S_n method	33
2.6.5	Self-shielding calculation	34
2.6.5.1	Bondarenko iterations	35
2.6.5.2	Sub-group method	35
2.6.5.3	Tone's method	36
2.6.6	Homogenization/condensation and fundamental mode approximation	38
2.6.7	Flux-volumes homogenization	39
2.6.8	Flux moments homogenization	39
2.6.9	Fundamental mode approximation and leakage models	40
2.6.10	Calculation scheme in APOLLO3 [®]	41
2.6.10.1	Creation of multigroup data library	41
2.6.10.2	Lattice calculation	41
2.6.10.3	Creation of homogenized/condensed multigroup library	43
2.6.10.4	Core calculation	43
2.7	Monte Carlo methods	43
3	Temperature-dependent phenomena in neutron transport	47
3.1	Thermal motion of nuclei	47
3.2	Doppler effect	47
3.2.1	Physical significance of the Doppler effect	49
3.2.2	Quantification of the Doppler effect	50
3.2.3	Doppler broadening in numerical calculations	52
3.3	Scattering kernel	52
3.4	Asymptotic kernel	53
3.5	Temperature-dependent scattering kernel	54
3.6	Resonance upscattering	55
3.7	Scattering kernels in numerical calculations	56
3.7.1	Scattering kernels in TRIPOLI-4 [®]	56
3.7.1.1	SVT model	57
3.7.1.2	DBRC model	58
3.7.1.3	WCM model	59
3.7.2	Scattering kernels in APOLLO3 [®]	59

4	Physical phenomena in moderated SFR core	61
4.1	Geometry	61
4.2	Materials	62
4.2.1	Moderator choice, comparison between materials	62
4.2.1.1	Comparison between beryllium and zirconium hydride	64
4.2.1.2	Moderator placements	66
4.2.2	Fuel, cladding and wrapper	67
4.2.3	Material temperatures	68
4.2.4	Reference — a standard SFR without moderator	68
4.3	Analysis of neutron distribution (APOLLO3 [®])	69
4.3.1	Calculation parameters	69
4.3.2	Neutron energy distribution	69
4.3.2.1	Neutron flux	69
4.3.2.2	Reaction rates	72
4.3.2.3	Distribution of neutrons in space	74
4.4	Comparison of scattering models (TRIPOLI-4 [®])	79
4.4.1	TRIPOLI-4 [®] calculation details	79
4.4.2	Scattering kernel settings in TRIPOLI-4 [®]	79
4.4.3	Impact on reactivity and Doppler constant	81
4.4.4	Impact on reaction rates	82
4.4.5	Extended scattering kernel settings	84
4.5	Conclusions	84
5	Validation of the calculation scheme	87
5.1	Description of the core geometries	87
5.1.1	Geometry of the fissile zone, differences between Core I and Core II	87
5.1.2	Detailed description of Core II	89
5.1.2.1	Radial description	89
5.1.2.2	Axial description	90
5.1.3	Materials	90
5.2	Description of the calculation scheme	90
5.2.1	Creation of multigroup library	91
5.2.2	Fine flux calculation and self-shielding	92
5.2.2.1	Critical fuel assembly	92
5.2.2.2	Subcritical core elements	92
5.2.2.3	Assemblies at core-reflector boundary	93
5.2.3	Creation of homogenized and condensed library	93
5.2.4	Core calculation	94
5.3	Comparison of assembly calculations	94
5.3.1	Solver parameters	95
5.3.2	Choice of energy mesh	95
5.3.3	Comparison of multiplication factors	96
5.3.4	Comparison of reaction rates	97
5.3.5	Comparison of Doppler feedback	98
5.3.6	Comparison of feedback of void effect	101

5.3.7	Comparison with ECCO code	102
5.3.7.1	Global effects	102
5.3.7.2	Reaction rates	105
5.3.7.3	Summary	105
5.3.8	Comparison of spatial mesh refinements	105
5.3.9	Spatial comparison of reaction rates	110
5.3.10	Resonance upscattering at the assembly level	110
5.3.11	Conclusions: single assembly calculations	113
5.4	Comparison of cluster calculations	114
5.4.1	Control rod assemblies	114
5.4.1.1	Capture rate in boron	116
5.4.2	Other clusters	117
5.4.3	Conclusions: cluster calculations	119
5.5	Comparison of core calculations	121
5.5.1	MINARET settings	121
5.5.2	Comparison of global parameters	121
5.5.2.1	Control rod worth	123
5.5.3	Comparison of absorption in fuel	124
5.5.4	Comparison with ERANOS calculation scheme	124
5.5.5	Resonance upscattering at the full core scale	126
5.5.6	Core calculation with 24 energy groups	129
5.6	Quantification of biases with deterministic-Monte Carlo scheme	130
5.6.1	Global bias on core reactivity	131
5.6.2	Bias on Doppler constant	132
5.6.3	Bias on void coefficient	135
5.6.4	Bias on control rods worth	135
5.7	Semi-heterogeneous assemblies in MINARET	136
5.8	Conclusions: core calculations	137
6	Quantification of the impact of nuclear data uncertainties	139
6.1	Introduction	139
6.2	Perturbation calculation	139
6.2.1	Sensitivities	141
6.3	Uncertainties of nuclear data	144
6.3.1	Multiplication factor	144
6.3.2	Reactivity effects	144
6.3.3	Power ratio	146
6.3.4	Summary	148
6.4	Conclusions	149
7	Transient simulations with MACARENa code	150
7.1	Principles of MACARENa calculations	150
7.2	APOLLO3 [®] -MACARENa coupling	153
7.2.1	Kinetic calculations	153
7.2.2	Calculation of the reactivity coefficients	154

7.3	ULOF and UTOP transients in MACARENa	155
7.4	Results of transient simulations	156
7.4.1	Breakdown of CADOR design features	157
7.4.2	Sensitivity of transient progression to variation of K_D	160
7.5	Remarks and conclusions	163
8	Conclusions	165
8.1	Impact of moderation on the neutron physics	165
8.2	Evaluation of the deterministic calculation scheme applied to moderated SFR	166
8.3	Uncertainties of nuclear data	168
8.4	Coupling with MACARENa code	168
8.5	Future prospects	169
A	Parameters of core geometries	179
B	Uncertainties of nuclear data	181
C	Additional results of transient simulations in MACARENa	186
	Résumé Étendu	192

List of Figures

1.1	Global electricity generation by source in years 1990–2015.	1
1.2	Average number of neutrons produced per each neutron absorbed as a function of incident neutron energy for three fissile isotopes.	4
1.3	Simplified scheme of an SFR with descriptions.	6
1.4	Schematic representation of the improvement of the Doppler effect between standard SFRs and CADOR.	12
1.5	Comparison of neutron spectrum of a standard SFR core and a CADOR core with 11% Be. The gray line represents the capture cross-section of ^{238}U	13
2.1	Total cross-section of some of the most important isotopes.	18
2.2	Vector of direction decomposed into polar angle φ and azimuthal angle θ	19
2.3	Schematic explaining the origin of the setup for derivation of the integral form of NTE.	23
2.4	Neutron energy discretization.	25
2.5	Example of division of solid angle into discrete ordinates of order S_8 (80 directions in total).	30
2.6	a) Single characteristic line t crossing the region b) The integration over the same region i by tracking of multiple characteristics.	32
2.7	a) A single finite element K with lightened boundary marked with blue color. The dots corresponds to nodes for the expansion into first order polynomials b) Example of a mesh of finite elements created in MINARET.	34
2.8	Simplified depiction of the two-step deterministic calculation scheme divided into five components.	42
2.9	Simplified depiction of an algorithm used for simulation of a neutron history.	45
3.1	Maxwell-Boltzmann distribution of speed of ^{238}U atoms for different temperatures.	48
3.2	Hard sphere collision in LAB and Center of Mass (CoM) frames of reference with notation for velocity vectors used in this thesis.	48
3.3	Resonance in absorption cross-section of ^{238}U at 6.67 eV for different material temperatures.	50
3.4	Values of the Doppler constant calculated between 0 °C and temperatures indicated on a horizontal axis.	51
3.5	Elastic scattering cross-section for a heavy (^{238}U) and a light (^9Be) nuclide.	55
3.6	Visual demonstration of the mechanism of resonance upscattering.	56

3.7	First resonances in cross-section of ^{238}U	57
4.1	Layout of the fuel assembly before adding moderating materials.	61
4.2	Neutron flux spectra for CADOR cores with different moderators. Results obtained with ECCO/ERANOS code, core calculation performed by BISTRO solver in r - z geometry.	64
4.3	Elastic scattering cross-section of ^1H and ^9Be	65
4.4	Values of K_D in a function of volume content of Be and ZrH_2 moderators.	66
4.5	CADOR assemblies with moderator pins included.	67
4.6	Comparison of neutron flux spectra for two CADOR fuel assemblies and one standard SFR assembly.	70
4.7	Difference in neutron flux spectrum for two types of moderated assembly and a standard SFR assembly.	71
4.8	Sum of absorption and fission rates in actinides in 33 groups.	73
4.9	Division of a pin-cell geometry into six angular segments and six rings inside the pellet.	74
4.10	Divergence from global average energy value in percent.	75
4.11	Average neutron energy across the C1 fuel assembly for different moderators.	75
4.12	Deviation from the global average reaction rate in fuel in percent for assemblies with Be and ZrH_2	77
4.13	Comparison of deviation from global average fission rate in two assemblies calculated with different spatial meshes.	78
4.14	Comparison of two scattering treatments used in the study.	80
4.15	Comparison of two scattering treatments used in the study. Results presented for C1 assembly with ZrH_2 with fuel temperature set to 2000 °C.	83
4.16	Difference of absorption rate in ^{238}U between $\text{SVT}_{4.95\text{eV}}$ and $\text{DBRC}_{10\text{keV}}$ for ZrH_2 -moderated C1 assembly at fuel temperature of 2000 °C.	85
5.1	Horizontal layout of Core II.	88
5.2	Comparison of assembly models of Core I and Core II (the real proportions are preserved). In both cases the layout with beryllium pins is shown.	89
5.3	Axial profile of a fuel assembly.	90
5.4	Description of the two-step deterministic calculation scheme used for SFR calculations in APOLLO3 [®]	91
5.5	Description of the assembly clusters used in the calculation scheme.	93
5.6	Comparison of neutron spectrum after lattice calculation with 1968 groups and after condensation to 33 groups	94
5.7	Comparison of neutron absorption rate in actinides in 33 groups for results of A3 computed with Tone's and Sub-group. Results are compared to pointwise T4 calculations.	99
5.8	Comparison of fission rate in 33 groups for results of A3 computed with Tone's and Sub-group. Results are compared to pointwise T4 calculations.	100
5.9	Neutron flux spectrum in C1 Be-moderated CADOR fuel assembly at nominal and voided conditions.	101
5.10	Depiction of the reference calculation scheme of ECCO/ERANOS.	104

5.11	Absorption rate in 33 groups for ECCO, A3 and T4.	106
5.12	Fission rate in 33 groups for ECCO, A3 and T4.	107
5.13	Types of mesh used in the study.	108
5.14	Relative difference of reaction rates in percent between APOLLO3 [®] and TRIPOLI-4 [®] for assembly with 91 Be pins.	111
5.15	Relative difference of reaction rates in percent between APOLLO3 [®] and TRIPOLI-4 [®] for assembly with 31 ZrH ₂ pins.	111
5.16	Relative difference of reaction rates in percent between APOLLO3 [®] and TRIPOLI-4 [®] for standard SFR assembly without moderator.	112
5.17	Two types of clusters of control rod assemblies and C1 fuel assemblies used in this study.	114
5.18	Comparison of neutron absorption rate in actinides in 33 groups for A3 results of DDC48 (control rod assembly) cluster with P3 anisotropy order. Results are compared to pointwise T4 calculations.	118
5.19	Comparison of neutron absorption rate in actinides in 33 groups for A3 results of core-reflector traverse with P3 anisotropy order. Results are compared to pointwise T4 calculations.	120
5.20	Reactivity difference between APOLLO3 [®] and TRIPOLI-4 [®] for different parameter values in MINARET (other parameters were kept unchanged).	122
5.21	Comparison of absorption rate for results of A3 for two different anisotropy expansions. Results are compared to pointwise T4 calculations.	125
5.22	Comparison of absorption rate for results of A3 (P3) and ERANOS core calculations. Results are compared to pointwise T4 calculations.	127
5.23	Depiction of two-step deterministic-Monte Carlo calculation scheme alongside fully deterministic APOLLO3 [®] scheme and reference Monte Carlo scheme.	131
5.24	Exact geometry of 1/12th of fuel assembly and three homogenization patterns.	132
5.25	Global core reactivity bias of A3-T4 scheme compared to T4 reference. Results for two energetic meshes.	133
5.26	Evaluation of biases due to homogenization and condensation.	134
5.27	Finite element mesh generated with radial mesh size 10 cm MINARET option for different homogenization patterns.	136
5.28	Example of average power distribution in several fuel assemblies in ZrH ₂ -moderated CADOR core modeled with HEX pattern	138
7.1	Model of a primary loop used in MACARENa.	151
7.2	Schematic of the heat transfer within a fuel assembly in MACARENa code.	152
7.3	One third of the CADOR core divided into eight derivations.	152
7.4	Principles of the three transient scenarios simulated in MACARENa.	155
7.5	Maximum fuel temperatures during three types of transients.	158
7.6	Comparison of the evolution of maximum fuel temperatures during two transient scenarios; “breakdown” of the CADOR design principles.	159
7.7	Evolution of maximum fuel temperatures during transients for different values of K_D	161
7.8	Maximum fuel temperature attained during transients for different values of K_D	163

C.1	Comparison of power profile and reactivity coefficients derived from APOLLO3 (“A3 Up” set of coefficients).	187
C.2	Comparison of coefficients for Doppler constant from “A3” and “A3 Up” sets for the derivation 2.	188
C.3	Evolution of core reactivity during transients. Calculations performed with “A3 Up” reactivity coefficients.	189
C.4	Evolution of global average fuel temperatures during transients for different values of K_D	190
C.5	Comparison of the evolution of thermal power of the core (as a percentage of nominal flow) during two transient scenarios.	191
C.6	Comparison of the evolution of sodium mass flow (as a percentage of nominal flow) during ULOF scenario.	191

List of Tables

1.1	Six groups of delayed neutrons emitted during the fission of ^{239}Pu	7
1.2	Summary of impact of different design modifications on the Doppler feedback.	13
2.1	Examples of statistical estimators of flux, reaction rate and k used in Monte Carlo codes.	45
4.1	Dimensions of the CADOR fuel assembly.	62
4.2	Comparison of isotopes commonly used as neutron moderators.	63
4.3	Densities of ZrH_2 and Be.	65
4.4	Fuel composition.	68
4.5	Composition of the stainless steel used in wrapper tube and fuel cladding.	68
4.6	Temperatures for the materials in the core.	69
4.7	Parameters linked to neutron energy distribution.	72
4.8	Summary of the spatial distributions.	76
4.9	Fractions of flux and absorption rates inside (0.1 eV, 360 eV) energy interval, calculated with APOLLO3 [®] without employing exact free gas scattering.	81
4.10	Reactivity differences for different DBRC _{360eV} settings in TRIPOLI-4 [®] compared to SVT _{4.95eV} method.	81
4.11	Values of the Doppler constant for DBRC _{360eV} and SVT _{4.95eV} scattering kernels, calculated between 900 °C and 2000 °C.	82
4.12	Relative difference of absorption rate [pcm] between DBRC _{360eV} and SVT _{4.95eV} kernels. Associated uncertainties are equal to 1σ	84
4.13	Reactivity difference between calculations with DBRC model with all actinides and DBRC model with only ^{238}U (as in previous tables) for C1 assembly.	85
5.1	Selected parameters of Core II.	88
5.2	Optimal TDT solver options for SFR lattice calculation.	95
5.3	Comparison of infinite multiplication factors for all three assembly types.	96
5.4	Comparison of reaction rates for all three assembly types. Uncertainties were omitted for clarity; 1σ does not exceed 3 pcm for any result.	97
5.5	Comparison of the Doppler constant K_D for inner core (C1) fuel assemblies.	98
5.6	Comparison of void effect for inner core (C1) fuel assemblies.	101
5.7	Comparison of ECCO and APOLLO3 [®] (Tone, P1) results with TRIPOLI-4 [®] pointwise calculations.	103

5.8	Discrepancies between APOLLO3 [®] and TRIPOLI-4 [®] reactivity for different mesh refinements in APOLLO3 [®] applied to C1 assembly.	108
5.9	Approximate calculation times in APOLLO3 [®] obtained on DELL computer with 32 Intel Xeon E5-2620 2.10GHz CPUs.	109
5.10	Discrepancies in pcm between APOLLO3 [®] and TRIPOLI-4 [®] for different mesh refinements in APOLLO3 [®]	110
5.11	Differences of reactivity and K_D in pcm between scattering treatments for C1 and C2 assemblies.	113
5.12	Comparison of infinite multiplication factors for clusters with two types of control rod assemblies, both in semi-heterogeneous and fully heterogeneous description.	115
5.13	Comparison of capture rate in boron (¹⁰ B and ¹¹ B). APOLLO3 [®] calculation with P3 anisotropy order.	116
5.14	Comparison of infinite multiplication factors for all three assembly types. . .	117
5.15	MINARET settings used for majority of the calculations in the study.	121
5.16	Comparison of APOLLO3 [®] /TRIPOLI-4 [®] discrepancies for multiplication factor, Doppler constant and void effect for all three assembly types.	123
5.17	Comparison of control rod worth calculated in APOLLO3 [®] core calculation and TRIPOLI-4 [®] reference calculation.	124
5.18	Reactivity differences between results of calculations in ERANOS and TRIPOLI-4 [®] reference calculations.	124
5.19	Differences of total absorption and fission rate in fuel inside the fissile zone in pcm for calculations in ERANOS, APOLLO3 [®] and TRIPOLI-4 [®] reference calculations.	126
5.20	Reactivity differences and Doppler constant differences in pcm between scattering treatments for a 3D CADOR core.	128
5.21	Full core with ZrH ₂ moderator at fuel temperature of 2700 °C.	129
5.22	Comparison of APOLLO3 [®] calculations performed with 33 and 24 energy groups with /TRIPOLI-4 [®] reference.	129
5.23	Bias of A3-T4 scheme on Doppler constant compared to T4 reference (in pcm). Absolute values of K_D are given in the column on the right.	132
5.24	Bias of A3-T4 scheme on void coefficient compared to T4 reference (in pcm). Absolute values of void effect are given in the column on the right.	135
5.25	Biases of control rods worth in pcm compared to T4 reference. Results obtained by using homogeneous geometry of control rod assemblies in T4 and A3 lattice calculations.	135
5.26	Number of finite elements in a mesh generated with MINARET option radial mesh size 10 cm. The value for 3D core was calculated with assumption of an axial mesh size of 5 cm.	137
5.27	APOLLO3 [®] /TRIPOLI-4 [®] (reference) reactivity difference of MINARET core calculations with HOM and HEX patterns applied to 2D core (P3 Legendre expansion).	137
6.1	Sensitivities of multiplication factor to variation of cross-sections of most important isotopes in CADOR core (in pcm/%)	142

6.2	Relative differences of sensitivities (in %)	143
6.3	Uncertainties of multiplication factor (in pcm) for most important isotopes.	145
6.4	Summary of the uncertainties of reactivity effects (in %) for all isotopes combined.	146
6.5	Sensitivities of void effect for cores with Be and without moderator.	147
6.6	Summary of the uncertainties of power ratio (in %) for all types of reaction rates (all isotopes combined).	148
6.7	Total uncertainties for all five types of studies performed in this chapter.	148
6.8	Total uncertainties related to cross-sections of isotopes in moderators for all five types of studies performed in this chapter.	149
7.1	Values of the Doppler constant K_D (900 °C \rightarrow 2000 °C) for CADOR with Be moderator, calculated with different methods.	156
7.2	Maximum fuel temperatures [°C] during nominal operation and during transients simulated with different neutronic coefficients.	157
7.3	Maximum fuel temperatures that appeared during transient simulations for different values of K_D ; comparison with results obtained with base value of $K_D = 2512$ pcm.	162
A.1	Densities of all materials used in fuel assemblies of Core I.	179
A.2	Volume fractions and densities of all materials used in fuel assemblies of Core I.	179
A.3	Composition of EM10 ferritic steel used for wrapper in Core II.	180
A.4	Composition of AIM steel used for cladding in Core II.	180
A.5	Fuel composition in Core II.	180
B.1	Relative differences of sensitivities (in %) between Be-moderated and ZrH ₂ -moderated CADOR core.	181
B.2	Uncertainties of Doppler effect (in %) for most important isotopes.	182
B.3	Uncertainties of void effect (in %) for most important isotopes.	183
B.4	Uncertainties of control rod worth (in %) for most important isotopes.	184
B.5	Uncertainties of power ratio between assembly in the center of the core and assembly in the outer core (in %) for most important isotopes.	185
C.1	Delayed neutron fraction and mean generation time used in MACARENa.	186

List of Acronyms

A3	APOLLO3 [®]
AK	Asymptotic Kernel
ASTRID	Advanced Sodium Technological Reactor for Industrial Demonstration
C1	Inner core
C2	Outer core
CADOR	French: <i>Cœur À effet DOppler Renforcé</i> , core with enhanced Doppler effect
CAI	French: <i>Couverture Axiale Inférieure</i> , lower axial blanket
CAS	French: <i>Couverture Axiale Supérieure</i> , upper axial blanket
CEA	French: <i>Commissariat à l'énergie atomique et aux énergies alternatives</i> , French Alternative Energies and Atomic Energy Commission
CFV	French: <i>Coeur à Faible Vidange</i> , low sodium void core
CoM	Center of Mass (frame of reference)
CPM	Collision Probability Method
CR	Control Rods
DBRC	Doppler Broadening Rejection Correction
FEM	Finite Element Method
LAB	Laboratory frame of reference
LWR	Light Water Reactor
MFP	Mean Free Path
MOC	Method Of Characteristics
MOX	Mixed Oxide Fuel
MPO	Multi-Parameter Output (library)
NPP	Nuclear Power Plant
NTE	Neutron Transport Equation
PNL	French: <i>Protection Neutronique Latérale</i> , radial neutron shield
PNS	French: <i>Protection Neutronique Supérieure</i> , upper neutron shield

PPS	Plant Protection System
PWR	Pressurized Water Reactor
RCCA	Rod Control Cluster Assembly
SFR	Sodium-cooled Fast Reactor
SVT	Sampling of the Velocity of the Target
T4	TRIPOLI-4 [®]
ULOF	Unprotected Loss Of Flow
ULOF/PP	Unprotected Loss Of Flow / Primary Pumps
ULOHS	Unprotected Loss Of Heat Sink
ULOSSP	Unprotected Loss Of Station Supply Power
UTOP	Unprotected Transient Overpower
VEI	French: <i>Vase d'Expansion Inférieure</i> , lower gas plenum
VES	French: <i>Vase d'Expansion Supérieure</i> , upper gas plenum
VVUQ	Verification, Validation and Uncertainty Quantification
WCM	Weight Correction Method
XS	Cross-section

Chapter 1

Introduction

1.1 Nuclear power and global energy needs

The constantly increasing energy demand, depletion of natural resources and threat of global warming are some of the major challenges facing the energy sector in the 21st century. The world is currently experiencing an increasing need for development of sustainable, low-carbon energy sources as a core of the future energy supply.

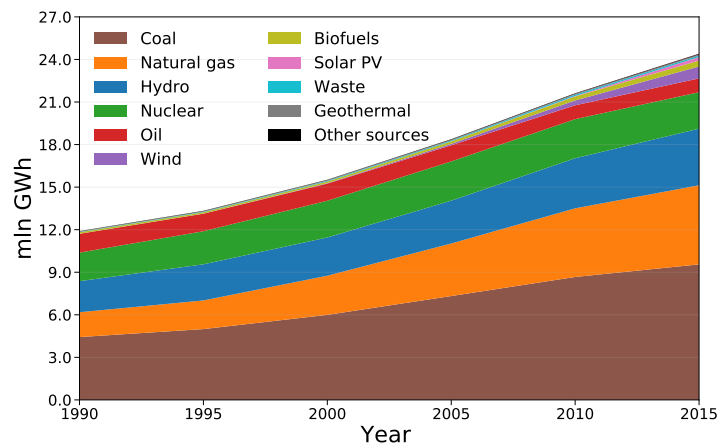


Figure 1.1: Global electricity generation by source in years 1990-2015 [1].

One of such sources is the nuclear power — a method of power generation based on energy released by nuclear reactions. Developed for commercial use in the second half of the 20th century, the nuclear power technology is now a well established means of electricity generation, used in more than 30 countries. With 442 reactor units operating worldwide and 390 GW total capacity installed the nuclear power accounts for more than 10 % of the global electricity generation [1, 2]. Nuclear energy is characterized by extremely low lifetime greenhouse gas emissions [3] and very high capacity factor, especially when compared to other low-emission energy sources [4].

However, the importance of nuclear power is starting to decline, especially in advanced economies [5]. The huge investment costs of Nuclear Power Plants (NPPs) combined with highly competitive energy market due to rising capacity of renewable sources and low natural gas prices make the nuclear energy less attractive from an economic standpoint. Furthermore, nuclear energy is associated with widespread concerns related to its safety and security. If not mitigated properly, a critical failure of NPP safety systems can result in a severe accident, leading to contamination of environment with radioactive isotopes and harmful irradiation of animals and humans [6]. The nuclear accidents in Chernobyl and Fukushima Daiichi power plants had a deep impact on the public opinion on nuclear power and prompted some countries to halt or abandon further investments in the nuclear sector [7]. The production of nuclear waste remains as a largely unresolved problem. The waste produced by NPPs continues to be highly radioactive for more than hundred thousand years and, despite ongoing research [8, 9], there exists no proven technology to destroy it in large quantities nor to store it safely until the radiation fades away sufficiently. In addition, similarly to fossil fuels, the uranium deposits in the Earth's crust are limited and not renewable. With current trends of energy demand, the recoverable uranium deposits are estimated to deplete in around 245 years [10]. Therefore, the nuclear power as it is used now cannot be regarded as a sustainable long-term energy source, unless new, more efficient technologies are introduced.

1.2 Generation IV reactors

Because of the previously mentioned shortcomings of the current reactor fleet, based on the technology of Generation II and Generation III nuclear fission reactors, significant efforts have been made to develop the next, fourth generation. Generation IV is meant to be a large step in the nuclear reactor evolution, providing advanced designs that significantly deviate from already established reactor technologies. Such a step requires a tremendous amount of research effort and international collaboration, however, if successful, it has a potential to solve many current problems of nuclear energy.

In the year 2000, the Generation IV International Forum (GIF) [11] initiative was created in order to establish an efficient international framework for research and development of Generation IV reactors, often simply named "Gen IV". To choose the most suitable designs out of hundreds of candidates, the forum defined the essential technology goals to be met by any nuclear energy system being part of Gen IV. The requirements were focused on four key areas of improvement:

1. **Sustainability** – long term availability of the system, low air pollution, efficient fuel utilization, limitation of nuclear waste
2. **Economics** – low life-cycle costs and financial risk comparable with other energy sources
3. **Safety and Reliability** – very high reliability, very low core damage probability, need for offsite emergency response eliminated
4. **Proliferation Resistance and Physical Protection** – system not prone to diversion or theft of weapon-usable materials, protection against terrorism

After extensive evaluations by a panel of experts, six most promising reactor concepts were selected for further development:

- Gas-cooled Fast Reactor (GFR)
- Lead-cooled Fast Reactor (LFR)
- Molten Salt Reactor (MSR)
- Supercritical Water-cooled Reactor (SCWR)
- Sodium-cooled Fast Reactor (SFR)
- Very High Temperature Reactor (VHTR)

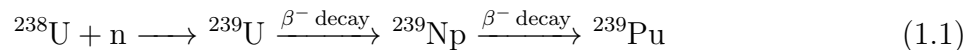
Many of the concepts listed above follow the principle of using fast neutron spectrum, as opposed to thermal spectrum typical for Gen II and Gen III reactors. The idea of using fast neutrons as a main fission initiators has been studied since the beginning of the nuclear era¹, primarily for the fuel breeding capabilities, but the technology never reached a large-scale commercial availability due to high costs and safety concerns. However, according to GIF technology roadmap [12], two of the fast reactor designs, SFR and LFR, are previewed to enter the demonstration phase during this decade.

1.3 Advantages of fast neutron reactors

The fast neutron reactors, commonly called fast reactors, are a category of nuclear reactors where majority of fission events are induced by neutrons with high kinetic energy, typically of the order from few keV to few MeV. While existing predominantly only as research reactors, the fast reactors are a constant field of research in hopes of commercial deployment due to their multiple advantages over thermal reactors.

Improved fuel economy

Arguably the biggest advantage of fast reactors is the increased efficiency of fuel utilization. Thermal reactors are able to use only a few percent of the total uranium mass in the fuel. Fast reactors, on the other hand, are theoretically capable of burning the entire uranium mass due to the possibility of breeding of new fissile material. Within the fast energy range the neutron production per neutron absorbed increases significantly, especially for ²³⁹Pu (Figure 1.2). The reactor can be thus optimized to use excess neutrons, not necessary for sustaining fission chain reaction, to create more fissile material via nuclear transmutation. Nuclei of ²³⁸U, which constitute a vast majority of the naturally occurring uranium² exhibit very small fission probability; yet, they can be transformed into fissile nuclei of ²³⁹Pu through a series of reactions initiated by a neutron capture



¹First reactor to produce electricity was in fact fast reactor Experimental Breeder Reactor I (EBR-I) in 1951 [13].

By efficiently using the surplus neutrons, the breeding ratio BR, defined as a ratio between number of fissile nuclei produced to fissile nuclei destroyed, can reach values higher than in any available thermal reactor technology. In some fast reactor designs the BR higher than one can be achieved, meaning that the amount of fissile material in the reactor increases over time. The high value of BR increases the maximum possible fuel burnup by burning

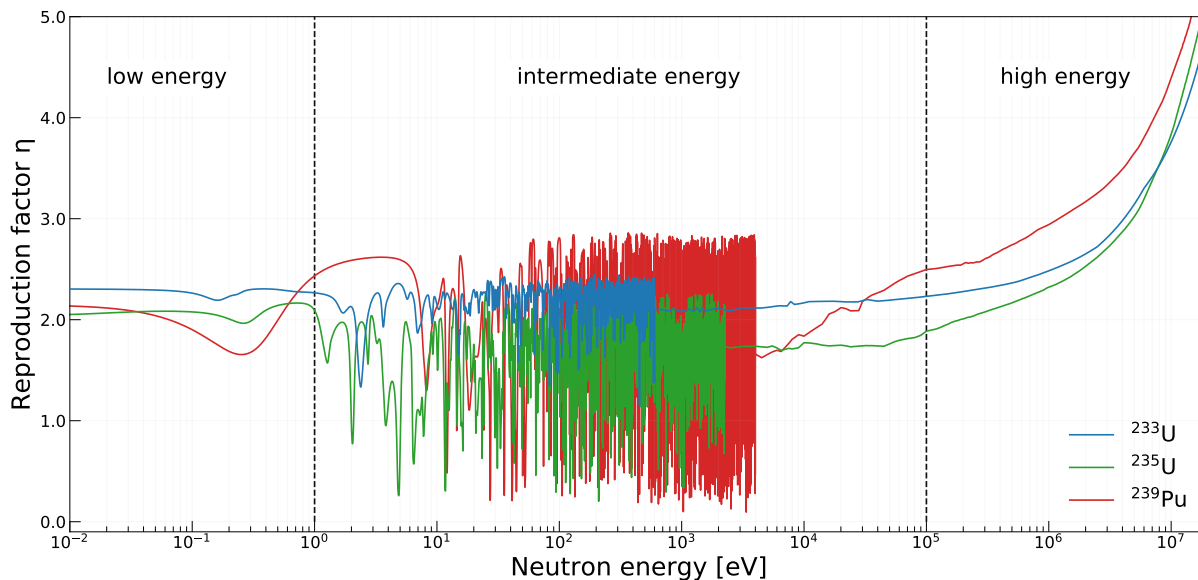


Figure 1.2: Average number of neutrons produced per each neutron absorbed (often referred to as reproduction factor or η) as a function of incident neutron energy. The values are given for three types of fissile isotopes considered to be best choices for nuclear fuel. In the fast energy range the highest η is exhibited by ^{239}Pu .

^{238}U . This increase in efficiency of fuel utilization can prolong the availability of uranium ore around 60 times, making it available potentially for thousands of years [14].

The breeding capability of fast reactors gives them an economic advantage in terms of variable costs of operation strongly related to fuel prices. It means that the fast reactors with high BR may become particularly profitable in case of increasing uranium prices, which is expected to happen due to depletion of natural deposits.

Transmutation capabilities

Minor actinides³, created through neutron capture, are highly radioactive and contribute to the long-term radiotoxicity of the fuel more than the fission products. On the other hand, many of minor actinides are unlikely to fission in a thermal spectrum due to insufficient neutron energies, which leads to significant build-up in spent fuel. In case of fast spectrum, the minor actinides can be efficiently burned via fast fission [15] and their concentration in spent fuel is thus expected to be much smaller. Because of that, the radiotoxicity of nuclear

²Around 99.3% of uranium found on Earth is isotope ^{238}U . Fissile isotope ^{235}U constitutes only 0.7% of natural uranium [10].

waste diminishes much faster and could potentially reach the level of natural uranium in just 300 years⁴ compared to roughly 250 000 years in case of a thermal spectrum [16].

Higher efficiency of thermal cycle

Liquid water, used as a coolant in most thermal reactors, boils at relatively low temperature (345 °C at 15.5 MPa, the pressure in Pressurized Water Reactor core). The coolants used in fast reactors — liquid coolants with high boiling point (sodium, lead) or gas coolants — allow for higher steam temperature at the turbine inlet and, as a consequence, higher thermal efficiency of the cycle (up to about 45 % in Phénix reactor [17] compared to 36 % in EPR [18] one of the newest Pressurized Water Reactor designs).

Lower impact of parasitic captures

High-energy neutrons tend to be captured less often than thermal, thus, some problematic effects present in thermal reactors are almost completely eliminated in fast reactors. The number of parasitic neutron captures in cladding, coolant and structure materials is generally lower. Moreover, the fast reactors are not affected by xenon or samarium poisoning, which facilitates reactivity control during reactor operation.

1.4 Sodium-cooled fast reactors

Among all fast reactors, the Sodium-cooled Fast Reactor (SFR) is arguably the design backed by the largest amount of conducted research and operating experience. SFR is a fast spectrum reactor with liquid sodium serving as a coolant in the primary loop, i.e., flowing through the reactor's core (Figure 1.3).

Throughout the history of nuclear energy, France has been a major contributor to the development of the SFR technology, with two reactors connected to the electrical grid in the past: Phénix (250 MW_e installed, operating from 1973-2009) and Superphénix (1240 MW_e, 1985-1998), and plans for a medium-size demonstration reactor ASTRID (project developed from 2009 to 2019).

Sodium as a coolant presents a variety of advantageous properties. It is an excellent heat conductor, allowing for smaller spacing between fuel pins and higher power density in the reactor core. Its low melting point (98 °C at 0.1 MPa [19]) makes it easy to keep it in liquid state, whereas high boiling temperature (883 °C at 0.1 MPa [19]) allows safe operation at core outlet temperature of 550 °C at near-atmospheric pressure [16]. Moreover, in general sodium causes little corrosion and absorbs neutrons at a low rate. The main drawbacks of using sodium are its strong exothermic reactions with water and oxygen as well as a lack of transparency which limits the possibility of visual inspection of the core.

³Minor actinides are all isotopes in actinide series other than U and Pu (which are sometimes referred to as major actinides).

⁴Providing that no actinides remain in the waste processed from the spent fuel.

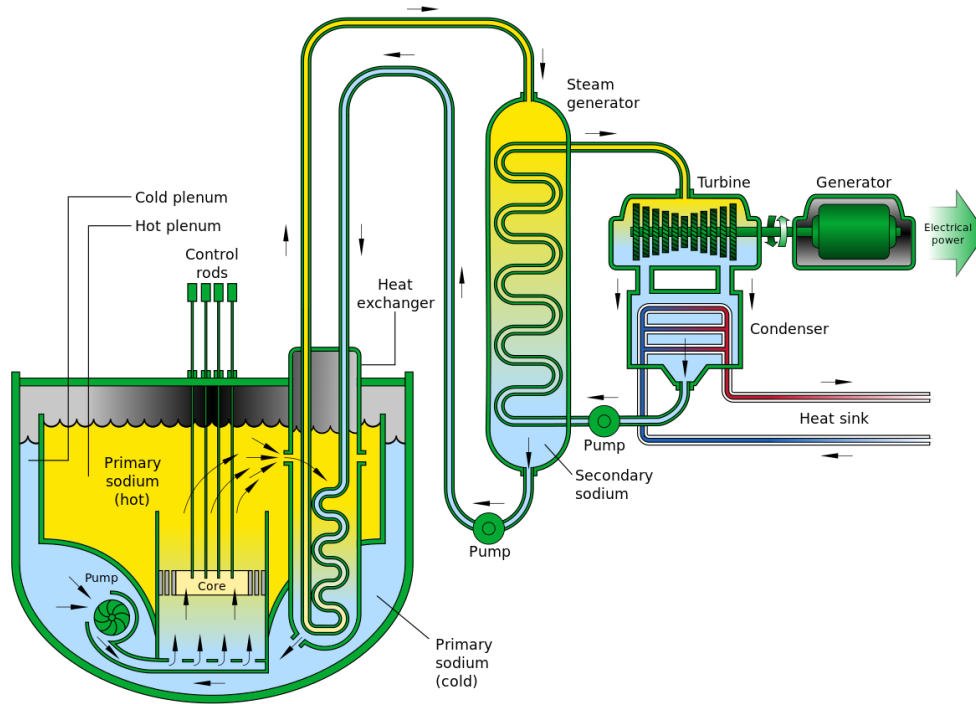


Figure 1.3: Simplified scheme of SFR with descriptions [11].

1.5 Criticality and delayed neutrons

1.5.1 Neutron multiplication via chain reaction

The heat generation in a nuclear reactor is sustained by a fission chain reaction: each generation of neutrons produces the next one through nuclear reactions, most notably nuclear fission. A ratio of neutrons in the next generation to neutrons in the previous generation is called a multiplication factor or k . If the neutron population is in balance, i.e., each consecutive neutron generation is of the same size ($k = 1$), the system is referred to as critical. If $k > 1$, the system is supercritical, i.e., the number of neutrons increases with each generation. Analogously, if $k < 1$ the system is subcritical and the neutron population will decrease over time.

To express a change in multiplication factor, a concept of reactivity ρ is commonly used

$$\rho = \frac{k - 1}{k} \quad (1.2)$$

Because the values of ρ that are useful in the context of nuclear reactors are often very small, a unit of per cent mille (pcm) is used ($\text{pcm} = 10^{-5}$).

1.5.2 Impact of delayed neutrons

The neutrons created almost immediately after fission are called prompt neutrons. A fraction of neutrons denoted as β , emerge from fission indirectly after a time delay, hence they are

referred to as delayed neutrons. Such a delay is possible because several fission products can emit a neutron only if preceded by a beta decay. Before the beta decay, the fission product possesses insufficient energy to release a neutron. The fission products that emit neutrons after decay are called precursors. The precursors are typically divided by their mean lifetime into several groups (Table 1.1), mainly to treat them collectively in kinetic calculations.

Table 1.1: Six groups of delayed neutrons emitted during the fission of ^{239}Pu [14].

Delayed neutron group	β [pcm]	mean lifetime [s]
Group 1	8	77.52
Group 2	60	32.15
Group 3	46	7.46
Group 4	71	3.02
Group 5	22	0.79
Group 6	8	0.31
All groups	215	14.6

The amount of reactivity provided to the system by the delayed neutrons alone is called effective delayed neutron fraction β_{eff} . In general $\beta_{\text{eff}} \neq \beta$ since, on average, the delayed neutrons are born with lower energies than the prompt neutrons. In fast reactors, β_{eff} tends to be lower than β , as in such a configuration the delayed neutrons are slightly less likely to multiply than the prompt neutrons.

The value of β_{eff} acts as a natural safety limit in fission reactors: the lifetime of the prompt neutrons in fast reactors is of the order of $0.1 \mu\text{s}$ [20], whereas the average lifetime of the delayed neutrons (from the fission event to the disappearance of the neutron) is typically larger than 10 s. This difference guarantees that the mean lifetime of all neutrons in one generation is sufficiently long to make the control of neutron multiplication feasible. However, if the value of reactivity reaches β_{eff} the criticality can be sustained with prompt neutrons alone, essentially decreasing the time between consecutive neutron generations by several orders of magnitude. Because of the exponential character of chain reaction, a reactivity insertion higher than β_{eff} would inevitably lead to extreme power surge and fuel meltdown if not balanced fast enough. In such a situation, the meltdown occurs in a time frame faster than response time of any active reactor safety system. Therefore, the reactivity has to be equalized by passive natural effects caused by variation in temperature, such as the Doppler effect.

The value of β_{eff} can serve as a reference point for nuclear criticality safety. The reactivity is often expressed as a fraction of the margin to prompt criticality, denoted as one dollar ($1 \$ = \beta_{\text{eff}}$). Keeping the reactivity below one dollar limit is one of the fundamental safety functions of nuclear power plants [6].

1.6 Transients in SFRs

A transient⁵ in reactor physics is often defined as a transition of a reactor from its nominal operating state into an abnormal state. There are many events that can lead to different type of transients of varying magnitude. The most general distinction among them is a division into protected and unprotected transients:

- **Protected transient** – the transient proceeds with all the Plant Protection Systems (PPS) operating as intended, thus, the evolution of the transient can be arrested by active systems e.g control rod insertion (SCRAM).
- **Unprotected transient** – the PPS are not operating properly due to one or more failures. The evolution of the transient can be arrested only by passive systems, e.g., reactivity feedback, natural convection; the SCRAM is not available.

The safety analysis of SFRs further divides Unprotected Transients into different categories, the main two of which are:

1. **Unprotected Loss of Flow (ULOF)** – the flow in one of the loops is interrupted, e.g., due to a pump failure, flow blockage or pipe rupture. Lack of circulation disrupts the heat exchange and quickly leads to an increase of sodium temperature in the core. We can distinguish a few types of ULOF transients: loss of flow caused by the failure of primary pumps (ULOF/PP), Unprotected Loss of Heat Sink (ULOHS) caused by the loss of the heat rejection capability and Unprotected Loss of Station Supply Power (ULOSSP) during which both primary and secondary pumps are stopped.
2. **Unprotected Transient Overpower (UTOP)** – an unintended positive reactivity is inserted into the reactor core, leading to a power increase. The most commonly studied UTOP initiators are: single control rod withdrawal, simultaneous withdrawal of multiple control rods due to the core support rupture, core compaction or passage of a gas bubble (void) through the core.

1.7 Reactivity feedback in SFR

As mentioned in the previous section, in a situation of an unprotected transient the neutron physics in the core is governed entirely by the passive reactivity effects. The reactivity feedback f caused by temperature variation is typically expressed in a differential form as a reactivity coefficients of a form

$$\alpha_f = \frac{d\rho}{dT} \quad (1.3)$$

Depending on the core design and the type of feedback considered, the coefficient can be positive ($\alpha > 0$) or negative ($\alpha < 0$). The most important mechanisms of reactivity feedback present in an SFR are described below.

⁵We are considering only *abnormal* transients and exclude intended transients, e.g., during reactor start up.

Sodium expansion — void effect

The expansion of sodium caused by the raising temperature affects the reactivity in multiple ways. Lower density of expanding sodium causes:

- higher neutron leakage due to lesser reflective capabilities of sodium at the core boundaries, a negative feedback
- lower chance for neutron capture in sodium, a positive feedback
- lower chance for neutron scattering in sodium, leading to higher average neutron energy, a positive feedback in fast reactors

The sodium expansion can cause both positive and negative reactivity effects. However, in standard commercial-size SFR designs the cumulative effect is generally positive. The feedback of sodium expansion tends to be the main positive contributor out of all temperature effects appearing during transient. A special case of the sodium expansion, the sodium voiding due to boiling, is thus an extremely dangerous event, most often seen in ULOF scenario, that causes a rapid positive reactivity insertion.

Fuel expansion

The axial dilatation of the fuel

- decreases the fuel concentration, a negative feedback,
- increases the core height, a positive feedback,
- increases the sodium to fuel ratio, a negative feedback.

Moreover, the axial expansion of fuel pellets can be influenced by the expansion of the cladding if both components are in tight contact (which is not the case for fresh fuel, but happens during reactor operation). The cumulative feedback of fuel expansion tends to be negative.

Structure dilatation

The expansion of cladding and hexagonal wrapper around a fuel assembly lowers the fraction of the volume available for sodium, causing a similar feedback as sodium voiding: spectrum hardening and a positive reactivity feedback. Furthermore, axial dilatation lowers the amount of structures in the core leading to lower number of parasitic captures, which is also a positive effect.

Core support dilatation

Radial dilatation of the core support widens the core, which means the sodium-to-fuel ratio increases. More sodium results in harder spectrum and, consequently, less captures in the coolant. The effect on reactivity is negative. The aforementioned core compaction functions in the opposite way: the amount of sodium in-between fissile material decreases causing a positive reactivity effect.

Doppler effect

Increased temperature of the fuel results in higher thermal motion of atoms, which in turn changes the shape of resonances in reaction cross-sections. In any reactor type this effect leads to higher neutron removal via captures, primarily in abundant ^{238}U , and thus, a negative reactivity feedback. A more detailed description of this phenomenon is given in Section 3.2.

1.8 The CADOR core

The improvement of passive reactivity feedback can be an effective way to strengthen the safety of SFRs. The principles of passive safety in a standard SFR design differ significantly from the thermal reactors. Compared to state-of-the-art thermal reactors, an SFR possesses:

- significantly lower reactivity coefficient of Doppler effect ($-0.3\text{ pcm}/^\circ\text{C}$ in the Phénix reactor [17] compared to -2 to $-4\text{ pcm}/^\circ\text{C}$ in EPR thermal reactor [21])
- lower margin to prompt criticality (360 pcm in Phénix [17] compared to 730-450⁶ in EPR [21])
- positive reactivity effects of core voiding and core compaction, which are negative in contemporary light water reactors

Those three factors are crucial during unprotected transient scenarios such as ULOF and UTOP. In the current SFR design, unprotected transient initiators such as passage of a gas bubble through the core, rupture of a core support plate or a loss of flow due to pump failure can lead to uncontrolled fuel temperature increase resulting in a potential fuel meltdown. The current safety approach to accident prevention during unprotected transients in SFR follows a principle of ensuring that the occurrence of initiating events severe enough to damage the core is sufficiently improbable to meet the current safety standards.

Many attempts have been made in the past to create improved SFR designs with better means of passive protection. A very recent example is CFV (French: *Coeur à Faible Vidange*, low sodium void core) implemented in the ASTRID reactor, where negative void coefficient was achieved by several modifications in the SFR core design [22]. The negative void feedback is an excellent passive mean of protection in case of ULOF transients, where the coolant heats up before other core elements. However, in case of a fast UTOP (insertion faster than an order of seconds) the temperature increase appears first in the fuel, hence the reaction time of the expansion effects outside of the fuel is limited by the time of temperature diffusion and might be too long to prevent the fuel meltdown. To effectively mitigate such quick power surges, a large negative reactivity effect is needed inside the fuel. Such feedback can be provided by the Doppler effect.

The Doppler effect takes place directly in the fuel and its mechanism is based on nuclear effects rather than thermal expansion. It is the fastest reactivity feedback available in nuclear

⁶The margin degrades with fuel burnup as ^{235}U isotopes are burned and Pu isotopes are created.

reactors during a power jump. For this reasons, the Doppler effect can be a reliable mean of protection against fast UTOP transients.

As mentioned before, one of the drawbacks of SFRs is a visibly lower magnitude of Doppler effect compared to thermal reactors. In standard SFRs, the total negative reactivity feedback of Doppler effect available before fuel meltdown is very often of the order of merely 0.2-0.3\$. During an UTOP such as passage of the gas bubble, in the most pessimistic scenarios the reactivity excursion can reach up to 5\$ [23]. In such a case, the Doppler feedback is too weak to keep the total reactivity below 1\$ limit. In other words, the reactivity feedback alone is not sufficient to prevent severe accidents in case of such fast transients and the only viable protection is to prevent the initiating events from happening.

To address this problem, CEA has started to develop a new core design named CADOR (French: *Cœur À effet DOppler Renforcé*, core with enhanced Doppler effect). Much like CFV core, CADOR is a modified SFR core designed to improve the passive safety during unprotected transients; however, in case of CADOR the modifications are introduced to improve primarily the feedback of Doppler effect. The final goal of the project is to achieve an SFR core that is passively protected from rapid UTOP transients, even in their highest postulated magnitude.

1.9 CADOR design features

In case of fast reactors, the available cumulative Doppler reactivity effect between nominal conditions and fuel meltdown, referred to as the Doppler integral to fusion later in the text, is often calculated with the following formula⁷ [24]:

$$\Delta\rho(T_{\text{nominal}} \rightarrow T_{\text{fusion}}) = K_D \ln\left(\frac{T_{\text{fusion}}}{T_{\text{nominal}}}\right) \quad (1.4)$$

where K_D stands for a Doppler constant, a parameter that is almost independent of the fuel temperature (more in Section 3.2.2). It is important to note that the reactivity effect in Eq. (1.4) is expressed as a product of two factors:

- $\ln(T_{\text{fusion}}/T_{\text{nominal}})$, a factor related directly to the temperature difference between accidental and nominal conditions
- K_D , a factor dependent on the neutron behavior in the core: their distribution in space and energy, interactions with core components and the resulting probabilities of being captured through the Doppler effect

Thus, the improvement of the maximum available Doppler feedback can be realized according to two independent pathways: changing the fuel temperature difference $\Delta T = T_{\text{fusion}} - T_{\text{nominal}}$ by manipulating the thermohydraulics and thermomechanics of the core (pathway 1), or by changing the neutron balance in the core (pathway 2). The two pathways are illustrated in Figure 1.4. The following subsections demonstrate the impact of both pathways, following the studies of CADOR core based on 1500 MW_{th} CFV core model, presented in [23].

⁷Both nominal and fusion temperatures have to be provided in kelvins.

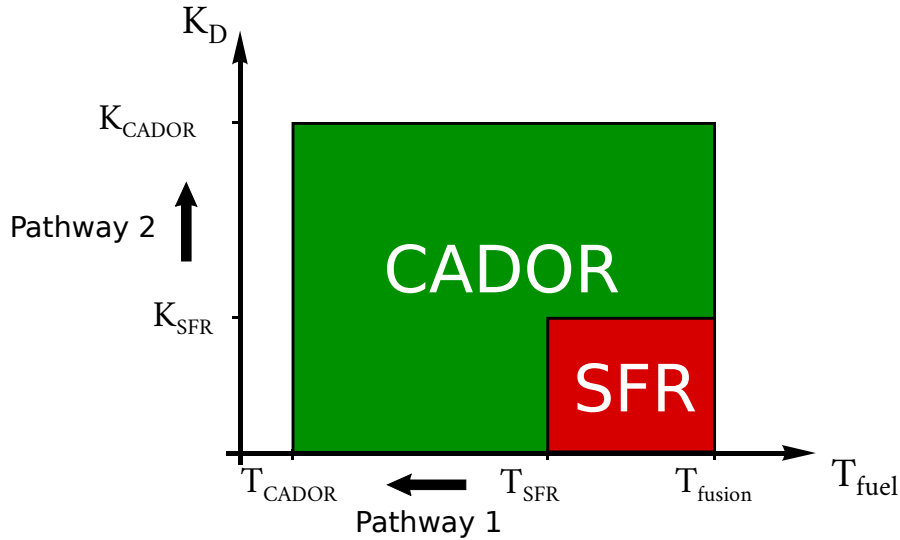


Figure 1.4: Schematic representation of the improvement of the Doppler effect between standard SFRs and CADOR, based on [23]. The horizontal axis represents the extension of ΔT margin, vertical axis represents improvement of Doppler constant by changing the properties of a neutron spectrum. Both approaches independently improve the magnitude of Doppler integral $\Delta\rho(T_{\text{nominal}} \rightarrow T_{\text{fusion}})$.

Pathway 1: increasing the temperature difference

The fusion temperature of MOX fuels is already very high (around 2750 °C, the exact value depends on PuO₂ content [25, 26]), hence the only solution for increasing the ΔT is to lower the fuel temperature at the nominal conditions. A simple way to achieve it is to decrease the power generation per each centimeter of a fuel pin, i.e., the linear power P_{lin} . In the discussed studies, decreasing the nominal linear power P_{lin} to $P_{\text{lin}}/2$ lowered the nominal average fuel temperature by around 400 °C and increased the Doppler integral to fusion from around -0.3% to -1.2% . When the linear power was further lowered to $P_{\text{lin}}/3$, the integral to fusion increased to -1.6% .

While it is possible to further decrease the linear power, the solution quickly becomes impractical and expensive. Dividing the P_{lin} by three requires three times more fuel assemblies and consequently enlarging the diameter of the core by 80% if the global power is to stay unchanged. Another issue is the uncertainty related to thermal behavior of MOX fuel at temperatures significantly lower than the typical range for which a large operational experience is available. For these reasons, there exist economical and safety limits of this approach.

Pathway 2: increasing the Doppler constant

The efficiency of the Doppler effect relies on the shape of the neutron spectrum. The effect is a consequence of an increase in resonance captures, therefore, to ensure higher Doppler feedback, the number of neutrons in the resonance energy range has to be increased, as only these neutrons can contribute to the Doppler effect. SFRs as fast reactors operates with

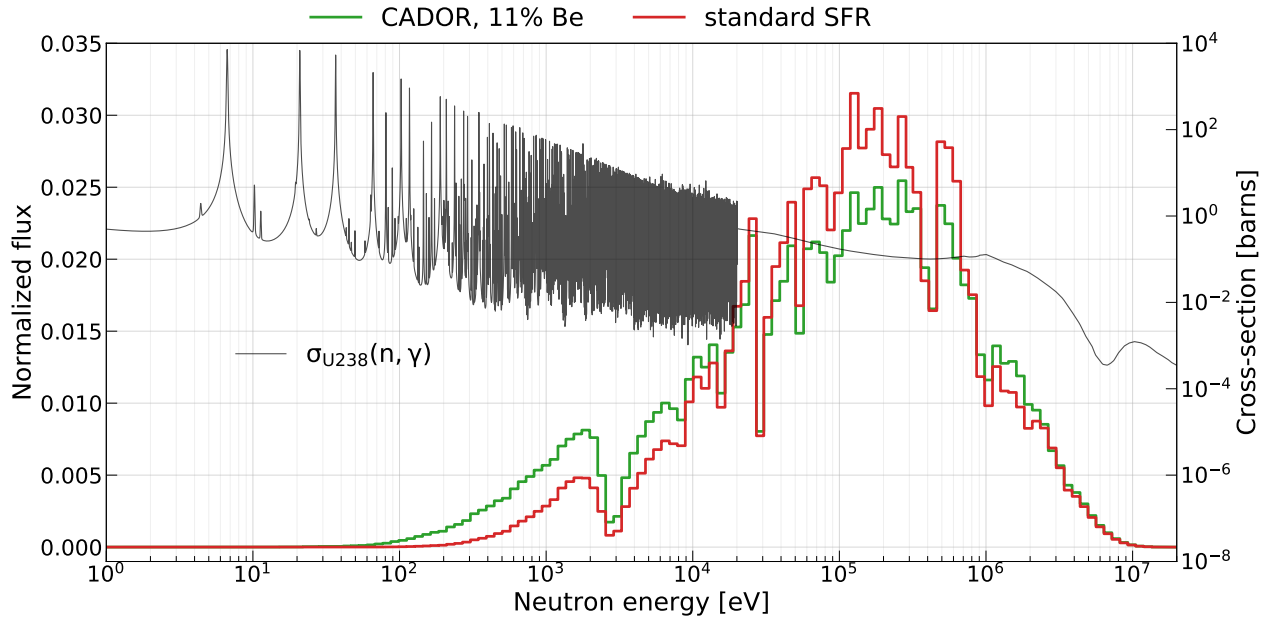


Figure 1.5: Comparison of neutron spectrum of a standard SFR core and a CADOR core with 11% Be. The gray line represents the capture cross-section of ^{238}U .

neutron energies predominantly above important part of the resonance range. To decrease the neutron energy, CADOR core employs a method of introducing neutron moderators, i.e., materials that can efficiently slow down neutrons through direct collisions. A relatively small amount of neutron moderator in the core can shift the neutron spectrum towards lower energies, while retaining most of the properties of typical SFR spectrum (Figure 1.5).

In the aforementioned study of CADOR, the addition of around 11% of metallic beryllium (Be) to the fissile zone, by replacing some of the fuel pins, increased the negative Doppler feedback by additional -2.8% . This way, when combined with P_{lin} division by a factor of 3 the core finally achieves a -4.4% Doppler integral to fusion. With two modifications in the core design, the main goal of CADOR is fulfilled. The negative Doppler feedback is powerful enough to protect the core from prompt criticality event even in case of an exceptionally strong transient of 5% . The impact of each modification is summarized in the Table 1.2.

Table 1.2: Summary of impact of different design modifications on the Doppler feedback.

	nominal P_{lin}	$P_{lin}/2$	$P_{lin}/3$	$P_{lin}/3$, 11% Be
$\Delta\rho(T_{nom} \rightarrow T_{fus})$	-0.3%	-1.2%	-1.6%	-4.4%

The addition of moderators interferes with design principles typically applied of fast reactor. Fast reactor cores are normally optimized to operate efficiently only with high neutron energies. The softening of neutron spectrum in the CADOR core can have additional benefits, e.g., lower void reactivity effect or lower material damage caused by neutron irradiation. At

the same time, it deteriorates some of the advantages characteristic for the fast spectrum, e.g., high capability for fuel breeding or large power density. From the point of view of numerical calculations, the atypical spectrum of CADOR may require a different approach with respect to the choices of numerical models and, more broadly, the calculation scheme that can provide an accurate representation of the phenomena in the core.

1.10 Numerical calculations and APOLLO3[®]

Numerical calculations are an essential tool in studying the physics of nuclear reactors. Because of the complexity of the problems that have to be solved and high costs of large scale experiments, the calculation codes are one of the most prevalent tools in reactor research, especially during core design phase. Even with modern day computers, the objective of representing the entire reactor is a challenging task with the thermohydraulics, thermomechanics and neutronics coupled together by a series of equations. Thus, different parts of reactor physics are often handled by separate codes, each using only a very simple representation of the phenomena from the remaining domains.

The aim of neutronics codes, also called neutron transport codes, is to describe the behavior of neutrons in a given system: their motion, distribution in space and energy and their interaction with matter. Even for today's computers, the straightforward solutions to the neutron transport problem in case of such complex system as a reactor core require enormous calculating power to achieve satisfying results. For this reason, many different calculation methods were developed over time to arrive at most accurate solutions in a acceptable calculation time and with reasonable memory constraints.

Broadly speaking, the numerical methods can be divided into two large categories:

- Deterministic methods, that rely on discretization with respect to space, angle and energy, to represent the problem as a set of linear equations that can be solved algebraically.
- Monte Carlo methods, that rely on statistical estimations performed by repeated random sampling of neutron histories.

In reactor physics, the deterministic codes are usually used for reactor design and safety studies due to their faster calculation times. Conversely, the Monte Carlo codes are used primarily as reference tools due to their superior accuracy; however, the calculations are typically more demanding in terms of computing power.

APOLLO3[®] [27] (abbreviated as A3 later in this work) is a deterministic neutron transport code currently developed by CEA. The code is a direct successor of three previous-generation codes: APOLLO2 [28], CRONOS2 [29] and ECCO/ERANOS [30]. Unlike the older codes, the applicability of which was limited to a rigidly defined set of problems, APOLLO3[®] was designed to be able to treat almost any kind of nuclear system thanks to its flexible architecture and a variety of solvers, calculation methods and algorithms readily available. The code can be used for analysis of both thermal and fast reactors as well as complex systems beyond these categories for which a custom calculation scheme can be built.

1.11 VVUQ process

As any tool used in research, the calculation codes must also undergo a series of tests to evaluate its applicability and reliability in solving a certain category of problems. In computational sciences the evaluation is generally performed through a three-step process called Verification, Validation and Uncertainty Quantification (VVUQ):

1. **Verification** – determines if the code solves the mathematical formulas intended by the designers
2. **Validation** – determines if the physical models used are adequate for a given real world application, i.e., if they accurately represent relevant laws of physics
3. **Uncertainty Quantification** – quantifies the uncertainties of input data and models as well as predicts their impact on the uncertainty of the final result via uncertainty propagation methods

The VVUQ is an essential evaluation method in the nuclear industry and is a necessary procedure to prove that the code is a reliable tool for design and safety studies of nuclear reactors, as required by the safety authorities, e.g., ASN in France [31]. For this reason the VVUQ is an important part of the APOLLO3[®] development [32].

1.12 Aim of the thesis

The deterministic codes such as APOLLO3[®] rely on certain assumptions and simplifications in order to achieve the results efficiently. The power of current computers is insufficient to define an accurate calculation scheme that can be applied to any kind of problem in neutronics. The approaches regarding discretization and numerical models have to be chosen according to the nature of the problem that needs to be solved. In practice, it means that the calculation schemes can differ significantly depending on the reactor geometry and type of spectrum, as every model has its range of applicability beyond which its predictions become unreliable.

As seen before in Figure 1.5, the CADOR spectrum is visibly softer than in case of standard SFRs. Localized, heterogeneous moderation within fuel assemblies and the associated neutron slowing down and absorption phenomena raise a question of how to perform accurate calculations with neutron transport codes.

The objective of this thesis was to develop a neutronics calculation scheme of APOLLO3[®] suitable for calculations of CADOR and other fast reactors containing moderating materials. The scheme was validated by comparisons with Monte Carlo calculations in TRIPOLI-4[®] code and the associated sources of uncertainties and biases were identified and quantified.

Chapter 2

Neutron transport theory and calculation methods

2.1 Neutron as a point particle

Neutrons in nuclear reactor analysis are treated as point particles, i.e., dimensionless points in space described completely by their position and velocity vector. While not true in a general case, the assumption is valid for reactor physics applications due to relatively high neutron energies. For example, at an energy of 0.01 eV, which is already below the thermal equilibrium, the de Broglie wavelength of a neutron is of the order of 10^{-8} cm — far smaller than the neutron mean free path even in highly absorbing media. The equations of neutron transport allow neutron to possess kinetic energies lower than the one proposed above; however, in any reactor the chance of such an event is very low and its impact is insignificant. Therefore, the classical mechanics is sufficiently accurate to describe the neutron behavior in the context of this work.

2.2 Neutron cross-section

Another important notion in reactor physics is the neutron cross-section. The neutron cross-section is a physical quantity related to the probability of interaction between a neutron and a given nucleus. The microscopic cross-section is the quantity that expresses the probability of neutron interaction with a single nucleus. With a monokinetic beam of neutrons of number density¹ n and speed v passing through a material, the microscopic cross-section $\sigma_\rho(v)$ for reaction ρ is given as a ratio

$$\sigma_\rho(v) = \frac{r_\rho}{nv} \quad (2.1)$$

where r_ρ is the number of reactions ρ in time (reaction rate) per each nucleus within the reach of the beam.

¹Number of neutrons per unit volume.

The microscopic cross-section is expressed in units of area, the traditional unit being one barn ($1 \text{ barn} = 10^{-28} \text{ m}^2$). The values of σ differ significantly for different isotopes and can strongly depend on the neutron–nucleus relative velocity. For this reason, the value of σ is typically given for a specific isotope and neutron kinetic energy.

In this thesis, the cross-sections are often presented in their macroscopic form

$$\Sigma = \sigma N \quad (2.2)$$

where N is the number density of nuclei in a given material. The macroscopic cross-sections are useful to quantify the reaction rate in a given volume of material and are convenient to use in the equations of neutron balance, especially when dealing with mixtures of isotopes in different proportions.

The cross-section which represents the probability of any kind of neutron–nucleus interaction is called a total cross-section and is written as σ_t or simply σ . The total cross-section can be decomposed into a set of cross-sections linked to specific reactions

$$\sigma_t = \sum_{\rho} \sigma_{\rho} \quad (2.3)$$

The most important neutron-induced reactions from reactor physics point of view are:

- neutron capture – a neutron is absorbed by the nucleus and remains there permanently. The excess energy of the reaction is then emitted, e.g., in a form of γ photon (n, γ), alpha particle (n, α)
- neutron-induced nuclear fission, (n, f) – a neutron is absorbed by the nucleus. The excess energy leads to fission of the nucleus, resulting in a formation of two (rarely three or more) fission fragments and consecutive gamma and neutron emissions. Energy released during fission is the primary heat source in a reactor core
- absorption – the sum of neutron capture and nuclear fission, the neutron is absorbed by the nucleus and either induces fission or remains trapped inside
- elastic scattering, (n, n) – the neutron is elastically scattered off the nucleus. The velocity vectors of neutron and nucleus change according to the laws of kinematics, however, the total kinetic energy is preserved
- inelastic scattering, (n, n') – the neutron is scattered off the nucleus, part of kinetic energy is lost for excitation of the nucleus
- (n, xn) reactions – the neutron–nucleus collision results in a release of x ($x > 1$) neutrons

2.3 Resonance in cross-section

The mechanism of neutron-induced reactions (excluding potential scattering) includes formation of a compound nucleus. For an isotope ${}^A_Z X$ the reaction can be described as



The mechanism of compound nucleus creation has two important consequences for reactor physics. Although the lifetime of the compound nucleus ${}^{A+1}_Z X^*$ is small, of the order of 10^{-14} s, it is sufficiently long for the surplus energy to distribute among all nucleons [33]. As a result, the decay mode of the compound nucleus is independent of the direction of the incident neutron; the emission of particles during decay is isotropic (equally probable for all directions). Secondly, the probability of compound nucleus formation increases sharply when the surplus energy deposited during formation (neutron binding energy + neutron kinetic energy) approaches one of the discrete excitation levels of the compound nucleus. This behavior is called a resonance in cross-section.

Each resonance corresponds to a separate excitation level of a given nucleus, and, as such, varies strongly between nuclides. Below around 0.1 eV the energy brought by absorbed neutron is not sufficient to reach even the lowest excitation level of any isotope used in reactor technology. For heavier isotopes the resonances generally occur in the energy range between 0.1 eV and 100 keV [34]. This large energy interval can be further divided into two important sections: the resolved and unresolved resonance range.

In the resolved energy range the resonances are visibly separated and can be identified with measurements. For higher energies the density of energy levels increases, causing the resonances to overlap. Above certain energy, typically above few keV, this overlapping makes the resonances impossible to discern experimentally, hence it is called unresolved resonance range. Although this range is usually represented as a smooth curve in the nuclear data libraries, the impact of the fine structure of resonances is still non-negligible for reactor analyses. Approximate structure of resonances in this region can be reconstructed by using probability laws of resonance distribution [35, 36].

For even higher energies the resonances overlap to a point where a continuum is reached. This corresponds to a fast energy range, also called continuum energy range.

An example of cross-section distribution is illustrated in Figure 2.1. To summarize, the

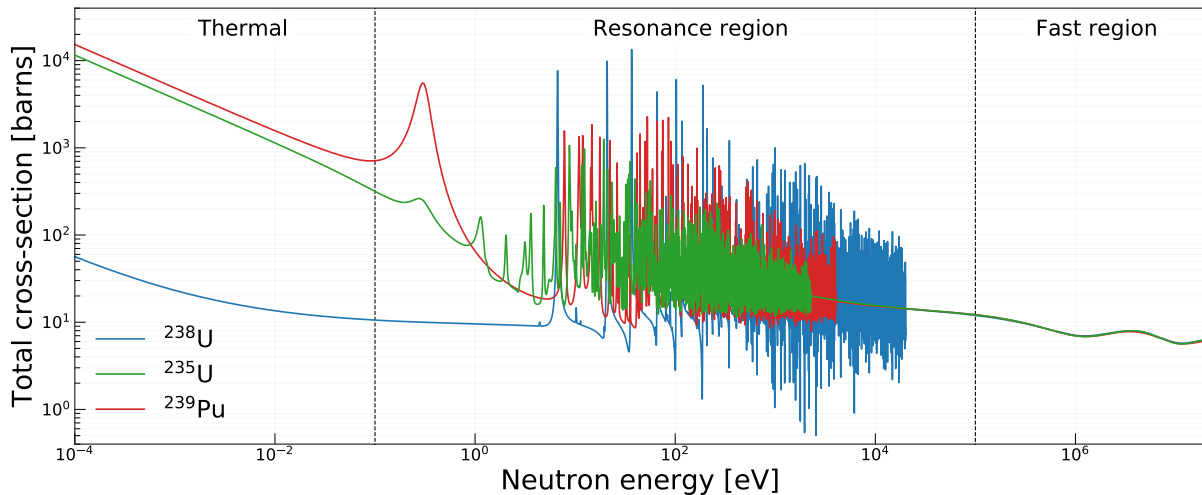


Figure 2.1: Total cross-section of some of the most important isotopes [37].

cross-section behavior falls into three (or four) categories:

- thermal energy range – below 0.1 eV, a smooth cross-section curve following closely $\frac{1}{\sqrt{E}}$ relation
- resonance energy range – between 0.1 eV–100 keV,
 - resolved resonance range – 0.1 eV–few keV, visible sharp peaks and valleys
 - unresolved resonance range – few keV–100 keV, high density of inseparable resonances
- fast energy range – roughly above 100 keV, a rather smooth cross-section curve is observed

2.4 Neutron transport equation

2.4.1 Definitions

As stated before, the free neutrons in the scope of reactor physics are treated as point particles defined by their position and velocity. Instead of using the velocity vector it is more useful to substitute it with kinetic energy E and direction vector $\vec{\Omega}$. In a general case

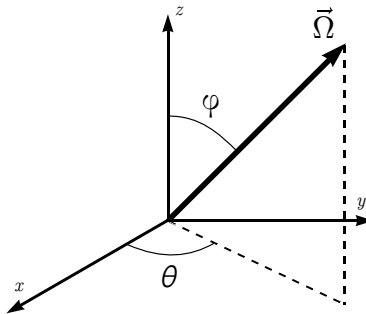


Figure 2.2: Vector of direction decomposed into polar angle φ and azimuthal angle θ .

of three-dimensional space, all neutrons at any given time t are defined by the following variables:

- a three-dimensional vector of position \vec{r}
- kinetic energy E
- a direction of motion $\vec{\Omega}$, a two-dimensional vector

These variables form a six-dimensional phase space.

To discuss the neutron transport theory it is first necessary to define several physical quantities and concepts. The density of neutrons with a given energy and direction of motion in a unit volume around \vec{r} is expressed as

$$n(\vec{r}, E, \vec{\Omega}, t) \quad (2.5)$$

however, a more useful quantity for expressing neutron balance is the angular flux ψ

$$\psi(\vec{r}, E, \vec{\Omega}, t) = v n(\vec{r}, E, \vec{\Omega}, t) \quad (2.6)$$

By integrating the angular flux over the entire solid angle $S^2 = 4\pi$ we arrive at the scalar flux ϕ

$$\phi(\vec{r}, E, t) = \int_{4\pi} d^2\Omega \psi(\vec{r}, E, \vec{\Omega}, t) \quad (2.7)$$

The scalar flux is especially useful due to its simple relation with reaction rate R per unit volume

$$R = \phi \Sigma \quad (2.8)$$

Both ψ and ϕ are scalar quantities. A vector quantity that is analogue to the angular flux is the angular neutron current \vec{j} , defined as

$$\vec{j}(\vec{r}, E, \vec{\Omega}, t) = \vec{\Omega} \psi(\vec{r}, E, \vec{\Omega}, t) \quad (2.9)$$

By integrating the \vec{j} over all directions we obtain neutron current \vec{J}

$$\vec{J}(\vec{r}, E, t) = \int_{4\pi} d^2\Omega \vec{j}(\vec{r}, E, \vec{\Omega}, t) \quad (2.10)$$

2.4.2 Neutron transport equation — integro-differential form

The neutron transport equation (NTE) describes the behavior and balance of neutrons in any given system. Let us consider a neutron balance in an infinitesimally small spatial domain d^3r around an arbitrary position \vec{r} , an infinitesimally narrow solid angle $d^2\Omega$ about direction $\vec{\Omega}$ and an infinitesimal energy interval dE about E . The rate of change of neutron density n with respect to time in this infinitesimal interval of the phase space is written as

$$\frac{\partial n(\vec{r}, E, \vec{\Omega}, t)}{\partial t} = \frac{1}{v} \frac{\partial \psi(\vec{r}, E, \vec{\Omega}, t)}{\partial t} \quad (2.11)$$

By expressing this change in time as a balance of removal rate and production rate of neutrons we arrive at the neutron transport equation. The full form of the neutron transport equation reads

$$\begin{aligned} \frac{1}{v} \frac{\partial \psi(\vec{r}, E, \vec{\Omega}, t)}{\partial t} &= -\vec{\Omega} \cdot \vec{\nabla} \psi(\vec{r}, E, \vec{\Omega}, t) - \Sigma_t(\vec{r}, E, t) \psi(\vec{r}, E, \vec{\Omega}, t) \\ &+ \int_0^\infty dE' \int_{4\pi} d^2\Omega' \Sigma_s(\vec{r}, E' \rightarrow E, \vec{\Omega}' \rightarrow \vec{\Omega}, t) \psi(\vec{r}, E', \vec{\Omega}', t) \\ &+ \frac{1}{4\pi} \sum_x \int_0^\infty dE' \chi_{p,x}(E' \rightarrow E) \nu_{p,x}(E') \Sigma_{f,x}(\vec{r}, E', t) \phi(\vec{r}, E', t) + \frac{1}{4\pi} \sum_y \chi_{d,y}(E) \lambda_y C_y(\vec{r}, t) \\ &+ S_{\text{ext}}(\vec{r}, E, \vec{\Omega}, t) \end{aligned} \quad (2.12)$$

This form of NTE is called the integro-differential form. There exist other forms of expressing NTE, most popular alternative being the integral form, explained in Section 2.4.4. All of the

forms are equivalent, the differences between them are of interest mainly for different solving methods and algorithms.

The equation can be used to describe the motion of any kind of neutron population relevant to problems of reactor analysis. All the assumptions made introduce only negligible errors from the point of view of reactor physics. Some of the assumptions are:

- interactions between free neutrons are not taken into account
- interactions of free neutrons with other free particles are not taken into account
- finite lifetime of free neutrons is not taken into account
- the force of gravity is ignored

Each term of NTE corresponds to a different way by which the neutrons can be removed or produced. The detailed explanation of each term is presented below.

Streaming term

$$-\vec{\Omega} \cdot \vec{\nabla} \psi(\vec{r}, E, \vec{\Omega}, t)$$

The streaming operator describes the balance of neutrons incoming and leaking through the surface of the infinitesimal volume around \vec{r} .

Neutron removal

$$-\Sigma_t(\vec{r}, E, t) \psi(\vec{r}, E, \vec{\Omega}, t)$$

where Σ_t is the macroscopic total cross-section.

The term accounts for the neutron removal from the phase space interval through interactions with matter. The absorption reactions remove neutrons completely, whereas reactions such as elastic or inelastic scattering preserve the global neutron population, but change the direction $\vec{\Omega}$ and energy E of a given neutron, thus removing it from the fragment of phase space under consideration.

Neutron arrival via scattering

$$\int_0^\infty dE' \int_{4\pi} d^2\Omega' \Sigma_s(\vec{r}, E' \rightarrow E, \vec{\Omega}' \rightarrow \vec{\Omega}, t) \psi(\vec{r}, E', \vec{\Omega}', t)$$

where $\Sigma_s(\vec{r}, E' \rightarrow E, \vec{\Omega}' \rightarrow \vec{\Omega}, t)$ is a macroscopic cross-section for transfer from E' to E and $\vec{\Omega}'$ to $\vec{\Omega}$.

In order for existing neutrons to arrive at energy E and direction $\vec{\Omega}$ they first need to undergo a scattering at their current energy E' and direction $\vec{\Omega}'$. To get the total neutron arrival rate, an integration over all energies and directions is performed.

The scattering cross-section $\Sigma_s(\vec{r}, E' \rightarrow E, \vec{\Omega}' \rightarrow \vec{\Omega}, t)$ encompasses the elastic, inelastic and (n,xn) scattering cross-sections for all isotopes present at \vec{r} . The value of Σ_s is a sum of all scattering cross-sections weighted by the number of outgoing neutrons per reaction.

Neutron production via fission

$$\frac{1}{4\pi} \sum_x \int_0^\infty dE' \chi_{p,x}(E' \rightarrow E) \nu_{p,x}(E') \Sigma_{f,x}(\vec{r}, E', t) \phi(\vec{r}, E', t) + \frac{1}{4\pi} \sum_y \chi_{d,y}(E) \lambda_y C_y(\vec{r}, t)$$

where

- $\Sigma_{f,x}$ is the macroscopic fission cross-section for isotope x
- $\nu_{p,x}$ is the average number of prompt neutrons emitted per fission of isotope x
- $\chi_{p,x}(E' \rightarrow E)$ is the probability of prompt neutron emission at energy E if the fission of isotope x was induced by a neutron of energy E'
- $\chi_{d,y}(E' \rightarrow E)$ is the probability of delayed neutron emission at energy E after a decay of precursor y
- C_y is the concentration of precursor y
- λ_y is the partial decay constant of precursor y corresponding to the decay channel that leads to neutron emission

This term quantifies the neutron production rate via nuclear fission. The fission reaction does not depend on the incident neutron direction and the neutron emission during fission is considered isotropic. Thus, instead of angular flux ψ a scalar flux ϕ can be used. The expression on the left quantifies the production of prompt neutrons, whereas the expression on the right quantifies the contribution of the delayed neutrons.

The production of the delayed neutrons depends on the concentration of precursors. These concentrations can be calculated with separate equations [38]:

$$\frac{dC_y(\vec{r}, t)}{dt} = -\lambda_y C_y(\vec{r}, t) + \sum_x \beta_{x,y} \int_0^\infty dE \nu_{t,x}(E') \Sigma_{f,x}(\vec{r}, E') \phi(\vec{r}, E', t) \quad (2.13)$$

where $\beta_{x,y}$ is a delayed neutron fraction emitted from a precursor y , that was created after a fission of isotope x and $\nu_{t,x}$ is the average number of neutrons created from a single fission.

In case of steady state or when the variation of neutron population in time is sufficiently slow, the contribution of delayed neutrons can be incorporated into expression for prompt neutron production by exchanging $\nu_{p,x}$ and $\chi_{p,x}$ with $\nu_{t,x}$ and $\chi_{t,x}$ defined to preserve the total production rate by fission.

Neutron production via external sources

$$S_{\text{ext}}(\vec{r}, E, \vec{\Omega}, t) \quad (2.14)$$

The last term includes the contributions from all external neutron sources, unrelated to neutron-induced fission and neutron scattering. The sources are independent of neutron flux, thus, the production rate is simply the source intensity at a given point in the phase space. An example of such sources are neutrons emitted via spontaneous fission of very heavy nuclei.

2.4.3 NTE at steady state

For all neutron transport calculations performed with APOLLO3[®] in this thesis, only the steady-state solutions of the transport equation are discussed (although time dependence is applied in a form of point kinetics equations in MACARENa code in Chapter 7). In a steady state, the neutron population is in balance and does not change over time. The time dependence can be removed from the equation, and the delayed and prompt neutrons can be treated collectively. The Eq. (2.12) simplifies to a following form:

$$\begin{aligned} \vec{\Omega} \cdot \vec{\nabla} \psi(\vec{r}, E, \vec{\Omega}) + \Sigma_t(\vec{r}, E) \psi(\vec{r}, E, \vec{\Omega}) = & \\ + \int_0^\infty dE' \int_{4\pi} d^2\Omega' \Sigma_s(\vec{r}, E' \rightarrow E, \vec{\Omega}' \rightarrow \vec{\Omega}) \psi(\vec{r}, E', \vec{\Omega}') & \\ + \frac{1}{4\pi} \sum_x \int_0^\infty dE' \chi_{t,x}(E' \rightarrow E) \nu_{t,x}(E') \Sigma_{f,x}(\vec{r}, E') \phi(\vec{r}, E') & \\ + S_{\text{ext}}(\vec{r}, E, \vec{\Omega}) & \end{aligned} \quad (2.15)$$

To simplify the equation even further, we can write it in terms of operators as follows

$$(\mathcal{L} - \mathcal{H}) \psi = \mathcal{F} \psi + S_{\text{ext}} \quad (2.16)$$

where

- $\mathcal{L} = \vec{\Omega} \cdot \vec{\nabla} + \Sigma_t$ is the transport operator responsible for calculation of streaming and removal via collisions
- \mathcal{H} is the scattering operator responsible for transfer via scattering
- \mathcal{F} is the fission operator responsible for neutron production via fission

2.4.4 Integral form of NTE at steady state

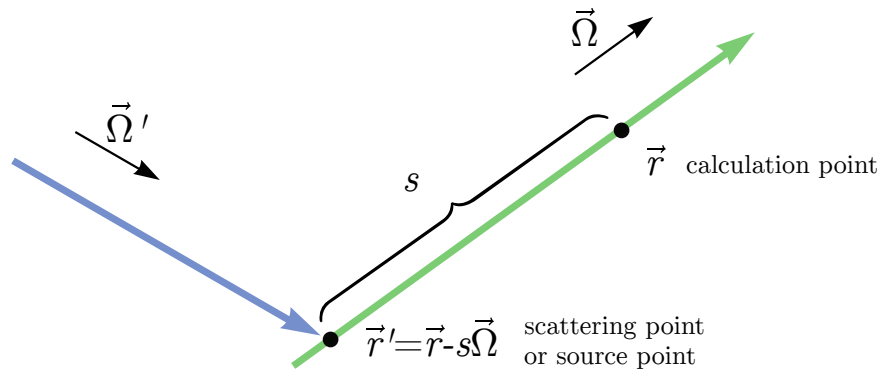


Figure 2.3: Schematic explaining the setup for derivation of the integral form of NTE [38]. Point \vec{r}' is an arbitrary point on the half-line crossing \vec{r} and spanning in the direction opposite to $\vec{\Omega}$.

Another way to express the neutron balance is to use the integral formulation of NTE. The name stems from the fact that there are no more derivatives in the equation, all the terms

are in a form of integrals. The equation is derived by considering the angular flux at a fixed point \vec{r} along direction $\vec{\Omega}$. The angular flux is then expressed as a sum of uncollided neutron angular fluxes traveling in the same direction, but originating at any point \vec{r}' such that $\vec{r}' = \vec{r} - s\vec{\Omega}$ where $s \in [0, \infty)$ (visual interpretation in Figure 2.3). The NTE in the integral form reads

$$\begin{aligned} \psi(\vec{r}, E, \vec{\Omega}) &= \int_0^\infty ds e^{-\int_0^s ds' \Sigma_t(\vec{r}-s'\vec{\Omega}, E)} S(\vec{r} - s\vec{\Omega}, E, \vec{\Omega}) \\ &+ \int_0^\infty ds e^{-\int_0^s ds' \Sigma_t(\vec{r}-s'\vec{\Omega}, E)} \int_0^\infty dE' \int_{4\pi} d^2\Omega \Sigma_s(\vec{r} - s\vec{\Omega}, E' \rightarrow E, \vec{\Omega}' \rightarrow \vec{\Omega}) \psi(\vec{r} - s\vec{\Omega}, E', \vec{\Omega}') \end{aligned} \quad (2.17)$$

The first term on the right-hand side represents the contribution of uncollided flux originating from the source S (fission source and external source). The second term represents uncollided flux that entered direction $\vec{\Omega}$ and energy E after scattering at point r' at incident direction of $\vec{\Omega}'$

The exponential term

$$e^{-\int_0^s ds' \Sigma_t(\vec{r}-s'\vec{\Omega}, E)} = e^{-\tau(s, E)} \quad (2.18)$$

expresses the chance for a neutron born at \vec{r}' to arrive at \vec{r} without collision. The exponent is often written simply as τ and called the optical length.

2.5 Solving NTE — the criticality problem

In this section we are going to look at the basics of solving the neutron transport equation for a multiplying medium, in particular a reactor core.

In a regular fission reactor, once the chain reaction is initiated, the neutron population is sustained by neutron-induced fission. The external source term S_{ext} is assumed to be equal to zero² which gives us the following form of NTE:

$$(\mathcal{L} - \mathcal{H})\psi = \mathcal{F}\psi \quad (2.19)$$

The steady-state formulation implies that production and removal of neutrons has to be in balance everywhere in the system. The situation of a perfect balance regarding neutron population would require a remarkable fine tuning. In most configurations, the system does not have any time-independent solutions, i.e., the initial neutron population will either die out completely (if $k < 0$) or increase indefinitely (if $k > 0$). In order to force the time-independent solution of Eq. (2.19), the equation is reformulated as an eigenvalue problem with an additional term $\frac{1}{k}$:

$$(\mathcal{L} - \mathcal{H})\psi = \frac{1}{k}\mathcal{F}\psi \quad (2.20)$$

The division of a fission term by k ensures a steady-state solution by artificially increasing or decreasing the neutron production by fission.

²Sources of neutrons other than fission do exist in a reactor core, e.g., spontaneous fission of actinides; however, their impact during nominal operation is negligible.

The solution to Eq. (2.20) are the eigenvalue k and flux distribution (eigenvector), which have to be found simultaneously. In general, the equation (2.20) has multiple solutions. However, it is possible to show that the only value of k that is physically correct, i.e., guarantees non-negative flux values everywhere in the system, is the highest one, most often called k_0 . Although useful in some applications, the remaining, “unphysical” values of k are not of interest for this thesis, thus, the symbol k will always denote the eigenvalue k_0 . It is important to note that the eigenvalue k is equivalent to the effective multiplication factor k that was introduced in the first chapter. In fact, solving the eigenvalue problem of Eq. (2.20) to find a stable solution is the same problem as seeking the multiplication factor of the system (together with the flux shape).

Solving the criticality problem is one of the most important tasks in the domain of reactor analysis. Because of the complexity of the transport equation (six variables, anisotropy and angular dependencies, complex behavior of cross-sections with respect to neutron energy) the equation can be solved analytically only for a very limited range of cases, none of which match the highly complex case of a reactor core. For this reason, a wide variety of numerical methods was conceived to aid the reactor studies.

The numerical computations are a huge branch of reactor physics and many different approaches were developed over time. The next section discusses the basics of the most important deterministic numerical methods used for solving the steady-state transport equation. The methods described are later used to create the deterministic calculation scheme for the CADOR reactor in APOLLO3[®] code.

2.6 Deterministic methods

2.6.1 Energy discretization

In all deterministic transport codes the NTE is transformed from its continuous-energy form to a discrete energy form. The continuous-energy domain is divided into N_g intervals called energy groups, ordered from the highest to lowest energy (Figure 2.4). After the discretization, all neutrons within a given energy group $g = [E^{g+1}, E^g]$ are considered to have the same kinetic energy. The flux in group g is determined by integration of continuous-energy flux

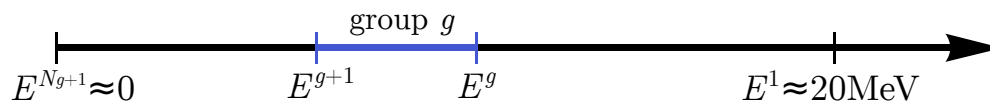


Figure 2.4: Neutron energy discretization.

over the limits of the energy group

$$\psi^g(\vec{r}, \vec{\Omega}) = \int_{E^{g+1}}^{E^g} dE \psi(\vec{r}, \theta E, \vec{\Omega}) \text{ for } g \in \{0, \dots, N_g\} \quad (2.21)$$

Because the values of cross-sections are also energy-dependent, they need to be discretized in a similar fashion, with ψ^g used as a weighting function

$$\begin{aligned}\Sigma_t^g(\vec{r}, \vec{\Omega}) &= \frac{1}{\psi^g(\vec{r}, \vec{\Omega})} \int_{E^{g+1}}^{E^g} dE \Sigma_t(\vec{r}, E) \psi(\vec{r}, E, \vec{\Omega}) \\ \Sigma_s^{g' \rightarrow g}(\vec{r}, \vec{\Omega}' \rightarrow \vec{\Omega}) &= \frac{1}{\psi^g(\vec{r}, \vec{\Omega})} \int_{E^{g+1}}^{E^g} dE \int_{E^{g'+1}}^{E^{g'}} dE' \Sigma_s(\vec{r}, E' \rightarrow E, \vec{\Omega}' \rightarrow \vec{\Omega}) \psi(\vec{r}, E, \vec{\Omega}) \quad (2.22) \\ \Sigma_f^g(\vec{r}) &= \frac{1}{\phi^g(\vec{r})} \int_{E^{g+1}}^{E^g} dE \Sigma_f(\vec{r}, E) \phi^g(\vec{r}, E)\end{aligned}$$

Analogical equations can be written for χ and ν .

Inserting Eq. (2.21) and Eqs. (2.22) into the transport equation results in a formulation known as multigroup transport equation. The transport equation (2.20) can be then represented as a set of N_g linear equations with a following matrix form:

$$\begin{bmatrix} \mathcal{L}^1 - \mathcal{H}^{1 \rightarrow 1} & \dots & -\mathcal{H}^{1 \rightarrow g} & \dots & -\mathcal{H}^{1 \rightarrow N_g} \\ \vdots & \ddots & \vdots & \ddots & \vdots \\ -\mathcal{H}^{g \rightarrow 1} & \dots & \mathcal{L}^g - \mathcal{H}^{g \rightarrow g} & \dots & -\mathcal{H}^{g \rightarrow N_g} \\ \vdots & \ddots & \vdots & \ddots & \vdots \\ -\mathcal{H}^{N_g \rightarrow 1} & \dots & -\mathcal{H}^{N_g \rightarrow g} & \dots & \mathcal{L}^{N_g} - \mathcal{H}^{N_g \rightarrow N_g} \end{bmatrix} \begin{bmatrix} \psi^1(\vec{r}, \vec{\Omega}) \\ \vdots \\ \psi^g(\vec{r}, \vec{\Omega}) \\ \vdots \\ \psi^{N_g}(\vec{r}, \vec{\Omega}) \end{bmatrix} = \frac{1}{k} \begin{bmatrix} \mathcal{F}^1 \psi^1(\vec{r}, \vec{\Omega}) \\ \vdots \\ \mathcal{F}^g \psi^g(\vec{r}, \vec{\Omega}) \\ \vdots \\ \mathcal{F}^{N_g} \psi^{N_g}(\vec{r}, \vec{\Omega}) \end{bmatrix} \quad (2.23)$$

Such a formulation is equivalent to the continuous-energy transport equation — the integrals over entire energy domain were replaced with a sum of piecewise integrals spanning over the same domain. However, it is easy to notice that to get the exact multigroup formulation, i.e., one that preserves the neutron balance of the continuous-energy formulation, the continuous angular flux $\psi(\vec{r}, E, \vec{\Omega})$, that is, a sought solution to the problem, has to be known beforehand. It means that, in practice, the multigroup formalism can only be applied as an approximation of its exact form if we want to use it for solving the NTE numerically. Another problem is that the multigroup cross-section resulting from angular flux weighting are angle-dependent.

In case of neutron transport codes, the multigroup cross-section libraries are first created by weighting the pointwise cross-sections with one of predefined angle-independent flux shapes $\varphi(E)$ (this way a problematic angular dependence of the total cross-section Σ_t^g also disappears) [36]. As a consequence, the initial guess of the weighting flux has to be later corrected in neutron transport calculation in a process called self-shielding calculation (Section 2.6.5).

The energy intervals from 1 to N_g constitute an energy mesh. In practice, the size of intervals is never equal. The sizes of energy groups are chosen to match the average neutron energy loss at collision and to account for important resonances in cross-section. The number of energy groups required to faithfully reproduce all the spectral effects is far higher than what is achievable with modern computers. Therefore the choice of energy mesh must be made carefully in order to get sufficiently accurate results within a reasonable computation time.

With the limitation on the number of energy groups a universal energy mesh cannot be conceived; each type of spectrum requires different choice of energy mesh. In case of state-of-the-art fast reactor calculations fine meshes are used, in case of APOLLO3[®] the most popular one having almost 2000 energy groups [39].

2.6.2 Power iteration method, external and internal iterations

Very generally, the equation (2.20) can be solved by iterative methods such as power iteration. The idea is to start with an initial guess of the flux distribution $\psi_{(e=0)}$ and the multiplication factor $k_{(e=0)}$. From this point, an iterative scheme is established. The fission source $S_{f,(e)}$ is calculated as

$$S_{f,(e)} = \frac{1}{k_{(e)}} \mathcal{F} \psi_{(e)} \quad (2.24)$$

To obtain the new flux $\psi_{(e+1)}$, the transport equation of a form

$$(\mathcal{L} - \mathcal{H}) \psi_{(e+1)} = S_{f,(e)} \quad (2.25)$$

has to be solved. Then, the new fission source $S_{f,(e+1)}$ is computed with Eq. (2.24). In each iteration the value of k is updated as

$$k_{(e+1)} = k_{(e)} \frac{\int_D d^3r \int_0^\infty dE \int_{4\pi} d^2\Omega \mathcal{F} \psi_{(e+1)}}{\int_D d^3r \int_0^\infty dE \int_{4\pi} d^2\Omega \mathcal{F} \psi_{(e)}} \quad (2.26)$$

where D is used to represent the entire spatial domain. This iterative scheme is known as a power iteration.

Updating the S_f and k is known as an external iteration. Within each external iteration an internal iteration is nested. The internal iteration handles the calculation of flux from a known fission source (Eq. (2.25)).

The iteration in the internal loop is established by using multigroup transport equations as presented in Eq. (2.23). The iteration starts in the highest energy group $g = 1$ and descends to the lowest group $g = N_g$ while calculating angular flux in each group one-by-one. The transport equation in group g within external iteration e can be written as

$$\left(\vec{\Omega} \cdot \vec{\nabla} + \Sigma^g \right) \psi_{(e+1)}^g(\vec{r}, \vec{\Omega}) = \int_{4\pi} d^2\Omega \Sigma_s^{g \rightarrow g} \psi_{(e+1)}^g + S_{(e+1)}^g \quad (2.27)$$

where the source $S_{(e+1)}^g$ is defined as

$$S_{(e+1)}^g = \underbrace{\sum_{g' > g} \int_{4\pi} d^2\Omega \Sigma_s^{g' \rightarrow g} \psi_{(e)}^{g'}}_{\text{upscattering}} + \underbrace{\sum_{g' < g} \int_{4\pi} d^2\Omega \Sigma_s^{g' \rightarrow g} \psi_{(e+1)}^{g'}}_{\text{downscattering}} + \underbrace{\frac{1}{k_{(e)}} \sum_x \sum_{g'=1}^{N_g} \chi_x^{g' \rightarrow g} \nu_x^{g'} \Sigma_{f,x}^{g'} \phi_{(e)}^{g'}}_{\text{fission}} \quad (2.28)$$

where downscattering is the neutron scattering from higher to lower energies and upscattering is the scattering from lower to higher energy. The variables \vec{r} and $\vec{\Omega}$ were skipped for clarity.

The Eq. (2.27) is a fixed source problem — all neutron sources outside of group g are included in a known term $S_{(e+1)}^g$. The solution of the NTE is therefore reduced to solving multiple monokinetic transport equations with a fixed source, one per each energy group. The down-scattering source for group g are already updated, as the equation was already solved for higher energy groups $g' < g$. Upscattering sources are taken from the previous external iteration. In practice, multiple inner iterations can be used to converge on the upscattering sources by updating them in each inner loop.

In real applications, many of the sources are equal to zero. Fission source appears almost exclusively in fast energy groups and the neutron upscattering is possible only at low neutron energies. On the other hand, the downscattering is always possible, which justifies why the iteration, and as a consequence the group numbering, starts at from the highest energy group.

2.6.3 Expansion of the scattering cross-section

Expansion of scattering cross-section Σ_s into Legendre polynomials is a technique widely adopted by deterministic transport codes. In an isotropic medium, which applies to all nuclear reactors, the Σ_s depends only on the cosine of the polar angle between incoming and outgoing direction $\vec{\Omega}' \cdot \vec{\Omega} = \mu$. The dependence on the cosine μ can be expressed in terms of Legendre polynomials P_l :

$$\Sigma^{g' \rightarrow g}(\vec{r}, \mu) \psi^g(\vec{r}, \vec{\Omega}) = \frac{1}{4\pi} \sum_{l=0}^L \Sigma_{sl}^{g' \rightarrow g}(\vec{r}) P_l(\mu) \quad (2.29)$$

where each moment of the scattering cross-section is expressed as

$$\Sigma_{sl}^{g' \rightarrow g}(\vec{r}) = (2l + 1) \int_{-1}^1 d\mu \Sigma_s^{g' \rightarrow g}(\vec{r}, \mu) P_l(\mu) \quad (2.30)$$

The scattering cross-section contained in nuclear data libraries are already tabulated in a form of Legendre moments, therefore using this kind of formalism in neutron transport codes is a straightforward solution.

The formulas above are exact for $L \rightarrow \infty$. In practice, only a limited order of the expansion is used during calculation, the remaining terms being truncated. Multigroup libraries of scattering cross-sections used in APOLLO3[®] are available up to $L = 5$, which is often called P5 anisotropy order. In case of fast reactors it is rare to apply higher order than P3.

To get the new form of the scattering term (Eq. (2.4.2)) using the moments of scattering cross-section, first, the Legendre polynomials P_l in Eq. (2.29) are replaced with real spherical harmonics [40]:

$$P_l(\vec{\Omega}' \cdot \vec{\Omega}) = \sum_{m=-l}^l A_{lm}(\vec{\Omega}') A_{lm}(\vec{\Omega}) \quad (2.31)$$

By inserting the resulting relation into the definition of the scattering term, the final formula is achieved:

$$[\mathcal{H}\psi]^g(\vec{r}, \vec{\Omega}) = \frac{1}{4\pi} \sum_{l=0}^L \sum_{m=-l}^l \Sigma_{sl}^{g' \rightarrow g}(\vec{r}) A_{lm}(\vec{\Omega}) \phi_{lm}^{g'}(\vec{r}) \quad (2.32)$$

where ϕ_{lm}^g are the moments of angular flux expanded on spherical harmonics

$$\phi_{lm}^g(\vec{r}) = \int_{4\pi} d^2\Omega A_{lm}(\vec{\Omega})\psi^g(\vec{r}, \vec{\Omega}) \quad (2.33)$$

It is worth noting that for $l = 0$ ϕ_{lm}^g is equal to the scalar flux ϕ^g .

2.6.4 Angular and spatial discretization methods

After discussing the energy discretization, present in all deterministic solutions of the transport equation, it is time to discuss the ways of handling the angular variable $\vec{\Omega}$ and the spatial variable \vec{r} . Unlike for multigroup formalism, there are many ways to discretize the transport equations with respect to angle and space, many of which differ significantly from each other. The choice of each method can be crucial from the point of view of accuracy and computation time, and should be chosen accordingly to the type of problem that needs to be solved.

The section contains a brief overview of the methods used in this work. The descriptions are by no means exhaustive and are meant to only provide explanations of the most crucial concepts, models and related assumption. For more information on each of the methods, the author recommends using the multiple sources cited in this section.

2.6.4.1 Discrete ordinates method (S_n)

The method of discrete ordinates (S_n) is a collocation method based on the discretization of the solid angle into a finite set of directions

$$\{\vec{\Omega}_n, n = 1, N_\Omega\} \quad (2.34)$$

By applying this approximation, the integrals over solid angle for any function $f(\vec{\Omega})$ can be replaced by a weighted sum of $f(\vec{\Omega}_n)$. In case of angular flux this approximation looks as follows:

$$\int_{4\pi} d^2\Omega \psi^g(\vec{r}, \vec{\Omega}) \approx \sum_{n=1}^{N_\Omega} w_n \psi_n^g(\vec{r}), \quad \psi_n^g(\vec{r}) = \psi^g(\vec{r}, \vec{\Omega}_n) \quad (2.35)$$

The set of angles and weights $\{\vec{\Omega}_n, w_n\}$ is chosen in accordance with the quadrature formula of choice. The discrete ordinates method allows for rewriting the transport equation into a set of n equations, each along one discrete direction. The equations are coupled through the source term only, therefore, for a fixed source problem the equations can be solved independently. This feature gives an easy method for establishing parallel calculations, taking advantage of a multi-thread architecture of modern computers.

The fission source is easy to distribute over the discrete directions as the source is always isotropic. In case of scattering sources, the source at any given direction can be calculated with Eq. (2.32), the only change being that in the S_n method the flux moments are approximated as

$$\phi_{l,m}(\vec{r}) = \int_{4\pi} d^2\Omega A_{lm}(\vec{\Omega})\psi(\vec{r}, \vec{\Omega}) \approx \sum_{n=1}^{N_\Omega} A_{lm}(\vec{\Omega}_n)w_n\psi_n^g \quad (2.36)$$

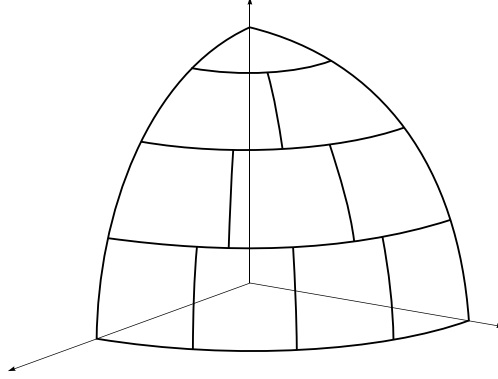


Figure 2.5: Example of division of solid angle into discrete ordinates of order S_8 (80 directions in total) [41].

2.6.4.2 Method of Spherical harmonics (P_n)

Another method to handle the angular variable is a projection on a set of real spherical harmonics $A_{lm}(\vec{\Omega})$, commonly called a P_n method [40, 42]. The angular flux is expressed as a sum

$$\psi^g(\vec{r}, \vec{\Omega}) = \sum_{l=0}^n \sum_{m=-l}^l A_{lm}(\vec{\Omega}) \phi_{lm}^g(\vec{r}) \quad (2.37)$$

where $\phi_{lm}^g(\vec{r})$ are the flux moments sought. The source term S is also expanded onto spherical harmonics analogically to the angular flux. For the purpose of numerical calculations, the expansion is truncated at a given finite order n , resulting in $(n+1)^2$ equations for each group g to be solved.

2.6.4.3 Collision probability method

The Collision Probability Method (CPM) is a method based on the integral form of transport equation (Eq. (2.17)). The underlying assumption of CPM is to consider all neutron sources to be isotropic, including the scattering sources ($\Sigma_s^{g' \rightarrow g}(\vec{r}, \mu) = \frac{1}{4\pi} \Sigma_s^{g' \rightarrow g}(\vec{r})$).

We start by writing the transport equation in the integral form for an energy group g :

$$\psi^g(\vec{r}, \vec{\Omega}) = \int_0^\infty ds e^{-\tau^g(s)} S^g(\vec{r} - s\vec{\Omega}) \quad (2.38)$$

By integrating over all possible angles $\vec{\Omega}$ and subsequent change of variables under integrals $d^3r' = s^2 d^2\Omega ds$ we obtain

$$\phi^g(\vec{r}) = \int_\infty d^3r' \frac{e^{-\tau^g(s)}}{s^2} S^g(\vec{r}') \quad (2.39)$$

Next, the spatial discretization is applied: the entire spatial domain is divided into a set of regions indexed as i . In each region the source S_i^g is assumed to be constant. By multiplying each side of equation Eq. (2.39) by $\Sigma_t^g(\vec{r})$ and integrating it over volume V_i of each region,

we get an expression

$$\int_{V_j} d^3r \Sigma_t^g(\vec{r}) \phi^g(\vec{r}) = \frac{1}{4\pi} \int_{V_j} d^3r \Sigma_t^g(\vec{r}) \sum_{i=1}^{N_i} S_i^g \int_{V_i} d^3r' \frac{e^{-\tau^g(s)}}{s^2} \quad (2.40)$$

j is the region of interest, an analogue of the position \vec{r} in Eq. (2.39). The regions with index i correspond to all regions in the domain, including j . Eq. (2.40) can be rewritten by defining a notion of first collision probability P_{ij}

$$P_{ij}^g = \frac{1}{4\pi V_i} \int_{V_i} d^3r' \int_{V_j} d^3r \Sigma_t^g(\vec{r}) \frac{e^{-\tau^g(s)}}{s^2} \quad (2.41)$$

After combining Eq. (2.39) with Eq. (2.41) we obtain

$$\Sigma_{t,j}^g \phi_j^g V_j = \sum_{i=1}^{N_i} P_{ij}^g S_i^g V_i \quad (2.42)$$

where

- ϕ_j^g is a volume-averaged scalar flux in group g and volume i
- $\Sigma_{t,j}^g$ is a flux-volume-averaged total macroscopic cross-section in group g and volume i

The collision probability P_{ij} is the probability for a neutron born uniformly and isotropically in the region i to undergo its first collision in the region j . Eq. (2.42) is the integral form of the transport equation expressed in terms of collision probabilities between different regions, instead of neutron streaming from \vec{r}' to \vec{r} .

Due to the assumptions made, in each region the neutrons are born isotropically, regardless of their origin. The neutrons then travel in a straight line until they collide, in which case they either disappear or contribute to the isotropic source in the region of collision (by scattering or fission). The values of collision probabilities are relatively easy to calculate; the collision probability for neutrons born along a line between region i and j can be calculated exactly. Typically, the solution involves tracking along sufficiently many of such lines at different angles and a subsequent numerical integration to calculate the values of collision probabilities. Such procedure results in creation of $N_i \times N_i$ matrix of collision probabilities for each group g . The matrices can then be used to calculate the fluxes in each region based on the fixed neutron sources in the inner iteration.

The biggest advantage of collision probability method is its low calculation time. On the other hand, the method operates with scalar fluxes and isotropic scatterings which can be an inaccurate approximation, in particular in case of highly scattering media. The calculation time can be further decreased by using multicell approximation [43] or a double-step method.

2.6.4.4 Method of Characteristics

The Method of Characteristics (MOC) [44, 45] is another method based on the integral form of the transport equation. The equations are solved along straight lines called characteristics. Characteristic lines span from boundary to boundary across the whole domain³. Each

characteristic line is also divided into segments within each spatial regions i of the domain (Figure 2.6a). Within each region, the flux, source and cross-sections are assumed to be constant.

The angular variable is discretized by using S_n method. The characteristic lines are laid in all discrete directions $\vec{\Omega}_n$. For the purpose of this section, we are going to consider that all trajectories t are constructed along one particular direction $\vec{\Omega}_n$. The equations have to be solved for each group g , but, for the sake of clarity, the group index was skipped.

By integrating the transport equation along a segment of a characteristic line t in region i , one obtains the transmission and balance equations written as

$$\psi_i^+(t) = e^{-\Sigma_i l_i(t)} \psi_i^-(t) + \frac{1 - e^{-\Sigma_i l_i(t)}}{\Sigma_i} S_i(\vec{\Omega}) \quad (2.43)$$

$$\Sigma_i \psi_i(t) = J_i^-(t) - J_i^+(t) + S_i(\vec{\Omega}) \approx \frac{\psi_i^-(t) - \psi_i^+(t)}{l_i(t)} + S_i(\vec{\Omega}) \quad (2.44)$$

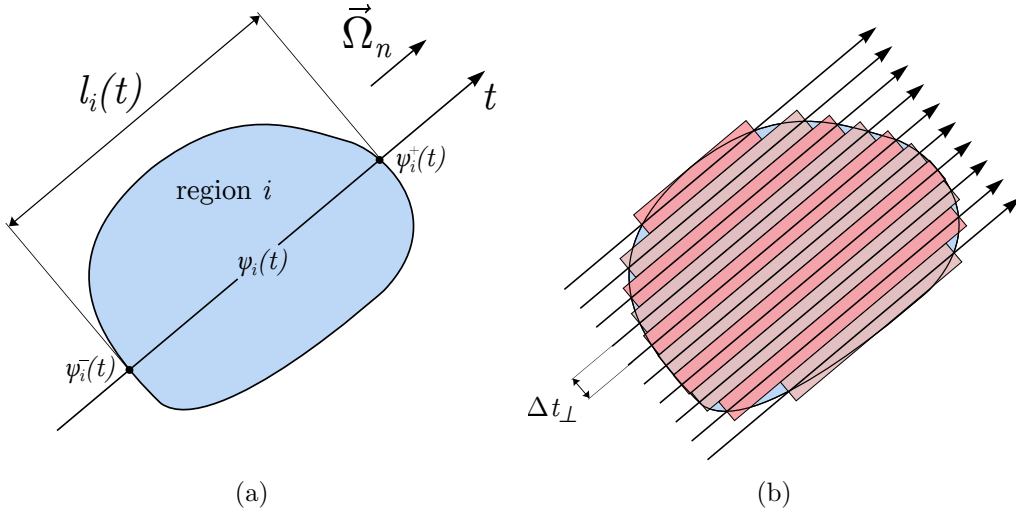


Figure 2.6: a) Single characteristic line t crossing the region i [45] b) The integration over the same region i by tracking of multiple characteristics [46].

The equations (2.43) and (2.44) the value of $\psi_i(t)$, i.e., the average flux in i along t can be calculated.

To calculate the average flux in the whole region i , a number of parallel trajectories t is laid across the region, with neighboring trajectories at a constant distance Δt_{\perp}

The volume-averaged angular flux in region i and direction $\vec{\Omega}_n$ can be calculated by integrating the results from all trajectories crossing the region (Figure 2.6b), e.g., with a simple

³More precisely this is true for so-called *long characteristics*, which is the only method discussed in this thesis.

rectangular rule

$$\psi_i(\vec{\Omega}_n) = \frac{1}{V_i} \int_{D_i} d^3r \psi(\vec{r}, \vec{\Omega}_n) \approx \frac{\sum_t \Delta t_\perp \psi_i(t) l_i(t)}{\sum_t \Delta t_\perp l_i(t)} \quad (2.45)$$

This type of calculation is repeated for all regions and all discrete directions.

The method of characteristics is a highly accurate method that requires very few assumptions, the main one being the form of variation of angular flux along the characteristic line (e.g., step, linear or polynomial). The tracking method makes it suitable for practically any kind of geometrical shapes. However, the method is generally too expensive computationally to be used in case of large geometries, especially in 3D.

2.6.4.5 Discontinuous Galerkin Finite Element Method and S_n method

Another method of solving the transport equation is to adopt the Finite Element Method (FEM), a popular numerical tool used in a variety of problems in computational physics [47]. The method subdivides the geometry into a mesh of regions called finite elements. The solution is then sought for one element at a time with a supposition that the solution must be represented in terms of basis functions. In each finite element the cross-sections are assumed to be constant.

The angular variable is projected on discrete ordinates. We are going to consider only the angular flux and source along one discrete direction ($\psi_n = \psi(\vec{r}, \vec{\Omega}_n)$ and $S_n = S(\vec{r}, \vec{\Omega}_n)$)

The first step is to transform the fixed source transport equation in group g to its weak formulation in a finite element K . The equation is multiplied by a test function $w(\vec{r})$ and integrated over entire finite element

$$\int_K w(\vec{r}) \vec{\Omega} \cdot \vec{\nabla} \psi_n + \int_K w(\vec{r}) \Sigma \psi_n = \int_K w(\vec{r}) S_n \quad (2.46)$$

After several manipulations (more details can be found in [48]) the Discontinuous Galerkin formulation of the transport equation is obtained:

$$\int_{\partial K^-} w(\vec{r}) \vec{\Omega} \cdot \vec{n}_e (\psi_n^+ - \psi_n^-) + \int_K w(\vec{r}) (\vec{\Omega} \cdot \vec{\nabla} \psi_n) + \int_K w(\vec{r}) \Sigma \psi_n = \int_K w(\vec{r}) S_n \quad (2.47)$$

where

- ∂K^- is the surface of the lightened boundary, i.e., the boundaries of the finite element K for which $\vec{\Omega}_n \cdot \vec{n} < 0$ where \vec{n} is the unit vector normal to the boundary
- ψ^- is the flux at ∂K^- in the element K
- ψ^+ is the flux at ∂K^- in adjacent finite elements that shares boundary ∂K^- with the element K

the equation introduces the so-called “upwind approximation” which assumes the discontinuity of angular flux at the lightened boundary. The jump of angular flux $\psi^+ - \psi^-$ is a non-physical behavior; however, such an approach provides a better stability of the solution [47].

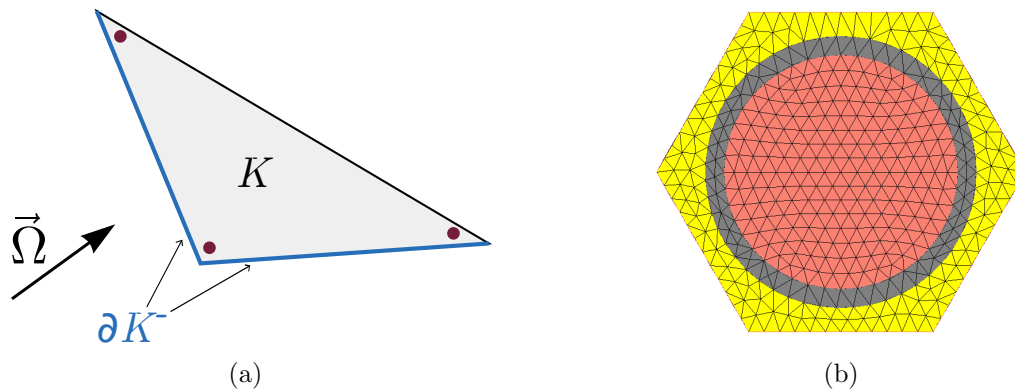


Figure 2.7: a) A single finite element K with lightened boundary marked with blue color. The dots corresponds to nodes for the expansion into first order polynomials b) Example of a mesh of finite elements created in MINARET.

The next step is to approximate the angular flux ψ_n with the expansion into polynomial basis $p(\vec{r})$:

$$\psi_n = \sum_{j=1}^{N_j} p_j(\vec{r}) \psi_n^j \text{ for } \vec{r} \in K \quad (2.48)$$

where N_j is the number of nodes per finite element. In MINARET solver [49], included as a part of APOLLO3[®], both the weights w and basis p are composed of Lagrange polynomials, i.e., $w(\vec{r}) = p_j(\vec{r})$ for each node j . Inserting Eq. (2.48) into Eq. (2.47) leads to a set of N_j equations to be solved. The finite elements are in a form of triangles for 2D geometries and prisms oriented along z axis for a 3D⁴ case. For each direction $\vec{\Omega}_n$, the finite elements are first sorted according to the propagation of angular flux. This way the upwind flux ψ_n^+ for each finite element is known, either from the boundary condition or from the angular flux solved for the previous finite element in the calculation. One inner iteration consists of a sweep through all finite elements for all discrete directions and energy groups.

The finite element method can be applied to majority of problems in reactor physics, especially in case of full core calculations. The method is not efficient in case of refined geometries that require a very fine mesh of small finite elements to properly cover the detailed areas (Figure 2.7b). High number of finite elements leads to an excessive number of equations to be solved and results in a long computation time and a huge memory footprint.

2.6.5 Self-shielding calculation

As mentioned in Section 2.6.1, the cross-sections contained in multigroup data libraries are created by the division of pointwise data weighted with a presupposed neutron flux shape. Such an approximation does not take properly into account the fine structure of resonances within each energy group. In case of in-group resonances, the flux shape within the group is typically far from being flat; instead, the flux also exhibit a fine structure, due to the sharp

⁴The prisms are created by extrusion of the plane of triangles of the 2D case along the z axis.

increase in absorption rate around resonance energies. The sharp dips in the shape of the flux cause the absorption rate in the resonances $R_a = \phi \Sigma_a$ to be in fact lower than if the flux was flat across the energy group. It is commonly stated that the resonance shields itself from neutrons, hence the name of the phenomenon — the energy self-shielding.

Analogically, spatial self-shielding describes a phenomenon where a given spatial zone is shielded from neutrons because a significant part of the neutrons is absorbed in other zones surrounding it. The spatial self-shielding effect is also dependent on the fine structure of cross-sections, as it is much less likely for neutrons at resonance energies to reach the zone of interest without being captured in its surrounding.

To accurately account for the fine structure without a need for corrections of multigroup cross-sections it would be necessary to use energy mesh of tens of thousands intervals. For a general case of a heterogeneous geometry this approach would require an impractical calculation time. In contemporary deterministic codes the impact of fine-structure and the heterogeneity of the geometry is taken into account in a separate calculation procedure called a self-shielding calculation.

There exist a number of different numerical methods used to perform the self-shielding calculation. In this section, only two of them are discussed: the Sub-group method [50, 51] and Tone's method [52, 53], as these methods are most commonly used in case of fast reactor analysis. A third method available in APOLLO3[®], a double equivalence method based on Livolant-Jeanpierre formalism [54, 41] is most often applied to thermal reactors and it was not used in the thesis.

2.6.5.1 Bondarenko iterations

In both Sub-group and Tone's method, the interference between resonances of different isotopes is resolved via so-called Bondarenko iteration. The idea of this method is to derive the self-shielded microscopic cross-section of the resonant isotopes one-by-one, while representing the impact of the remaining isotopes collectively as a sum of their group cross-sections (constant within the group). The self-shielding calculation is performed to solve the slowing down equation and obtain the corrected value of σ_x^g for a resonant isotope x , then the procedure is repeated for the next resonant isotope with the updated group cross-section of isotope x from the previous calculation. The iteration is performed until a convergence of all group cross-section is achieved.

While discussing the self-shielding methods, the equations are written for a single isotope x , although it is implicitly assumed that the procedure is repeated for the other resonant isotopes via Bondarenko iteration.

2.6.5.2 Sub-group method

The idea of sub-group method is to represent the fine in-group structure of cross-sections by defining a set of probability tables for each group. A probability table is a quadrature set consisting of values of cross-section σ_k and associated weights in a form of discrete probabilities p_k for the cross-section in group g to have a value in a given interval $\Delta\sigma_k$ around σ_k ,

where k denotes a given sub-group in group g . The tables are created by an integration of the probability density of cross-section in group g ; for a group g and an isotope x , the set takes a following form

$$\left\{ \sigma_{t,x,k}^g, p_{x,k}^g, \{ \sigma_{\rho,x,k}^g \}_\rho \text{ for } k = 1, K^g \right\} \quad (2.49)$$

where index t signifies total cross-section and index ρ stands for reaction type.

In case of APOLLO3[®] the probability tables are created by a CALENDF code [55], a part of GALILEE processing tool [56]. By using this approach, the distribution of resonances within group g is represented in terms of probabilities rather than their actual location and shape. Because of that, it is necessary for the method to assume that the neutron source is distributed evenly within each group; the resonances and slowing-down sources are seen as independent.

By combining the multigroup and sub-group formalism the solution of the equation of self-shielded group cross-section can be approximated as [51]:

$$\sigma_{x,\rho}^g = \frac{\int_g \sigma_{\rho,x} \phi(E) dE}{\int_g \phi(E) dE} \approx \frac{\sum_k \sigma_{\rho,x,k}^g p_{x,k}^g \phi_{x,k}^g}{\sum_k p_{x,k}^g \phi_{x,k}^g} \quad (2.50)$$

where $\phi_{x,k}^g$ is a scalar flux in group g and sub-group k , assuming that the cross-section of isotope x is $\sigma_{x,k}^g$.

To calculate the values of fluxes $\phi_{x,k}^g$ the neutron source in group g has to be known first. To obtain the source, it is necessary to couple the sub-group method with a multigroup solver of flux calculation. Once the sources are known the solver of sub-group method solves the transport equation for one sub-group k at a time:

$$\vec{\Omega} \cdot \nabla \psi_k^g + \Sigma_{t,k}^g \psi_k^g = S_k^g \quad (2.51)$$

Because of the approximation of Bondarenko iterations, only the isotope x is subjected to sub-group formalism, thus, the total cross-section used in the transport equation for group g and sub-group k is represented as

$$\Sigma_{t,k}^g = N_x \sigma_{t,x,k}^g + \sum_{y \neq x} \Sigma_{t,y}^g \quad (2.52)$$

The procedure is iteratively solved for all self-shielding zones, energy groups, sub-groups and resonant isotopes until a stable solution is achieved.

Because of its high accuracy, sub-group methods is considered as a reference method for fast reactor calculations in APOLLO3[®]. The coupling with flux solver is a factor with important consequences on the computational cost of the method [51]. For this reason, the sub-group method is often replaced by other, faster self-shielding methods.

2.6.5.3 Tone's method

The Tone's self-shielding method uses a homogeneous-heterogeneous equivalence technique, which makes it similar in this respect to Livolant-Jeanpierre double equivalence method.

First, we define the slowing-down equation for an infinite homogeneous medium with resonant isotope x

$$\left[N_x \sigma_{t,x} + \sum_{y \neq x} \Sigma_{t,y}(E) \right] \phi(E) = S(E) \quad (2.53)$$

By applying the narrow resonance approximation ($S(E) \approx \Sigma_p$) we can express the neutron flux as

$$\phi(E) = \frac{C_x}{\sigma_{t,x}(E) + \sigma_{b,x}^g} \quad (2.54)$$

where $C_x = \frac{\Sigma_p}{N_x}$ is a constant term and $\sigma_{b,x}^g = \frac{1}{N_x} \sum_{y \neq x} \Sigma_y^g$ is a background cross-section composed of all isotopes other than x . Now, let us consider the heterogeneous situation. The neutron balance in region i can be written by using collision probability formalism

$$\phi_i(E) \Sigma_{t,i}(E) V_i = \sum_j P_{ij}(E) S_j(E) V_j \quad (2.55)$$

The assumption of Tone's method is that the value of P_{ij} is dependent only on the region of arrival i (and independent of j). The following relation can be thus written:

$$P_{ij}(E) = f_i^g(E) P_{ij}^g \quad (2.56)$$

where f is a coefficient for group g , dependent only of i and E .

By applying reciprocity and conservation relations of collision probabilities ($\Sigma_{t,i}^g P_{ij}^g V_i = \Sigma_{t,j}^g P_{ji}^g V_j$ and from $\sum_{V_i} P_{ij}^g = 1$) together with Tone's approximation and Narrow Resonance approximation the flux in group i is

$$\phi_i = \frac{\sum_j P_{ij}^g \Sigma_{p,j} V_j}{\sum_j P_{ij}^g \Sigma_{t,j}(E) V_j} \quad (2.57)$$

By defining the total cross-section $\Sigma_{t,j}$ as $N_x \sigma_{x,j}(E) + \sum_{y \neq x} \Sigma_{y,j}^g$, a suitable form for Bondarenko iterations, and rearranging equation. We get the final formulation of the flux

$$\phi_{x,i}(E) = \frac{D_x^g}{\sigma_{x,i}(E) + \sigma_{0,x,i}^g} \quad (2.58)$$

where

$$D_x^g = \frac{\sum_j P_{ij}^g V_j \Sigma_{p,j}}{\sum_j P_{ij}^g V_j N_{x,j}}, \quad \sigma_{0,x,i}^g = \frac{\sum_j P_{ij}^g V_j \sum_{y \neq x} \Sigma_{y,j}^g}{\sum_j P_{ij}^g V_j N_{x,j}} \quad (2.59)$$

D_x^g is a constant term and $\sigma_{0,x,i}^g$ is an equivalent background cross-section of the heterogeneous case. The equation can be used to compute the flux $\phi_{x,i}$ that is then used for the weighting of the group cross-sections $\sigma_{x,i}^g$. To perform this weighting accurately without necessity of using ultra-fine energy mesh, the probability tables (as presented before in Eq. (2.49)) are used as quadrature formulas.

The collision probability solver is used to calculate the values of P_{ij} . Contrary to the subgroup method, it is not necessary for the solver to calculate the neutron sources for each group and region which significantly speeds up the calculations.

The description in this section is based on the collision probability method as does the original derivation by Tone [52] and as is most commonly used in APOLLO3[®]. The method can be however generalized to be compliant with other formulations of the transport equation [51].

2.6.6 Homogenization/condensation and fundamental mode approximation

Even with all approximations and methods described in this chapter, solving the NTE for a large and complex geometry of a reactor core is a difficult task. The number of unknowns to be determined in the CADOR core used in this study can be estimated as follows:

- 606 fuel assemblies (202 if symmetry condition is applied), 271 fuel pins per assembly
- each pin-cell divided into at least 4 regions (sodium, cladding, gap, fuel pellet)
- 1760 energy groups
- at least 36 directions (S_4 order)
- assembly height equal to 350 cm, that has to be divided into radial planes of at most 10 cm of height

This rough estimation gives more than 10 billion unknowns to be found. If we consider also additional space discretization into finite elements or segments of characteristics, the number will increase even further. The computation time and memory storage necessary to solve this problem directly is still not feasible for current computers.

Solving this problem requires using neutron transport calculations with a different strategy. The key idea is to divide the calculation into two steps:

1. Lattice calculation that is performed with exact geometries and fine energy mesh; however, the geometries are relatively small: typically one fuel assembly or even one pin-cell
2. Core calculation that uses coarse energy mesh and simplified geometry description with homogenized macro-regions replacing the exact, fine description

The link between this two steps is the homogenization/condensation procedure. The goal of homogenization is to decrease the number of spatial regions by transforming the regions i used in lattice calculation into larger homogeneous macro-regions I . The cross-sections are assumed to be constant in each macro-region and their value has to be determined from the cross sections defined for smaller regions contained within. Analogically, the goal of condensation is to transform cross-sections defined for a fine energy mesh of groups g into a coarse mesh of macro-groups G . The result of the homogenization/condensation procedure is a new library of multigroup cross-sections with coarser energy mesh defined for each macro-region. With sufficient homogenization and condensation of the multigroup library, the transport equation can be solved for a problem size of an entire core within reasonable time and memory constraints, due to drastically reduced number of parameters.

The accuracy of core calculation relies strongly on the adequate homogenization/condensation scheme. The sizes and numbers of macro-regions and macro-groups have to be chosen in a way that preserves the most important characteristics of the neutron balance in the core while sufficiently reducing the complexity of the problem. The information about the fine structure of cross-sections and local characteristics of the geometry are lost after the procedure and thus the averaged coarse-meshes values have to be calculated in a way that minimizes the bias introduced.

It is generally accepted that the most important physical quantities to be preserved are the reaction rates. As the reaction rates are the product of cross-sections and flux, the conservation during procedure is imposed on the flux-weighted cross-sections. This means that the angular and scalar flux are not preserved in a general case.

2.6.7 Flux-volumes homogenization

A rather straightforward approach is to use only the group scalar flux ϕ^g integrated over regions i as a weighting function. Such a method is called flux-volumes homogenization. The following equations show the method applied to total and scattering cross-sections

$$\Sigma_{t,I}^G = \frac{\sum_{i \in I} \sum_{g \in G} \Sigma_{t,i}^g \phi_i^g}{\sum_{i \in I} \sum_{g \in G} \phi_i^g} \quad (2.60)$$

$$\Sigma_{sl,I}^{G' \rightarrow G} = \frac{\sum_{i \in I} \sum_{g' \in G'} \sum_{g \in G} \Sigma_{sl,i}^{g' \rightarrow g} \phi_i^{g'}}{\sum_{i \in I} \sum_{g' \in G'} \phi_i^{g'}} \quad (2.61)$$

The other cross-sections can be calculated analogically.

2.6.8 Flux moments homogenization

In case of neutron distribution with strong net currents, e.g., when solving NTE at the interface of two different assemblies, the weighting by scalar flux can be an insufficient approximation. A solution to that could be to create homogenized/collapsed cross-sections calculated with angle-dependent weights that preserve the reaction rates as they appear in the transport equation. However, when applied directly, the method results in a different form of cross-sections compared to flux-volumes: the total cross-section after homogenization is now angle-dependent (Σ_{tl}^g) and the scattering cross-section depends on azimuthal rank m ($\Sigma_{slm,I}^{G' \rightarrow G}$). A solution to this problem is the flux moments homogenization [57], which uses a neutron flux expanded into spherical harmonics as a weighting function. In this method, the scattering cross-sections are calculated as

$$\hat{\Sigma}_{sl,I}^{G' \rightarrow G} = \frac{\sum_{m=-l}^l \left(\phi_{lm,I}^G \sum_{i \in I} \sum_{g' \in G'} \sum_{g \in G} \Sigma_{sl,i}^{g' \rightarrow g} \phi_{lm,i}^{g'} \right)}{\sum_{m=-l}^l \left(\phi_{lm,I}^{G'} \right)^2} + \delta_{G,G'} \left(\Sigma_{t,I}^{G'} - \Sigma_{tl,I}^{G'} \right) \quad (2.62)$$

where δ is the Kronecker delta and $\Sigma_{tl,I}^G$ is equal to

$$\Sigma_{tl,I}^G = \frac{\sum_{m=-l}^l \left(\phi_{lm,I}^G \sum_{i \in I} \sum_{g \in G} \Sigma_{t,i}^g \phi_{lm,i}^g \right)}{\sum_{m=-l}^l \left(\phi_{lm,I}^G \right)^2} \quad \text{for } l > 0 \quad (2.63)$$

The Eq. (2.62) produces scattering cross-sections without dependence on rank m . The idea behind the equation is to minimize the difference of source term between $\hat{\Sigma}_{sl,I}^{G' \rightarrow G}$ and m -dependent $\Sigma_{slm,I}^{G' \rightarrow G}$ by applying a least-square reduction. Additionally, the rightmost term in Eq. (2.62) allows using the flux-volume weighted total cross-section $\Sigma_{t,I}^G$ from Eq. (2.60) instead of $\Sigma_{tl,I}^G$ that depends on expansion order l .

2.6.9 Fundamental mode approximation and leakage models

As explained at the beginning of this section, the homogenized and condensed cross-sections are calculated with a small geometry, e.g., a single fuel assembly or a limited set of assemblies. Such a calculation is typically performed with reflective boundary conditions imposed. This situation is equivalent to solving the transport equation for an infinite periodic lattice of such geometry.

In reality, even for large cores the neutron leakage is an important element of the neutron balance. Thus, the infinite lattice is not an accurate representation of the finite core behavior. On the other hand, to evaluate the leakage directly it would be necessary to use the whole core geometry, which is an unfeasible task. The solution is to use leakage models that simulate the finite dimensions of the core in the lattice calculation.

The fundamental mode approximation in an infinite homogeneous medium assumes that the angular flux can be factorized as [58]

$$\psi^g(\vec{r}, \vec{\Omega}) = \varphi^g(\vec{\Omega}) e^{i\vec{B} \cdot \vec{r}} \quad (2.64)$$

where i is the imaginary unit. The φ represents the energetic and angular dependence of the angular flux. The space-dependence of the angular flux is expressed by a combination of exponential functions $e^{i\vec{B} \cdot \vec{r}}$ defined through an arbitrary vector \vec{B} .

Eq. (2.65) is then inserted into a transport equation defined for an infinite homogeneous medium. By solving the transport equation in such a form we can obtain the value of critical buckling $B^2 = |\vec{B}|^2$ and associated leakage coefficients D^g

$$D^g = \frac{i\vec{B} \cdot \vec{J}^g}{B^2 \varphi^g} \quad (2.65)$$

Depending on the order of Legendre expansion of the scattering, the method is called homogeneous B_0 or homogeneous B_1 model.

To find the critical conditions, the leakage model is applied to the lattice calculation in the following way:

1. the heterogeneous flux calculation is performed with reflective boundaries and without leakage model
2. the cross-sections are homogenized into a single medium
3. the transport equation is solved for fundamental mode of infinite homogeneous medium to obtain values of B^2 and D^g
4. the heterogeneous flux calculation is repeated, this time with leakage cross-section $D^g B^2$ acting as an additional capture cross-section
5. the procedure is repeated until the values of $D^g B^2$ are such that heterogeneous lattice calculation results in k sufficiently close to 1

Once the critical configuration is found the homogenization/condensation procedure can be applied.

2.6.10 Calculation scheme in APOLLO3[®]

The goal of this section is to summarize the numerical methods discussed in the chapter by providing a general overview of deterministic two-step calculation scheme used in fast reactor analysis. The scheme presented in Figure 2.8 is a simplified and generalized version of the full scheme. More detailed description of the particular scheme used in this thesis is given later in Section 5.2.

2.6.10.1 Creation of multigroup data library

Before the flux calculation can begin, the multigroup library must be created. The library is calculated based on existing evaluated nuclear data libraries such as JEFF [59], ENDF/B [60] or JENDL [61]. The multigroup formalism is applied as described in Section 2.6.1. The multigroup library has to be created only once, there is no need to recompute it before each calculation. Typically the meshes are recomputed only when a new energy mesh is to be used or when a new evaluation of nuclear data is released.

The multigroup library contains the multigroup cross section in a form of arrays or matrices in case of scattering cross-section. Additionally, the information about fine structure of resonances and probability tables are also included to be used during self-shielding calculation.

In case of fast reactors a high number of energy groups is necessary as the neutrons lose their kinetic energy less efficiently during scatterings; moreover, finer energy mesh allows for more accurate representation of threshold reactions such as inelastic scattering [38]. The fine energy mesh is also a requirement to accurately apply the self-shielding methods based on probability tables.

2.6.10.2 Lattice calculation

The general goal of the lattice calculation is to compute a set of cross-sections suitable for efficient calculation on the full core scale. In practice, this means that cross-section used in

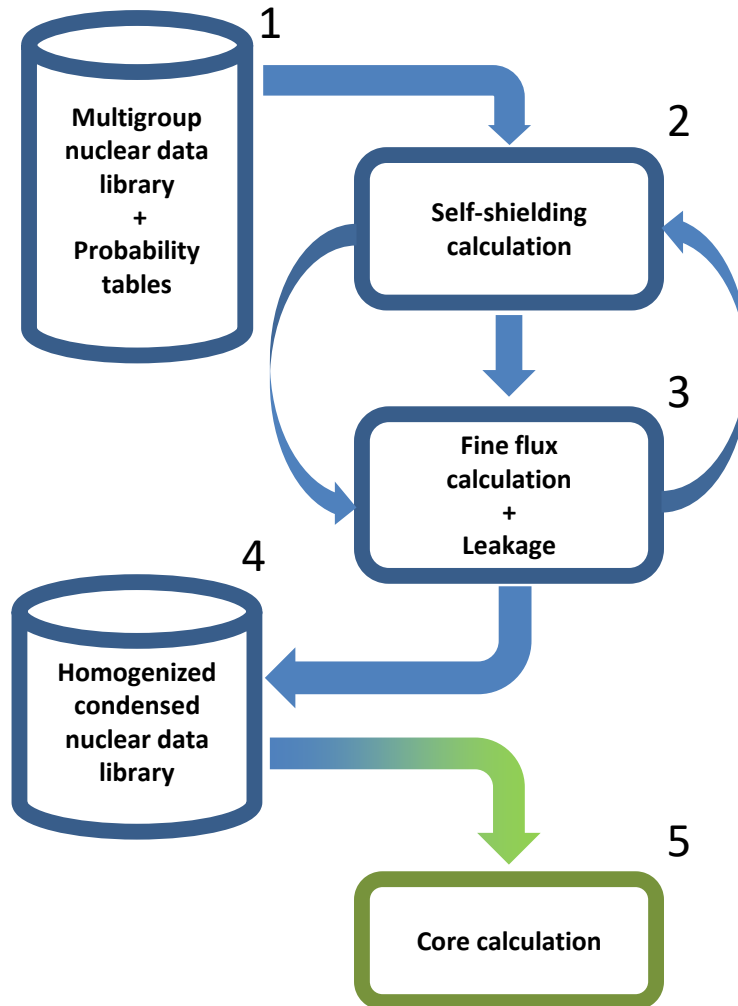


Figure 2.8: Simplified depiction of the two-step deterministic calculation scheme divided into five components.

lattice calculations are spatially homogenized into fewer regions and condensed into coarser energy mesh. In order to ensure a high accuracy in the core calculation, the homogenization/-condensation has to be performed using weighting by a representative neutron flux.

The neutron flux calculated for an isolated part of core, e.g., one fuel assembly, can be regarded as representative if it is similar to the actual flux when that element makes part of an operating core. To obtain flux shapes that are sufficiently representative, various techniques can be employed in lattice calculations depending on the part of the core to be represented. In case of a single fuel assembly, the leakage models can be applied to find the critical buckling, and subcritical assemblies can be represented as clusters (also known as colorsets) made of subcritical assembly surrounded by fuel assemblies (more in Section 5.2.2). The geometries used in this step are as detailed as possible. Normally, for such small problems the exact geometries can be used even when combined with energy mesh of few thousands

energy groups.

First, the multigroup cross-sections are corrected by performing a self-shielding calculation (Section 2.6.5). The calculation is typically performed with faster neutron transport solvers, e.g., collision probability method. Next, the self-shielded cross-sections are used in a fine flux calculation. At this stage the high accuracy solvers are used. One of the most popular choices is the method of characteristics, as it relies on very few approximations and can be easily applied to any kind of unstructured geometry. If the sub-group method of self-shielding was chosen, the coupling between self-shielding and flux calculation is necessary and both calculations are solved in a loop, with flux calculation used to update slowing-down sources in self-shielding calculation. For Tone's method, the coupling is not included, thus, self-shielding is done only once. After the calculation is over, the homogenization/condensation procedure is applied.

2.6.10.3 Creation of homogenized/condensed multigroup library

At this point, the cross-sections are homogenized into fewer spatial regions and coarser energy mesh. The cross-sections are transferred to a new multigroup library that can be used multiple times; however, because the library was created to accurately represent only one specific reactor it is generally not applicable to any other reactor geometry.

The data can be stored for several different parameters defined by user; useful parameters are, for example, coolant density, fuel temperature, or fuel burnup. The parametrization of the library allows changing parameter values in the core calculation without necessity to repeatedly recalculate the library. The cross-section for values of parameters not included explicitly in the library can still be deduced by an interpolation between the existing points.

2.6.10.4 Core calculation

Thanks to the cross-section library created in the previous step, APOLLO3[®] is now able to perform calculation with a full-scale homogeneous core model in 3D. The calculation is handled by neutron transport discrete ordinates (S_n) method with FEM (described in Section 2.6.4.5).

Due to all the simplifications applied through the entire calculation scheme, the final result of the core calculation can be affected by a noticeable systematic bias. Therefore, it is crucial to choose the most suitable modeling in each element of the scheme to minimize the accuracy issues of the final result.

2.7 Monte Carlo methods

The Monte Carlo methods [62] represent another way to solve the neutron transport equation – the stochastic approach. Instead of solving the neutron transport equation explicitly in the discretized phase space, the Monte Carlo methods focus on estimating the macroscopic quantities, such as reaction rate or neutron flux, by performing a large number microscopic simulations of single neutron histories. Each history is based on a statistical sampling: the

place of birth, initial energy or points of collision of a simulated neutron are determined by sampling of random variables. The variables are sampled from known probability distributions that represent the laws of physics, e.g., fission spectrum, angular distribution after scattering, probability of traversing a given length without collision, etc. The random sampling is in fact performed with pseudo-random numbers — numbers calculated with deterministic algorithms characterized by high statistical randomness.

A history of a single neutron can be simulated as a Markov chain — a sequence of random events where the next step is based on the state of neutron attained in the previous one. The process can be described by the following simplified algorithm [38] (Figure 2.9):

1. The neutron is born with initial parameters sampled from probability distribution of the source (distribution of the source in space, isotropic direction of emission, energy distribution according to Watt spectrum).
2. A path length traveled in a homogeneous medium until collision is sampled from the probability distribution $p(s) = \Sigma(E)e^{-\Sigma(E)s}$. If the neutron crosses an interface of two media before colliding, the path length is sampled again on the same trajectory by taking into account the cross-sections of both media. If the neutron reaches the boundary of the system, the neutron history either ends or the neutron is reflected back, depending on the settings of the simulation.
3. At the point of collision, the target nucleus x and reaction type ρ are sampled by using discrete probabilities of a form $p(\rho, x) = \frac{\Sigma_{\rho,x}}{\Sigma}$.
4. Depending on the type of reaction, a few outcomes are possible:
 - If capture is selected then the neutron history ends.
 - If fission is selected then the neutron is re-emitted, the number of neutrons born and their initial parameters are sampled. In case of criticality calculation, the neutron disappears, but the fission event contributes to the neutron source in the next iteration.
 - If scattering is selected then the kinematics of the scattering are calculated, new energy and direction is sampled from resulting distribution and the neutron continues its history.

The number of neutron histories simulated in one Monte Carlo calculation is many orders of magnitude lower than the number of free neutrons present in an actual reactor core. Typically the total number of histories simulated does not exceed few billion. However, by applying the law of large numbers we can deduce that if a sufficiently large number of neutron histories is simulated, the conditions in the actual core can be estimated statistically with an arbitrarily small uncertainty. The central limit theorem states, that the observed mean value of a random variable \bar{X} approaches the expected value μ as the number of observations N approaches infinity, with the associated standard deviation σ_X decreasing proportionally to the $\frac{1}{\sqrt{N}}$ law.

To obtain the physical quantities of interest, e.g., flux or reaction rate, the scoring procedure is performed while simulating neutron histories. The physical quantities are assessed with

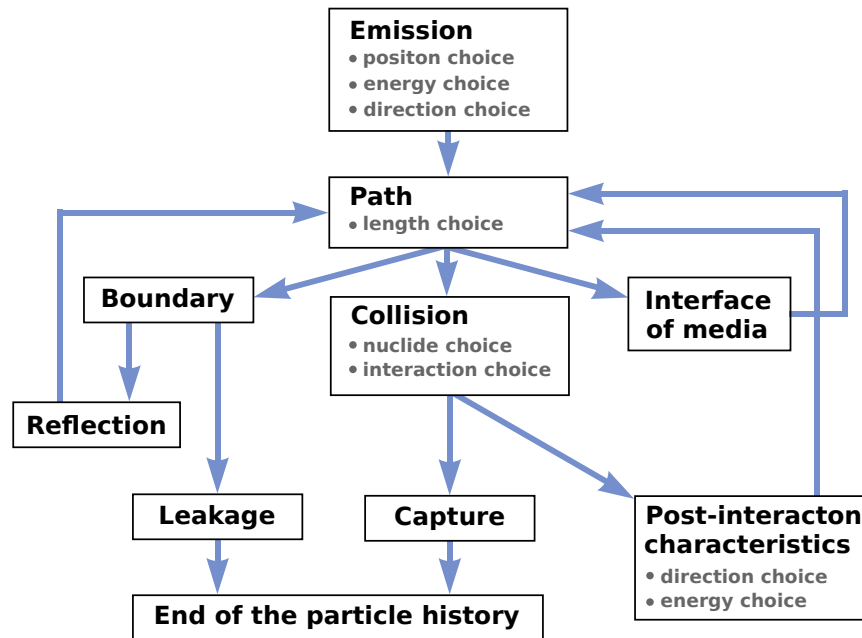


Figure 2.9: Simplified depiction of an algorithm used for simulation of a neutron history (based on [38]).

estimators — mathematical functions of the statistical observations [63]. For example, to estimate the flux in a given volume V we can either sum the total track length traversed inside V by simulated neutrons or count the total number of collisions in V . These two approaches are called track length estimator and collision estimator respectively [38, 64] (see Table 2.1).

Table 2.1: Examples of statistical estimators of flux, reaction rate and k used in Monte Carlo codes [38]. w stands for neutron weight (equal to 1 in analog simulations). In case of k the scoring must be performed in the entire volume of the system.

	multiplication factor k	neutron flux	reaction rate ρ
track length estimator	$w \nu \Sigma_f l$	$w l$	$w \Sigma_\rho l$
collision estimator	$w \frac{\nu \Sigma_f}{\Sigma}$	$w \frac{1}{\Sigma}$	$w \frac{\Sigma_\rho}{\Sigma}$
step estimator	$w \nu$	—	—

Much like the deterministic methods, the Monte Carlo methods can be used to solve criticality problems. The solution is calculated iteratively in a way similar to the deterministic power iteration (Section 2.6.2). The total number of simulated neutron histories is divided into M batches of N neutrons. The calculation starts with a guess of the neutron source distribution in the system $S_{(0)}$. Next, the source is updated iteratively: the source in batch n is calculated

according to the number of neutron multiplication reactions in batch $n - 1$. The source is normalized to preserve the same number of neutrons per batch. The value of k can be derived directly from the number of new neutrons produced per number of neutrons simulated in a batch (step estimator), or by using estimators of neutron production in the entire system based on the analogical approach as reaction rates (as described previously in Table 2.1).

The biggest advantage of continuous-energy Monte Carlo method is the lack of assumptions used in deterministic methods. Each simulation of neutron history is in fact using the exact form of transport equation, pointwise in space, energy and angle. In case of static calculations, the only approximations are related to the nuclear data and technological data used⁵. Compared to deterministic methods:

- + energy self-shielding is calculated directly as the cross-sections are continuous in energy
- + problem of spatial self-shielding does not occur as there is no assumption of flat flux in homogeneous region
- + any shape of 3D geometry can be used
- + angular distribution after collision is taken into account directly through mean cosine distributions stored in the nuclear data libraries; it is not limited by a finite number of Legendre moments or finite number of discrete ordinates
- + no need for two-step calculation scheme and homogenization/condensation of libraries
 - in order to achieve statistically meaningful results, millions or even billions of neutron histories have to be simulated. The computation time is significantly longer

Because of all these advantages and long calculation time, the continuous-energy Monte Carlo transport calculations are typically used as a high-accuracy reference for the deterministic calculation methods and schemes. This was the main way the Monte Carlo code TRIPOLI-4[®] was used in the thesis. For other applications, several simplifications can be applied to increase the efficiency of calculations, e.g., the multigroup approximation. Such compromise is not suitable to be used for reference calculations; however it can be a useful tool in other applications. In this work, the multigroup Monte Carlo calculations with homogenized cross-sections were used as a tool for validation and bias decomposition of the deterministic calculation scheme later in the text (Section 5.6).

⁵In case of time-dependent problems the approximations are bound to be introduced, e.g., to calculate the fuel burnup a coupling with deterministic depletion solver is used.

Chapter 3

Temperature-dependent phenomena in neutron transport

So far we have discussed a very general approach to neutron transport without explicitly including the temperature dependencies in the equations. This chapter is an overview of some of the effects of non-zero temperature of media on the neutron–nuclei interactions, that will become relevant during discussion of the neutron transport calculation scheme in later chapters.

3.1 Thermal motion of nuclei

At any temperature above absolute zero (0 K) every atom and molecule is subject to a thermal agitation — a random microscopic motion of particles. We are going to focus on a simple representations of the thermal motion, treating materials as an ideal free gas, regardless of their actual state. This so-called free gas model is a common way to represent the thermal motion for reactor physics applications. The random motion of free gas particles follows a Maxwell-Boltzmann distribution:

$$M_T(V) = \frac{4}{\sqrt{\pi}} \beta^{\frac{3}{2}} V^2 e^{-\beta V^2}, \quad \beta = \frac{m}{2k_B T} \quad (3.1)$$

where V is a speed of a particle, m is its mass and k_B is the Boltzmann constant. The probability distribution changes with temperature, with a general trend of average speed increasing with higher temperature (Figure 3.1). The free gas model is a very good approximation for neutron energies above few eV. For lower energies the chemical binding and the crystalline structure of some materials can require more accurate treatment e.g the Crystal Lattice Model [65]. However, in this work we focus exclusively on the free gas approximation.

3.2 Doppler effect

One of the consequences of the thermal agitation of nuclei is the Doppler effect. The microscopic cross-sections available in nuclear data libraries are tabulated as a function of kinetic

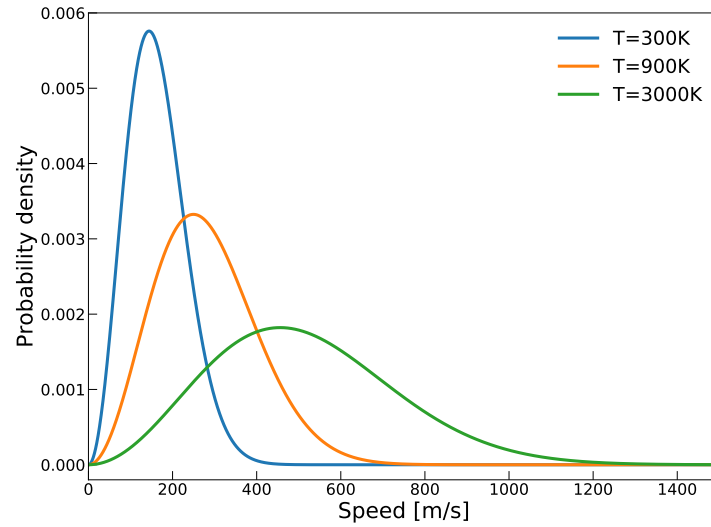


Figure 3.1: Maxwell-Boltzmann distribution of speed of ^{238}U atoms for different temperatures.

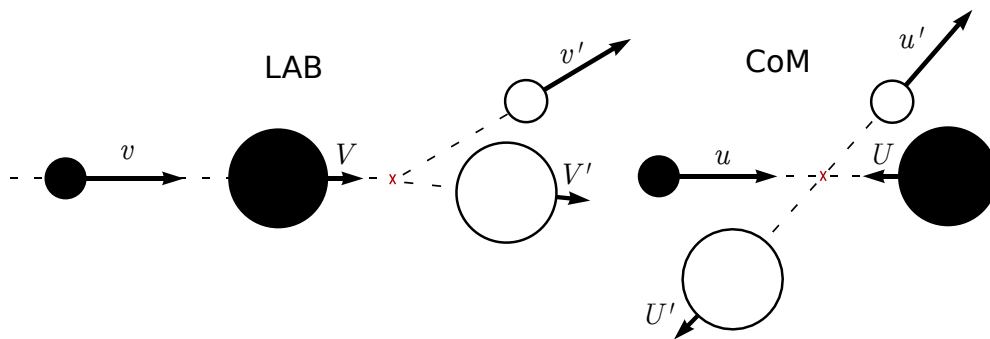


Figure 3.2: Hard sphere collision in LAB and Center of Mass (CoM) frames of reference with notation for velocity vectors used in this thesis.

energy calculated from neutron speed at the target-at-rest (TR) reference frame, i.e., a reference frame attached to the target nucleus. The neutron speed in TR is always a relative neutron–nucleus velocity

$$v_r = |\vec{v} - \vec{V}| \tag{3.2}$$

where \vec{v} and \vec{V} stand for neutron and nucleus velocity in LAB respectively. To obtain correct cross-sections as a function of v at a temperature T , denoted as $\sigma^T(v)$, the frame of reference in which the cross-sections are defined has to be changed from TR to LAB. The conversion is done by stating that the reaction rate r (per one nucleus) calculated with cross-sections in any reference frame has to be equal.

From the standpoint of solving the transport equation, we want the reaction rate r to be expressed as a product of neutron speed and corresponding value of temperature-dependent cross-section at temperature T :

$$r = v \sigma^T(v) \tag{3.3}$$

In the TR system, the relative neutron–nucleus velocity \vec{v}_r changes constantly due to thermal motion of the nucleus. To calculate the reaction rate from cross-sections given in TR, it is therefore necessary to take into account all possible values of \vec{v}_r by integrating over the Maxwell-Boltzmann probability distribution of the target speed $M_T(\vec{V})$:

$$r = \int_{\text{All } \vec{V}: v_r > 0} v_r \sigma^0(v_r) M_T(\vec{V}) d\vec{V} \tag{3.4}$$

By combining Eq. (3.3) and Eq. (3.4) we arrive at the general formula for cross-section as a function of v at a given temperature T :

$$\sigma_T(v) = \frac{1}{v} \int_{\text{All } \vec{V}: v_r > 0} v_r \sigma_0(v_r) M_T(\vec{V}) d\vec{V} \tag{3.5}$$

The equation (3.5) is often referred to as the Doppler broadening formula. The “Doppler broadening” refers to the effect of increasing temperature on the shape of resonances in cross-section: as the material temperature increases, the resonances become broader and flatter (Figure 3.3) due to a stronger variability of v_r .

3.2.1 Physical significance of the Doppler effect

At low temperatures, before the Doppler broadening, a neutron has a chance of interacting with a resonance only if its energy is in a very narrow interval around the the resonance energy. For broadened cross-sections at higher temperatures however, the effective energy span of a resonance can increase significantly.

The area under the cross-section curve remains almost unchanged during the broadening [66]. Nevertheless, the broadened resonance is more effective at “trapping” neutrons than it would be at 0 K, i.e., causes more neutron–nucleus reactions on average. The wider sides of the resonance can now trap much more neutrons than before broadening, while for energies close to the resonance peak the cross-section is still high enough to trap practically all neutrons in range. Moreover, a flatter resonance is associated with a lower self-shielding effect which further increases the reaction rate [41].

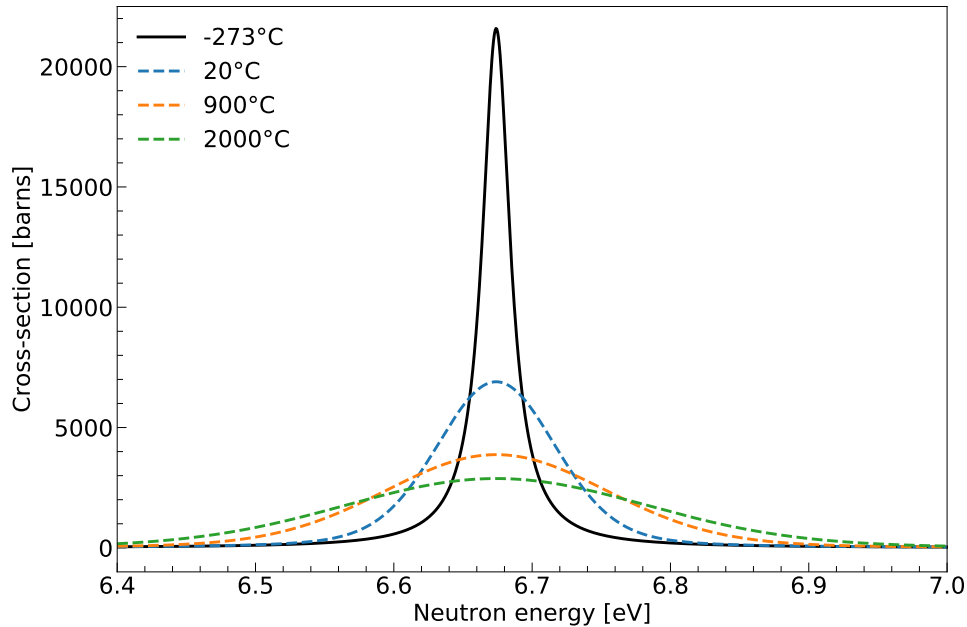


Figure 3.3: Resonance in absorption cross-section of ^{238}U at 6.67 eV for different material temperatures. The resonances are represented according to Single-Level Breit-Wigner distribution.

As stated in Chapter 1, the Doppler effect plays a central role in the negative feedback loop counteracting power variations in the nuclear core. During a transient, when the fuel temperature starts to increase, the Doppler effect raises the rate of neutron capture, primarily in ^{238}U . The surge of captures has a negative effect on further multiplication of neutrons and thus allows the temperature to go down again, which closes the feedback loop.

3.2.2 Quantification of the Doppler effect

There are many ways of estimating the magnitude of the Doppler effect. A common way is to represent it in terms of the Doppler coefficient α_D . The value of α_D corresponds to an infinitesimal change in reactivity due to the Doppler broadening caused by an infinitesimal change in temperature of a medium:

$$\alpha_D = \frac{d\rho_D}{dT} \quad (3.6)$$

However, α_D on its own is not a convenient measure of the effect during transients, as its value varies significantly with temperature. For safety studies, the integral effect over finite temperatures difference is more useful. The empirical studies show that the value of α_D in fast reactors follows an approximate relation [24]

$$\alpha_D(T) = \frac{K_D}{T} \quad (3.7)$$

where K_D is a constant of proportionality. As mentioned in Chapter 1, K_D is commonly known as the Doppler constant. By integrating Eq. (3.7) from an initial temperature T_1 to

a perturbed temperature T_2 we arrive at the formula

$$\Delta\rho_{T_1 \rightarrow T_2} = \int_{T_1}^{T_2} \alpha_D dT = K_D \ln\left(\frac{T_2}{T_1}\right) \quad (3.8)$$

that represents a total reactivity feedback caused by the temperature perturbation. If we take T_1 as the nominal fuel temperature and T_2 as the temperature of fuel fusion, we arrive at the formula for the Doppler integral to fusion, presented previously in Eq. (1.4) in Chapter 1 — the maximum available reactivity feedback before fuel meltdown. The assumption in formula (3.7) indicates that the value of K_D is independent of the two temperatures chosen for Eq. 3.8. As demonstrated in Figure 3.4, the statement is indeed a mostly accurate approximation.

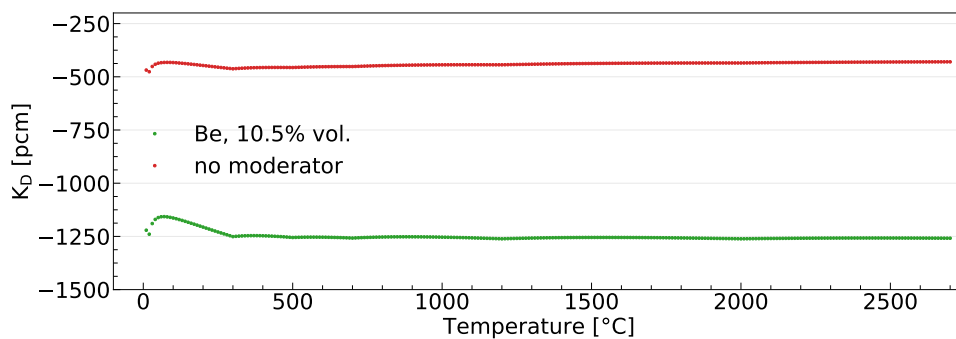


Figure 3.4: Values of the Doppler constant calculated between 0 °C and temperatures indicated on a horizontal axis. Calculations performed in APOLLO3[®] lattice module for a single fuel assembly with reflective boundary conditions.

The formula used to calculate the Doppler integral requires only one value of temperature per reactor state, which is only a coarse approximation. In real life applications, the temperature of fuel is never homogeneously distributed over the entire fuel pin. In an actual nuclear core the distribution depends on a number of factors, e.g., local power profile and heat transfer between components. Multiphysics calculations can be used to estimate the temperature distribution in the fuel pellets, for example, by dividing the pellets into several concentric rings. However, such a solution requires a coupling between neutronics and thermohydraulics codes and, as a consequence, substantially larger computation power. Instead, to easily calculate the Doppler effect, a concept of effective temperature T_{eff} is often used. The effective temperature is a single value of temperature that results in a Doppler reactivity effect of the same magnitude as for a realistic temperature distribution in fuel. The formulas for calculating T_{eff} are most often derived experimentally. One of the most popular ones is “Rowlands effective temperature” [41] given as

$$T_{\text{eff}} = \frac{5}{9}T_{\text{surface}} + \frac{4}{9}T_{\text{center}} \quad (\text{for cylindrical shape of fuel}) \quad (3.9)$$

In case of the MOX fuels used in this thesis, the T_{eff} corresponding to the onset of fusion at the center of the pellet is around 2300 °C, significantly lower than the fusion temperature

itself (about 2750 °C). In this work, when discussing the magnitude of Doppler effect, the temperatures given should always be treated as effective temperatures.

3.2.3 Doppler broadening in numerical calculations

The cross-section libraries used in calculation codes typically contain cross-sections processed for several different temperatures. In a popular nuclear data processing code NJOY [36] the computation of broadened cross-sections is handled by the BROADR module. The module uses an exact deterministic method of broadening of tabulated cross-sections called SIGMA1, developed in 1976 by Cullen and Weisbin [67].

An alternative, less common method is to perform on-the-fly Doppler broadening each time the cross-section is needed. Such solution was implemented, for example, in Monte Carlo codes MCNP [68] and PATMOS [69].

3.3 Scattering kernel

So far in this chapter we discussed only the temperature dependence of cross-section as a function of velocity of a neutron before the collision. In case of scattering reaction however, the outgoing neutron direction and energy are equally important and have to be taken into account when computing the neutron balance.

The scattering cross-section can be represented as a derivative of the scattering cross-section $\sigma_s(E)$ with respect to the energy E' and direction $\vec{\Omega}'$ of the neutron after the scattering:

$$\sigma_s(E \rightarrow E', \vec{\Omega} \rightarrow \vec{\Omega}') \quad (3.10)$$

In case of isotropic medium, the cross-sections are independent of the direction of the incoming neutron and the energy transfer depends only on the cosine of neutron scattering angle $\vec{\Omega} \cdot \vec{\Omega}' = \mu$. In such a case, the cross-section can be expressed as follows:

$$\sigma_s(E \rightarrow E', \vec{\Omega} \rightarrow \vec{\Omega}') = \frac{1}{2\pi} \sigma_s(E) P(E \rightarrow E', \mu) \quad (3.11)$$

where P is a joint probability distribution for neutron scattering from initial energy E to E' and at a scattering cosine equal to μ , commonly known as a scattering kernel. The scattering kernel is normalized so that

$$\int_0^\infty dE \int_{-1}^1 d\mu P(E \rightarrow E', \mu) = 1 \quad (3.12)$$

Much like cross-section σ_s , the scattering kernel is also dependent on the temperature of the medium. However, dealing with exact representation of temperature-dependent scattering kernel is a cumbersome task even when free gas model is assumed and, therefore, several simplified approaches were developed.

3.4 Asymptotic kernel

Asymptotic Kernel (AK) is the most simplified version of scattering kernel used in reactor physics. AK assumes that the target nucleus is always at rest during the collision ($V = 0$). In this case the center-of-mass speed depends solely on the incoming neutron speed v and masses of neutron and nucleus.

Because the rest mass of every neutron is exactly the same, instead of using masses, it is customary to substitute them with their ratio

$$A = \frac{M}{m} \tag{3.13}$$

where m and M are mass of neutron and mass of nucleus respectively. Since the target is at rest, the expression for the speed of the center of mass V_C is reduced to

$$V_C = \frac{1}{A+1}v \tag{3.14}$$

and consequently the neutron and target velocities in CoM are described as

$$\vec{U} = -\vec{V}_C = \frac{1}{A+1}\vec{v}, \quad \vec{u} = \frac{A}{A+1}\vec{v} \tag{3.15}$$

By applying the momentum and energy conservation laws to the state before and after collision we arrive at an expression

$$\frac{E'}{E} = \frac{A^2 + 1 + 2A\mu}{(A+1)^2} \tag{3.16}$$

that links the ratio of kinetic energy of neutron before and after collision to μ_C — a cosine of scattering angle in CoM, and mass ratio A . The maximum kinetic energy loss (or minimum of E') happens at the backscattering angle $\theta = 180^\circ$ ($\mu_C = -1$). In such a case the fraction E'/E can be written as

$$\frac{E'_{\min}}{E} = \frac{(A-1)^2}{(A+1)^2} = \alpha \tag{3.17}$$

The value of α depends only on the mass of the nucleus. The equation (3.16) is very often expressed in terms of α as

$$\frac{E'_{\min}}{E} = \frac{(1+\alpha) - (1-\alpha)\mu}{2} \tag{3.18}$$

With the assumption of isotropic scattering in CoM the value of μ follows a uniform distribution $\mathcal{U}(-1, 1)$. The probability distribution of E' can be expressed as

$$P_{AK} = \mathcal{U}(\alpha E, E) = \begin{cases} \frac{1}{(1-\alpha)E} & \text{for } E \in [E, \alpha E] \\ 0 & \text{otherwise} \end{cases} \tag{3.19}$$

P_{AK} is a uniform distribution between E and αE . We can therefore conclude that the average energy after collision is equal to

$$\bar{E}' = \frac{1+\alpha}{2}E \tag{3.20}$$

The distribution (3.19) gives zero probability for any E' out of $[E, \alpha E]$ interval. Therefore, according to the asymptotic kernel, collisions can only cause neutron downscattering, i.e., decrease the energy of the neutron.

The asymptotic kernel finds use as an easy and fast scattering model, applicable only in case of sufficiently large neutron speeds. If the momentum of the incident neutron is far larger than the average momentum of nuclei (typically for neutron energies above from several eV to a few hundred eV [70]) the AK approximation remains accurate.

3.5 Temperature-dependent scattering kernel

As a momentum of the neutron approaches momenta of nuclei in thermal agitation, the Asymptotic Kernel can become unacceptably inaccurate, thus, taking into account the target speed V becomes imperative in high fidelity calculations. By using the same reasoning as in case of Eq. 3.5, a similar formula can be written while explicitly including scattering kernel (as a function of neutron speeds):

$$\sigma_s^T(v \rightarrow v', \vec{\Omega} \rightarrow \vec{\Omega}') = \frac{1}{v} \int_{\text{All } V: v_r > 0} v_r \sigma_s^0(v_r) P(v_r \rightarrow v', \vec{\Omega} \rightarrow \vec{\Omega}') M_T(\vec{V}) d\vec{V} \quad (3.21)$$

Historically the equation (3.21) was often simplified to a form

$$\sigma_s^T(v \rightarrow v', \vec{\Omega} \rightarrow \vec{\Omega}') = \frac{\sigma_s^0(v)}{v} \int_{\text{All } V: v_r > 0} v_r P(v_r \rightarrow v', \vec{\Omega} \rightarrow \vec{\Omega}') M_T(\vec{V}) d\vec{V} \quad (3.22)$$

The assumption here is that the integral scattering cross-section σ_s^0 at the right-hand side of the equation is considered to be constant with respect to relative velocity v_r and, therefore, can be substituted by $\sigma_s^0(v)$. In such a case, the kinematics of the collision takes into account the velocity of the nucleus \vec{V} , but the probability of collision itself does not.

There are many arguments supporting this assumption. The σ_s^0 outside the resonance range is characterized by an almost-constant value regardless of the neutron speed, therefore, small variations of v_r about v shouldn't be able to change the value of σ_s^0 significantly. Moreover, in thermal reactors the majority of scatterings occur on light nuclei of neutron moderator. Light nuclei possess resonances located only at high energies (Figure 3.5) where thermal motion becomes negligible. In such a case, the temperature dependence can be safely omitted by using Asymptotic Kernel. On the other hand, very heavy nuclei, e.g actinides, do possess resonances in cross-sections at lower energies; however, their contribution to the total number of scatterings is far smaller than for moderating material and, due to their high mass, their impact on neutron slowing down is generally small. In case of fast reactors, the justification for constant cross-section is even more trivial as, by definition, the number of low-energy scatterings is low.

The ‘‘constant XS’’ assumption dates back to the article by Wigner and Wilkins [71] from 1944. In recent years, the accuracy of the assumption has been questioned by several authors. In 1991 Ouislounen and Sanchez [72] derived a formula for Legendre moments of the exact scattering kernel and demonstrated that the variation of relative speed v_r at energies close

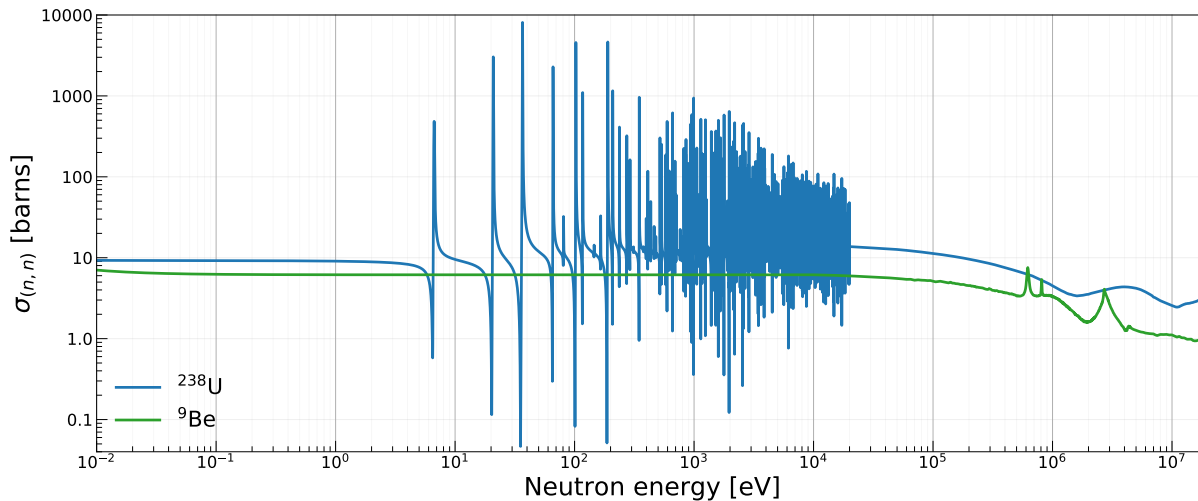


Figure 3.5: Elastic scattering cross-section for heavy (^{238}U) and light (^9Be) nuclide. First resonance occurs at around 6.67 eV for ^{238}U and 620 keV for ^9Be [37].

to resonance can have a significant impact on neutron slowing down. The transition from approximate to exact scattering kernel was also shown to have an impact on core reactivity (around -200 pcm for Light Water Reactors [73]) and the Doppler effect (increase of up to a few percent [74]). Therefore, state-of-the-art calculation codes, including APOLLO3[®] and TRIPOLI-4[®], allow for utilization of both exact and simplified temperature-dependent scattering kernels.

3.6 Resonance upscattering

The main physical phenomenon responsible for the reactivity difference mentioned in the previous paragraph is the resonance upscattering, i.e, resonance scattering event which leads to an increase of neutron energy. As mentioned before, the Asymptotic Kernel makes impossible for neutron to gain energy after collision, as it ignores the thermal motion of nuclei. In case of temperature-dependent scatterings with “constant XS” approximation, the neutron upscattering phenomenon is taken into account; however, due to the assumption made, the model is incapable of representing accurately the scatterings in the vicinity of resonances, where the cross-section varies rapidly even for small changes in neutron speed. For this reason, the model is not able to accurately estimate the rate of upscattering close to a resonance energy.

For a neutron of kinetic energy around a resonance energy, the probability of colliding with nucleus of velocity \vec{V} so that $v_r = |\vec{v} - \vec{V}|$ is higher if v_r is close to the speed for which the resonance occurs. In other words, in case of variation in cross-sections, the collision with nuclei of certain velocities is more probable than for other nuclei, depending on the incident neutron velocity. In particular, in case of neutrons with energies slightly below the resonance, the collisions at $v_r > v$ are more preferential, as shown in Figure 3.6. The reaction cross-

section is therefore effectively higher for targets moving towards the incident neutron. This bias towards collisions with higher v_r results in a visibly higher rate of neutron upscattering.

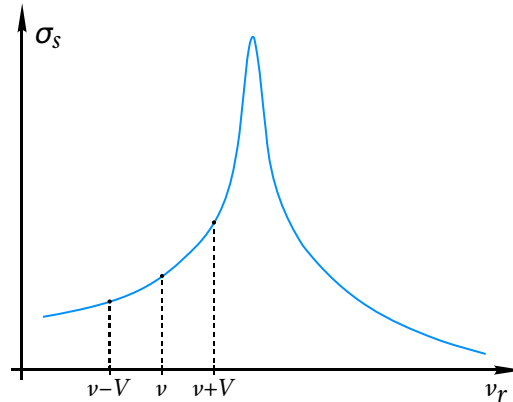


Figure 3.6: Visual demonstration of the mechanism of resonance upscattering (based on [75]). The neutron of speed v in LAB has a higher chance to collide with nucleus of speed V when the particles are moving towards each other ($v_r = v + V$) than when they are moving in the same direction ($v_r = v - V$). The collisions with (relatively) faster nuclei are more probably, hence the chance of upscattering is generally higher than if the resonance was not present.

The resonance upscattering can provide a non-negligible negative contribution to reactivity in case of high epithermal neutron population. As presented in Figure 3.7, the scattering resonances coincide with capture resonances. As a result, the neutrons upscattered from below a scattering resonance are likely to end up with energy closer to the resonance and be captured in consequence.

This effect can have a visible impact on the reactivity of a system. Moreover, the mechanism described is related to magnitude of Doppler effect, as it effectively increases the number of resonance captures.

3.7 Scattering kernels in numerical calculations

This section gives a short overview of different methods of treating the scattering kernel through numerical calculations. The treatment is explained on the example of APOLLO3[®] and TRIPOLI-4[®] codes. The methods described here will be used in the study of the CADOR core and validation and verification of the calculation scheme in the upcoming chapters.

3.7.1 Scattering kernels in TRIPOLI-4[®]

There are four scattering models currently available in TRIPOLI-4[®] [76]:

- Asymptotic Kernel

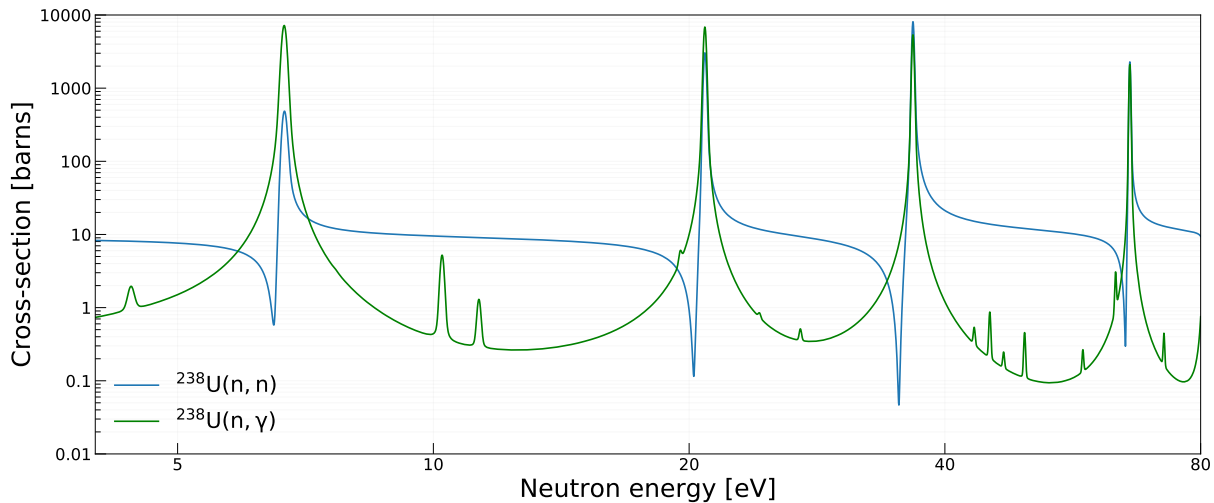


Figure 3.7: First resonances in cross-section of ^{238}U [37].

- Sampling of Velocity of the Target (SVT) – temperature-dependent, free gas kernel; “constant cross-section” is assumed
- Doppler Broadening Rejection Correction (DBRC) [77] – exact free gas kernel
- Weight Correction Method (WCM) [73, 78] – exact free gas kernel

The AK model works as explained in Section 3.4, the calculation of neutron energy after collision is realized by a simple random sampling from a uniform distribution in Eq. 3.19. The algorithms associated with remaining methods are described below.

3.7.1.1 SVT model

In Monte Carlo codes the sampling of velocity of the target takes place on-the-fly during simulation of each neutron history. First, the scattering event is selected by a random sampling according to a Doppler-broadened scattering cross-section $\sigma_s^T(v)$ of the material at a predefined temperature T . Once the collision with a given nuclide of the material is selected the role of SVT model is to sample the velocity of the target \vec{V} from a proper probability distribution.

To get the probability distribution we start by rewriting the equation (3.5):

$$\sigma_T(v) = \frac{1}{v} \int_{\text{All } V: v_r > 0} v_r \sigma_0(v_r) M_T(\vec{V}) d\vec{V} \quad (3.23)$$

Since the nucleus velocity in Maxwell-Boltzmann distribution is isotropic we can integrate the Eq. (3.23) over azimuthal angle, getting as a result

$$\sigma_T(v) = \frac{1}{2v} \int_{\text{All } V: v_r > 0} v_r \sigma_0(v_r) M_T(V) dV d\mu_t \quad (3.24)$$

where $\mu_t = \frac{\vec{V} \cdot \vec{v}}{|\vec{V}| |\vec{v}|}$ is the cosine between velocity vectors of the incident neutron and the target nucleus.

Following the Monte Carlo principles, the equation 3.24 is transformed into a probability distribution

$$P(V, \mu_t) dV d\mu_t = \frac{v_r \sigma_0(v_r) M_T(V)}{2v \sigma_T(v)}, \quad v_r = \sqrt{V^2 + v^2 - 2Vv\mu_t} \quad (3.25)$$

with two correlated random variables V and μ_t . The distribution (3.25) is so far given in its exact form without simplifications.

As mentioned before, SVT model utilizes the ‘‘constant XS’’ approximation of a form $\sigma_0(v_r) = \sigma_0(v)$. By extension, it can be argued that the Doppler-broadened $\sigma_T(v)$ is approximately equal to $\sigma_0(v)$, as the Doppler broadening applied to constant cross-sections has a negligible effect (providing the v isn't in thermal range). The Eq. 3.25 is thus simplified to

$$P(V, \mu_t) = \frac{v_r M_T(V)}{2v} \quad (3.26)$$

For easier sampling the Eq. 3.26 can be written as [79]

$$P(V, \mu_t) = C_1 \cdot \underbrace{\left(\frac{\sqrt{v^2 + V^2 - 2Vv\mu_t}}{v + V} \right)}_{R_{SVT}} \cdot \underbrace{\left(V^3 e^{-\beta V^2} + vV^2 e^{-\beta V^2} \right)}_{\text{sampling of } V} \quad (3.27)$$

where C_1 is a normalization constant.

The SVT algorithm works as follows:

1. μ_t is sampled from a uniform distribution $[-1, 1]$
2. V is sampled from distribution $V^3 e^{-\beta^2 V^2} + vV^2 e^{-\beta^2 V^2}$
3. rejection test R_{SVT}^1 is applied: if the test fails, the algorithm has to be repeated from step 1 until a (V, μ_t) pair is accepted

After the velocity of the nucleus is successfully sampled, the outcome of collision can be determined by solving classical equations of kinematics, similarly to what was shown in Section 3.4.

3.7.1.2 DBRC model

The idea behind DBRC model is to realize the sampling from exact probability distribution by introducing another rejection rule R_{DBRC} to the SVT algorithm. The new rejection rule is meant to make the probability distribution proportional to the value of $\sigma_s^0(v_r)$. The corrected probability distribution now reads

$$P(V, \mu_t) = C_2 \cdot \underbrace{\left(\frac{\sigma_s^0(v_r)}{\sigma_{s,\max}^0} \right)}_{R_{DBRC}} \cdot \underbrace{\left(\frac{\sqrt{v^2 + V^2 - 2Vv\mu_t}}{v + V} \right)}_{R_{SVT}} \cdot \underbrace{\left(V^3 e^{-\beta V^2} + vV^2 e^{-\beta V^2} \right)}_{\text{sampling of } V} \quad (3.28)$$

¹An additional random number r is sampled from $\mathcal{U}(0, 1)$. If $r > R_{SVT}$ the test fails.

where $\sigma_{s,\max}$ stands for the highest value of elastic scattering cross-section in the vicinity of v . The use of $\sigma_{s,\max}^0$ ensures that the value of R_{DBRC} is smaller than 1 regardless v_r . The algorithm for DBRC starts exactly as presented for SVT method, however, before the (V, μ_t) pair is accepted, another rejection rule R_{DBRC} is performed. As before, if rejection happens at any point the algorithm has to be repeated.

The double rejection algorithm has practical downsides from the point of view of calculation efficiency. Close to a large scattering resonance the value of $\sigma_{s,\max}^0$ can be orders of magnitude higher than $\sigma_s^0(v_r)$ for most probable values of v_r , making the rejection test exceptionally hard to pass (as $R_{\text{DBRC}} \approx 0$). In such a case, significant computation power has to be sacrificed to generating sufficiently many random numbers to eventually pass both R_{DBRC} and R_{SVT} tests. The numerous rejections in DBRC model lead to longer calculation times and, therefore, the model is typically used only when it can provide visible accuracy improvements, that is, only for scatterings at a limited energy range and only for small set of most important heavy isotopes.

3.7.1.3 WCM model

As an alternative to DBRC, the exact scattering kernel can be realized by the WCM method. The method applies a very similar idea of starting with SVT sampling and then correcting the results. However, instead of using another rejection test, the weight of neutron after collision is corrected by a factor f

$$f = \frac{\sigma_s^0(v_r)}{\sigma_s^T(v)} \quad (3.29)$$

Using WCM method can diminish the calculation cost compared to DBRC, as the nucleus velocity sampled by SVT algorithm is always accepted (albeit with varying weights). On the other hand, the differences in weights after scattering can cause variance issues and thus the method is best used together with variance reduction techniques [78].

3.7.2 Scattering kernels in APOLLO3[®]

In case of deterministic codes such as APOLLO3[®], the scattering cross-section $\sigma_s(E \rightarrow E', \vec{\Omega} \rightarrow \vec{\Omega}')$ is represented in a discrete form as a consequence of multigroup energy approximation and expansion of angular variable into a finite set of Legendre polynomials. The discrete scattering cross-sections can be calculated as shown in Sections 2.6.1 and 2.6.3. For energy mesh of size N_g the scattering cross-sections can be tabulated as $N_g \times N_g$ transfer matrices, one matrix per each Legendre moment (and per each type of scattering reaction if considered separately). Correction of the matrices by the temperature dependence is applied during processing of the multigroup library, therefore there is no need for on-the-fly corrections during neutron transport calculation.

In NJOY processing tool, the scattering treatment is realized by the THERM module, responsible for creation of cross-sections and matrices in the thermal energy range. The free gas scattering kernel is not available in the official distribution of NJOY, however, the implementation of the exact free gas kernel was realized in CEA for internal usage as described

in [70]. A detailed description of derivation of the formulas and an overview of numerical implementations can be found in [72] and [75].

Chapter 4

Physical phenomena in moderated SFR core

This chapter is focused on demonstration and discussion of the most important physical phenomena related to the neutronics of moderated SFR cores such as CADOR. In the scope of this thesis, an important physical phenomenon should fulfill two main criteria. First of all, the effect should be CADOR-specific ,i.e., less important (possibly negligible) in a standard SFR due to an absence of moderator. Secondly, such an effect should have an impact on the calculation methods: their accuracy and applicability.

4.1 Geometry

The studies in this chapter were performed with a single two-dimensional CADOR fuel assembly model based on SFR-V2B [80] core. The layout of the assembly (before addition of

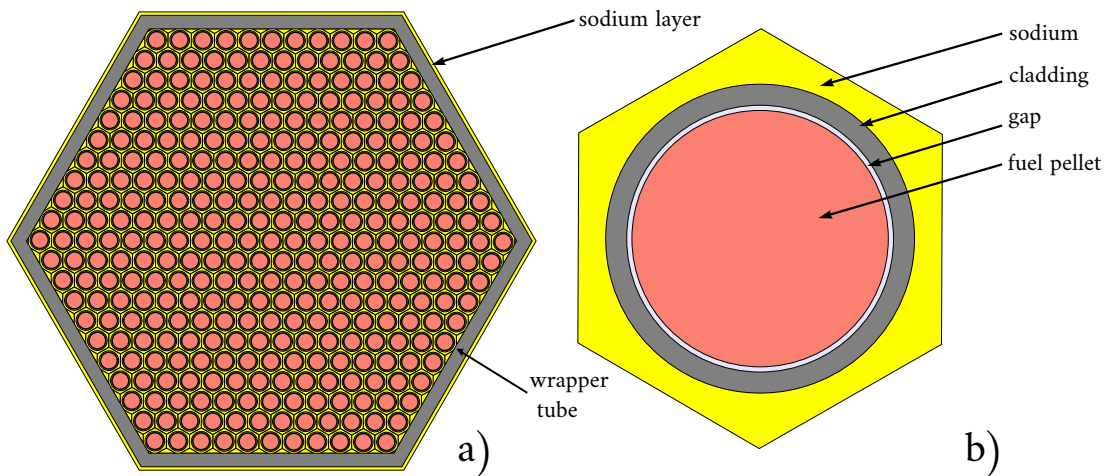


Figure 4.1: Layout of the fuel assembly before adding moderating materials.

neutron moderator) is illustrated in Figure 4.1. Some of the most important parameters of

the geometry can be found in Table 4.1.

Table 4.1: Dimensions of the CADOR fuel assembly.

Parameter	Value
number of pins per ass.	331
pellet radius	2.715 mm
inner cladding radius	2.825 mm
cladding thickness	0.45 mm
hexagonal tube pitch	150 mm
hexagonal tube thickness	4.5 mm

4.2 Materials

4.2.1 Moderator choice, comparison between materials

There are many parameters used to characterize neutron moderators. A defining feature of any neutron moderator is a high capability to absorb kinetic energy of neutrons via collisions. As discussed in Section 3.4, the amount of energy absorbed is directly linked to the mass of a nucleus — the lower the mass ratio A , the more efficient the moderation is. This potential for absorption of kinetic energy can be represented as α , a maximum possible fraction of energy lost during a single collision, or by using average logarithmic energy decrement ξ equal to

$$\xi = \overline{\ln E - \ln E'} = 1 + \frac{\alpha}{1 - \alpha} \ln(\alpha) \quad (4.1)$$

Larger ξ signifies more energy absorbed on average. Another option is to estimate the average number of scatterings needed to slow-down a neutron from energy E_1 to E_2 calculated with the following formula:

$$n_{\text{coll}}(E_1 \rightarrow E_2) = \frac{\ln\left(\frac{E_1}{E_2}\right)}{\xi} \quad (4.2)$$

Parameters α , ξ and n_{coll} are very similar in nature as all three can be calculated by knowing only the value of A .

A good moderator should also be characterized by an advantageous behavior of reaction cross-section. The efficiency of moderation depends on the rate of scattering, proportional to the value of microscopic scattering cross-section σ_s and the atomic density of the material N . Moreover, a good moderator should cause minimal number of neutron captures. The probability of neutron survival per collision can be estimated with a simple ratio $\frac{\sigma_s}{\sigma_a}$. High absorption cross-section σ_a can be a disqualifying trait, as typically many consecutive collisions are needed to slow-down a neutron sufficiently (in case of CADOR, up to resonance energy range). Additionally, combinations of the aforementioned parameters can be used,

quantities such as Macroscopic Slowing Down Power $\xi\Sigma_s$ or Moderating Ratio $\xi\frac{\sigma_s}{\sigma_a}$. A summary of moderation parameters for a number of common neutron moderators is presented in Table 4.2.

Table 4.2: Comparison of isotopes commonly used as neutron moderators. Values of cross-sections correspond to energy of 100 keV.

Isotope	α	ξ	$n_{\text{coll}}(2\text{ MeV} \rightarrow 10\text{ keV})$	σ_s	$\xi\sigma_s$
^1H	0	1	6	2.92	12.76
^2H	0.111	0.726	8	2.54	2.34
^9Be	0.638	0.208	26	1.61	1.06
^{11}B	0.692	0.173	31	1.96	0.76
^{12}C	0.714	0.159	34	1.67	0.70
^{16}O	0.777	0.121	44	1.59	0.44
^{24}Mg	0.846	0.081	66	2.04	0.67

It is worth noting, that features outside of the scope of nuclear physics have to also be taken into account during core design, e.g., parameters such as:

- cost and availability of the material
- existing feasible methods of incorporating the material into a core design
- possible chemical interactions with other components
- thermal properties: conductivity, thermal expansion, fusion and boiling temperatures, thermal degradation, etc.
- consequences of neutron irradiation of the material

In general, the only moderators practical to use inside an SFR core are solid materials. Water, the most common moderator used in thermal reactors, is not considered as a suitable candidate due to its interaction with sodium. To determine the best available choices, a large number of different neutron moderators was evaluated during internal preliminary design studies of CADOR. Figure 4.2 presents neutron flux spectra resulting from using several different types of moderator inside an SFR core.

For majority of moderators the flux shape is similar. The two most distinct shapes belong to the core moderated with ZrH_2 moderator. Zirconium hydride is a very efficient moderator — even addition of only 3.9% volume fraction of ZrH_2 caused a visible distortion of the flux. The flux between 3 keV and 1 MeV was much lower than for all other moderating materials visible in Figure 4.2. This change was compensated by higher flux in lower energies below approximately 400 eV.

The data illustrates an important observation. Broadly speaking, the moderator materials suitable for use in SFRs can be divided into two categories: strong moderators based on hydrogenated materials and moderators based on other light isotopes that possess weaker moderating capabilities. Common hydrogenated materials other than ZrH_2 include calcium hydride CaH_2 and yttrium hydride YH_2 . Other viable materials, without hydrogen, include

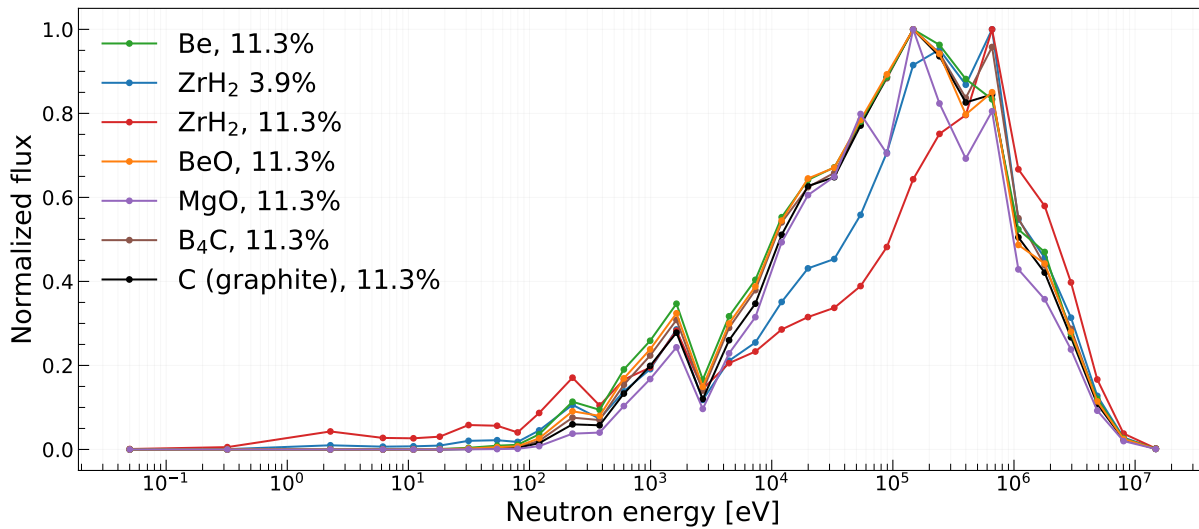


Figure 4.2: Neutron flux spectra for CADOR cores with different moderators. Results obtained with ECCO/ERANOS code, core calculation performed by BISTRO solver in r - z geometry. Results from internal document of CEA (personal communication, July 2020).

beryllium, magnesium oxide (MgO), graphite or boron. However, even for Be, the lightest element considered in the study other than H, the moderating power is considerably lower than for hydrogenated materials. By looking again at Table 4.2 we see that the average number of collisions to slow down a neutron from 2 MeV to 10 keV is more than four times higher for ${}^9\text{Be}$ compared to ${}^1\text{H}$. To ensure that our studies can account for such a visible difference in moderating properties, while keeping the amount of calculations feasible in the time frame of the thesis, throughout most of this work we considered simultaneously CADOR core with two moderating materials: zirconium hydride ZrH_2 and beryllium.

4.2.1.1 Comparison between beryllium and zirconium hydride

Beryllium is a light metallic chemical element with atomic number 4. Isotope ${}^9\text{Be}$ is the only stable isotope of beryllium, it is also the only isotope of Be occurring naturally in significant amounts. It is characterized by a low density of around 1.85 g cm^{-3} , relatively high thermal conductivity and fusion temperature. At the time of writing this thesis, it is also the most studied candidate for the moderator material in the CADOR design.

The idea of softening spectrum by Be has been studied in the past: BeO was included in Core 1 of SEFOR experimental reactor [81] as well as used in low void effect design evaluated in [82]. Softening spectrum by Be was also proposed to be used in fast reactors to limit neutron irradiation damage [83].

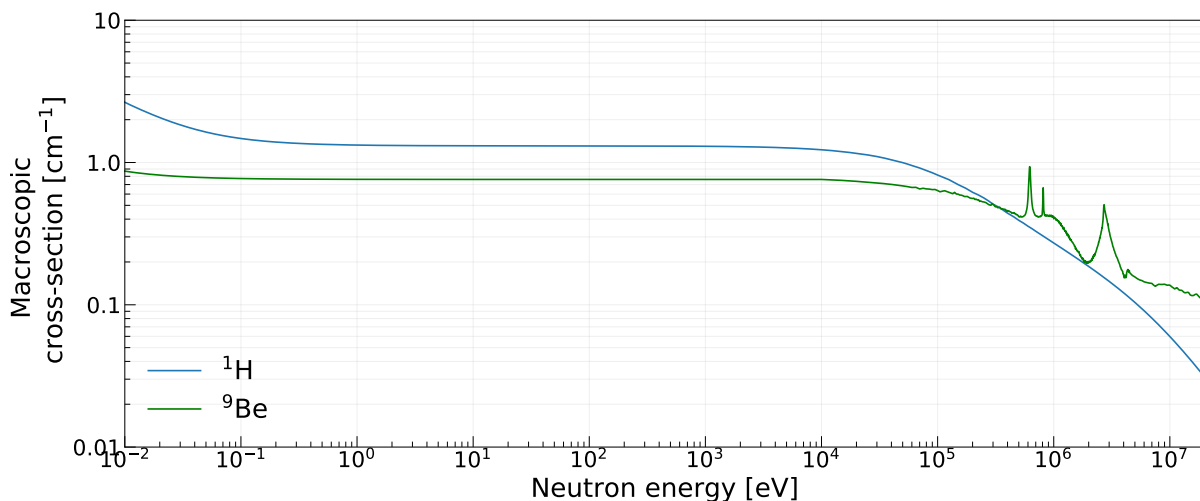
Zirconium hydride is an alloy made by combining hydrogen and zirconium. The nuclei of Zr do not take significant part in moderation due to their high atomic mass (around 91.2 amu). The material is, however, an excellent moderator thanks to high density of hydrogen atoms. Because zirconium hydride is an alloy rather than a compound, the hydrogen content can

be adjusted during fabrication. In case of this work, a stoichiometric ratio of 1.78 hydrogen atoms per one zirconium atom was used. Formally speaking, the material name should be abbreviated as $\text{ZrH}_{1.78}$, however, for simplicity the ZrH_2 notation is used in the text. Zirconium hydride is one of the most widely applied moderator in case of fast reactor studies, used mainly to improve the void effect and/or the Doppler effect in several designs [84, 85, 86, 87, 88].

Table 4.3: Densities of ZrH_2 and Be.

Material	Mass density	Atomic density
Be	1.85 g/cm ³	1.24×10^{23} Be atoms/cm ³
ZrH_2	5.56 g/cm ³	6.41×10^{22} H atoms/cm ³

As mentioned before, the atoms of ^1H have stronger energy absorption capabilities per collision compared to Be. Furthermore, the macroscopic scattering cross-section of ^1H in ZrH_2 is higher than for metallic Be for majority of energies (Figure 4.3), even when we account for the difference in mass densities (atomic density of Be is almost two times higher than for H in ZrH_2 , as shown in Table 4.3). By combining these two points, we can see that ZrH_2 is a much more potent moderator. The moderator quantity per fuel assembly has to be different to achieve similar effect. In case of assembly with beryllium, the fraction of volume occupied by moderator was set to approximately 10.5 %, whereas for assembly with ZrH_2 a fraction of 3.6 % was used. The different efficiency of moderation of these two materials allow using only about a third of moderator concentration of Be to achieve similar results in terms of Doppler effect.

Figure 4.3: Elastic scattering cross-section of ^1H and ^9Be [37].

Interestingly, the moderator percentage of 3.6 % is very close to the local maximum of improvement of Doppler effect achievable with ZrH_2 . Figure 4.4 compares the values of the

Doppler constant K_D for cores with Be and ZrH_2 at different volume fractions per fuel assembly. According to the results, in case of Be the value of K_D is approximately proportional to the moderator content in each assembly, while for ZrH_2 we initially observe a much steeper curve that flattens with increasing moderator content and reaches maximum value of K_D at moderator fraction of around 7–8%. After that point, the additional moderation decreases the value of K_D . The same behavior was also observed for CaH_2 and YH_2 moderators; the effect is explained by a significant increase of positive contribution to Doppler effect coming from higher fission rate. For high content of hydride materials the effect starts to outweigh the gain of negative reactivity related to neutron captures. For this reason, increasing ZrH_2 concentration beyond 3.6% seems to be unreasonable, as the possible gain in terms of K_D is very limited and could be reached only through severe deterioration of other parameters due to excessive neutron moderation.

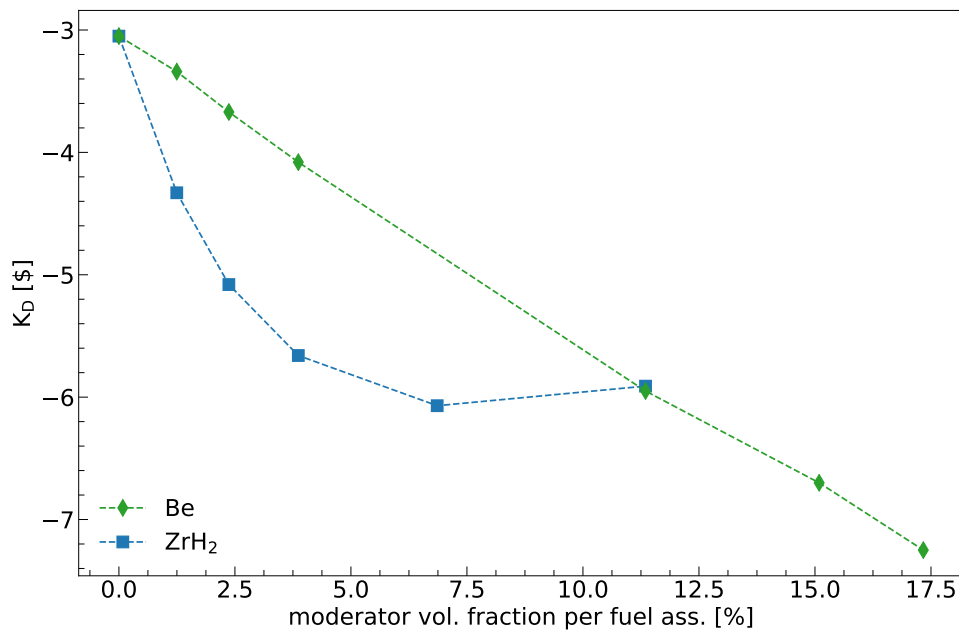


Figure 4.4: Values of K_D for entire core as a function of volume content of Be and ZrH_2 moderators per fuel assembly. Results from internal document of CEA (personal communication, July 2020).

4.2.1.2 Moderator placements

The moderator is introduced by replacing some of the fuel pins with moderator pins in each fuel assembly. This solution is the most often postulated method of moderator placement in CADOR design. Other possible methods, e.g., including moderator inside the structure materials or using separate moderating assemblies distributed through the core, are not going to be discussed in this work. The number of possible core designs would be too high to perform an in-depth validation study for each of them in the limited time of the thesis.

The replacement of fuel pins has a disadvantage of decreasing the fuel mass possible to stock

in each assembly. It is therefore necessary to increase the fuel enrichment in fissile material to keep a sufficiently high multiplication factor. On the other hand, the method provides several important advantages. Encasing the moderator pins in steel cladding ensures minimal interaction with other components. Furthermore, keeping moderator in a pure form instead of doping pre-existing core elements guarantees that the thermal and chemical properties of the latter do not deteriorate. The method is a conservative approach to moderator placement — one that seems to require the lowest number of assumptions to be deemed feasible in a real reactor core (such feasibility analysis is beyond the scope of this work).

The final shape of CADOR assemblies is shown in Figure 4.5. In case of Be-moderated assembly, 91 fuel pins were replaced with the moderator. Analogically, in ZrH_2 -moderated assembly 31 pins were replaced. In each case the radius of moderator pins is exactly the same as the radius of fuel pellets. It can be noticed that the pin replacement method results in a heterogeneous moderator distribution, most notably in the case of ZrH_2 , where some fuel pins are adjacent to more moderator pins than others. The impact of this heterogeneity is studied in a later part of the chapter.

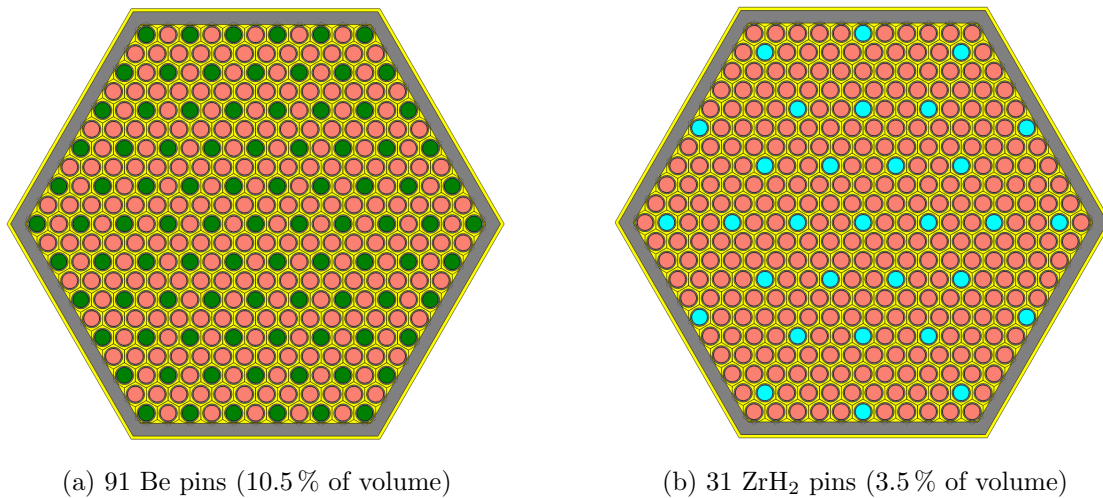


Figure 4.5: CADOR assemblies with moderator pins included.

4.2.2 Fuel, cladding and wrapper

The fuel used in this CADOR model is a simplified fresh MOX fuel based on UO_2 fuel reprocessed after one reactor cycle. The exact composition of the fuel is included in the Table 4.4

The fuel composition is slightly simplified, e.g., the presence of isotopes such as ^{241}Am or ^{238}Pu was omitted and some of the concentrations were rounded. The core was divided into two plutonium enrichment zones: inner core C1 with 20% Pu enrichment and the outer core C2 with enrichment increased to 26.2% to counterbalance the losses due to leakage in outermost layers of the core.

Table 4.4: Fuel composition.

Enrichment zones		U comp.		Pu comp.	
C1	20.0 % Pu	^{238}U	99.8 %	^{239}Pu	60 %
				^{240}Pu	26 %
C2	26.2 % Pu	^{235}U	0.2 %	^{241}Pu	7 %
				^{242}Pu	7 %

The material of the wrapper tube and the fuel cladding was chosen to be a simple nickel-chromium steel containing only three elements (Table 4.5).

Table 4.5: Composition of the stainless steel used in wrapper tube and fuel cladding.

Element	Concentration
natural Fe	70 %
natural Cr	15.5 %
natural Ni	14.5 %

4.2.3 Material temperatures

The temperatures of materials were chosen to be close to realistic operating temperatures for CADOR design. The temperatures were selected according to their availability in pre-processed cross-section libraries, allowing for easier comparisons with TRIPOLI-4[®] (on-fly temperature interpolation is not possible in TRIPOLI-4[®] for the time being). Some of the values can deviate from what is expected for CADOR design. However, highly realistic temperatures are not mandatory in this work as the main goal is to analyze the numerical calculations rather than the design itself. The values of temperatures are visible in Table 4.6. The temperature is homogeneously distributed in each material and, as discussed in Section 3.2.2, it should be treated as an effective temperature of Rowlands. The nominal fuel temperature was purposefully chosen to be relatively low compared to typical SFR design, as it is one of the primary features of CADOR core (as explained in Chapter 1).

4.2.4 Reference — a standard SFR without moderator

A third assembly model used in the studies is a fuel assembly without moderator (as in Figure 4.1), referred to as a “no moderator” case or a “standard SFR” assembly later in the text. The addition of non-moderated assembly gives a reference point for the results obtained with moderated CADOR assemblies.

Table 4.6: Temperatures for the materials in the core.

Material	Temperature
Fuel	900 °C / 1174 K (nominal)
Cladding and Wrapper	373 °C / 647 K
Sodium	373 °C / 647 K
Beryllium	373 °C / 647 K
Zirconium Hydride	326 °C / 600 K

4.3 Analysis of neutron distribution (APOLLO3[®])

4.3.1 Calculation parameters

The calculations in this section were conducted with APOLLO3[®] lattice calculation module. The TDT-CPM solver (collision probability method) was used to perform self-shielding calculations with Tone's method. Flux calculations were handled by TDT-MOC solver (method of characteristics). In all calculations the reflective boundary conditions were used (no neutron leakage). Because of the symmetries, a segment equal to 1/12th of initial geometry was sufficient to represent an assembly in the calculations. All calculations were performed by using JEFF-3.1.1 nuclear data library with energy mesh of 1968 groups. More details on the parameters of each solver will be given in Chapter 5.

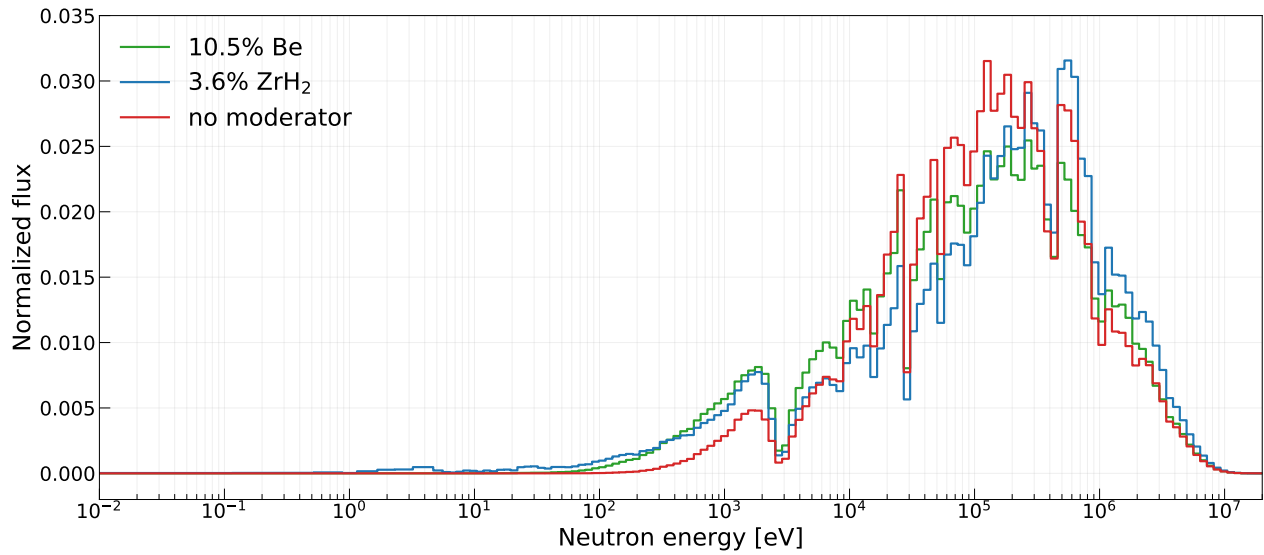
It's important to note that the library used in this study does not take into account the exact scattering kernel, discussed in the Section 3.5. A study of the impact of different scattering kernels performed with TRIPOLI-4[®] code will be presented at the end of this chapter.

4.3.2 Neutron energy distribution

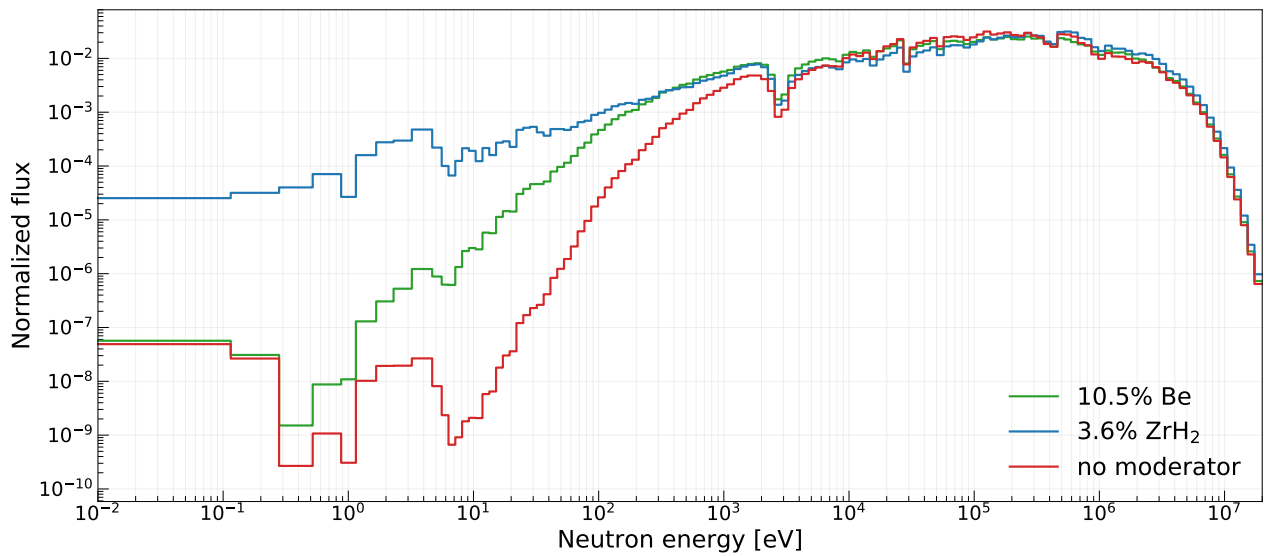
4.3.2.1 Neutron flux

Let us first consider the neutron distribution with respect to energy. Figure 4.6 depicts neutron flux spectra of each assembly, presented both in linear and logarithmic scales. As explained before, the neutron spectrum behaves differently depending on the moderator configuration, although the amount of moderator in each case was calibrated to achieve a similar Doppler effect. For 3.6% ZrH₂ the 'tail' of slower neutron flux extends to lower energies than 10.5% Be. Below around 300-400 eV, the neutron population in case of ZrH₂ is visibly higher. The flux below 3.5 keV (before lower hump in the spectrum) is about equal for both moderators. The differences are shown more clearly in Figure 4.7. Moderation with Be increases the flux between 100 eV and 15 keV. Conversely, the presence of ZrH₂ increases flux from 6 keV, but extends to few eV.

Table 4.7 lists some of the parameters related to the behavior of a neutron spectrum. The neutron mean free path (MFP) is equal to $1/\Sigma_t$, where Σ_t is a flux-weighted macroscopic total cross-section. The average neutron energy was reduced by around 40 to 50 % thanks to



(a) linear Y scale



(b) logarithmic Y scale

Figure 4.6: Comparison of neutron flux spectra for two CADOR fuel assemblies and one standard SFR assembly.

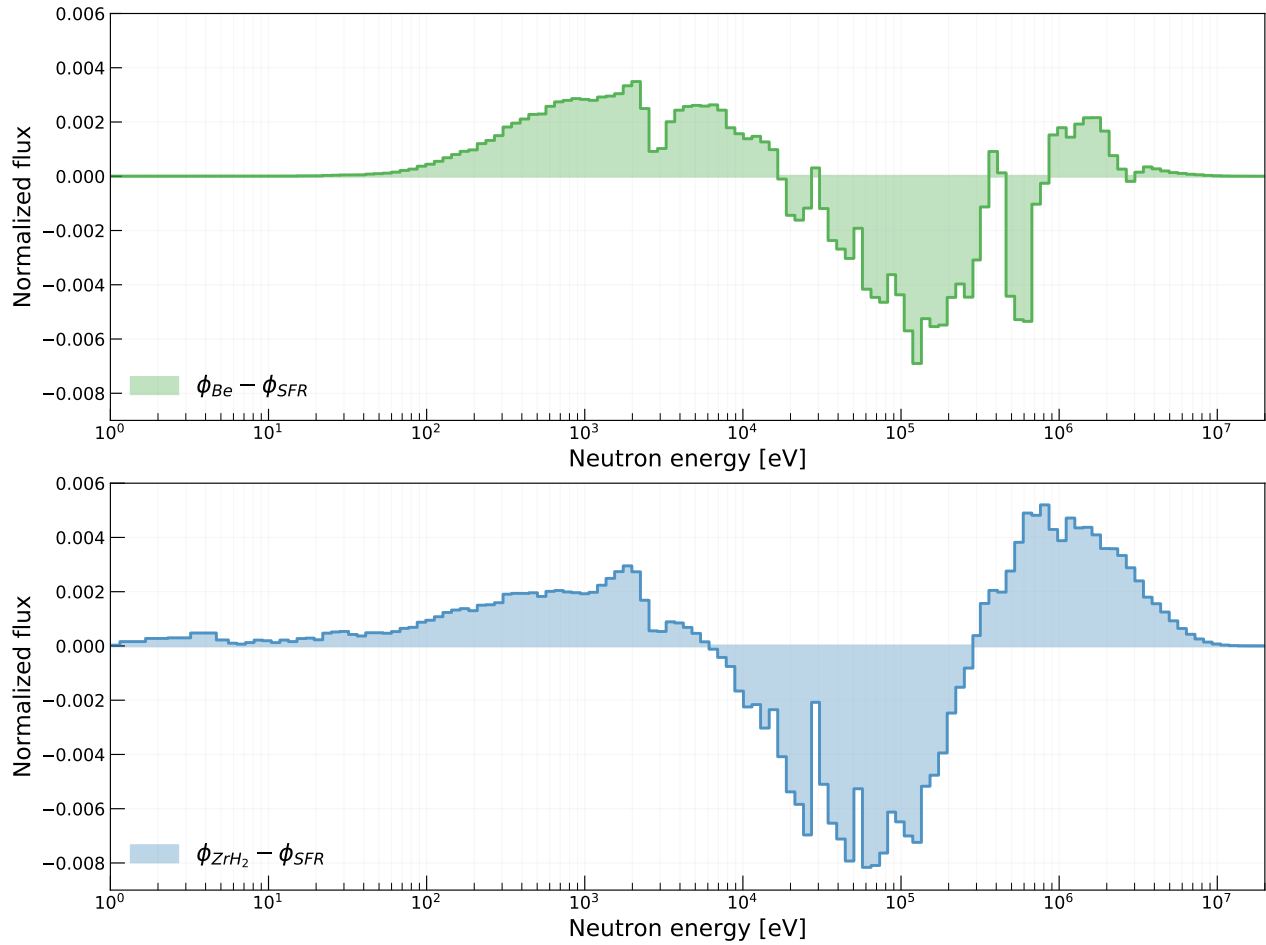


Figure 4.7: Difference in neutron flux spectrum for two types of moderated assembly and a standard SFR assembly.

the neutron moderators. The addition of moderators also changed significantly the fraction of flux below 10 keV, 1 keV and 100 eV. Notably, the flux below 1 keV constituted only 1 % of the global flux if the moderator was not present, whereas for ZrH₂ moderator the flux was still noticeable even below 100 eV. Percentage of flux below 1 keV was quite similar for Be and ZrH₂ and is 4–5 times larger than for the case without moderator.

For both moderators the MFP in the whole assembly was shorter by around 7 % when compared to assembly without moderator. The length of MFP in the assembly was found to be almost identical regardless if Be and ZrH₂ was used. However, the differences were visible when MFP in moderator and fuel media were compared. The mean free path in ZrH₂ was almost 45 % lower than in Be. On the other hand, the MFP in fuel was shown to be shorter in case of Be, although the difference was less than 4 %. In general, the difference in mean free path in the fuel was rather low for all three kinds of assembly. The MFP averaged over the whole assembly volume was lower for moderated assemblies mainly thanks to the shorter MFP in the moderator pins themselves.

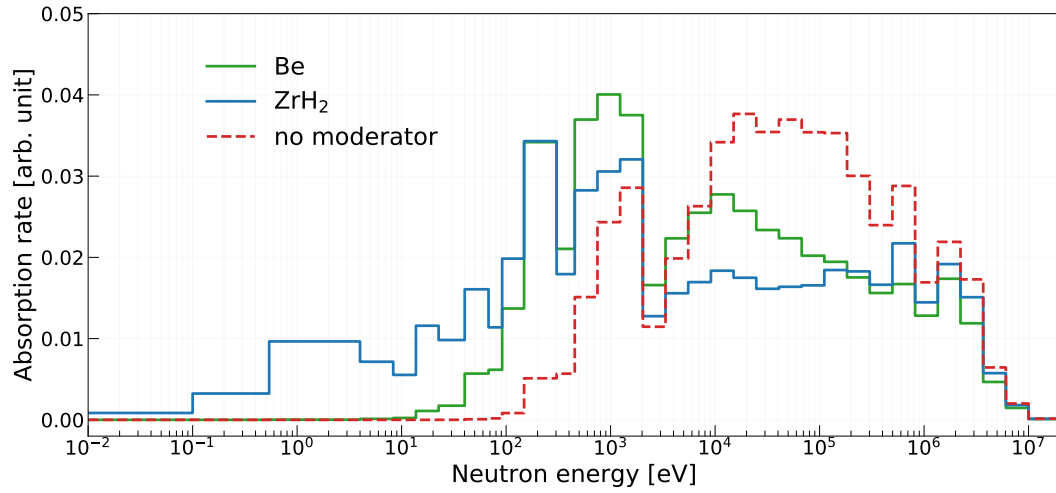
Table 4.7: Parameters linked to neutron energy distribution.

	10.5 % Be		3.5 % ZrH ₂		no moderator	
	C1	C2	C1	C2	C1	C2
Average neutron energy [keV]	55.1	63.8	49.9	66.5	98.7	113.7
Neutron flux below 10 keV [%]	19.0	18.0	17.8	16.2	10.2	8.7
Neutron flux below 1 keV [%]	5.1	4.7	6.6	5.5	1.5	1.0
Neutron flux below 100 eV [%]	0.21	0.16	1.32	1.02	0.0045	0.0016
Neutron MFP, whole ass. [cm]	2.93	2.96	2.93	2.96	3.15	3.20
Neutron MFP, fuel [cm]	2.16	2.17	2.24	2.25	2.24	2.26
Neutron MFP, moderator [cm]	1.73	1.75	0.98	1.00	–	–

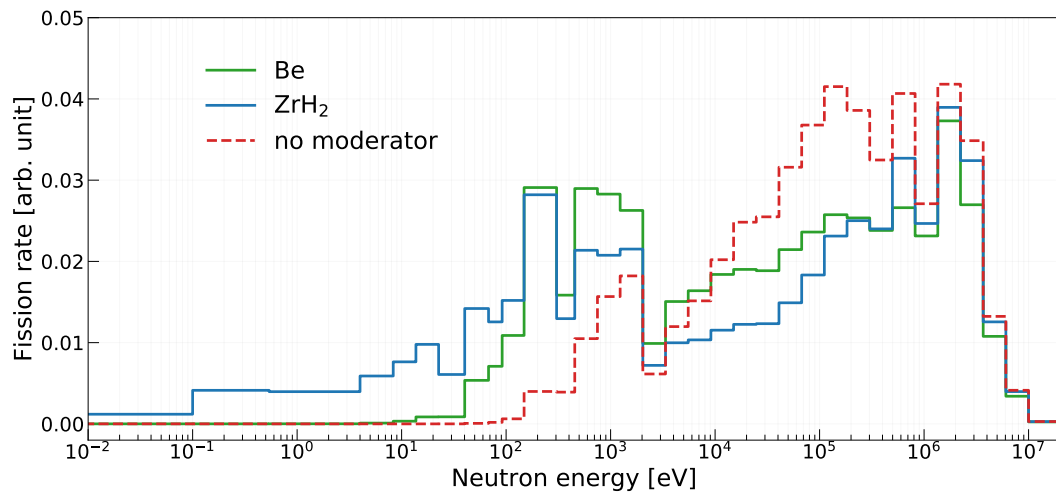
4.3.2.2 Reaction rates

Figure 4.8 compares the distributions of absorption and fission rates as a function of neutron energy. We see a far greater importance of epithermal absorption and fission in both moderated assemblies. Below around 1 keV, the reaction rates in assembly without moderator start to die out with lower neutron energies, whereas for moderated assemblies the same point signifies a large peak of reaction rate. At energies below 100 eV the reaction rate in Be moderated assembly became less important, while in case of assembly with ZrH₂ the rates remain relevant until under around 0.1 eV.

Because of the tendency of cross-sections to increase with decreasing neutron energy, the difference in absorption/fission rate between the three assembly models was even more pronounced than the in case of flux spectra discussed previously. A notable fraction of neutron absorption occurs at the lower part of the resonance energy range, where the impact of resonance upscattering is the most prominent.



(a) Absorption rate



(b) Fission rate

Figure 4.8: Sum of absorption and fission rates in actinides in 33 groups.

4.3.2.3 Distribution of neutrons in space

The design of CADOR assembly discussed in this work introduces moderating materials in a heterogeneous way. The assemblies retains six axes of symmetry, typical for hexagonal assemblies, and the moderator pins are distributed as evenly as possible; however, given their small number, the gaps between the pins are inevitable. By looking at the pin distribution in the previously presented Figure 4.5 it can be estimated that, on average, the distance between neighboring moderator pins is equal approximately to 2 pin-cell pitches (1.6 cm) for 91 Be pins and 3 pitches (2.3 cm) for 31 ZrH₂ pins. The distances are thus comparable (although slightly smaller) to the length of neutron MFP. It can be expected that the heterogeneous distribution might cause uneven reaction rate distribution across the assembly volume.

Let us examine the average neutron energy in each cell of the spatial mesh of assemblies. The average neutron energy in cell i was calculated with a formula

$$\bar{E}_i = \frac{\sum_{g=1}^{G=1968} E_g w_{g,i}}{\sum_{g=1}^{G=1968} w_{g,i}}, \quad w_{g,i} = \frac{\phi_{g,i}}{\sqrt{E_g}} \quad (4.3)$$

where $w_{g,i}$ is a weight proportional to the number of neutrons per unit volume in group g and cell i . Subsequently, the relative deviation from the global average neutron energy \bar{E} was calculated as

$$D_i = \left(\bar{E}_i / \bar{E} - 1 \right) \cdot 100\%, \quad \bar{E} = \frac{\sum_{i=1}^{N_i} V_i \bar{E}_i}{\sum_{i=1}^{N_i} V_i} \quad (4.4)$$

where V_i is the volume of cell i . To achieve better spatial resolution the number of cells N_i was increased by dividing every hexagonal pin-cell into a six triangular segments as well as by dividing every fuel and moderator pellet into six concentric rings, as shown in Figure 4.9. The final results for all three types of assembly are represented in a form of 2D heat maps in

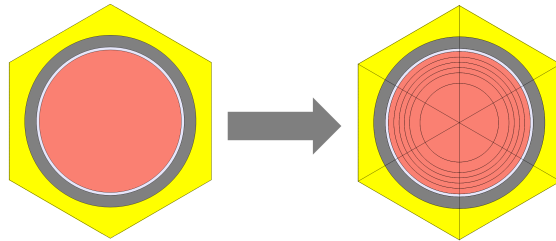


Figure 4.9: Division of a pin-cell geometry into six angular segments and six rings inside the pellet.

Figure 4.10. It is visible that the average neutron energy varies significantly in the vicinity of moderator pins. The effect is more pronounced in case of assembly with ZrH₂ pins, as the moderator is, at the same time, more powerful and distributed more sparsely. In the center of ZrH₂ pins, the dip in neutron energy reached more than 30% of the global average. The distribution is sparse enough to create difference between fuel pins depending on their distance from moderator. For Be-moderated assembly, the heterogeneity of average energy distribution was noticeable, but the amplitude of variation was far lower, only up to 9.4%.

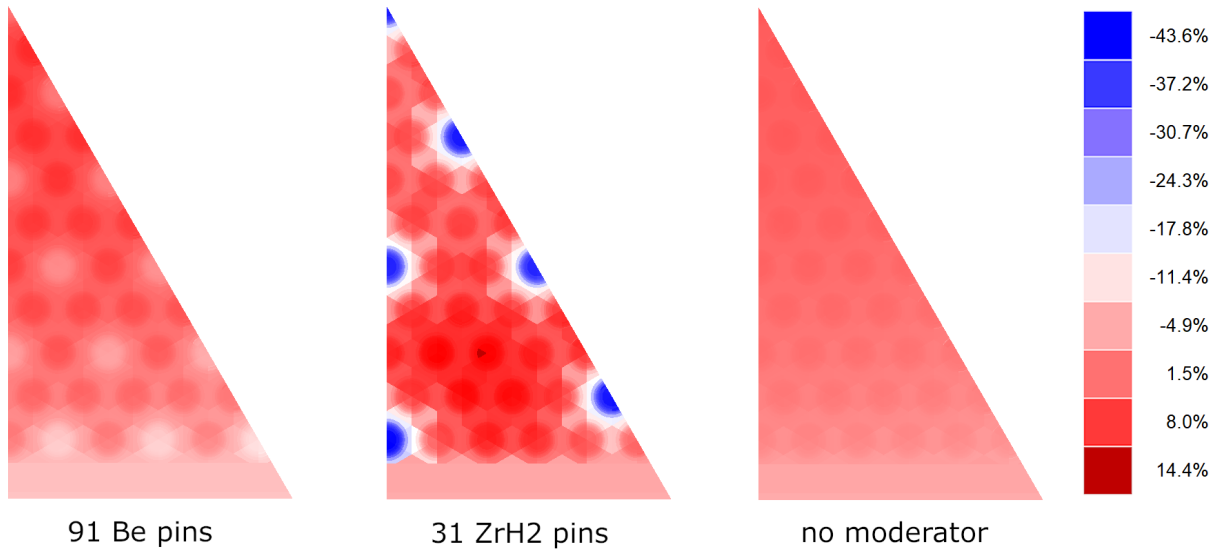


Figure 4.10: Divergence from global average energy value in percent.

The grid of moderator pins is tighter than in case of ZrH_2 , which prevented large differences between individual fuel pins (every fuel pins is neighboring exactly two beryllium pins).

The amplitudes of neutron energy are better visible in Figure 4.11, where the local average energy was plotted along the assembly pitch. For the two moderators, the average neutron energy in the assembly was very similar (difference of around 5 keV), but the oscillations about the average value were few times higher in case of ZrH_2 .

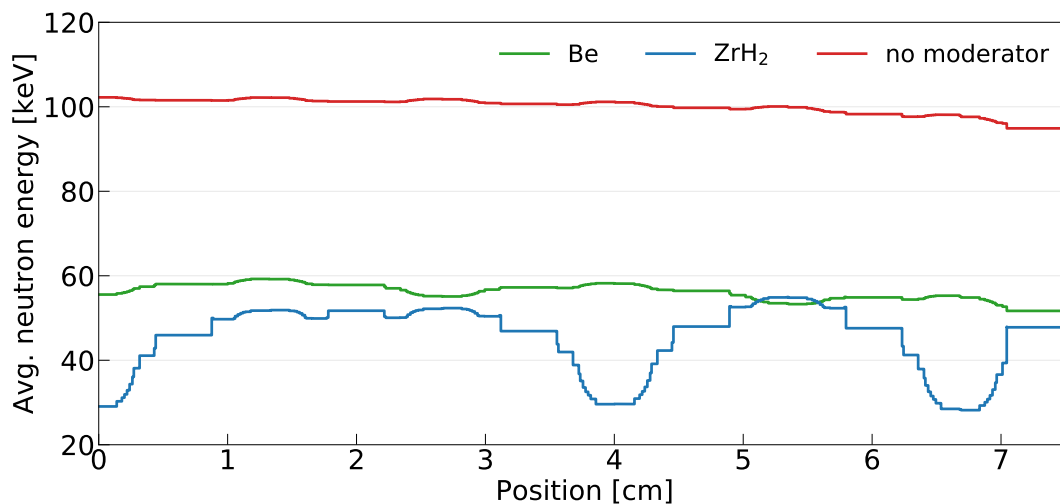


Figure 4.11: Average neutron energy across the C1 fuel assembly for different moderators.

Due to variations in cross-sections with respect to energy, the reaction rates are energy-dependent as well. It is therefore of interest to apply similar methodology to obtain spatial

distributions of reaction rates. The reduced average neutron speed observed in previous subsection can lead to similar peaks and depressions in capture and fission rates, as was observed for the average neutron energy. Figure 4.12 presents a set of heat maps for fission and capture rates in fuel. The values in the heat maps are again deviations from the average value for whole fuel volume in the assembly, calculated analogically to Eq. (4.4).

Since slower neutrons are absorbed more often due to favorable cross-section behavior, we notice elevated capture and fission rates in the vicinity of moderator. In case of Be-moderated assembly the problem was less pronounced and is partially shadowed by a similar effect caused by the presence of wrapper tube (at the bottom of the heat map). The ZrH₂-moderated assembly experienced much higher heterogeneity of reaction rate — up to around 10% for fission and 44% for capture. The impact of wrapper tube was not visible, as the moderation effects of ZrH₂ was far stronger in comparison. The increase in reaction rates was visible mainly in the outer rim of fuel pellets at the side facing a ZrH₂ pin.

Because the thermal power generated is proportional to the fission rate, the uneven fission rate distribution in CADOR assemblies implies the existence of in-assembly power peaks of magnitude much higher than in standard SFR assembly. Analogically, higher capture rate leads to higher local plutonium breeding, which in turn can affect the power distribution after prolonged period of reactor operation. Naturally, both fission and capture rates in fuel also influence the value of the multiplication factor k .

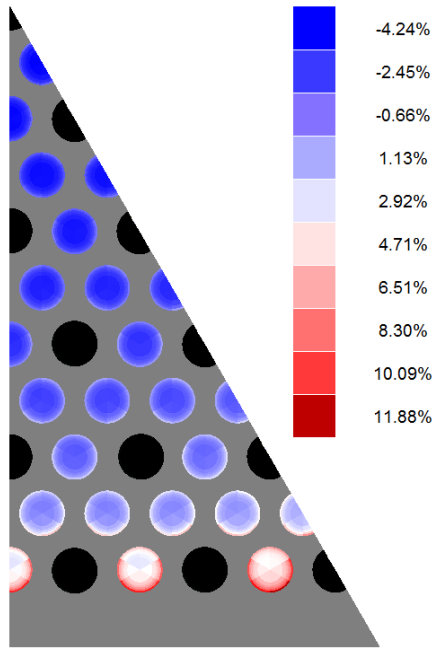
A similar effect is also expected to manifest in the vicinity of control rods. The additional moderation in the outer layer of fuel assembly at the side neighboring the control rod cluster may increase the efficiency of neutron captures in absorber and, as a consequence, the value control rod worth.

A summary of several quantities related to the heat maps is presented in the Table 4.8.

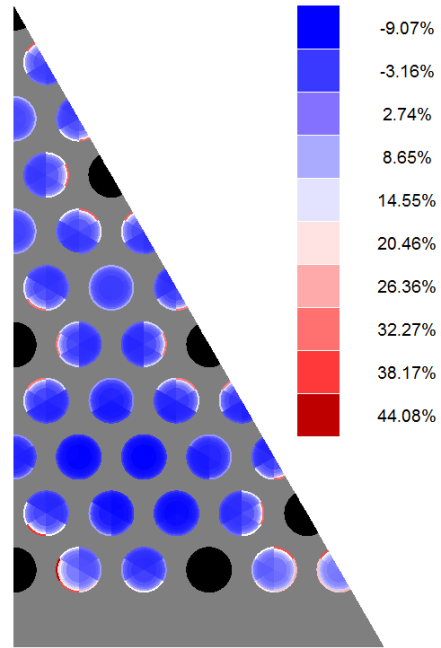
Table 4.8: Summary of the spatial distributions.

	10.5 % Be		3.5 % ZrH ₂		no moderator	
	C1	C2	C1	C2	C1	C2
Avg. neutron energy per cell						
Min deviation [%]	-9.4	-9.4	-43.5	-43.6	-4.3	-4.3
Max deviation [%]	7.6	7.7	14.4	14.4	3.6	3.5
Capture rate per cell						
Min deviation [%]	-4.4	-4.2	-9.1	-9.1	-2.0	-2.0
Max deviation [%]	14.6	12.0	47.5	44.1	5.1	4.5
Fission rate per cell						
Min deviation [%]	-1.5	-1.4	-4.1	-3.8	-0.2	-0.2
Max deviation [%]	2.9	2.7	10.8	10.2	0.4	0.4

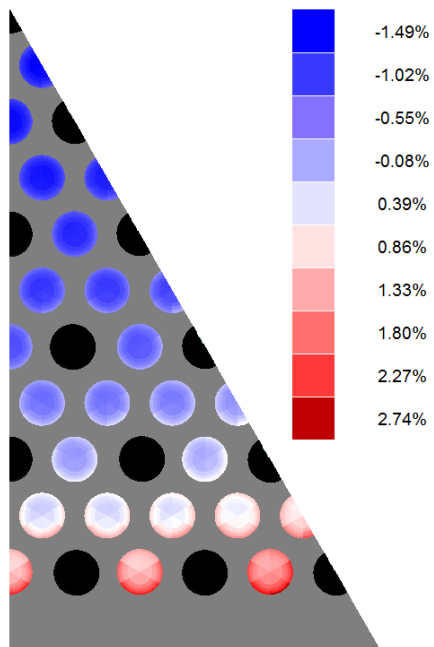
The uneven reaction rate distribution is undesirable from the point of view of reactor safety and control. The effect has an impact on the power peaking factor, an important safety



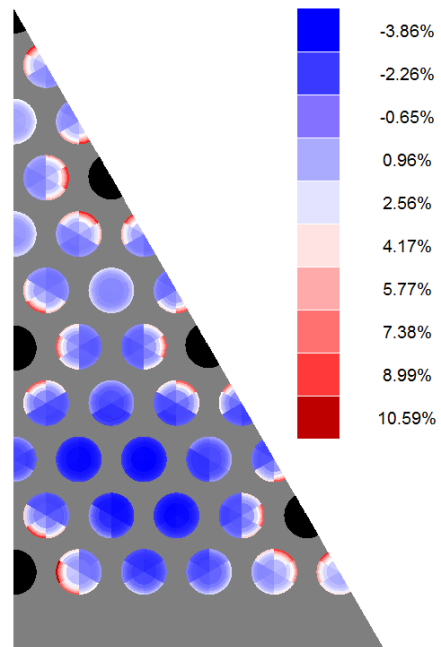
(a) capture rate, Be moderator



(b) capture rate, ZrH₂ moderator



(c) fission rate, Be moderator



(d) fission rate, ZrH₂ moderator

Figure 4.12: Deviation from the global average reaction rate in fuel [%] for assemblies with Be and ZrH₂. The black circles signify positions of the moderator pins, gray-colored areas are parts of assembly without fuel.

parameter, and the evolution of the fuel, with different fuel pins burning faster than others. Unfortunately, localized peaks and valleys are visible only in case of very refined spatial mesh. In case of coarse mesh with fewer cells, as commonly used in fast reactor calculations, it is impossible to reproduce the fast changes of reaction rates. To illustrate this point graphically, Figure 4.13 compares two heat maps obtained for ZrH_2 assembly, both calculated with the same solver parameters, but with two different spatial meshes (as in Figure 4.9). It is worth

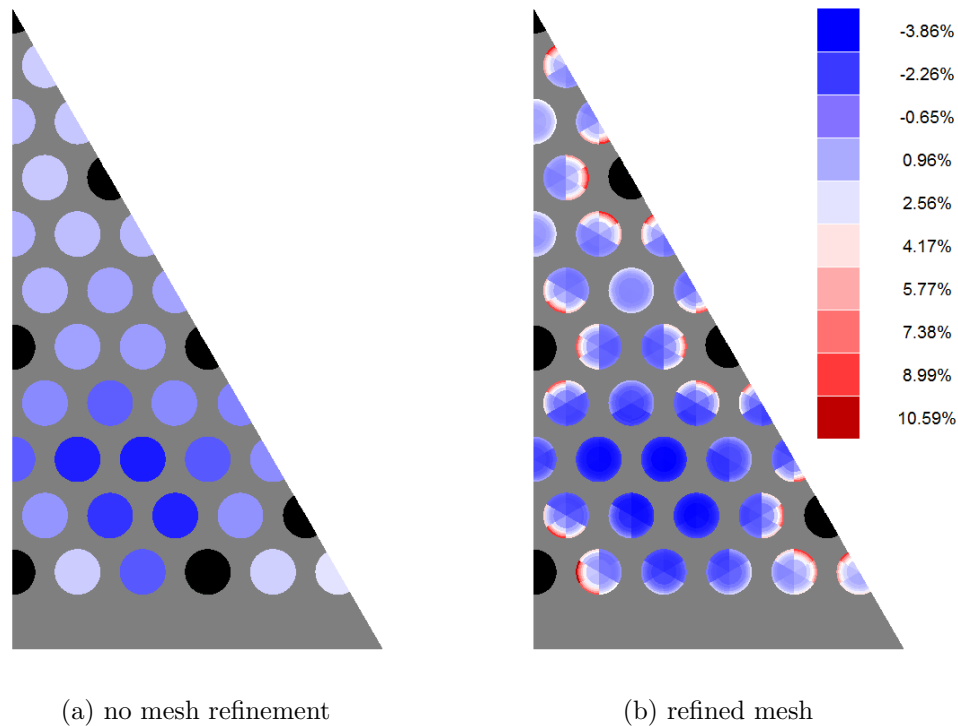


Figure 4.13: Comparison of deviation from global average fission rate in two assemblies calculated with different spatial meshes.

noting that the problem of heterogeneous moderation extends to the second calculation step — the core calculation. To manage neutron transport calculation at the full core scale it is required to reduce the number of cells, typically a fissile zone of each fuel assembly is transformed into a single homogeneous medium. In such a case the information about distribution of cross-sections and reaction rates within assembly is irreversibly lost, making accurate calculation harder to perform.

Moreover, the problem could extend beyond the neutronic analysis. The peaks in power distribution lead to different temperature distribution in the fuel, possibly decreasing the actual margin to fuel meltdown.

4.4 Comparison of scattering models (TRIPOLI-4[®])

This section focuses on evaluating the impact of different approaches to neutron scattering treatment. At this point, the study is limited to methods provided by Monte Carlo code TRIPOLI-4[®]. For more details about those methods, see Section 3.7 in the previous chapter.

The exact scattering kernel was proven in the past to provide significant accuracy improvement in some nuclear systems, especially in case of thermal reactors [74, 73]. On the other hand, in case of standard fast reactors, the effect of resonance scattering is typically neglected. A hard, not moderated neutron spectrum is mostly confined in the high energy region where Asymptotic Kernel is a sufficient approximation to correctly model neutron–nucleus collisions. For reactors such as CADOR, however, we observe a non-negligible flux values at low energies, especially when using ZrH₂ moderator. From the point of view of CADOR, the accurate modeling of neutron scattering is crucial due to a link between resonance scatterings and the Doppler effect, one of the primary parameters of the design.

4.4.1 TRIPOLI-4[®] calculation details

The TRIPOLI-4[®] calculations were conducted with pointwise cross-sections and exact geometry. All calculations were performed with 100 000 batches per 10 000 neutrons (in total one billion neutrons simulated) which resulted in a standard deviation of k of around 4 pcm.

4.4.2 Scattering kernel settings in TRIPOLI-4[®]

As explained in Section 3.7, there are four scattering models available in TRIPOLI-4[®]: AK – assumes lack of thermal motion, SVT – represents the “constant XS” approximation to free gas kernel, DBRC and WCM methods – represent the exact free gas scattering kernel. As DBRC and WCM methods are equivalent when it comes to the physics of the scattering, only the former was used in this thesis.

Typically, it is sufficient to apply the correction to SVT model only for scatterings with ²³⁸U, as it is the major actinide in the nuclear fuel. The range of applicability of DBRC method begins at energies around 0.1 eV and ends at few hundred eV. Below 0.1 eV no resonances in cross-section occur and, thus, the “constant cross-section” approximation of SVT method is accurate to a reasonable margin of error. Conversely, for energies beyond few hundred eV the momentum of nuclei becomes negligible even for head-on collisions and, thus, the AK model can be safely used instead.

A series of TRIPOLI-4[®] simulations was carried out for all three types of assemblies with different settings regarding the scattering kernel. Because the average speed of a nucleus is proportional to the square root of temperature, the study was conducted for three different temperature points: nominal temperature 900 °C (1174 K), close-to-accidental temperature 2000 °C (2274 K) and beyond-accidental temperature 2700 °C (2974 K). Initially two types of scattering treatment were used:

1. **SVT_{4.95eV}**: SVT model for scatterings at $E < 4.95$ eV, AK model above

2. **DBRC_{360eV}**: in case of ²³⁸U, SVT model below 0.1 eV, DBRC model for at $E \in (0.1 \text{ eV}, 360 \text{ eV})$, AK model above 360 eV. Other isotopes treated as for SVT_{4.95eV} in point 1

The Figure 4.14 shows comparison between the two scattering options. In TRIPOLI-4[®] the SVT upper limit of $400k_B T$ is used by default. The $400k_B T$ limit is more conservative than 4.95 eV used in the study ($400k_B T \approx 10 \text{ eV}$ for a room temperature). The fixed limit of 4.95 eV is, however, used in APOLLO3[®] pre-processed libraries, therefore, to be able to consistently compare the results from both codes, this threshold was used in TRIPOLI-4[®] as well. Similarly, the applicability of exact scattering kernel in APOLLO3[®] for thermal

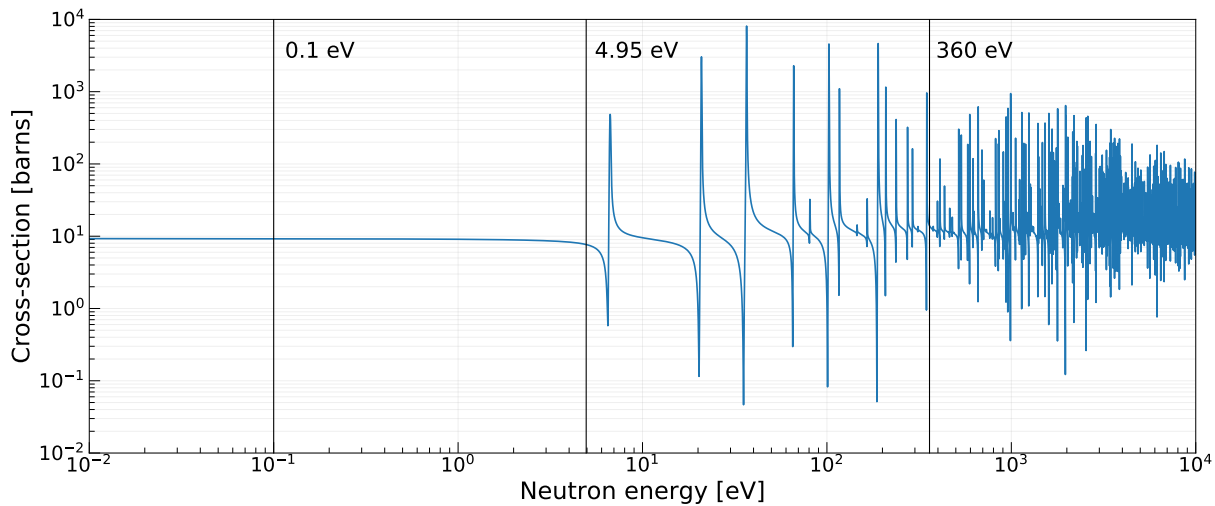
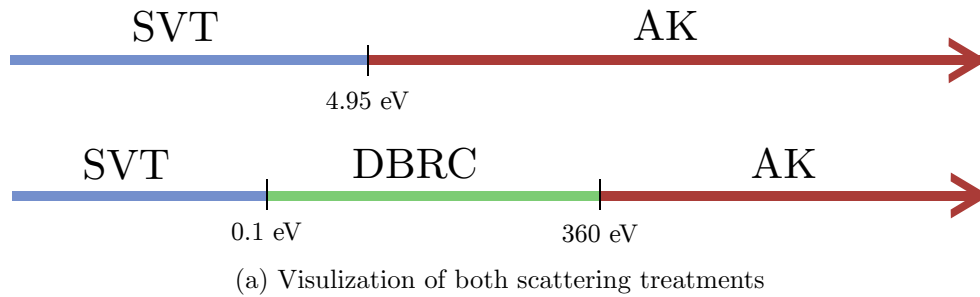


Figure 4.14: Comparison of two scattering treatments used in the study.

reactors was estimated to be reasonable up until 360 eV [70]. For this reason, in this study 360 eV is used as well.

The values of flux within 0.1 eV–360 eV interval for the CADOR model used in the study are given in Table 4.9. For a standard SFR design the flux in the DBRC domain constituted little more than 0.1 % of total neutron flux. For moderated CADOR assemblies the fraction of flux exceeded 1 %, around one order of magnitude higher. Similar behavior was observed for the reaction rates — the fractions were noticeably higher if the moderator was present, particularly ZrH₂. The fractions were also higher for C1 assemblies.

Table 4.9: Fractions of flux and absorption rates inside (0.1 eV, 360 eV) energy interval, calculated with APOLLO3[®] without employing exact free gas scattering.

Assembly type	Fraction of flux		Fraction of absorption rate					
			fuel		U238		Pu239	
	C1	C2	C1	C2	C1	C2	C1	C2
CADOR, 10.5 % Be	2.0	1.4	14.6	11.2	9.8	7.5	17.7	13.1
CADOR, 3.6 % ZrH ₂	3.3	2.6	27.4	23.5	18.3	15.9	30.8	25.3
Standard SFR	0.2	0.1	1.7	1.0	1.1	0.6	2.2	1.2

4.4.3 Impact on reactivity and Doppler constant

Table 4.10 presents the results of the first series of calculations. All the results are presented as a reactivity difference between a DBRC_{360eV} and SVT_{4.95eV} settings for the same assembly geometry and fuel temperature.

Table 4.10: Reactivity differences for different DBRC_{360eV} settings in TRIPOLI-4[®] compared to SVT_{4.95eV} method. Standard deviation of all results equal to 3 pcm.

T _{fuel}	$\Delta\rho(\text{SVT} - \text{DBRC})$	
	C1	C2
Be moderator		
900 °C	-2	-1
2000 °C	52	22
2700 °C	85	39
ZrH ₂ moderator		
900 °C	20	11
2000 °C	111	63
2700 °C	154	93
no moderator		
900 °C	1	-2
2000 °C	5	2
2700 °C	-1	-1

For the temperature of 900 °C the differences between the two scattering options were almost unnoticeable, most of the differences being confined within $\pm\sigma$. However, for the higher temperatures the differences become much more pronounced, notably in the case of ZrH₂ moderator. As expected, the difference was strongly increasing with the fuel temperature, for 2700 °C reaching a reactivity difference of little more than 150 pcm for ZrH₂-moderated assembly, but only about 85 pcm in case of Be moderator. The differences are about two times higher in case of C1 assembly when compared to C2. In case of lack of moderator, the

differences for all three temperatures were statistically insignificant.

The discrepancies were relatively high if we take into account the magnitude of the Doppler feedback in both cases. As the magnitude of Doppler constant for both moderated assemblies is of the order of 1200-2000 pcm, the discrepancies of few dozens to more than 100 pcm can become important. The comparison of values of Doppler constant calculated for the case of SVT_{4.95eV} model and DBRC_{360eV} is shown in Table 4.11.

Table 4.11: Values of the Doppler constant for DBRC_{360eV} and SVT_{4.95eV} scattering kernels, calculated between 900 °C and 2000 °C. Associated uncertainties are equal to 1σ .

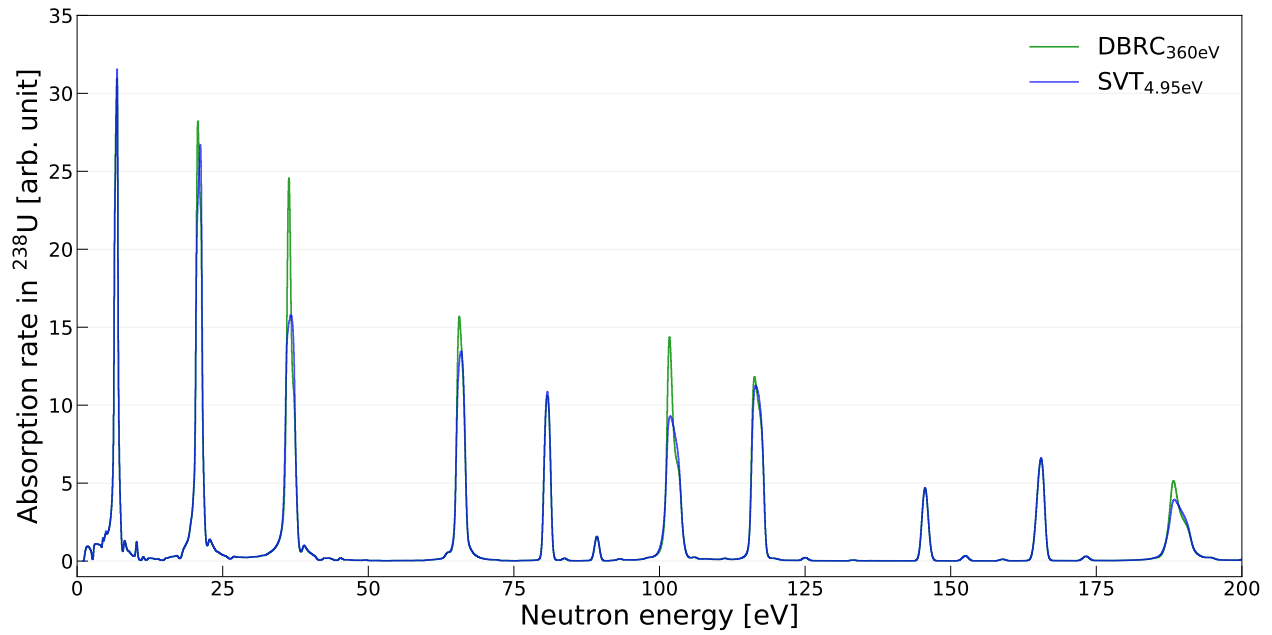
	C1	C2
Be moderator		
$K_D(\text{SVT})$ [pcm]	-1978 ± 5	-1244 ± 5
$K_D(\text{DBRC})$ [pcm]	-2061 ± 5	-1279 ± 5
$\Delta K_D(\text{SVT-DBRC})$ [pcm]	82 ± 7	35 ± 7
$\Delta K_D(\text{SVT-DBRC})/K_D(\text{DBRC})$ [%]	-4.0 ± 0.4	-2.8 ± 0.5
ZrH ₂ moderator		
$K_D, (\text{SVT})$ [pcm]	-1899 ± 5	-1299 ± 4
$K_D, (\text{DBRC})$ [pcm]	-2027 ± 5	-1377 ± 5
$\Delta K_D(\text{SVT-DBRC})$ [pcm]	138 ± 7	78 ± 6
$\Delta K_D(\text{SVT-DBRC})/K_D(\text{DBRC}) - 1$ [%]	-6.8 ± 0.4	-5.7 ± 0.5

The exact scattering treatment of DBRC model led to differences of up to 4.0% and 6.8% for Be and ZrH₂, respectively. As shown before, the DBRC model did not bring significant improvement in case of calculations with nominal fuel temperature. However, for calculations with accidental conditions the difference reached up to more than hundred pcm. For this reason, the Doppler constant calculated using both the reactivity at nominal and accidental temperatures is strongly affected by the inaccuracy of SVT_{4.95eV} model at high temperatures.

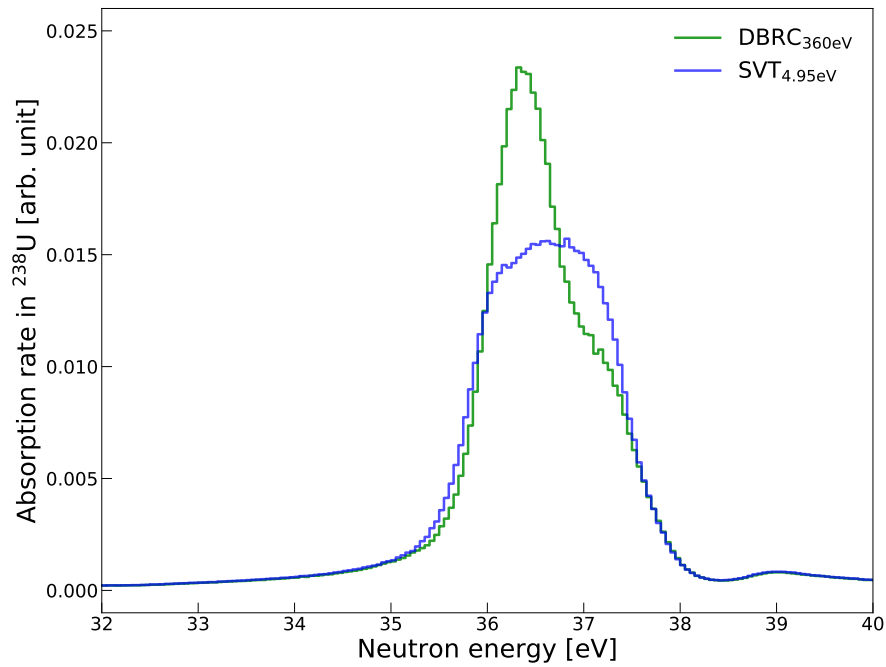
4.4.4 Impact on reaction rates

If we take a look at the absorption rates in ²³⁸U close to resonance energies (Figure 4.15a), we can see the characteristic asymmetric shape produced with DBRC model. As discussed in the previous chapter, the resonance upscattering increases the absorption rate at the lower part of a resonance which increases its efficiency in absorbing neutrons. This effect is impossible to reproduce with SVT scattering kernel due to the “constant XS” assumption; as a consequence, the absorption rates tend to be visibly underestimated.

Table 4.12 quantifies the differences between models for absorption and fission rates in ²³⁸U and ²³⁹Pu. The reaction rates were normalized with respect to the fission source, so that



(a) Comparison of absorption rate in ^{238}U in the first several resonances up to 200 eV



(b) Absorption rate in U_{238} in the vicinity of 36 eV resonance

Figure 4.15: Comparison of two scattering treatments used in the study. Results presented for C1 assembly with ZrH_2 with fuel temperature set to 2000 °C.

$\frac{1}{k}\mathcal{F}\psi = 1$ (the default normalization in TRIPOLI-4[®] for multiplying systems). The differences between SVT and DBRC were calculated as

$$\Delta R = (R_{\text{SVT}} - R_{\text{DBRC}}) \cdot 10^5 \text{ [pcm]} \quad (4.5)$$

Table 4.12: Relative difference of absorption rate [pcm] between DBRC_{360eV} and SVT_{4.95eV} kernels. Associated uncertainties are equal to 1σ .

	10.5 % Be		3.6 % ZrH ₂	
	C1	C2	C1	C2
T _{fuel} =900 °C				
ΔR, ²³⁸ U	-11 ± 2	-3 ± 2	-40 ± 2	-28 ± 2
ΔR, ²³⁹ Pu	-6 ± 2	-2 ± 2	5 ± 2	5 ± 3
T _{fuel} =2000 °C				
ΔR, ²³⁸ U	-46 ± 2	-26 ± 2	-115 ± 2	-85 ± 2
ΔR, ²³⁹ Pu	27 ± 2	16 ± 2	60 ± 2	41 ± 3
T _{fuel} =2700 °C				
ΔR, ²³⁸ U	-76 ± 2	-44 ± 2	-167 ± 2	-122 ± 2
ΔR, ²³⁹ Pu	48 ± 2	27 ± 2	87 ± 2	62 ± 3

The results show that the approximate scattering kernel of SVT method underestimates the absorption in ²³⁸U and, at the same time, but to a lower extent, overestimates absorption rate in ²³⁹Pu. Even though the exact scattering kernel for ²³⁹Pu is not realized in the DBRC methods used in this study, the exact kernel for ²³⁸U still visibly influences the absorption rate in ²³⁹Pu. Both ²³⁸U and ²³⁹Pu absorptions are competing with each other.

4.4.5 Extended scattering kernel settings

In case of APOLLO3[®] libraries, the exact free gas scattering is applied to three isotopes: ²³⁸U, ²⁴⁰Pu and ²⁴²Pu. To see if extending the number of isotopes treated by DBRC model beyond just ²³⁸U results in a significant difference, a next series of calculations was performed, this time with all actinides present in the fuel treated with DBRC method. The reactivity difference between this approach and using just ²³⁸U is presented in Table 4.16. Inclusion of additional five actinides had a very low effect on the final reactivity. Similarly, we determined that the extension of DBRC cutoff energy beyond 360 eV also does not bring significant improvement of accuracy. As shown in Figure 4.16, the difference between SVT and DBRC applied to ²³⁸U above 360 eV was negligible.

4.5 Conclusions

This chapter presented some of the features of the softened spectrum of CADOR that can have an impact on the way neutron transport calculations are performed. The goal of softening

Table 4.13: Reactivity difference between calculations with DBRC model with all actinides and DBRC model with only ^{238}U (as in previous tables) for C1 assembly.

	$\Delta\rho\left(\text{DBRC}_{360\text{eV}}^{\text{U}^{238}} - \text{DBRC}_{360\text{eV}}^{\text{all}}\right)$	
T_{fuel}	10.5 % Be	3.6 % ZrH ₂
2000 °C	10 ± 4	0 ± 4
2700 °C	-3 ± 4	-8 ± 4

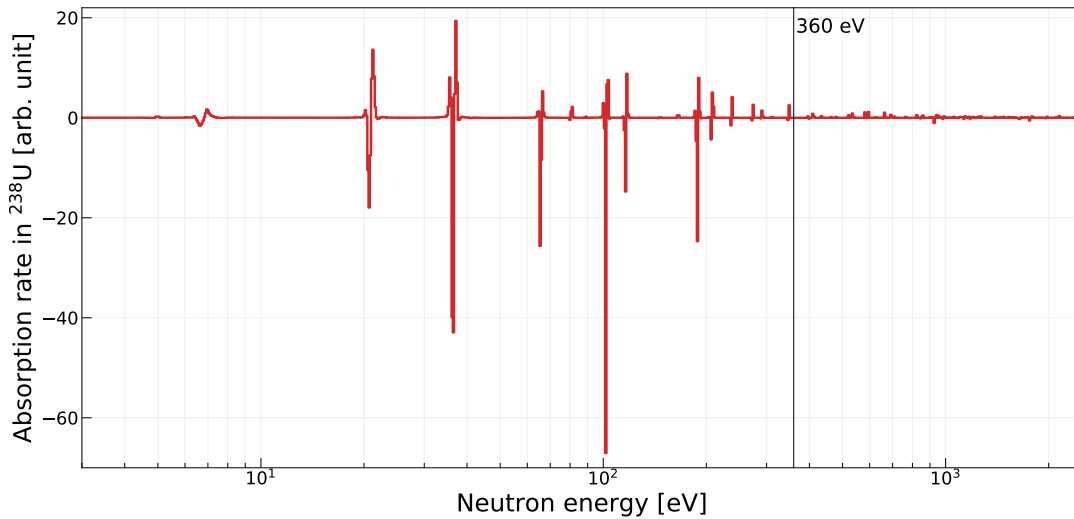


Figure 4.16: Difference of absorption rate in ^{238}U between $\text{SVT}_{4.95\text{eV}}$ and $\text{DBRC}_{10\text{keV}}$ for ZrH₂-moderated C1 assembly at fuel temperature of 2000 °C.

by neutron moderators was achieved: the average neutron energy was lowered from around 110 keV to 65 keV and the neutron flux below 10 keV was increased by 77 % and 109 % for Be and ZrH₂ moderators, respectively. Lower average energy was followed by the mean free path in the entire assembly lowered by up to 7 %, although the difference was much smaller if we consider only the fuel pellets.

Shorter mean free path combined with heterogeneous moderator placement gave rise to uneven neutron distribution in fuel assemblies. Slower neutrons, concentrated in the vicinity of moderator pins, were absorbed at higher rates causing an uneven power distribution and potentially uneven fuel evolution, mainly in the outer rim of fuel pellets. In case of ZrH₂ pins, the effect was more prevalent; moreover, stronger and more localized moderation caused the distribution of reaction rates in fuel pellets to be different depending on which side faces the moderator.

Secondly, the resonance scattering was identified as an important physical phenomenon if sufficiently many low energy neutrons are present. While in a standard SFR without moderator the effects of using the “constant cross-section” assumption, implemented in SVT

model, did not cause any visible loss of accuracy, the same was not true for CADOR. The exact scattering kernel of the DBRC model did not bring noticeable improvement for fuel at temperature of 900 °C, although, at accidental temperatures the differences became significant. For the fuel temperature of 2700 °C, the reactivity difference between $\text{DBRC}_{360\text{eV}}$ and $\text{SVT}_{4.95\text{eV}}$ scattering options reaches 32 and 88 pcm for Be and ZrH_2 , respectively. This variation of importance of resonance scattering at different temperatures led to noticeably different values of the Doppler constant for the two scattering models. The results suggest that relying solely on SVT model causes the Doppler constant to be lower by few percent (up to 6.8% in case of assemblies with ZrH_2), a result that is consistent with other studies conducted for thermal reactors.

All the phenomena described in this chapter are caused by the presence of neutron moderator and are generally insignificant in conventional SFR core designs. As such, each of them can have an impact on the applicability of the generic calculation scheme designed for typical fast reactors. The exact way in which the scheme is affected, the quantification of biases introduced by calculation methods as well as the possible solutions to reduce them are studied in the next chapter.

Chapter 5

Validation of the calculation scheme

This chapter covers the description of the CADOR core geometry and the standard calculation scheme used to treat such fast reactors in APOLLO3[®]. The second part of the chapter presents multiple APOLLO3[®]/TRIPOLI-4[®] comparisons for cases from a single fuel assembly to the entire 3D core.

5.1 Description of the core geometries

In this section we present the main CADOR core design selected for the thesis. The design is based on the 1500 MW_{th} core with 11% Be described in an internal report of CEA (personal communication, January 2019).

The fuel assemblies used in the previous studies belonged to a very large CADOR core with a thermal power of 3600 MW, that we are going to refer to from now as Core I. The new Core II model is significantly smaller which allows more demanding calculations to be performed in a reasonable amount of time. Moreover, Core II is closer to other ongoing CADOR studies conducted in CEA.

The entire horizontal arrangement of the core is visible in Figure 5.1. The most important design parameters are given in Table 5.1. The core was originally designed for assemblies with 11.5% beryllium content; however, for the purpose of the thesis, analogical assembly versions with ZrH₂ moderator and without moderator were also created, resulting in three different core models (as for assembly models of Core I in the previous chapter).

5.1.1 Geometry of the fissile zone, differences between Core I and Core II

The fuel assembly layout of Core II differs in several ways from the one used in Core I. The size and number of pins, structure materials and plutonium enrichment has been slightly modified compared to Core I; however, the moderator-to-fuel ratio was kept almost unchanged. The number of Be and ZrH₂ pins was lowered to match the lower total pin number (271, instead of 331 used in Core I). The three types of Core II fuel assemblies are:

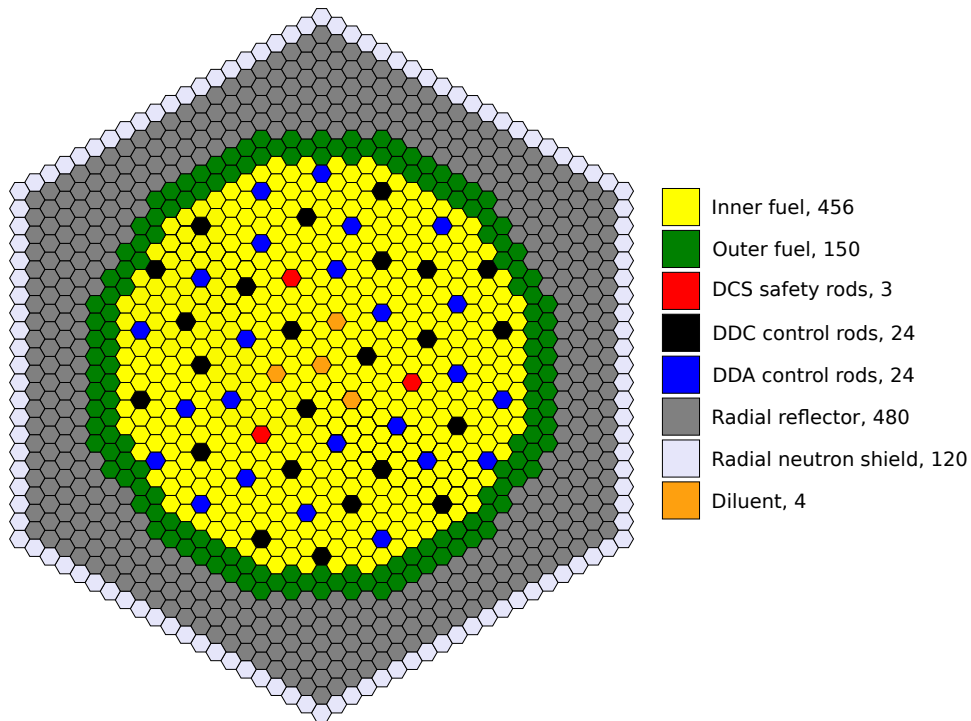


Figure 5.1: Horizontal layout of Core II. The legend on the right lists the types of assemblies and their respective number in the core.

Table 5.1: Selected parameters of Core II.

Parameters	Values
thermal power	1500 MW
average linear power	102 W/cm
number of fuel assemblies (C1/C2)	456 / 150
equivalent core radius	245 cm
equivalent inner core radius	213 cm
core height	350 cm
number of pins per ass.	271
number of moderator pins per ass.	73 (Be) / 25 (ZrH ₂)
enrichment (C1/C2)	19.8% / 22.0%
Pu vector used	REP MOX _j
assembly pitch	18.96 cm
cladding radius	0.485 cm
fuel pellet radius	0.4205 cm
moderator pellet radius	0.395 cm

1. assembly with 73 Be pins – 11.5 % of assembly volume (10.5 % in Core I)
2. assembly with 25 ZrH₂ pins – 3.9 % of assembly volume (3.6 % in Core I)
3. assembly without moderator, all pins containing only fuel

Figure 5.2 presents the comparison of the two layouts. Core II is characterized by a larger size of the assembly as well as larger pin size. Unlike in Core I, the radius of moderator pellets and fuel pellets in Core II is not exactly the same: the moderator radius is smaller, the difference is compensated by a larger gap between moderator and cladding. Additionally, the central hole was included explicitly in the fuel pellets description. Despite the differences mentioned above, the material proportions and general layout of both assembly designs remains very similar.

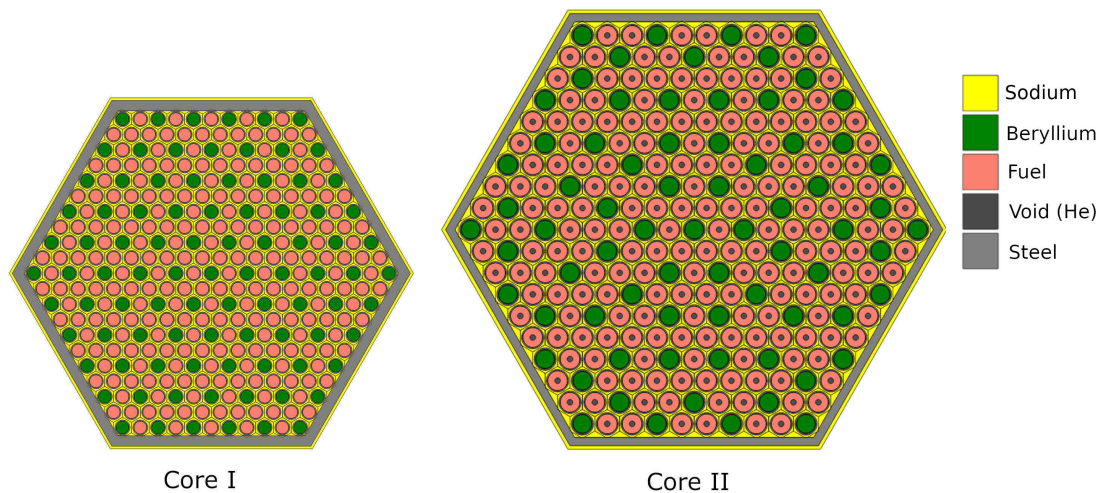


Figure 5.2: Comparison of assembly models of Core I and Core II (the real proportions are preserved). In both cases the layout with beryllium pins is shown.

5.1.2 Detailed description of Core II

5.1.2.1 Radial description

The core exhibits a relatively homogeneous design with only two radial fissile zones: inner core C1 composed of 456 assemblies and outer core C2 containing 150 assemblies. Assemblies of inner and outer core differ only by the Pu enrichment, their geometries are identical.

The core is surrounded by four layers of MgO reflector assemblies and an outermost layer of radial neutron protection assemblies (PNL) made primarily of B₄C. At the center of the core, the DILUANT assemblies are placed. The assemblies are primarily made of steel and their goal is to flatten the neutron flux in the center of the core, where it tends to be the highest.

The core possesses three types of rod cluster control assembly (RCCA): two types, DDC and DDA used for precise reactivity control (24 assemblies each) and three DCS hydraulic safety rods that are inserted passively when the sodium flow in the core drops below certain value.

If not specified otherwise, the rods are always withdrawn from the fissile zone (the absorbers are placed at the height at which the fissile zone ends).

5.1.2.2 Axial description

Each fuel assembly consists of six axial zones (Figure 5.3). The large fissile zone of $H=120$ cm is covered from the top and bottom with 20 cm of fertile axial blankets (CAS and CAI). The model includes also upper and lower gas plena (VEI and VES) and a 80-cm-thick neutron protection at the top of the assembly (PNS).

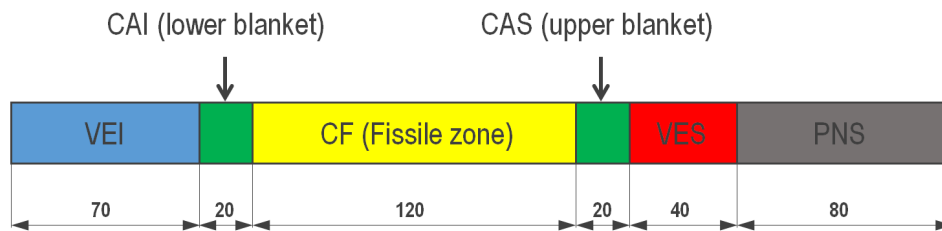


Figure 5.3: Axial profile of a fuel assembly.

5.1.3 Materials

Unlike in Core I, the fuel cladding and the hexagonal wrapper tube are made of different materials: AIM steel for cladding and EM10 steel for wrapper tube.

The fuel composition used is closer to the real MOX fuel used in fast reactors. New fuel composition includes eight actinides instead of six. The fraction of ^{239}Pu in plutonium is visibly lower (38% instead of 60%), but the fraction of heavier plutonium isotopes is increased. The Pu enrichment is set to be 19.8% for inner core and 22% for outer core.

The moderators composition remains the same; however, as mentioned before, because of the differences in pin sizes the exact percentage of volume occupied by moderators is not identical. Compared to Core I, the volume fraction of both Be and ZrH_2 in their respective assemblies was increased by approximately 10%.

Detailed values for dimensions of assemblies and material compositions are contained in Appendix A.

5.2 Description of the calculation scheme

As presented before in Section 2.6.10, the deterministic neutron transport codes often utilize two-step calculation scheme that can be further divided into five general components. This chapter presents a detailed look at the state-of-the-art reference calculation scheme used to treat SFR cores (Figure 5.4).

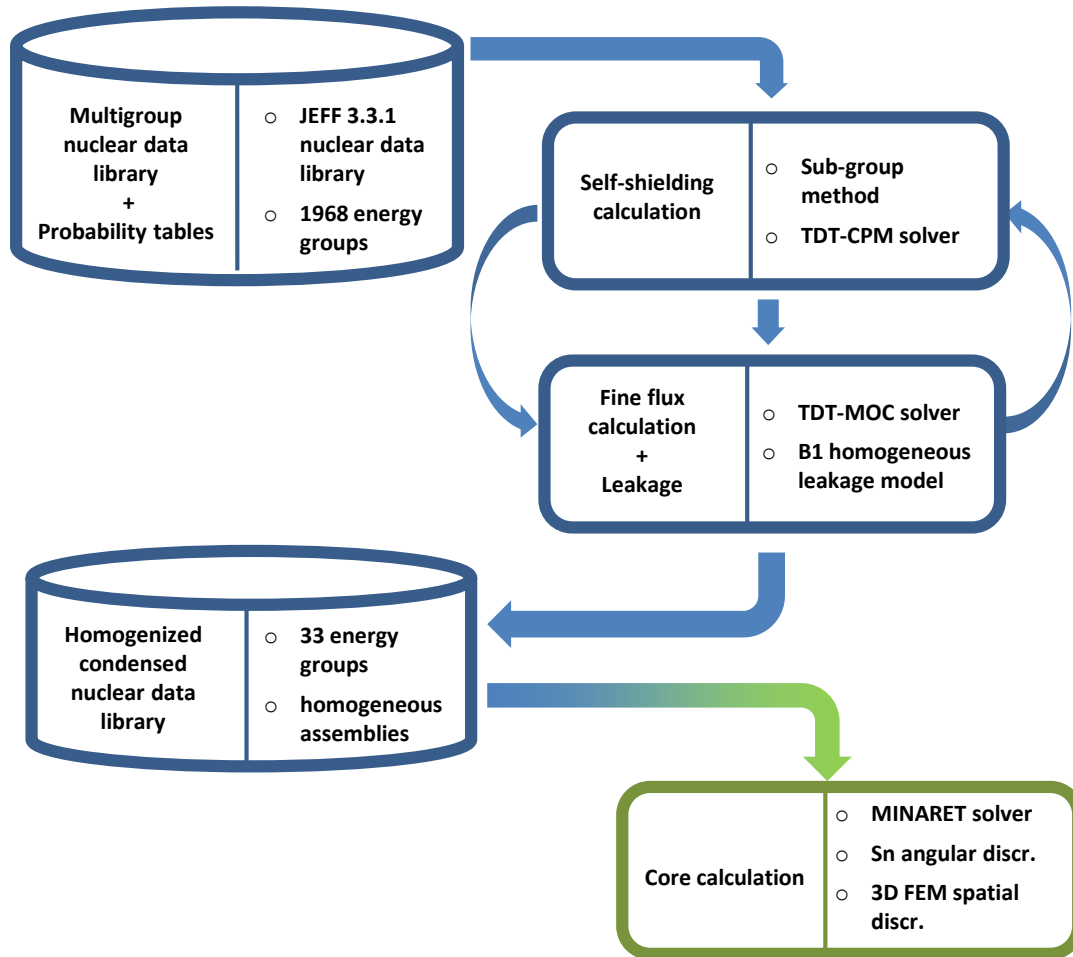


Figure 5.4: Description of the two-step deterministic calculation scheme used for SFR calculations in APOLLO3[®].

5.2.1 Creation of multigroup library

First, the multigroup data library is created based on Joint Evaluated Fission and Fusion (JEFF) library. In case of this thesis the version used was JEFF 3.1.1. The multigroup libraries based on newer version JEFF 3.2 are already available, however they were not fully validated at the time of writing this work. The library is processed by GALILEE processing tool [56]. The continuous distributions of cross-sections are approximated with multigroup arrays and matrices, as explained in Section 2.6.1.

As mentioned in Section 2.6.1, the calculations of SFR use very fine energy meshes. The most popular choice in APOLLO3[®] is the mesh consisting of 1968 groups, first time used for ECCO lattice transport code [39]. An alternative choice is a more recent mesh consisting of 1760 groups, created to improve accurate handling of self-shielding effects.

5.2.2 Fine flux calculation and self-shielding

At this stage, a series of calculations has to be performed to obtain self-shielded and homogenized/condensed cross-section libraries, to use later in core calculation. The reference SFR scheme of APOLLO3[®] utilizes two variants of TDT solver. Self-shielding calculation uses collision probability method of TDT-CPM solver to solve the slowing-down equation, whereas flux calculation uses method of characteristics of TDT-MOC solver. The Sub-group method is the reference method of self-shielding; however, in many fast reactor applications it can be substituted by a faster Tone's method to achieve a similar level of accuracy. In each fuel assembly, the fuel pellets in the outermost ring are treated as a separate self-shielding zone to take into account the influence of the steel wrapper. An exact geometry description is used for all of the most important components. This means that fuel pellets, cladding and the gap between them are included explicitly in the geometry.

5.2.2.1 Critical fuel assembly

To get the cross-sections for C1 and C2 fuel assemblies, the calculation with a single 2D assembly is performed. In order to get the most representative approximation of the assembly behavior in a finite core, the B1 homogeneous leakage model is used (Section 2.6.6).

5.2.2.2 Subcritical core elements

To obtain cross-sections of subcritical zones of the core such as reflectors, gas plena, fertile blankets or control rods, the cluster setup of a subcritical component surrounded by multiple fuel assemblies is used. The role of fuel assemblies is to provide a neutron source representative of conditions in the full core.

In case of subcritical reactor components, such as control rods, gas plena or fertile blankets, the representative flux must be calculated while taking into account their surroundings. In the reactor core, the flux within subcritical elements is generated by neighboring fuel assemblies. To simulate the conditions in the full core, a setup of a subcritical element surrounded by six C1 fuel assemblies is used. Because of the symmetries a triangular piece with reflective boundary conditions applied is enough to represent the entire geometry (Figure 5.5).

The geometry of four subcritical components: fertile blankets (CAS, CAI) and gas plena (VES, VEI), are recreated exactly. In most of calculations in this thesis the cross-sections for other components, e.g., reflectors, shields, control rods and diluent were calculated with a fully homogeneous geometry of central assembly composed of just one medium. However, in case of control rod worth calculations, media of DDC, DDA and DCS absorbers were computed in cluster calculations with heterogeneous central assembly.

For elements present on the same height as fissile zone, the geometry of cluster is a good representation of actual situation in the core. Other subcritical elements such as fertile blanket or gas plena are never surrounded by fissile material, but are rather placed on top or below the fissile zone, making clusters a relatively coarse representation. Despite that, in case of CADOR assembly we decided to use cluster representation, as the aforementioned subcritical elements are found outside of the main part of the core and, thus, they bring

relatively small contribution to the global neutron balance. To get a more accurate results for vertically stacked elements, a 2D-1D calculation [89] scheme or 3D-MOC calculation of entire assembly [90] could be used. These techniques are most useful in case of strong vertical heterogeneity of core geometry, for example, the sodium plenum at the top of CFV core of ASTRID reactor [91].

5.2.2.3 Assemblies at core-reflector boundary

At the core-reflector boundary the interaction between C2 fuel assemblies and radial reflector becomes important. The standard cluster representation in this case is flawed, as it assumes reflector being surrounded by fuel assemblies, when in reality it is attached to fuel assemblies only from one side. To solve this problem, another type of cluster called “traverse” can be used. The traverse is a long strip of 2D assemblies containing fuel assemblies and assemblies of the reflector in representative proportions. In case of CADOR core used in the study, the reflector is made of four REFL assemblies and radial neutron shield (PNL) assemblies in the last ring. The traverse constructed consists of seven assemblies in total (Figure 5.5c). The left, top and bottom boundary have reflective conditions applied, but the right boundary is left open, enabling neutron to leak out of the geometry (“void” boundary conditions). This way, a realistic neutron current can be simulated in the lattice calculation. The cross-sections obtained via traverse are more representative but a fine calculation with such a large geometry requires longer computation time than in case of a standard cluster.

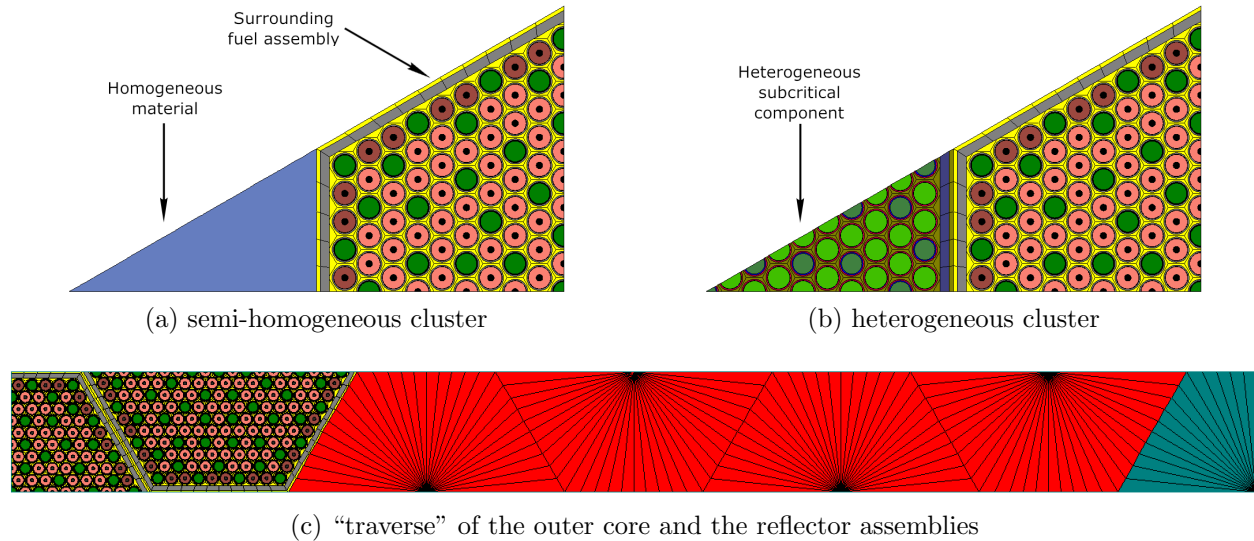


Figure 5.5: Description of the assembly clusters used in the calculation scheme.

5.2.3 Creation of homogenized and condensed library

The next step is the homogenization of the media in space and condensation in energy to create a coarse library used in the core calculations. The reference calculation route involves condensation of the cross-sections to 33 energy groups and full homogenization of

the assemblies, transforming them into a single medium with evenly distributed isotope mix. Because MINARET, the core solver of APOLLO3[®], is capable of using unstructured geometries of almost any shape, it is possible to preserve some level of heterogeneity by performing only a partial homogenization. The partial homogenization can be used most effectively with respect to areas with high variation of neutron flux such as control rods.

The homogenization/condensation is performed at the end of each lattice calculation. The resulting cross-sections are then stored in a Multi-Parameter Output (MPO) library format. For most media it is sufficient to perform the homogenization/condensation according to the flux-volume weighting. In some areas with particularly high flux anisotropy, e.g., at the core-reflector boundary, it is often beneficial to use the weighting by flux moments.

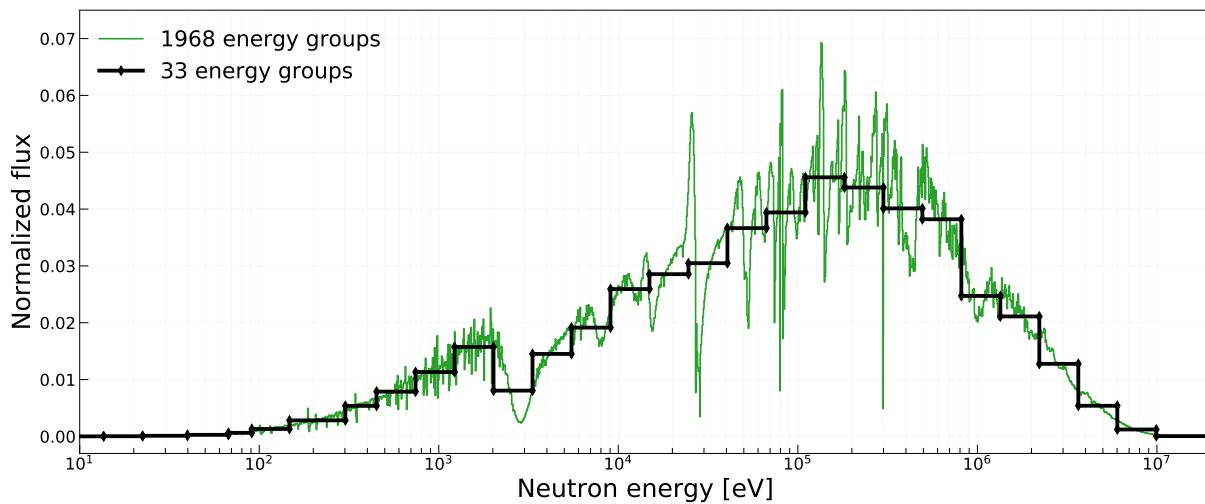


Figure 5.6: Comparison of neutron spectrum after lattice calculation with 1968 groups and after condensation to 33 groups

5.2.4 Core calculation

Core calculation in APOLLO3[®] uses Finite Element Method provided by the MINARET [49] S_n neutron transport solver. The angular variable is treated with discrete ordinates method. The geometry is discretized spatially into set of triangular (2D) or prismatic (3D) finite elements. Typically, the first order polynomials projection is used in both axial and radial directions. The size of finite elements and the number of discrete ordinates has to be specified so that they guarantee a satisfactory convergence of results.

5.3 Comparison of assembly calculations

The validation of the calculation scheme begins with a case of a single fuel assembly in the lattice calculation. For the validation purposes, in this section the reflective boundary

Table 5.2: Optimal TDT solver options for SFR lattice calculation, according to [92].

	CPM	MOC
No of horizontal angles	12	24
No of vertical angles	3	4
Transv. integration step	0.1	0.04
Max. inner iterations	10	10
Max outer iterations	200	200

conditions without a leakage model were applied, to allow easy comparison with Monte Carlo calculations (as no leakage model is available in TRIPOLI-4[®]).

Because the Core II was introduced in the second year of the thesis, the first part of the validation, dedicated to single assembly calculations, was performed with the assembly design belonging to Core I. The results starting from Section 5.4 were calculated with Core II.

5.3.1 Solver parameters

The assembly geometry used in this section was the same as used in the previous chapter (a detailed description in Section 4.1). The geometry was defined in both APOLLO3[®] and TRIPOLI-4[®] codes. The calculation parameters (Table 5.2) for TDT-CPM and TDT-MOC solvers were chosen accordingly to the recommendations included in [92]. The validity of this options in case of CADOR assembly was successfully verified in a series of preliminary calculations. The first part of the calculations until Section 5.3.10 were performed with simplified scattering kernel, i.e., the resonance upscattering phenomenon was not taken into account in both APOLLO3[®] and TRIPOLI-4[®].

As before, the TRIPOLI-4[®] calculations were conducted with 1 billion neutron histories each (100 000 batches of 10 000 histories), resulting in uncertainties of multiplication factor in a range of σ at 3.5-5 pcm. Initially, the calculations were performed with SVT_{4.95eV} scattering options. A comparison of DBRC_{360eV} treatment with upscattering treatment of APOLLO3[®] is presented later in this chapter.

5.3.2 Choice of energy mesh

Instead of using the usual 1968-group energy mesh used in the reference SFR scheme, for this thesis the fine mesh of 1760 energy groups was primarily used. This new energy mesh, created in CEA for APOLLO3[®] code, is designed to be the successor of the 1968 energy mesh, originally developed for ECCO/ERANOS tool. Although smaller in size by roughly 200 energy groups, the group definition is claimed to be better optimized for treatment of the spectrum of SFR cores. In addition, an advantage of using 1760-group library is the availability of both versions with simplified and exact scattering treatment; the exact scattering is currently not available in any 1968-group library.

5.3.3 Comparison of multiplication factors

Table 5.3 presents the comparison of multiplication factors from assembly calculation performed with APOLLO3[®] and the TRIPOLI-4[®] reference with exact geometry and pointwise cross-sections. The comparison was carried out for two different anisotropy orders (P1 and P3), two different methods of self-shielding and two core regions: C1 – inner core assembly, C2 – outer core assembly.

As mentioned before, the sub-group method is considered to be a reference method in case of fast reactor calculations. However, the necessity of performing iterative coupling with flux solver to update the slowing down sources results in a longer calculation time. Therefore, it is of interest to verify if simpler Tone’s method is a sufficiently accurate substitute for SG method. The self-shielding calculation in Tone’s method is performed only once per calculation, hence it can be computed much faster. On the other hand, Tone’s method assumes that the fine structure depends only on the neutrons region of arrival which can lead to inaccurate estimation of spatial self-shielding. For that reason Tone’s method may be inadequate to treat softer neutron spectra, as was observed in PWR studies.

Table 5.3: Comparison of infinite multiplication factors for all three assembly types.

	$k_{T4} \pm \sigma$	$\Delta\rho(\text{A3} - \text{T4})$ [pcm]			
		Tone		Sub-group	
		P1	P3	P1	P3
Be moderator, C1	1.20703 ± 4 pcm	29	39	50	59
Be moderator, C2	1.37194 ± 4 pcm	32	39	30	38
ZrH ₂ moderator, C1	1.27008 ± 4 pcm	-47	-36	-47	-37
ZrH ₂ moderator, C2	1.42549 ± 4 pcm	-27	-19	-36	-30
no moderator, C1	1.35893 ± 4 pcm	6	11	-13	-5
no moderator, C2	1.55705 ± 5 pcm	1	5	-18	-14

None of the reactivity differences exceeded 60 pcm. In case of assembly without moderator, the values were noticeably lower than for other cases, with most discrepancies remaining in $\pm 3\sigma$ interval of TRIPOLI-4[®] results. Nevertheless, the reactivity discrepancy for all assembly types were of a similar order of magnitude. In case of ZrH₂, the reactivity calculated by APOLLO3[®] was underestimated, whereas for Be the opposite relation was observed. A better agreement between codes was achieved for C2 assembly for all moderator types, which might be linked to higher average neutron energy compared to C1, e.g., 55 keV compared to 64 keV for Be moderator (Section 4.3.2).

There was no consistent improvement observed linked to using Sub-group method instead of Tone’s method. Notably, in case of C1 assembly with Be moderator a 20 pcm difference between Tone’s and Sub-group was obtained, however, for most assembly types the difference was insignificant. Similarly, the P3 anisotropy order did not bring visible benefits for most cases in this study.

5.3.4 Comparison of reaction rates

Table 5.4 shows the differences in reaction rates for the most important isotopes in fuel. Similarly to Section 4.4.4 the reaction rates were normalized with respect to fission source.

Table 5.4: Comparison of reaction rates for all three assembly types. Uncertainties were omitted for clarity; 1σ does not exceed 3 pcm for any result.

	R_{T4} [pcm]		$R_{A3} - R_{T4}$ [pcm]			
			Tone, P1		SG, P1	
	C1	C2	C1	C2	C1	C2
Be moderator						
absorption ^{238}U	$37\,035 \pm 2$	$30\,532 \pm 2$	88	57	22	8
absorption ^{239}Pu	$42\,927 \pm 2$	$48\,182 \pm 3$	-11	-2	58	55
absorption ^{240}Pu	7250 ± 1	8096 ± 1	-87	-88	-100	-99
absorption ^{241}Pu	6487 ± 1	7344 ± 1	17	19	7	7
fission ^{238}U	3467 ± 1	3202 ± 1	-20	-20	-21	-21
fission ^{239}Pu	$29\,718 \pm 1$	$34\,142 \pm 2$	16	23	46	44
fission ^{241}Pu	5297 ± 1	6030 ± 1	26	28	4	4
ZrH ₂ moderator						
absorption ^{238}U	$33\,386 \pm 1$	$27\,715 \pm 2$	50	33	28	18
absorption ^{239}Pu	$43\,864 \pm 2$	$48\,601 \pm 2$	-30	-20	10	14
absorption ^{240}Pu	8331 ± 1	8993 ± 1	0	3	-31	-26
absorption ^{241}Pu	7039 ± 1	7792 ± 1	6	8	-12	-11
fission ^{238}U	4089 ± 1	3777 ± 1	-19	-20	-20	-20
fission ^{239}Pu	$30\,554 \pm 1$	$34\,666 \pm 1$	-13	-7	12	14
fission ^{241}Pu	5682 ± 1	6338 ± 1	16	18	-12	-11
no moderator						
absorption ^{238}U	$37\,886 \pm 1$	$30\,554 \pm 1$	-2	-5	-37	-29
absorption ^{239}Pu	$42\,102 \pm 2$	$47\,958 \pm 2$	4	6	34	29
absorption ^{240}Pu	6833 ± 1	7896 ± 1	-2	-2	-3	-3
absorption ^{241}Pu	6448 ± 1	7293 ± 1	8	8	1	1
fission ^{238}U	4670 ± 1	4314 ± 1	-22	-23	-22	-23
fission ^{239}Pu	$32\,450 \pm 1$	$37\,805 \pm 1$	21	22	21	18
fission ^{241}Pu	5405 ± 1	6148 ± 1	12	11	1	0

As in case of k , the discrepancies between APOLLO3[®] and TRIPOLI-4[®] were small for all types of assemblies. A noticeable underestimation of absorption rate appeared in Be-moderated assemblies for ^{240}Pu isotope, where the difference reached 100 pcm. A similar behavior did not appear in ZrH₂ moderator and no moderator cases. In general, except for

some particular cases as the one mentioned, the agreement was very similar for all moderator types.

Figures 5.7 and 5.8 depict the spectra of combined reaction rates for all actinides in the fuel. The data were condensed to 33 energy groups for better visibility.

For both Tone's and Sub-group method the spectra aligned rather tightly with TRIPOLI-4® results. The only visible misaligned point was the absorption rate in the energy interval (0.54 eV, 4 eV) in case of Be moderator. Majority of this difference was caused by the discrepancy in absorption rate in ^{240}Pu . The energy interval contains the first and largest resonance of ^{240}Pu with its peak at around 1.06 eV. None of the two self-shielding methods were able to correctly account for the absorption in this resonance. The issue did not appear for assembly with ZrH_2 where an increased absorption rate in the interval was observed both in T4 and A3. The issue also did not appear in case of lack of moderator as any reaction rate below 100 eV was negligible. More research is needed to explain the abnormal behavior of absorption in ^{240}Pu for Be-moderated assembly.

The biggest discrepancy appeared in the resonance energy range, roughly in 100 eV–10 keV limits. The discrepancies were similar for both self-shielding methods for Be and ZrH_2 moderator. In the assembly without moderator, the Sub-group method performed relatively inaccurately in that region. However, the negative and positive discrepancies compensated each other, resulting in a more accurate reaction rate estimates globally than for certain energy groups.

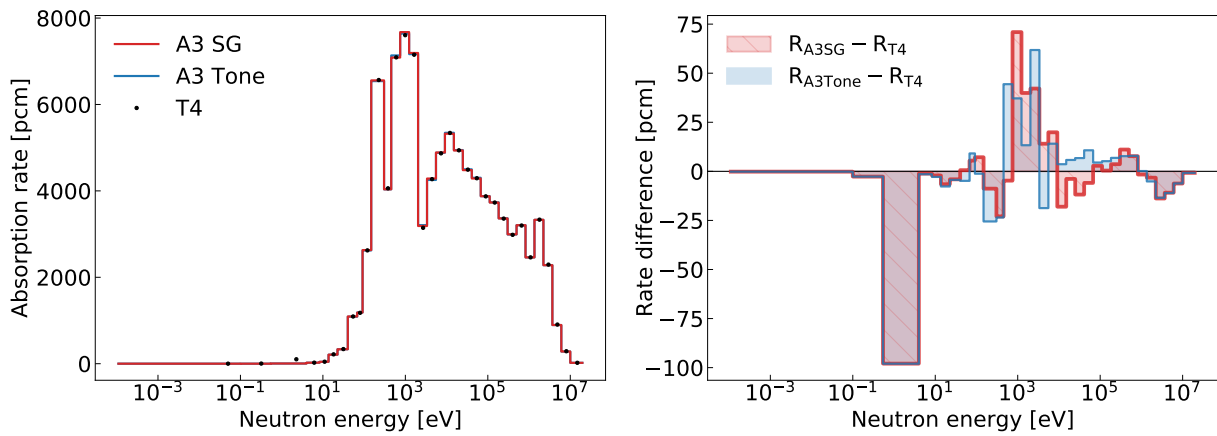
5.3.5 Comparison of Doppler feedback

To estimate the value of the Doppler effect, the Doppler constants K_D were calculated for all assembly types by using multiplication factors for $T_{\text{fuel}}=900\text{ }^\circ\text{C}$ and $2000\text{ }^\circ\text{C}$. The values obtained for C1 assembly, the worst case in terms of accuracy, are presented in Table 5.5.

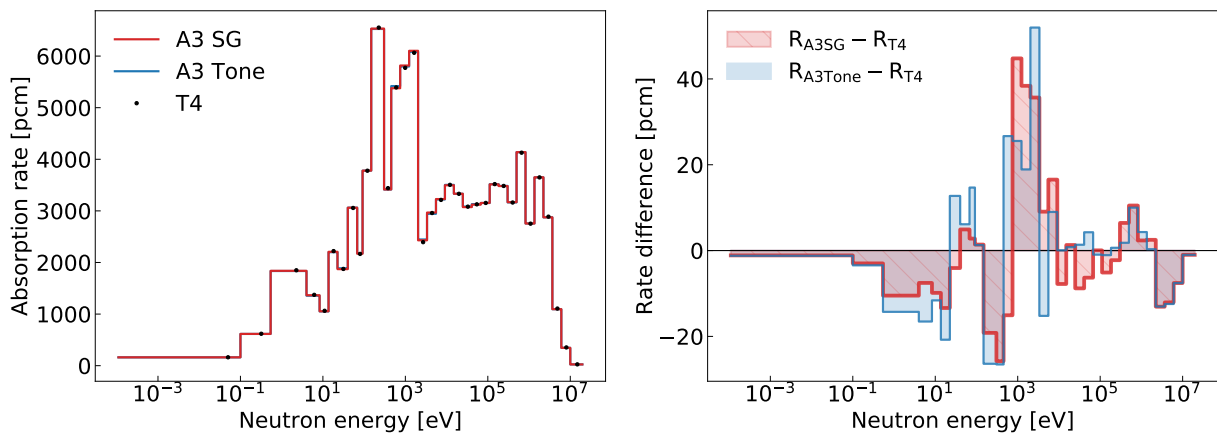
Table 5.5: Comparison of the Doppler constant K_D for inner core (C1) fuel assemblies.

	$K_D(\text{T4})$ [pcm]	$\Delta K_D(\text{A3} - \text{T4})$ [pcm]	A3/T4 rel. diff [pcm]
Be moderator	-1978 ± 7	-79	4.0
ZrH_2 moderator	-1889 ± 6	-87	4.6
no moderator	-714 ± 6	-19	2.7

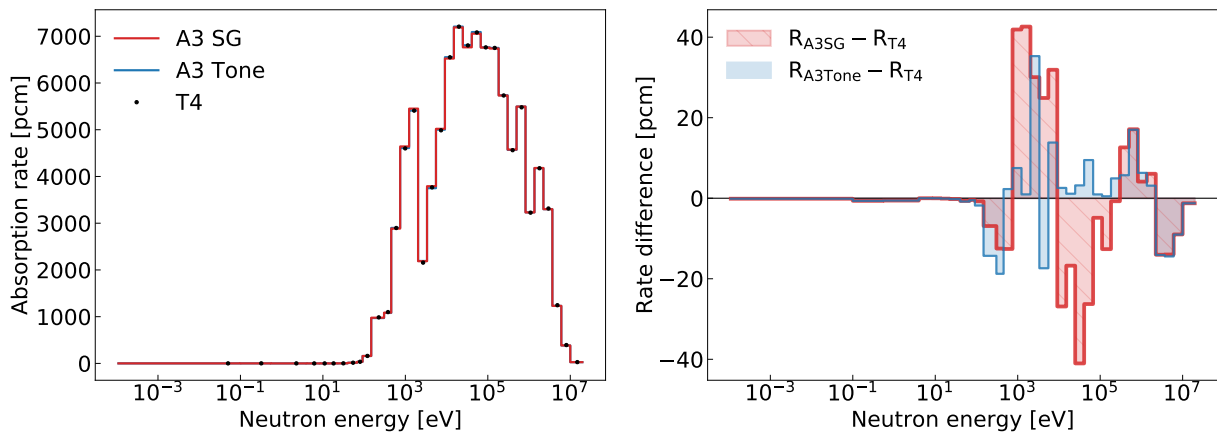
The small differences between the codes in values of k produced a relative discrepancy of a few percent in case of the Doppler constants. The largest discrepancy was obtained for ZrH_2 moderator: 4.6%. The lowest absolute difference was achieved for SFR assembly without moderator; however, due to much lower absolute value of K_D for this particular design, the relative difference of K_D is close to moderated assemblies, especially the assembly with Be.



(a) Be moderator

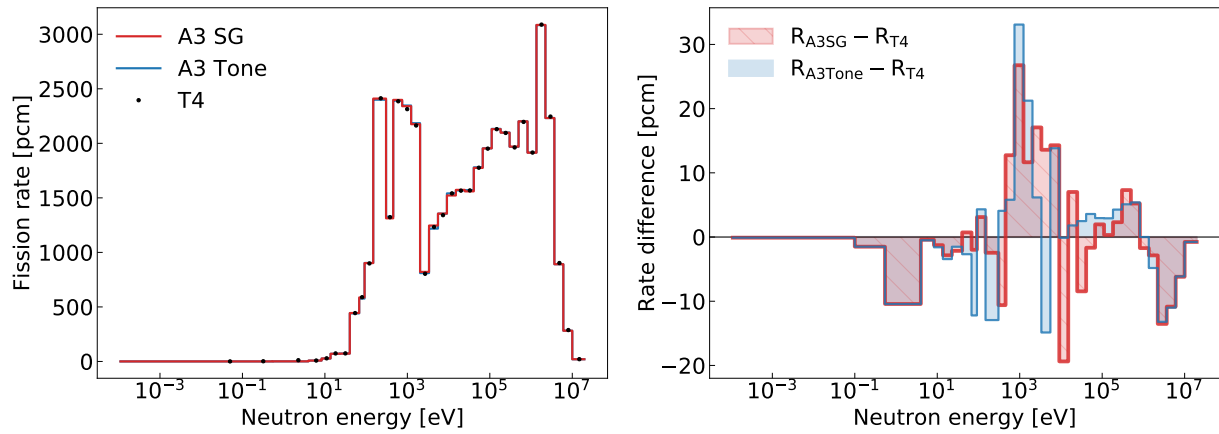


(b) ZrH₂ moderator

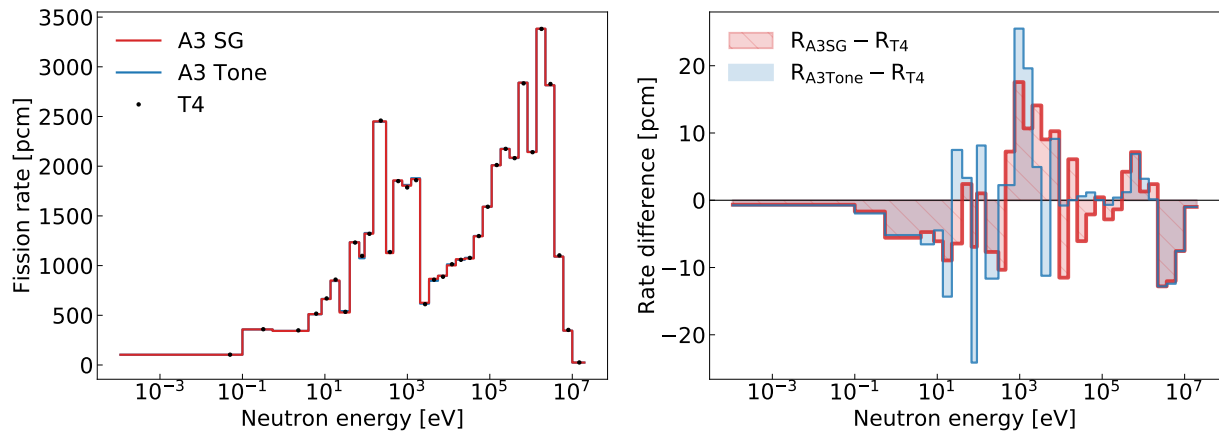
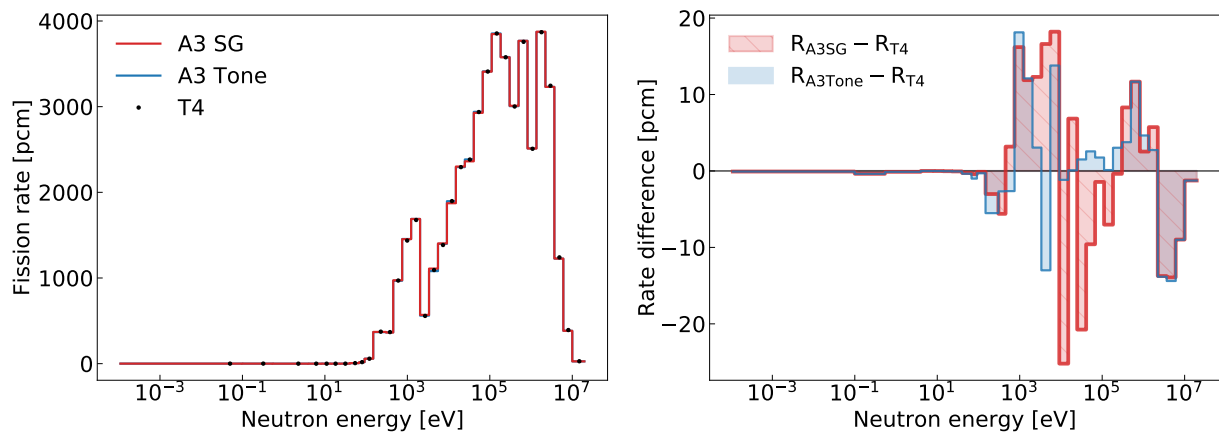


(c) no moderator

Figure 5.7: Comparison of neutron absorption rate in actinides in 33 groups for results of A3 computed with Tone's and Sub-group. Results are compared to pointwise T4 calculations.



(a) Be moderator

(b) ZrH_2 moderator

(c) no moderator

Figure 5.8: Comparison of fission rate in 33 groups for results of A3 computed with Tone's and Sub-group. Results are compared to pointwise T4 calculations.

5.3.6 Comparison of feedback of void effect

The void effect was calculated by comparing a nominal state of the core to a voided state where 100 % of sodium volume was removed from the assembly. The results for C1 assemblies are presented in Table 5.6.

Table 5.6: Comparison of void effect for inner core (C1) fuel assemblies.

	$\Delta\rho_{\text{void}}(T4)$ [pcm]	$\Delta(\Delta\rho_{\text{void}})(A3 - T4)$ [pcm]	A3/T4 rel. diff. [%]
Be moderator	2160 ± 5	44	2.1
ZrH ₂ moderator	2128 ± 5	24	1.1
no moderator	3181 ± 4	54	1.7

The performance of APOLLO3[®] for all three assembly types was similar. The discrepancies for moderated assemblies were smaller than the ones obtained with assembly without moderator; moreover, the discrepancies were smaller than for Doppler effect both in absolute and relative terms.

The void effect can be seen as an opposing effect to the softening caused by the presence of moderators, as it leads to spectral hardening (example given in Figure 5.9). It can be argued that the spectrum of CADOR in voided conditions is closer to a conventional SFR spectrum than the CADOR core at nominal state. This consideration suggests that it is unlikely to experience higher accuracy issues when calculating the core at the voided state than those seen at the nominal state.

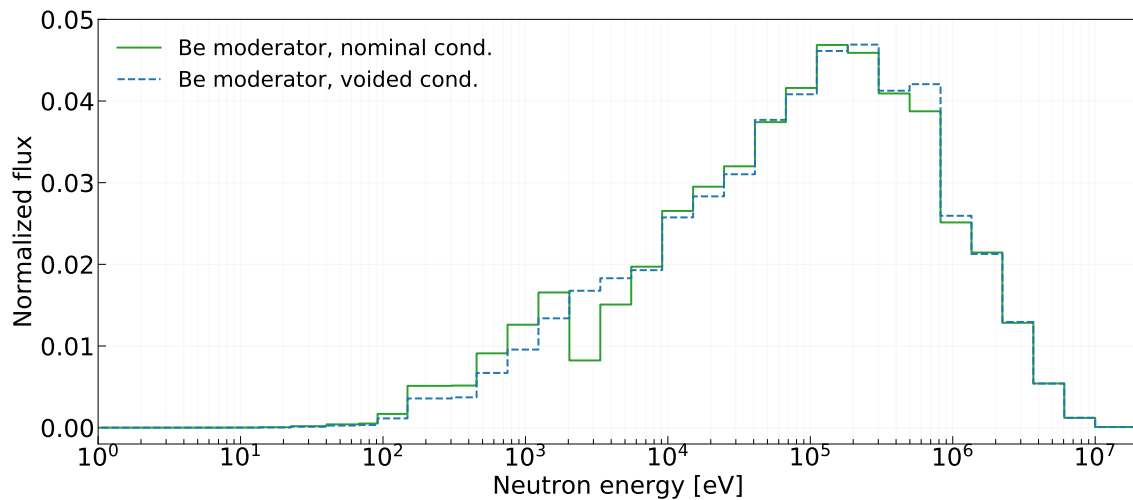


Figure 5.9: Neutron flux spectrum in C1 Be-moderated CADOR fuel assembly at nominal and voided conditions.

The absolute reactivity effect of voiding is lower when moderators are present. Because of the softer spectrum, the spectral shift caused by sodium voiding has a smaller effect on

neutron multiplication as it would have for flux spectrum of a standard SFR. Furthermore the presence of moderator diminishes the spectrum hardening — in voided conditions the solid moderators are still present and are easier for neutrons to reach as they are no longer shielded by sodium, thus the hardening is less pronounced. It is, however, worth mentioning that the absolute values obtained in calculations with a single assembly are not representative of the core behavior. The reflective boundary conditions and the lack of leakage model nullify the effect of higher leakage at voided state, which would normally compensate the positive reactivity effect.

5.3.7 Comparison with ECCO code

In this section the aim was to compare the calculation scheme of APOLLO3[®] to a calculation scheme for fast reactors used in previous-generation code ECCO [93]. ECCO is a lattice neutron transport code, a part of a two-step calculation scheme based on ECCO/ERANOS tool [30] for fast reactor analysis. ECCO belonging to the second generation of transport codes developed in CEA, alongside APOLLO2 and CRONOS2 (both developed for LWR applications). Figure 5.10 represents a visual summary of the reference calculation scheme used by ECCO/ERANOS [94].

Compared to APOLLO3[®], the two main changes in the lattice calculation are:

- double step CPM method is used both in self-shielding and flux calculation, MOC method is not available
- cross-sections of less essential isotopes are represented in 33 energy groups, even before the condensation procedure

The moderator isotopes such as Be or H are typically treated in 33 groups, as they are rarely present in conventional fast reactors. However, special libraries with all isotopes represented in fine mesh (1968 groups) are also currently available. In such a case, the only major difference between the schemes is the double step CPM used in ECCO solver.

In the double step method, the geometry is subdivided into smaller parts. For example, in case of hexagonal fuel assembly, the lattice of fuel pins is treated as a separated sub-geometry. The collision probabilities are first calculated for the internal sub-geometries. After this step, the sub-geometries are homogenized. In the second step, the remaining homogeneous regions are then cylindrified: all regions are transformed into annular shape, forming an equivalent cylindrical assembly. The cylindrified geometry of an assembly is then used to calculate the collision probabilities the second time. Thanks to the homogenization and cylindification the calculation can be realized much faster than with the exact CPM. A more detailed description of this approach can be found in [95].

5.3.7.1 Global effects

Table 5.7 contains a comparison between results of ECCO, APOLLO3[®] and reference TRIPOLI-4[®] calculations with the same JEFF 3.1.1 library.

Large discrepancies of ECCO results compared to TRIPOLI-4[®] are immediately noticeable.

Table 5.7: Comparison of ECCO and APOLLO3[®] (Tone, P1) results with TRIPOLI-4[®] pointwise calculations. For Doppler constant and void effect both the differences of reactivity in pcm and relative difference in % (in parenthesis) are given.

	$\Delta\rho$ [pcm]			
	ECCO – T4	A3 – T4		
Be moderator, C1	900	29		
Be moderator, C2	703	32		
ZrH ₂ moderator, C1	383	–47		
ZrH ₂ moderator, C2	306	–27		
no moderator, C1	114	6		
no moderator, C2	80	1		
	ΔK_D [pcm (%)]			
	ECCO – T4		A3 – T4	
Be moderator, C1	–65	(3.3)	–79	(4.0)
Be moderator, C2	–35	(2.8)	–47	(3.7)
ZrH ₂ moderator, C1	–73	(3.8)	–87	(4.6)
ZrH ₂ moderator, C2	–53	(4.0)	–66	(5.1)
no moderator, C1	–17	(2.3)	–19	(2.7)
no moderator, C2	–10	(2.6)	–13	(3.1)
	$\Delta(\Delta\rho_{\text{void}})$ [pcm (%)]			
	ECCO – T4		A3 – T4	
Be moderator, C1	154	(7.1)	44	(2.1)
Be moderator, C2	149	(7.2)	36	(1.7)
ZrH ₂ moderator, C1	44	(2.1)	24	(1.1)
ZrH ₂ moderator, C2	40	(2.1)	16	(0.8)
no moderator, C1	–91	–(2.9)	54	(1.7)
no moderator, C2	–75	–(2.8)	42	(1.5)

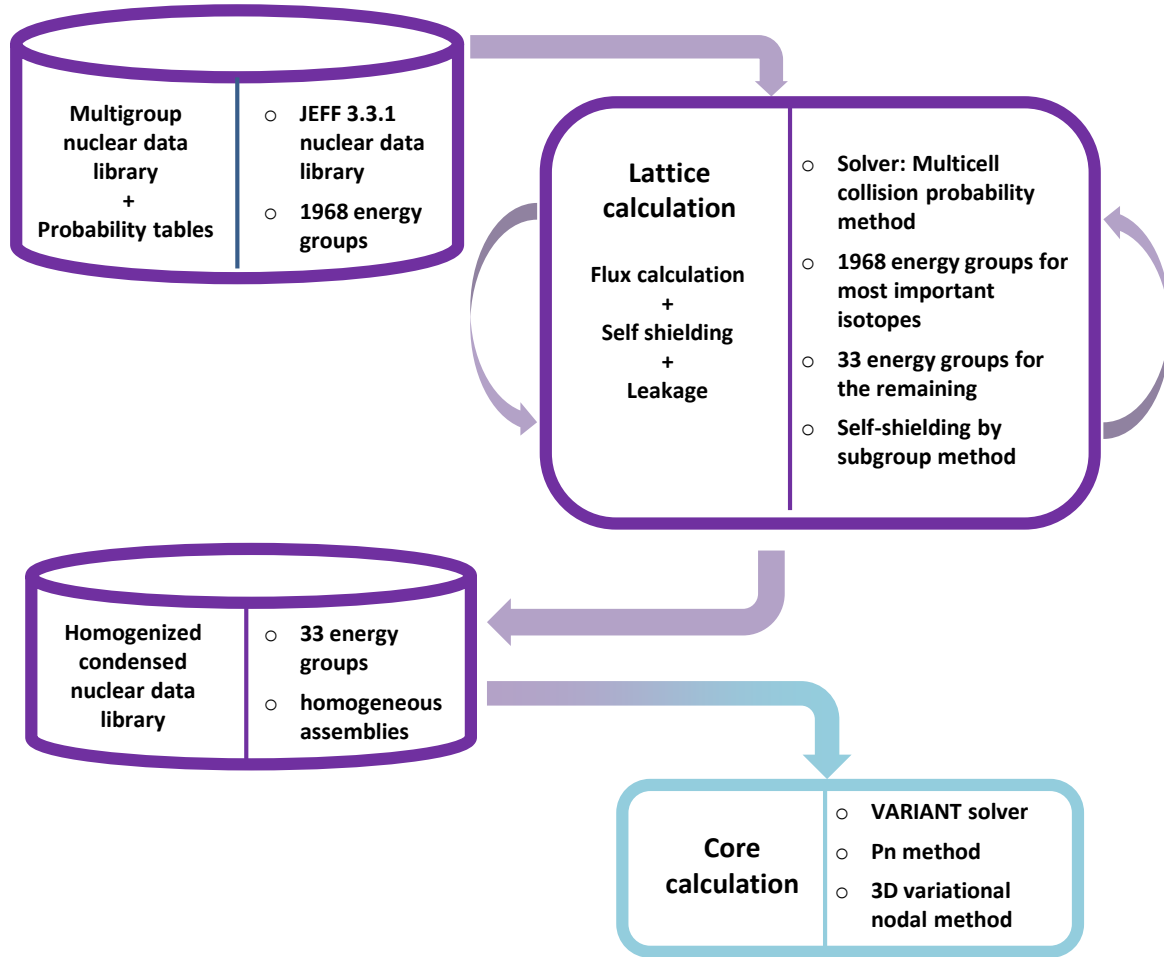


Figure 5.10: Depiction of the reference calculation scheme of ECCO/ERANOS.

The differences were at least an order of magnitude higher than in case of APOLLO3[®] code. The lowest discrepancies were reached for assembly without moderator, where the bias reached 114 pcm at most. In case of the CADOR assemblies, a visibly higher of bias was observed. In the worst case, the C1 assembly with Be moderator, the bias reached 900 pcm which is an order of magnitude higher than in case of no moderator. This effect can be attributed to the double step CPM, that can be expected to perform poorly in a heterogeneous assembly arrangement with two very different pin types.

In case of the Doppler and void effect, the differences were not as pronounced as in case of reactivity. These two effects are differential in nature and are calculated between two different reactor states. This condition makes it likely that the biases of individual calculations will compensate each other. Therefore, despite high bias on multiplication factor, the values of the Doppler constant were calculated more accurately in ECCO than APOLLO3[®]. The difference is, however, not significant, if we take into account standard deviation of K_D of about 6 pcm in case of TRIPOLI-4[®] results.

For void effect, the discrepancies of ECCO were again larger than for APOLLO3[®], particularly for Be moderator. In case of remaining assembly types, however, the differences

were similar for both deterministic codes. This suggests that the bias introduced by ECCO calculation method, most likely double step CPM is similar for different temperatures and different sodium densities.

5.3.7.2 Reaction rates

Figures 5.11 and 5.12 present the spectra of reaction rates, generated with the same methodology as in Section 5.3.4 with all three codes. The differences of ECCO were visibly larger than those obtained with APOLLO3[®]. For Be moderator, a large overestimation for both absorption and fission rate appeared in fast and resonance energy region. In case of ZrH₂ a major overestimation appeared for thermal energies. Interestingly, for all kind of assemblies, ECCO tended to inaccurately represent the reaction rates for the highest neutron energies around 1 MeV-10 MeV.

5.3.7.3 Summary

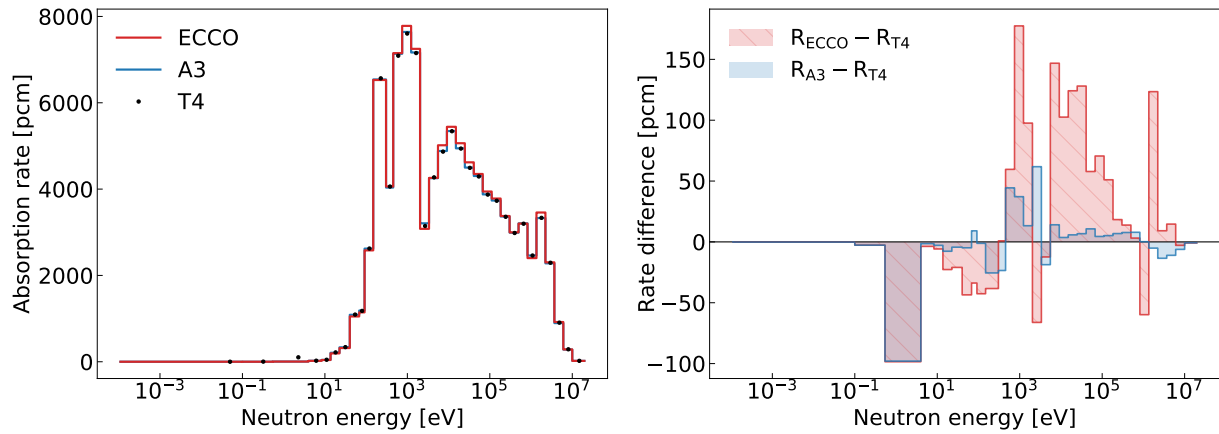
The calculation scheme for ECCO lattice calculation performed noticeably less accurately than the analogical scheme of APOLLO3[®], when applied to moderated SFR assembly. The ECCO code was designed and validated exclusively for fast reactor analysis (the role of lattice calculation code for thermal reactors was previously fulfilled by APOLLO2 code), and is not the most suitable choice for analysis of CADOR assembly. The numerical models of ECCO lack the flexibility and adaptability of APOLLO3[®] code — the possibilities of customization of the scheme are very limited. The rigid calculation route requires utilization of double step CPM solver, that relies heavily on approximation not present in exact CPM available in APOLLO3[®]. On the other hand, calculations performed in ECCO are much faster — single assembly calculation takes around 2 min despite the utilization of Sub-group method. (compared to around 1 h in APOLLO3[®] if Sub-group method is used).

High discrepancies regarding the multiplication factor show a clear advantage of APOLLO3[®] calculation scheme. However, lattice calculation is only the first step of a larger scheme and the inaccuracies obtained here might not be reflected in the core calculation due to compensations coming from other factors. The comparison of the full two-step calculation scheme of both ECCO/ERANOS and APOLLO3[®] is presented later in this chapter.

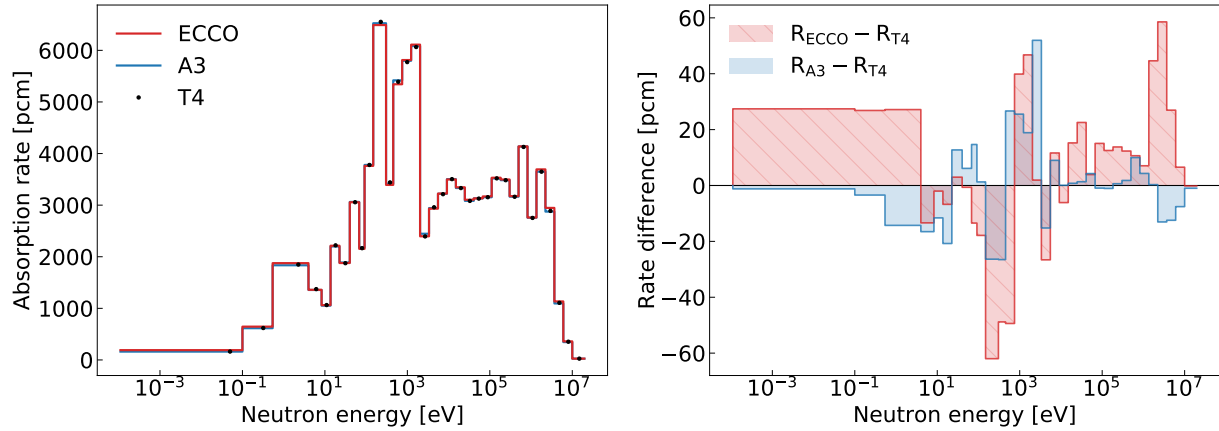
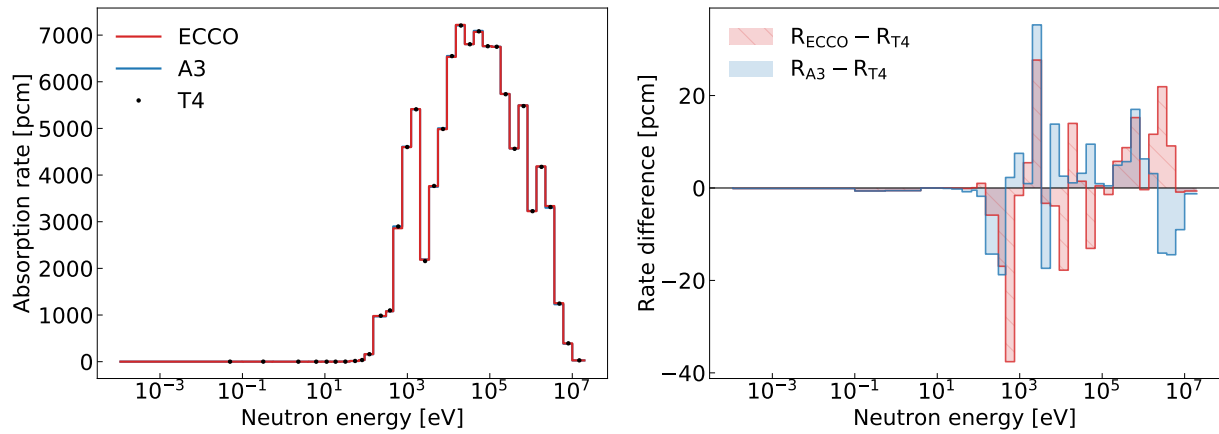
5.3.8 Comparison of spatial mesh refinements

In a standard lattice calculation scheme for fast reactors a division of individual fuel pellets is generally unnecessary. The sufficiently large neutron mean free path results in relatively small spatial self-shielding effects compared to thermal reactors. In case of moderated CADOR assembly, the finer discretization of the spatial mesh is worth investigating for two main reasons:

- the neutron mean free path is reduced due to enhanced moderation
- the heterogeneous assembly design can lead to reaction rate increase in the parts of fuel close to moderating pins, especially in the outermost part of pellets (rim effect)

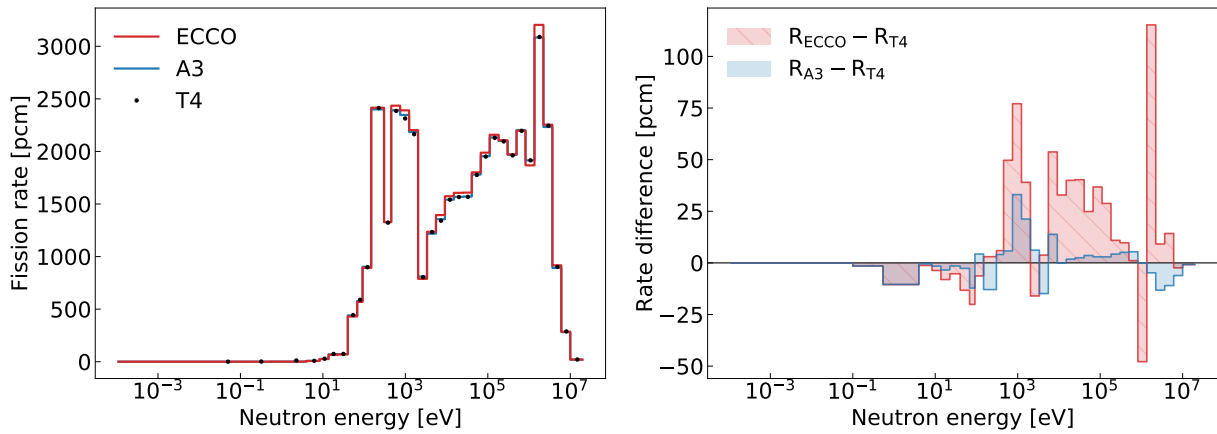


(a) Be moderator

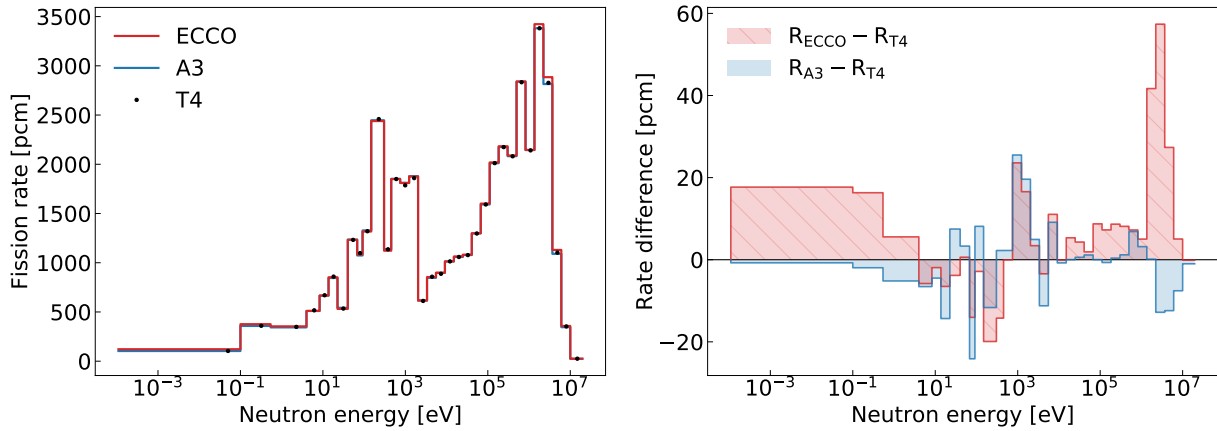
(b) ZrH₂ moderator

(c) no moderator

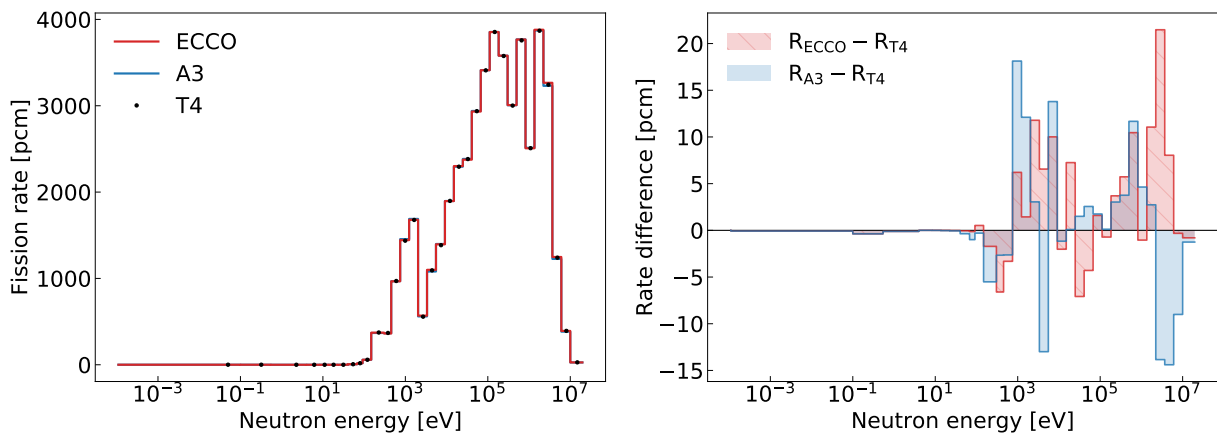
Figure 5.11: Absorption rate in 33 groups for ECCO, A3 and T4.



(a) Be moderator



(b) ZrH₂ moderator



(c) no moderator

Figure 5.12: Fission rate in 33 groups for ECCO, A3 and T4.

To verify if the division of fuel pellet can improve the accuracy of APOLLO3[®] calculations, additional three spatial meshes were created (Figure 5.13):

- division of each fuel pellet or moderator rod into six annular regions of 27.15, 25, 23, 21, 19 and 15 mm radii (most refined at the periphery of the pellet)
- angular division of each pin-cell into six circular sectors of equal size
- both previous refinements combined

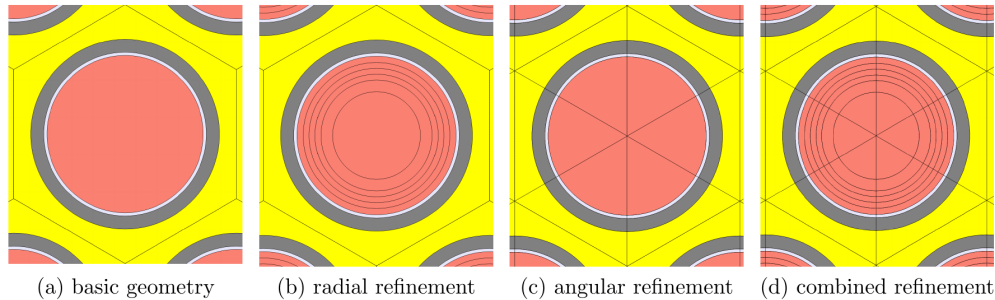


Figure 5.13: Types of mesh used in the study.

The comparison of reactivity difference between reference TRIPOLI-4[®] and APOLLO3[®] calculations with different spatial meshes is presented in Table 5.8.

Table 5.8: Discrepancies between APOLLO3[®] and TRIPOLI-4[®] reactivity for different mesh refinements in APOLLO3[®] applied to C1 assembly. Self-shielding performed with Tone's method. Standard deviation of TRIPOLI-4[®] results as in Table 5.3 (not larger than 5 pcm).

	no refinement	radial refinement	angular refinement	combined refinement
Be moderator				
$\Delta\rho$ $T_{\text{fuel}}=900$ °C	29	46	27	43
$\Delta\rho$ $T_{\text{fuel}}=2000$ °C	-23	-17	-39	-18
ΔK_D	-79	-95	-100	-92
ZrH ₂ moderator				
$\Delta\rho$ $T_{\text{fuel}}=900$ °C	-47	-24	-48	-26
$\Delta\rho$ $T_{\text{fuel}}=2000$ °C	-104	-80	-111	-79
ΔK_D	-87	-86	-95	-80
no moderator				
$\Delta\rho$ $T_{\text{fuel}}=900$ °C	6	9	6	13
$\Delta\rho$ $T_{\text{fuel}}=2000$ °C	-6	-7	-10	-6
ΔK_D	-19	-24	-24	-29

The results presented in Table 5.8 show that the mesh refinement can provide an improvement of accuracy not larger than 25 pcm. The best results were achieved for refinement of 6 rings.

The benefits of angular refinement were relatively low, thus, the combined effect did not differ significantly from the radial refinement alone. More refined meshes led to the largest improvement in case of ZrH_2 -moderated assembly, which was also the worst case in terms of $\Delta\rho$ before the refinement was applied; the discrepancy was lowered from 104 to 80 pcm in case of 2000 °C fuel temperature. In many cases the refinement decreased the accuracy. As expected, no significant change was observed for the assembly without moderator.

It is also worth noting that none of the improvements resulted in a lower discrepancy of Doppler constant K_D . In many cases, the value of k changed in the same direction for both 2000 °C and 900 °C, therefore K_D , representing a differential temperature effect remained almost constant. On the other hand, for Be moderator an increased discrepancy of up to 100 pcm was observed.

Although the accuracy improvement was achieved for some cases, the refinements presented above are tied to higher computation times (Table 5.9). For this reason, this kind of a scheme improvement should be used only when high accuracy is of the utmost importance, regardless of the time of calculation. However, the results suggest that, despite longer calculation time, improvement in accuracy is not guaranteed. The refinements can be also justified for performing detailed analyses of spatial distributions of flux or power, as already presented in Section 4.3.

Table 5.9: Approximate calculation times in APOLLO3[®] obtained on DELL computer with 32 Intel Xeon E5-2620 2.10GHz CPUs.

refinement type	calculation time [min]	
	Tone	Sub-group
no refinement	3 min	56 min
radial refinement	3 min 40 sec	245 min
angular refinement	6 min 20 sec	—
combined refinement	23 min	—

Because the pellet refinement is directly linked to the spatial self-shielding problem, another series of calculation was performed, this time with the reference method of Sub-groups. Table 5.10 present discrepancies of k obtained with APOLLO3[®] calculation with Tone's and Sub-group methods for a standard spatial mesh, as well as radially refined mesh.

The improvement observed was not large in absolute terms — no more than 20 pcm was achieved. On the other hand the results of APOLLO3[®] and TRIPOLI-4[®] were already close to each other before the refinements were applied. Therefore, the reactivity gap between the codes was narrowed by a significant percentage. For the most divergent result of ZrH_2 -moderated assembly, the discrepancy was reduced by around 20 pcm. However, for Be moderator at $T_{\text{fuel}} = 900$ °C, both the radial refinement and transition from Tone's to Sub-group method caused a loss of accuracy.

Table 5.10: Discrepancies in pcm between APOLLO3[®] and TRIPOLI-4[®] for different mesh refinements in APOLLO3[®].

	no refinement		radial ref.	
	Tone	SG	Tone	SG
Be moderator				
$\Delta\rho$, $T_{\text{fuel}}=900\text{ }^\circ\text{C}$	29	50	46	56
$\Delta\rho$, $T_{\text{fuel}}=2000\text{ }^\circ\text{C}$	-23	-23	-17	-5
ΔK_D	-79	-94	-95	-92
ZrH ₂ moderator				
$\Delta\rho$, $T_{\text{fuel}}=900\text{ }^\circ\text{C}$	-47	-47	-24	-28
$\Delta\rho$, $T_{\text{fuel}}=2000\text{ }^\circ\text{C}$	-104	-112	-80	-84
ΔK_D	-87	-93	-86	-86
no moderator				
$\Delta\rho$, $T_{\text{fuel}}=900\text{ }^\circ\text{C}$	6	-13	9	10
$\Delta\rho$, $T_{\text{fuel}}=2000\text{ }^\circ\text{C}$	-6	-30	-7	-28
ΔK_D	-19	-26	-24	-26

5.3.9 Spatial comparison of reaction rates

For comparison of the reaction rates, a visual method was employed. The TRIPOLI-4[®] results were projected on APOLLO3[®] spatial meshfields – an object-oriented data model used by APOLLO3[®] post-processing tools. Thanks to the visualization tool available in APOLLO3[®], the results were then compared by producing 2D heat maps. In order to achieve more detailed heat maps, the radial refinement of six rings was applied. The maps are presented in the Figure 5.14.

The differences between APOLLO3[®] and TRIPOLI-4[®] were low for most of the geometry cells. The outermost part of the assembly (bottom right corner) appears as the most problematic spot, with the relative APOLLO3[®]/TRIPOLI-4[®] discrepancy of up to 2.37%. This value is about two times higher than in case of standard SFR assembly. The large discrepancy in the corner might come from the enhanced moderation, as in the corner the neutrons experience slowing down due to both interactions with moderator as well as with the wrapper tube. The low neutron speed and presence of wrapper tube could create unfavorable conditions for deterministic calculation code. It is, however, worth noting that the local discrepancies of reaction rates did not translate to high discrepancy of the global reaction rates. The global reaction rates (Table 5.4) as well as values of k (Table 5.3) corresponded very precisely to the values of TRIPOLI-4[®].

5.3.10 Resonance upscattering at the assembly level

Previously, the results presented in Section 4.4 covered the exact scattering treatment realized in TRIPOLI-4[®] code only. This time, we apply a similar treatment to APOLLO3[®] code,

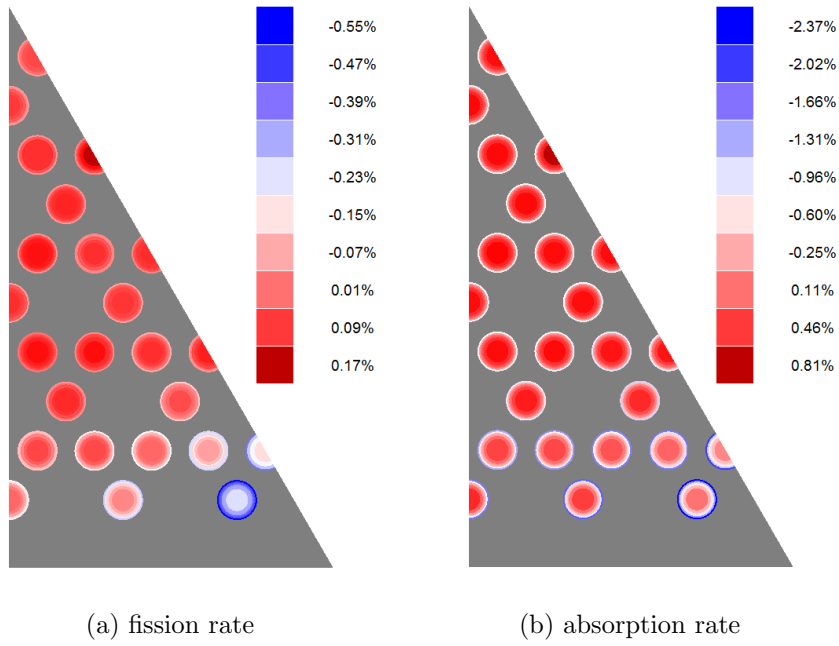


Figure 5.14: Relative difference of reaction rates in percent between APOLLO3[®] and TRIPOLI-4[®] for assembly with 91 Be pins.

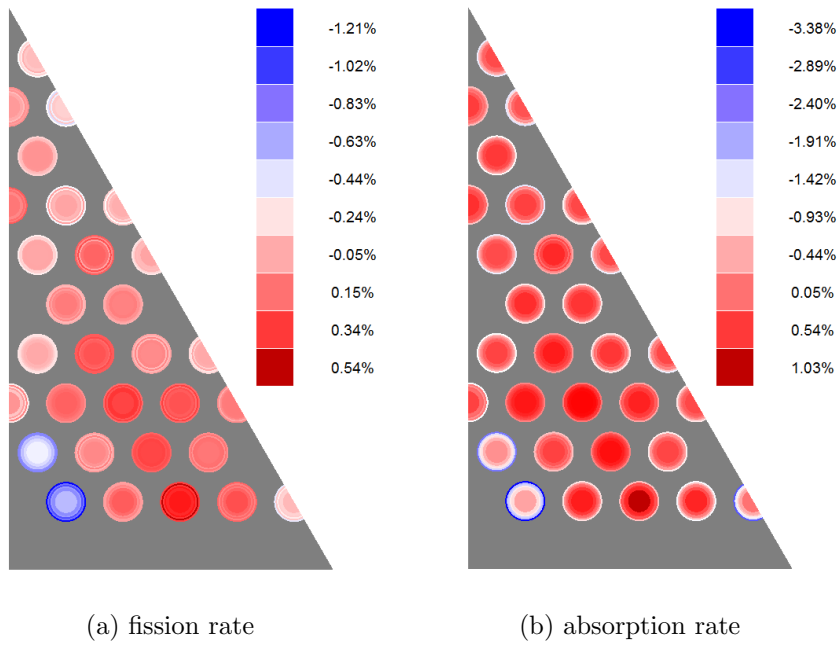


Figure 5.15: Relative difference of reaction rates in percent between APOLLO3[®] and TRIPOLI-4[®] for assembly with 31 ZrH₂ pins.

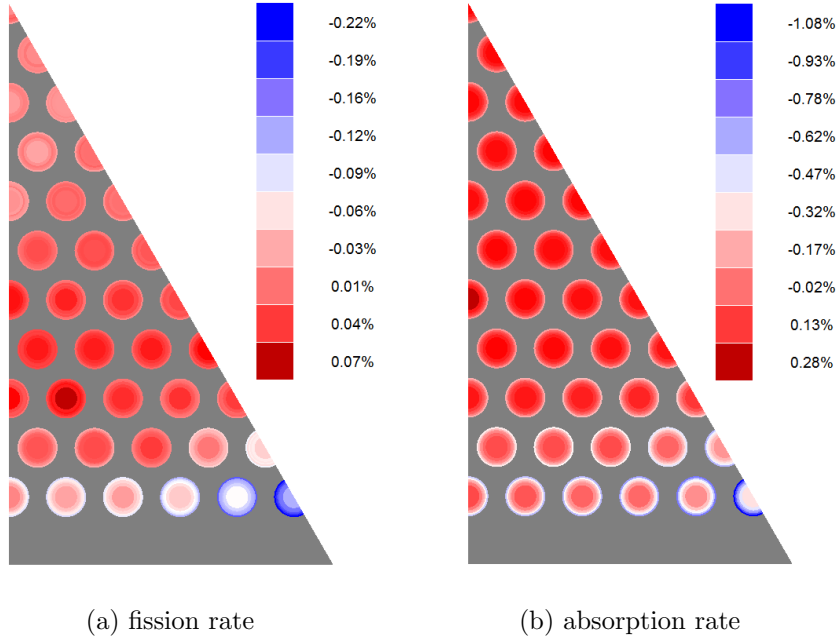


Figure 5.16: Relative difference of reaction rates in percent between APOLLO3[®] and TRIPOLI-4[®] for standard SFR assembly without moderator.

to investigate the impact of resonance upscattering, taken into account only by the exact scattering kernel. As explained in Section 3.7.2, the different scattering kernels in deterministic codes are applied during processing of multigroup nuclear data library. Such a library is available for 1760 energy groups mesh. Tables 5.11 presents the differences arising from using different scattering models in both TRIPOLI-4[®] and APOLLO3[®]. The reactivity differences were calculated according to the formula

$$\Delta\rho = \left(\frac{1}{k_{\text{ups}}} - \frac{1}{k_{\text{std}}} \right) \cdot 10^5 \text{ [pcm]} \quad (5.1)$$

where subscript “ups” stands for method using exact free gas scattering kernel, and “std” signifies the “constant cross-section” approach to scattering kernel. The values can be interpreted as a bias on reactivity related to using simplified scattering treatment instead of the exact one. In case of TRIPOLI-4[®] the “ups” stands for DBRC_{360eV} scattering options, and “std” for SVT_{4.95eV} (as in Section 4.4). In APOLLO3[®], the difference was obtained by comparing results obtained with two different libraries: both with 1760 groups but only the “ups” library accounts for exact scattering kernel in the scattering transfer matrices. The results for assembly without moderator are not presented, as the reactivity differences are insignificant.

We can see a relatively good agreement between the two codes, the discrepancies obtained reached no more than several dozens of pcm. The APOLLO3[®] code tended to consistently underestimate the bias by around 20-30 pcm. In terms of difference between scattering models, we observed higher discrepancies for high fuel temperature. Despite slight underes-

Table 5.11: Differences of reactivity and K_D in pcm between scattering treatments for C1 and C2 assemblies.

	$\Delta\rho$, C1 ass.		$\Delta\rho$, C2 ass.	
	A3	T4	A3	T4
Be moderator				
$\Delta\rho$, $T_{\text{fuel}}=900\text{ }^\circ\text{C}$	-19	-5 ± 6	-16	-2 ± 6
$\Delta\rho$, $T_{\text{fuel}}=2000\text{ }^\circ\text{C}$	18	45 ± 6	11	37 ± 6
ΔK_D	56	75 ± 8	42	59 ± 8
ZrH ₂ moderator				
$\Delta\rho$, $T_{\text{fuel}}=900\text{ }^\circ\text{C}$	8	26 ± 6	3	29 ± 6
$\Delta\rho$, $T_{\text{fuel}}=2000\text{ }^\circ\text{C}$	72	108 ± 6	60	94 ± 6
ΔK_D	108	125 ± 8	91	99 ± 8

timation, the results of APOLLO3[®] presented similar behavior as TRIPOLI-4[®] results: the calculations with exact scattering kernel gave lower multiplication factor at high fuel temperatures due to higher absorption rate in ²³⁸U resonances, which, in consequence, improved the magnitude of the Doppler effect.

5.3.11 Conclusions: single assembly calculations

The results obtained with a single assembly suggest that the discrepancy of APOLLO3[®] and TRIPOLI-4[®] almost never exceeds 100 pcm. The discrepancies were consistently higher for moderated CADOR assemblies compared to the standard SFR assembly without moderator. The discrepancies also tended to be slightly higher for C1 assemblies with lower Pu enrichment, which were also the assemblies with lower average neutron energy.

Regardless of the assembly type, no consistent means was found to decrease the bias. Additional refinement of geometry, higher Legendre order or using Sub-group method did bring a minor improvement in several cases, but for other cases the discrepancy remained almost constant or even increased.

In the comparison with ECCO code, the results of APOLLO3[®] appear to be much more accurate when compared with reference TRIPOLI-4[®] calculations. The inaccuracy of ECCO was particularly pronounced for moderated assemblies; the discrepancy in reactivity for Be-moderated C1 assembly reached 900 pcm. These high values most likely stem from the two-step collision probability method of ECCO that is a simpler approach than combination of exact collision probability method and method of characteristics of APOLLO3[®].

The 1760 energy group “ups” library brought a significant improvement when we look at the magnitude of correction that was achieved compared to the same library that does not use exact scattering kernel. The impact of resonance upscattering was slightly underestimated by APOLLO3[®] when compared to reference TRIPOLI-4[®] calculations. Nevertheless, the benefits of including exact scattering kernel in APOLLO3[®] calculations of the CADOR core are measurable and important for higher fuel temperatures. For this reason, the “ups” library

is recommended in case of moderated SFRs and therefore was used to conduct the remaining studies described in the thesis.

5.4 Comparison of cluster calculations

This section discusses the studies of accuracy of cluster calculations in APOLLO3[®]. In total, to produce the cross-sections for the core calculation of 1500 MW_{th} CADOR, 12 different cluster calculations are needed per each core version. Because of the high number of cluster types, the section covers only a selected number cluster geometries.

5.4.1 Control rod assemblies

First, we are going to look at the results of clusters containing control rod assemblies as the central component of the cluster. Out of three different control rod types we are going to discuss only the DDC control rod as it is the one with the highest content of absorber (over 32% of volume is B₄C). Vertically, the control rod is composed of two absorbing zones: DDC48 containing enriched boron with 48% of isotope ¹⁰B and DDCNAT with natural boron (around 20% of ¹⁰B). The calculations were carried out for two different cluster geometries: fully heterogeneous, where both surrounding and central assembly used pin-by-pin discretization and semi-homogeneous, where the central assembly (control rods) is one homogeneous material with the same volume fraction of isotopes as the heterogeneous model (Figure 5.17). As the heterogeneous model of CRs was not available until the third year of the thesis, a majority of core calculations were performed with the homogeneous models (more information in Section 5.5) Table 5.12 presents the differences of multiplication factor

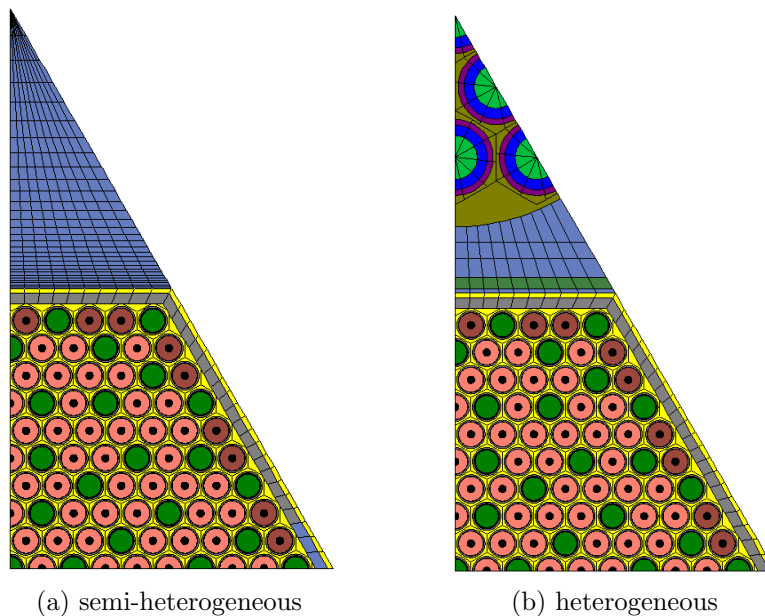


Figure 5.17: Two types of clusters of control rod assemblies and C1 fuel assemblies used in this study.

for different DDC clusters.

Table 5.12: Comparison of infinite multiplication factors for clusters with two types of control rod assemblies, both in semi-heterogeneous and fully heterogeneous description.

	$k_{T4} \pm \sigma$	$\Delta\rho(\text{A3} - \text{T4})$ [pcm]		
		P1	P3	P5
Semi-homogeneous clusters				
DDCNAT, Be moderator	0.74543 ± 3 pcm	-690	-552	-694
DDCNAT, ZrH ₂ moderator	0.87052 ± 4 pcm	-381	-257	-336
DDCNAT, no moderator	0.87493 ± 3 pcm	-332	-216	-299
DDC48, Be moderator	0.66326 ± 3 pcm	-1736	-1451	-1441
DDC48, ZrH ₂ moderator	0.79083 ± 4 pcm	-1024	-777	-769
DDC48, no moderator	0.78599 ± 3 pcm	-935	-694	-686
Heterogeneous clusters				
DDCNAT, Be moderator	0.80906 ± 4 pcm	-890	-720	-714
DDCNAT, ZrH ₂ moderator	0.92926 ± 4 pcm	-571	-424	-419
DDCNAT, no moderator	0.92587 ± 4 pcm	-516	-363	-359
DDC48, Be moderator	0.75151 ± 4 pcm	-1478	-1226	-1218
DDC48, ZrH ₂ moderator	0.87483 ± 4 pcm	-931	-715	-709
DDC48, no moderator	0.86241 ± 3 pcm	-914	-689	-682

It is easy to notice that the A3-T4 discrepancies were at least an order of magnitude higher than in case of a single fuel assembly from the previous section. In each case, the value of k were underestimated by APOLLO3[®]. The worst accuracy was observed for clusters with Be moderator. The difference between ZrH₂ and the absence of moderator were not as pronounced, however the “no moderator” case performed slightly better in every calculation.

The discrepancies were visibly higher for more absorbing DDC48 zone and exceed 1000 pcm in case of Be moderator. An improvement of few hundred pcm was obtained by increasing Legendre expansion to P3, however, further increase to P5 did not result in any substantial improvement.

Such high discrepancies were related to the very high impact of the absorbers introduced in the infinite lattice. For the worst case, the homogeneous DDC48 control rod assembly, the reactivity worth of control rods (reactivity difference between an infinite lattice of clusters and an infinite lattice of fuel assemblies) varies from 44 000 pcm for ZrH₂ to 63 000 pcm for Be moderator. In such a case, even a slight inaccuracy of flux calculation can produce a pronounced difference in reactivity. The high discrepancies observed translate to less than 3% discrepancy on the worth of the control rod assembly, which, while still rather high, can be acceptable if the goal is to only obtain the homogenized/condensed cross-sections.

Interestingly, a significantly smaller discrepancies were observed for DDCNAT absorbers, even though their reactivity worth is less than 30 % lower than for DDC48.

Even after refining the geometry with additional fuel rings, adding more cells in the control rod assembly and expanding the number of self-shielding zones, a relatively small improvement of around 60 pcm was achieved for the largest discrepancy of 1451 pcm (Semi-homogeneous DDC48 and Be moderator), despite significantly longer calculation time. Despite the efforts to decrease the bias, the discrepancies observed in this study were order of magnitude larger than in other similar studies [92, 91], therefore, the problem requires further investigation.

5.4.1.1 Capture rate in boron

In case of cluster calculations, the reactivity differences can serve as an indicator of accuracy of the results, however, the goal of the calculations is to compute the homogenized/condensed cross-sections of the central assembly. The cross-sections computed for C1 fuel assembly in the cluster are not used in the core calculation. It is thus important to study mainly the reaction rates in the control rod assembly in particular in the B_4C absorber. The normalized capture rates in ^{10}B and ^{11}B are contained in Table 5.13.

Table 5.13: Comparison of capture rate in boron (^{10}B and ^{11}B). APOLLO3[®] calculation with P3 anisotropy order.

	$R_{T4} \pm \sigma$ [pcm]	$R_{A3} - R_{T4}$ [pcm]	rel. difference [%]
Semi-homogeneous cluster			
DDCNAT, Be moderator	40533 ± 3	456	1.12
DDCNAT, ZrH ₂ moderator	31700 ± 2	264	0.83
DDCNAT, no moderator	37729 ± 3	171	0.45
DDC48, Be moderator	50557 ± 3	733	1.45
DDC48, ZrH ₂ moderator	40648 ± 3	488	1.20
DDC48, no moderator	48123 ± 3	373	0.78
Heterogeneous cluster			
DDCNAT, Be moderator	33194 ± 3	592	1.78
DDCNAT, ZrH ₂ moderator	25388 ± 2	405	1.59
DDCNAT, no moderator	32427 ± 3	289	0.89
DDC48, Be moderator	40198 ± 3	839	2.09
DDC48, ZrH ₂ moderator	31492 ± 3	588	1.87
DDC48, no moderator	39883 ± 3	511	1.28

The relative difference between the codes was oscillating between around 0.5 and 2 %. The absorption in boron was always overestimated by APOLLO3[®], likely due to inaccurate representation of spatial self-shielding, which is a particularly important phenomenon in case of highly absorbing materials. The accuracy in case of Be moderator and ZrH₂ moderator

was similar when looking at the capture rate, as the absolute capture rate was visibly smaller for clusters with ZrH₂-moderated assembly compared to Be. The energy spectra of captures in boron are illustrated in Figure 5.18.

For most energy groups APOLLO3[®] overestimated the capture rate. There are very few groups for which the rate was underestimated, thus the deviations did not compensate each other and the integrated impact of all energy groups was strongly positive as seen in Table 5.13.

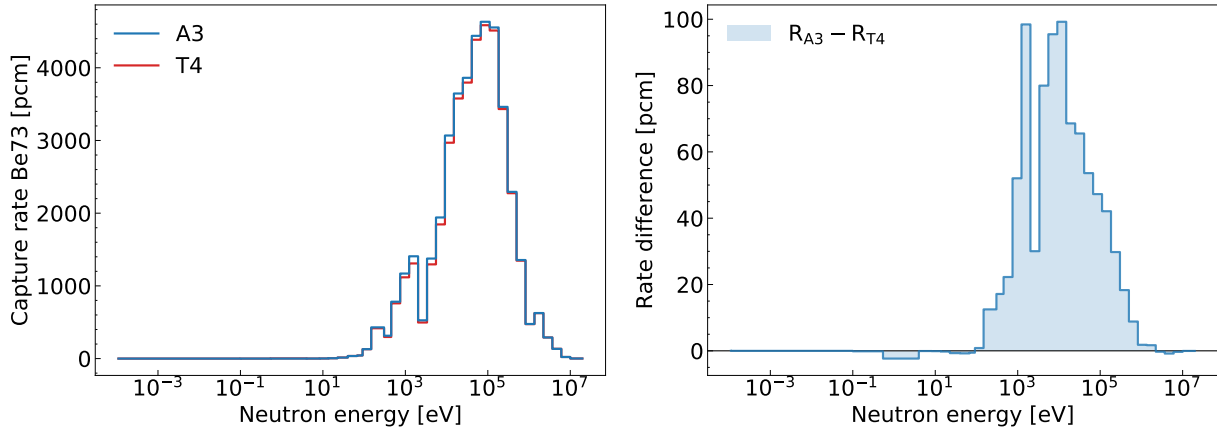
5.4.2 Other clusters

Table 5.14 summarizes the comparison of multiplication factors of several important clusters other than control rod assemblies.

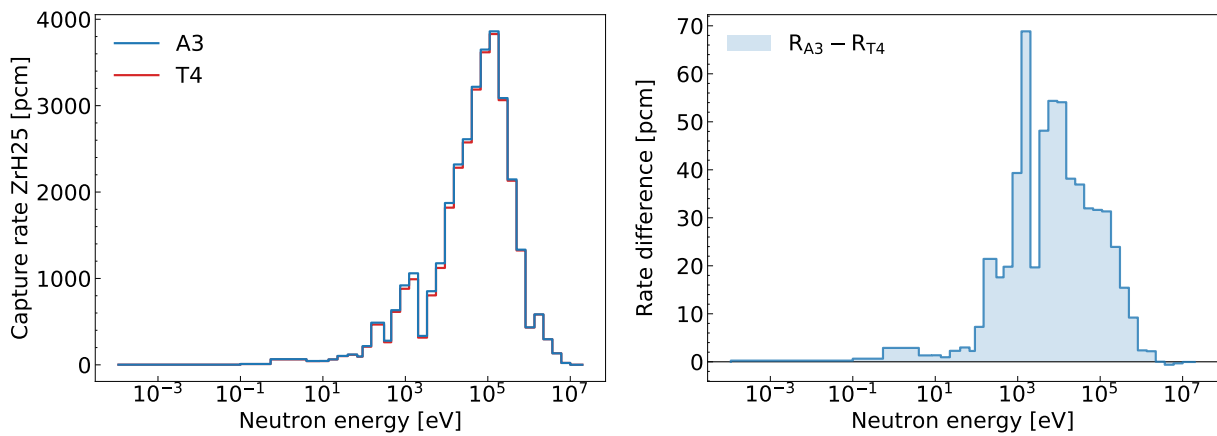
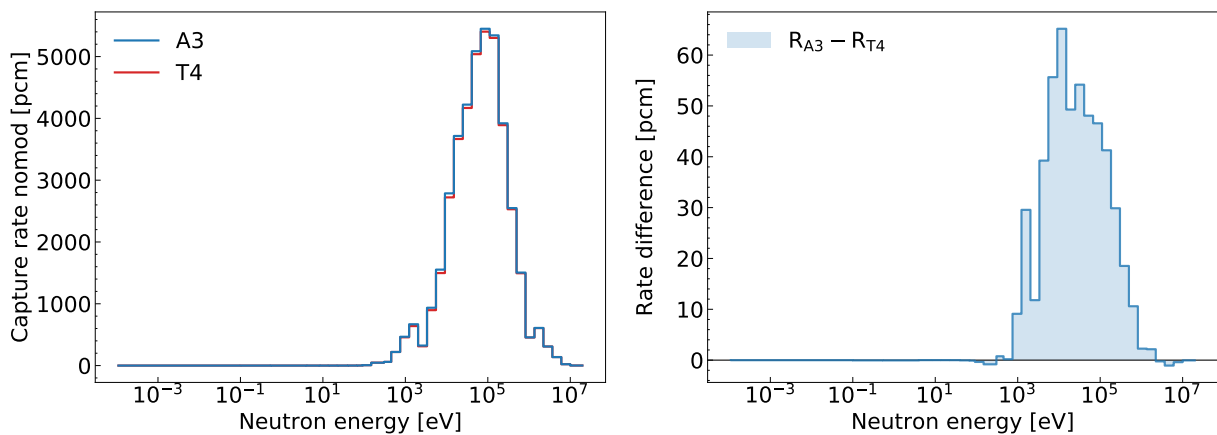
Table 5.14: Comparison of infinite multiplication factors for all three assembly types.

	$k_{T4} \pm \sigma$	$\Delta\rho(\text{A3} - \text{T4})$ [pcm]	
		P1	P3
cluster FERT			
Be moderator	0.97286 ± 4 pcm	-138	-81
ZrH ₂ moderator	1.04454 ± 4 pcm	-134	-67
no moderator	1.09278 ± 4 pcm	-125	-73
DILUANT cluster			
Be moderator	1.05446 ± 4 pcm	44	110
ZrH ₂ moderator	1.13239 ± 5 pcm	-8	56
no moderator	1.18490 ± 6 pcm	-15	41
VES cluster			
Be moderator	1.09050 ± 4 pcm	139	175
ZrH ₂ moderator	1.16352 ± 5 pcm	61	98
no moderator	1.22281 ± 5 pcm	68	100
VEI cluster			
Be moderator	1.10810 ± 5 pcm	65	86
ZrH ₂ moderator	1.17946 ± 5 pcm	10	35
no moderator	1.24237 ± 5 pcm	-3	16
core-reflector traverse			
Be moderator	1.02435 ± 4 pcm	633	681
ZrH ₂ moderator	1.02435 ± 5 pcm	816	862
no moderator	1.14570 ± 5 pcm	244	286

The agreement between APOLLO3[®] and TRIPOLI-4[®] was substantially better compared to the control rod clusters. For clusters with FERT, VEI and DILUANT assemblies, the



(a) Be moderator

(b) ZrH₂ moderator

(c) no moderator

Figure 5.18: Comparison of neutron absorption rate in actinides in 33 groups for A3 results of DDC48 (control rod assembly) cluster with P3 anisotropy order. Results are compared to pointwise T4 calculations.

discrepancies did not exceed 110 pcm when P3 anisotropy order was used. The slightly higher reactivity differences were found for cluster with VES assembly. Compared to VEI, in the VES assembly 33 % of helium was replaced by AIM1 steel, which increases the number of neutron captures. This difference can be responsible for the higher A3–T4 reactivity deviation.

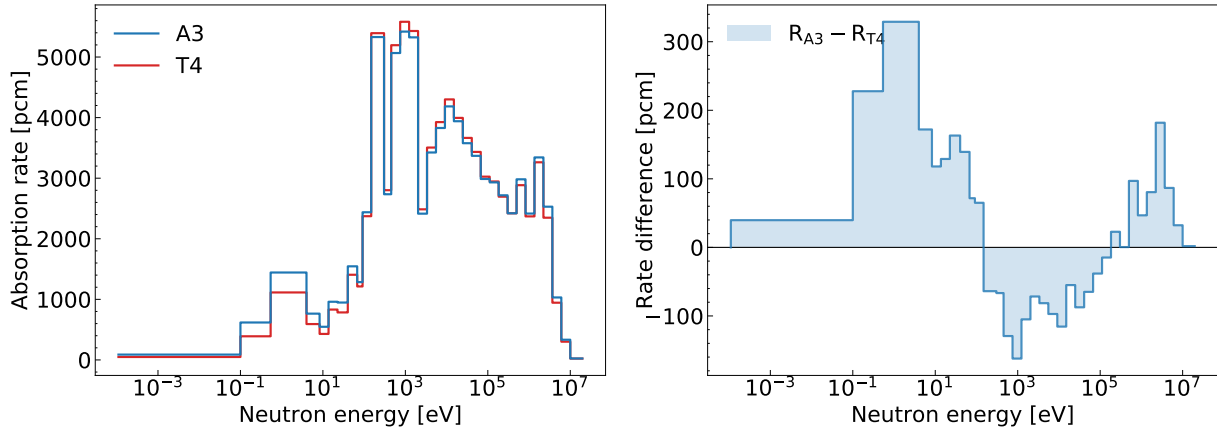
By far the highest difference was obtained in case of core-reflector traverse. While the A3–T4 difference in case of standard SFR assembly does not exceed 300 pcm, the difference for clusters with moderated fuel assemblies is significantly larger and reaches more than 600 pcm and more than 800 pcm for Be and ZrH₂ respectively. The comparison of absorption rate in fuel is shown in Figure 5.19. The most important discrepancies appeared at energies below 100 eV. The fraction of low-energy neutron absorptions was significant even in case of cluster without moderator as the moderation is provided by the MgO reflector. The number of low energy absorptions was visibly higher in case of ZrH₂ moderator as well as the difference between A3 and T4. This can explain why the highest deviation of k is also the highest for traverse with ZrH₂.

5.4.3 Conclusions: cluster calculations

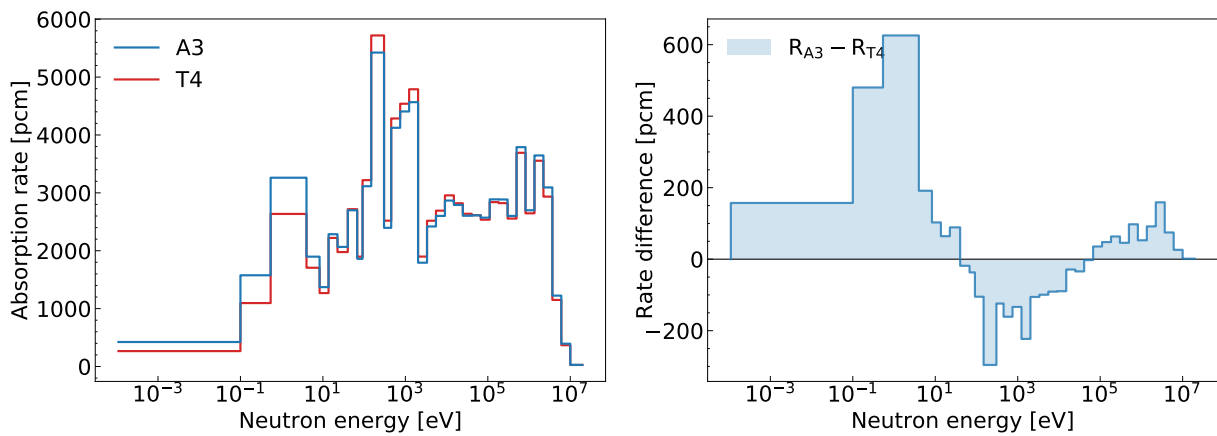
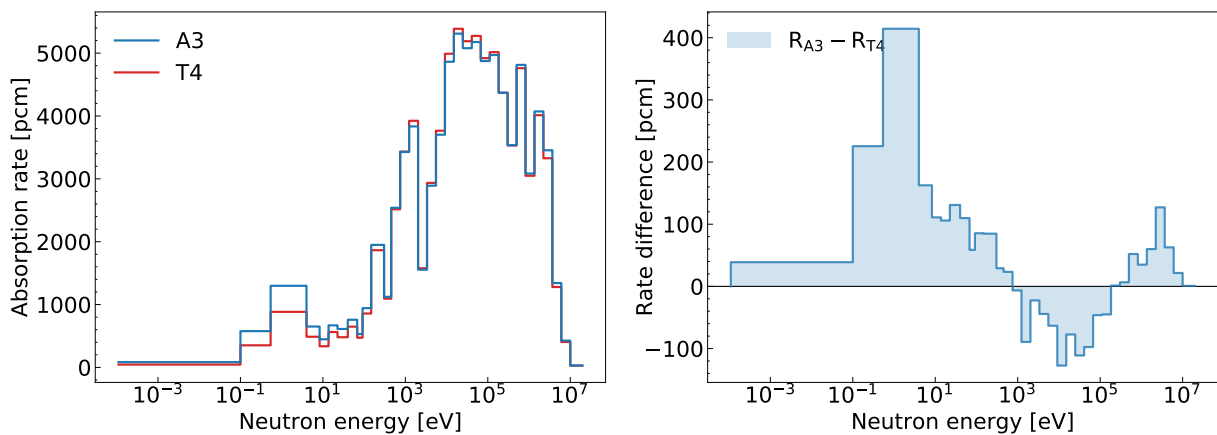
Depending on the cluster geometry, the results produced with APOLLO3[®] presented varying degree of agreement with reference TRIPOLI-4[®] calculations. In case of strongly absorbing central assemblies such as control rod clusters, the reactivity difference between the codes was few hundred pcm for best cases, and up to 1400 pcm for the worst case (P3 anisotropy). The discrepancy was visibly lower when using P3 anisotropy order compared to P1. On the other hand, increasing the order from P3 to P5 had only a marginal effect of a few pcm. The neutron capture rate in boron was overestimated by APOLLO3[®] in each calculation performed. The highest relative difference was found to be 2.1 %. A general trend of higher discrepancies for moderated clusters was observed, especially in case of Be.

For clusters composed of less absorbing materials, such as gas plena or fertile zone, the agreement between codes was better and exceeded 100 pcm only for several results. In case of traverse, high discrepancies were observed for Be and ZrH₂ while a significantly better agreement was found in case of absence of moderator in the fissile zone. Largest deviation from TRIPOLI-4[®] in terms of absorption rate in fuel was identified for low energy regions.

The results of cluster calculations have only an indirect impact on the final outcome of the calculation scheme, as the goal of flux calculation here is to provide a representative weighting function for homogenization and condensation of cross-sections of the subcritical components. In case of control rod, the bias introduced into the core calculation should be negligible as long as the rods are extracted from the fissile zone of the core, which is the case for majority of calculations performed in the next section. However, the bias is expected to manifest more visibly as the control rods are introduced into the core. In case of traverse the bias could become noticeable in the outer core that is in direct contact with reflector assemblies. However, even if the impact of cluster calculation could be of low importance from the point of view of the entire calculation scheme, the problem of high inaccuracies of APOLLO3[®] identified for the clusters requires further examination.



(a) Be moderator

(b) ZrH₂ moderator

(c) no moderator

Figure 5.19: Comparison of neutron absorption rate in actinides in 33 groups for A3 results of core-reflector traverse with P3 anisotropy order. Results are compared to pointwise T4 calculations.

5.5 Comparison of core calculations

In this section the results of the calculation for the whole core are presented. The calculations are based on the MPO libraries created as previously described. The assemblies are fully homogenized, i.e., each zone in the assembly, e.g., fissile zone, or fertile zone is represented as a hexagon made of one homogeneous material. The calculations are performed with FEM solver MINARET with discrete ordinates method.

All results other than the control rod worth were calculated with control rods fully extracted and with cross-sections for control rods obtained from semi-homogeneous clusters in lattice calculation. The reference TRIPOLI-4 calculations were performed with core models that matched those of APOLLO3[®] in the lattice calculation (heterogeneous CR models in case of study of rod worth and homogeneous models in other sections).

5.5.1 MINARET settings

The calculations were performed with a 3D core model. Both the axial and radial boundary conditions were set to void — the neutrons disappear after crossing the boundary, there is no incoming neutron flux at the boundaries. To shorten the calculation time, symmetries were applied so that in reality only one third of the core was used in calculations. The order of finite elements was set to one both in radial and axial directions. Other important MINARET options, number of S_n order and the number of finite elements in both radial plane and axial direction, were determined by a series of core calculations (Figure 5.20). The preliminary analysis of the convergence enabled us to state that S_n order 4, 12 triangles per assembly and axial mesh of 5 cm are producing sufficiently converged results. The final MINARET settings resulting from the convergence analysis are summarized in Table 5.15. The comparison shows that the convergence is achieved for the same parameters regardless of the moderator type used. In other words CADOR core used in this study requires approximately the same solver settings as the standard SFR core.

Table 5.15: MINARET settings used for majority of the calculations in the study.

Parameter	Value
Radial FEM order	1
Axial FEM order	1
No. of triangles per assembly	12
Axial size of finite elements	5 cm
S_n order	4 (24 directions)

5.5.2 Comparison of global parameters

Table 5.16 presents the computed values of multiplication factor, Doppler constant and void effect in comparison to exact geometry, pointwise TRIPOLI-4[®] results. In calculation labeled as “flux moments” the cross-sections homogenized with flux moments method were used in

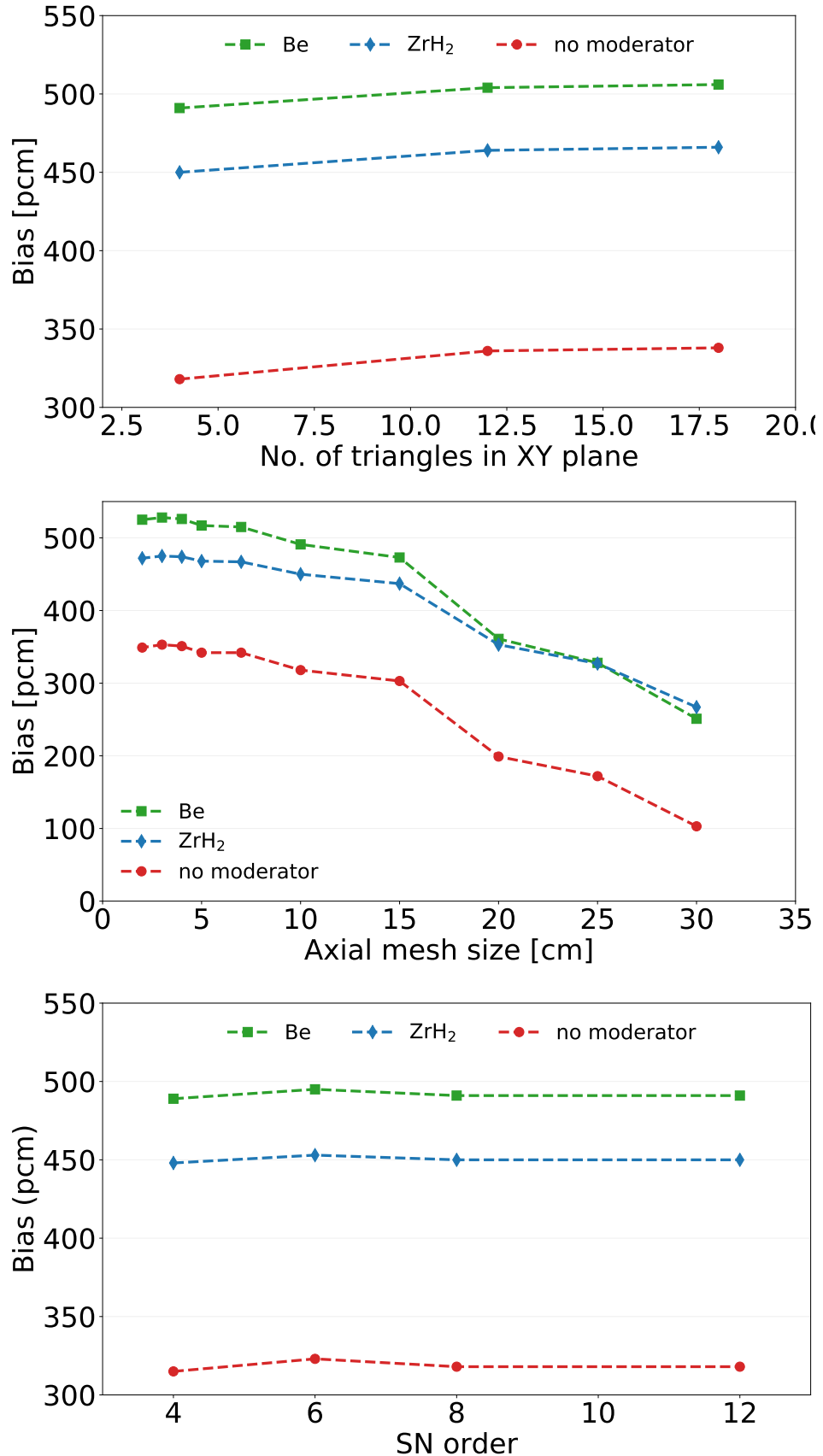


Figure 5.20: Reactivity difference between APOLLO3[®] and TRIPOLI-4[®] for different parameter values in MINARET (other parameters were kept unchanged).

case of all neutron absorbers (DDC, DDA, DCS), the radial reflector and the neutron shield. The difference between APOLLO3[®] and TRIPOLI-4[®] was the largest for Be-moderated

Table 5.16: Comparison of APOLLO3[®]/TRIPOLI-4[®] discrepancies for multiplication factor, Doppler constant and void effect for all three assembly types.

	$k_{T4} \pm \sigma$	$\Delta\rho(A3 - T4)$ [pcm]			
		Flux-volumes		Flux moments	
		P1	P3	P1	P3
k / $\Delta\rho$					
Be moderator	1.03335 ± 3 pcm	517	532	554	477
ZrH ₂ moderator	1.11403 ± 3 pcm	468	505	531	465
no moderator	1.15646 ± 3 pcm	342	366	305	331
Doppler constant					
Be moderator	-2415 ± 6 pcm	55	-62	-86	-64
ZrH ₂ moderator	-2308 ± 6 pcm	89	-83	-68	-84
no moderator	-855 ± 6 pcm	-7	-43	0	-44
Void effect					
Be moderator	937 ± 4 pcm	71	93	-27	90
ZrH ₂ moderator	1070 ± 4 pcm	90	93	-22	88
no moderator	1737 ± 4 pcm	109	112	78	84

core, and slightly less pronounced in case of ZrH₂-moderated core. The discrepancy was the lowest for core without moderator, the agreement was better by approximately 150 pcm compared to moderated cores.

The differences between P1 and P3 anisotropy order were rather low, up to about 50 pcm. In some cases switching to P3 resulted in better agreement between APOLLO3[®] and TRIPOLI-4[®], however, in others the difference was increased. Analogically, the impact of using homogenization by flux moments weighting did not lead to consistent improvement. In both cases the agreement was expected to improve. The effect could be attributed to compensatory errors, however, because of the small magnitude of these differences compared to the global bias, it is difficult to investigate it.

5.5.2.1 Control rod worth

The control rod worth was calculated by comparing the core reactivity with control rods fully extracted (as in case of all other calculations) with core reactivity with the DDC and DDA control rods inserted to the bottom of the fissile zone (120 cm). The three DCS control rod clusters were kept extracted in both cases. For both cores with inserted and extracted control rods the homogenized cross-sections were based on fully heterogeneous cluster calculations for absorber materials (Section 5.4.1). To better account for the presence of strongly absorbing materials in the core, the number of triangles per assembly was increased from 12 to

Table 5.17: Comparison of control rod worth calculated in APOLLO3[®] core calculation and TRIPOLI-4[®] reference calculation.

	CR worth T4 $\pm\sigma$	$\Delta\rho(\text{A3} - \text{T4})$ [pcm]		rel. diff [%]	
		P1	P3	P1	P3
Be moderator	-6721 ± 5	159	96	-2.4	-1.4
ZrH ₂ moderator	-4677 ± 5	64	59	-1.4	-1.3
no moderator	-5653 ± 4	-102	-125	1.8	2.2

22. Table 5.17 presents the comparison of APOLLO3[®] results with TRIPOLI-4[®]. Despite large discrepancies obtained during lattice calculation of absorber/fuel assembly clusters, the APOLLO3[®]/TRIPOLI[®] difference in this study, from 1.3% to 2.4%, was close to values obtained with standard SFR designs [92, 96]. The results suggest that the calculation scheme used in APOLLO3[®] achieves similar accuracy for all three types of cores used in the study.

5.5.3 Comparison of absorption in fuel

The total absorption rate in actinides of the fuel is visible in Figure 5.21. The results are shown for both P1 and P3 anisotropy.

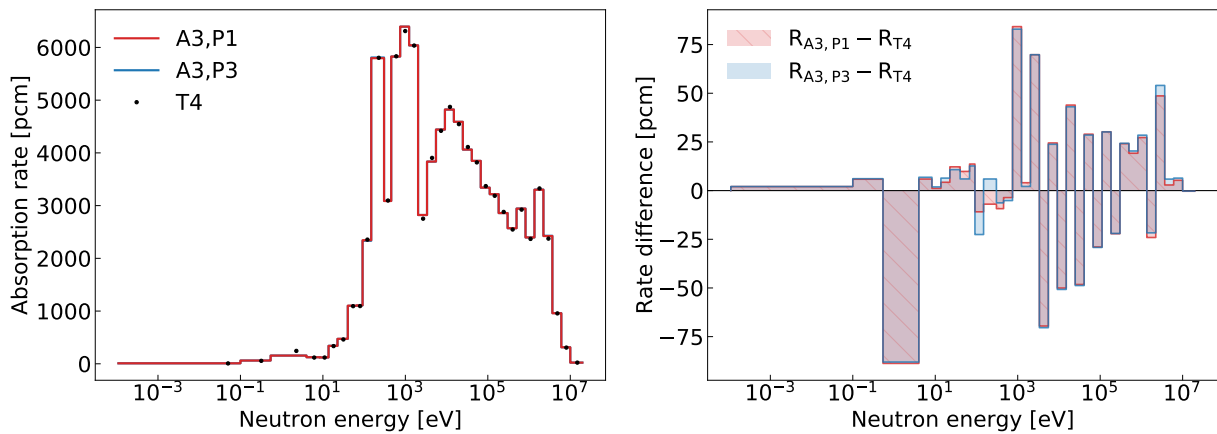
We observe a good overlap of APOLLO3[®] and TRIPOLI-4[®] results. The results were very similar for P1 and P3 anisotropy. Again, we see a large discrepancy caused by ²⁴⁰Pu at the lower part of the spectrum of Be-moderated core. For ZrH₂-moderated core the biggest discrepancies appeared below 10 eV. For higher energies we notice an oscillation of A3/T4 deviation.

5.5.4 Comparison with ERANOS calculation scheme

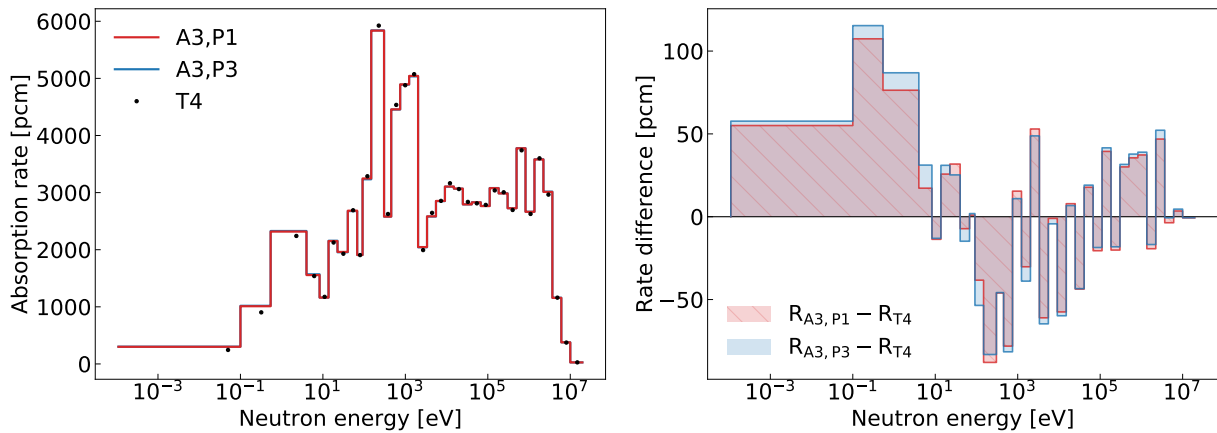
The core solver used in ERANOS calculations in this thesis was VARIANT [97], a P_n solver using variational nodal method. The flux was expanded into P3-order spherical harmonics and P1 scattering anisotropy. The homogenized/condensed cross-sections were computed by performing ECCO lattice calculations on subcritical assembly components with imposed fixed neutron source imported from a fuel assembly calculation. The results of these calculation are in Table 5.18.

Table 5.18: Reactivity differences between results of calculations in ERANOS and TRIPOLI-4[®] reference calculations.

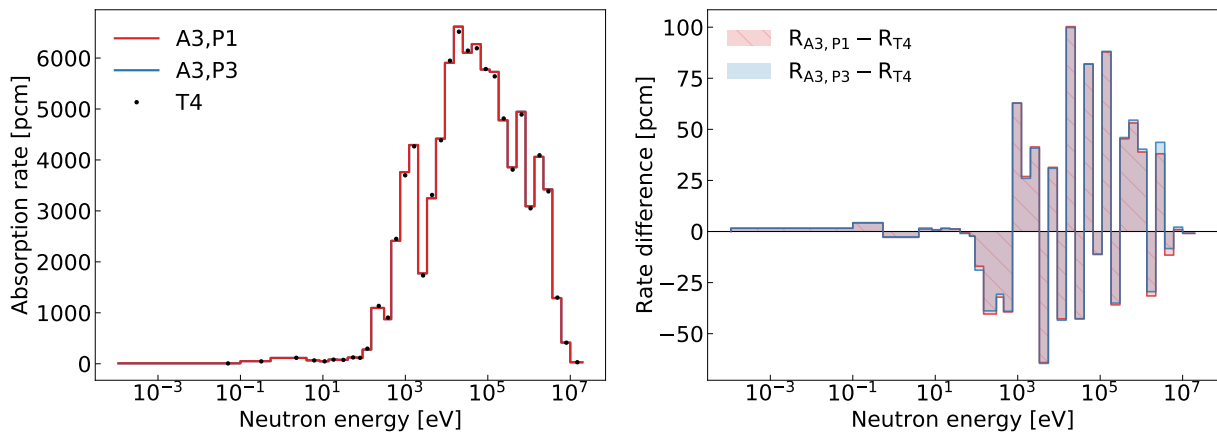
	$\Delta\rho$	ΔK_D	$\Delta(\Delta\rho_{\text{void}})$
Be moderator	-202 ± 3	97 ± 6	-78 ± 4
ZrH ₂ moderator	442 ± 3	51 ± 6	31 ± 4
no moderator	147 ± 3	-13 ± 6	44 ± 4



(a) Be moderator



(b) ZrH₂ moderator



(c) no moderator

Figure 5.21: Comparison of absorption rate for results of A3 for two different anisotropy expansions. Results are compared to pointwise T4 calculations.

We see that the results of ECCO/ERANOS scheme are actually visibly closer to multiplication factor estimated by TRIPOLI-4[®] in case of the cores with Be and without moderator. Despite the problems encountered in ECCO calculations, that were described in the previous section, the full two-step calculation scheme of ECCO/ERANOS was able to produce results with lower deviation from TRIPOLI-4[®] reference than APOLLO3[®]. It is likely the much simpler way of obtaining cross-sections for subcritical assemblies that results in the compensation of biases; however, this hypothesis was not tested.

If we look at the absorption rate (Figure 5.22) we see similar order of deviation from reference TRIPOLI-4[®] calculations for both APOLLO3[®] and ERANOS. Interestingly, in case of ZrH₂-moderated core the deviation were visibly smaller for APOLLO3[®] than for ERANOS. However, due to large compensation between lower and higher energy regions, the cumulative deviation of absorption rates was almost the same in both codes (deviations summed over all energy groups are summarized in Table 5.19). Compared to APOLLO3[®], ERANOS

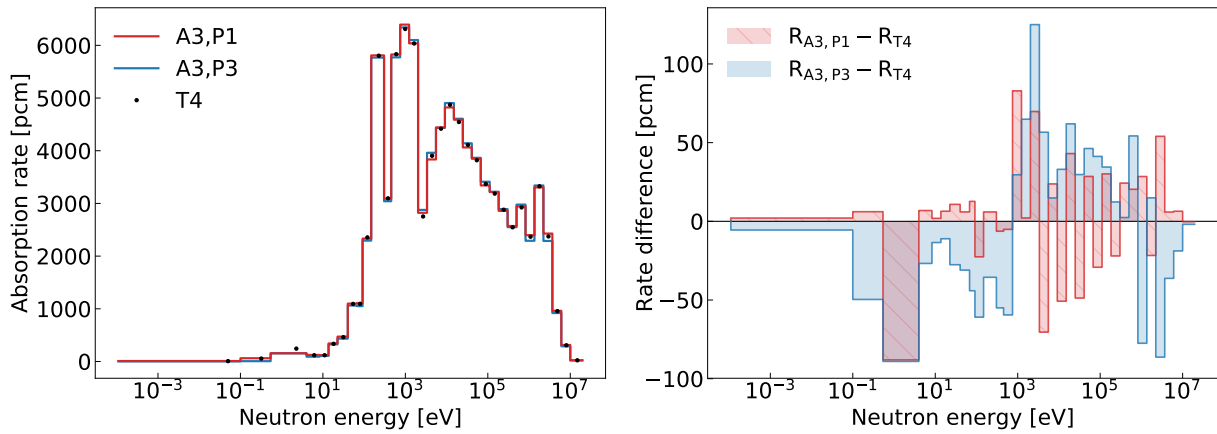
Table 5.19: Differences of total absorption and fission rate in fuel inside the fissile zone in pcm for calculations in ERANOS, APOLLO3[®] and TRIPOLI-4[®] reference calculations.

	$R_{\text{ERANOS}} - R_{\text{T4}}$	$R_{\text{A3}} - R_{\text{T4}}$
Absorption rate		
Be moderator	227 ± 3	-216 ± 3
ZrH ₂ moderator	168 ± 3	195 ± 3
no moderator	519 ± 3	-354 ± 3
Fission rate		
Be moderator	359 ± 4	-128 ± 4
ZrH ₂ moderator	372 ± 4	343 ± 4
no moderator	353 ± 4	100 ± 4

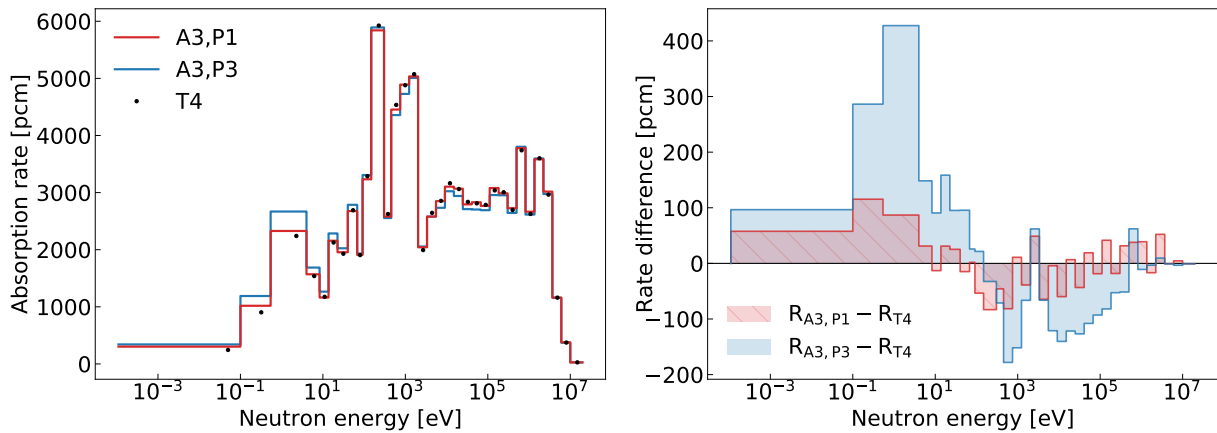
presented a lower accuracy for the low energy region, similarly to what was seen in case of lattice calculations in ECCO. The difference was however compensated by the discrepancies for other energy groups, most often around unresolved energy region. The smaller discrepancy of APOLLO3[®] in that region may be attributed to the exact CPM solver used in self-shielding calculation, not available in ECCO code.

5.5.5 Resonance upscattering at the full core scale

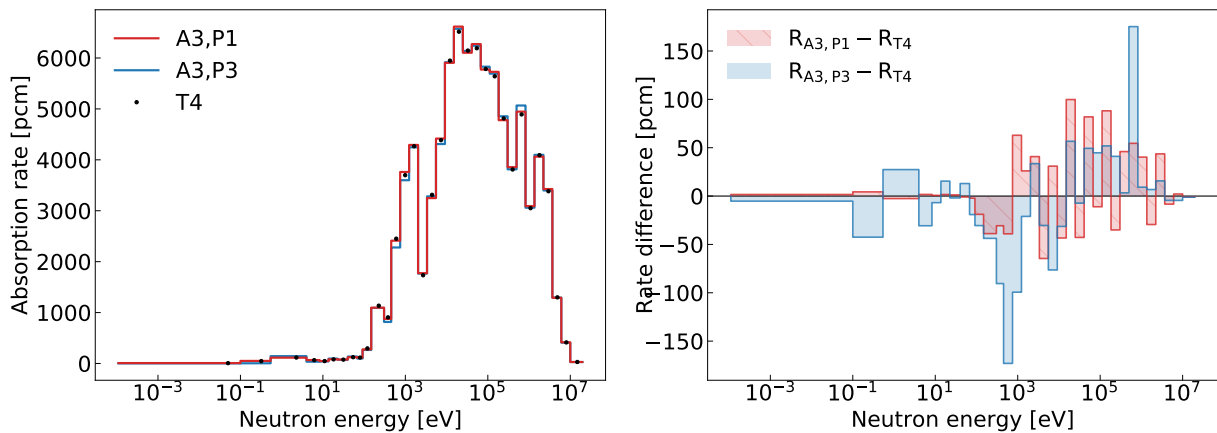
While the previous studies concerned the resonance upscattering phenomenon calculated at the assembly scale it is equally important to study the phenomenon on a scale of a full 3D core. Using full scale core model allows us to examine the impact of resonance upscattering on the results of an entire calculation scheme. As in the case of lattice calculations, we present both the results obtained with the APOLLO3[®] code (with two-step calculation scheme) and the reference TRIPOLI-4[®] calculation, with exactly the same parameters as before. In case of APOLLO3[®] the improved scattering treatment is derived directly from the usage of particular nuclear data library before the calculation and thus there is no difference between this



(a) Be moderator



(b) ZrH₂ moderator



(c) no moderator

Figure 5.22: Comparison of absorption rate for results of A3 (P3) and ERANOS core calculations. Results are compared to pointwise T4 calculations.

study and the one described before. The comparison between improved scattering treatment is presented in the Table 5.20. We see that at nominal fuel temperature the reactivity differ-

Table 5.20: Reactivity differences and Doppler constant differences in pcm between scattering treatments for a 3D CADOR core.

	APOLLO3 [®]	TRIPOLI-4 [®]
Be moderator		
$\Delta\rho$ $T_{\text{fuel}}=900\text{ }^{\circ}\text{C}$ [pcm]	-16	-8 \pm 4
$\Delta\rho$ $T_{\text{fuel}}=2000\text{ }^{\circ}\text{C}$ [pcm]	4	49 \pm 4
ΔK_D [pcm]	69	86 \pm 6
$(\Delta K_D/K_{D,\text{Ups}})-1$ [%]	-2.8	-3.5 \pm 0.4
ZrH ₂ moderator		
$\Delta\rho$ $T_{\text{fuel}}=900\text{ }^{\circ}\text{C}$ [pcm]	30	30 \pm 4
$\Delta\rho$ $T_{\text{fuel}}=2000\text{ }^{\circ}\text{C}$ [pcm]	77	112 \pm 4
ΔK_D [pcm]	111	124 \pm 6
$(\Delta K_D/K_{D,\text{Ups}})-1$ [%]	-4.7	-5.2 \pm 0.4

ences between the scattering models are insignificant for both types of assembly. However, when using a higher fuel temperature of 2000 °C we observed a pronounced difference of up to over 100 pcm. The highest differences were obtained in case of ZrH₂ moderator due to the largest neutron population at epithermal energies, where upscattering occurs with the highest probability. Because of such a significant difference between 900 °C and 2000 °C, the Doppler constant calculated from the two temperatures varied strongly between scattering models. The underestimation of Doppler constant reached up to 112 pcm for ZrH₂ moderator, more than 5% of the value of K_D , which is particularly relevant in safety studies.

We see that the magnitude of the reactivity difference was transferred almost unchanged from the lattice calculation to the full core calculation.

There was no noticeable alleviation or propagation of the effect. Because of the strong differences obtained, all the calculations in the further sections included the improved upscattering treatment. Moreover, we can again conclude that the scattering treatment in APOLLO3[®] is giving results of the same order of magnitude as TRIPOLI-4[®]. While the results deviate from each other in some cases (APOLLO3[®] results tend to underestimate the bias) the major trends are similar in both codes.

As mentioned before the importance of resonance upscattering increases with decreasing Pu enrichment. To demonstrate it, a series of TRIPOLI-4[®] pointwise calculations was performed with different Pu enrichment in the fissile zone. The results are presented in Table 5.21. The dependence on amount of Pu is clearly visible. We can conclude that the total effect of neglecting resonance upscattering in CADOR core at high temperatures can reach up to few hundred pcm depending on the amount of highly absorbent fuel isotopes such as ²³⁹Pu and ²⁴¹Pu. Moreover, the amount of ²³⁸U is decreasing with higher Pu enrichment which further diminishes the effect of resonance upscattering.

Table 5.21: Full core with ZrH_2 moderator at fuel temperature of 2700°C .

Pu enrichment	18 %	19.8 %	22 %	24 %	26 %
$\Delta\rho_{\text{SVT-DBRC}}$ [pcm]	199 ± 4	174 ± 4	151 ± 4	122 ± 4	107 ± 4

5.5.6 Core calculation with 24 energy groups

Because of a different neutron flux spectrum, it is reasonable to ask if the 33 group mesh used for standard SFR is a suitable choice for CADOR core. To give a rough first-estimate answer to this question, we performed APOLLO3[®] core calculations with 24 energy groups instead of 33. The 24 group mesh was created by simply condensing the ten last energy groups into a single large group spanning from 0.01 meV to 148 eV. The groups above 148 eV were left identical as in 33-group mesh. Comparison of the results obtained for 24 and 33 group meshes is presented in Table 5.22.

Table 5.22: Comparison of APOLLO3[®] calculations performed with 33 and 24 energy groups with /TRIPOLI-4[®] reference. Standard deviations of TRIPOLI-4[®] results are below 4 pcm.

	$\Delta\rho(\text{A3} - \text{T4})$ [pcm]			
	24 groups		33 groups	
	P1	P3	P1	P3
Be moderator	484	515	517	532
ZrH_2 moderator	444	480	468	505
no moderator	335	360	342	366

It appears that removal of all thermal and some epithermal groups resulted in a rather low impact on reactivity. The results obtained with 24 groups were remarkably similar to results of 33 group mesh, especially in case of P3 anisotropy order. The highest difference obtained was 33 pcm. Unsurprisingly, the difference between the meshes is the lowest for core without any moderator — only 6 pcm, both for P1 and P3.

This simple study shows that the low energy range can be condensed into fewer amount of groups without risk of losing significant accuracy. The homogenization/condensation procedure is able to preserve the most important quantities related to the flux shape, and even in case of CADOR core with relatively high neutron population at low energies only a few groups are needed in core calculation to achieve accurate results. Although the study presents first and incomplete approach, the result suggests that the 33 groups are sufficiently refined in the lower part of the spectrum to be applied to CADOR core and new coarse mesh is not needed, at least below around 150 eV.

5.6 Quantification of biases with deterministic-Monte Carlo scheme

The purpose of this study is to quantify the bias related to homogenization and condensation of cross-section library. During the homogenization/condensation process part of the information about exact shape of the assemblies and neutron spectrum is lost and can't be transferred to the core calculation. In case of CADOR the treatment used for standard SFR, i.e., homogenization of entire fuel assembly into one region and condensation into 33 energy groups can lead to large numerical bias due to following reasons:

1. fully homogeneous assembly is less representative in case of lower-mean free path combined with heterogeneous moderator placement that is lost entirely in the process
2. lower mean neutron energy may require higher number of energy groups in the lower part of flux spectrum that is less important in conventional SFR

To test this hypotheses we employed a new calculation scheme based on the previous one. The new scheme is combining deterministic and Monte Carlo methods. The idea of the A3-T4 scheme is explained in the schematic in Figure 5.23. The calculation begins as in our standard A3 scheme: the lattice calculation is performed for all elements to obtain the self-shielded homogenized and condensed cross-section library. However, unlike in A3 scheme, the library is now translated into an Apotrim format that can be used as an input library for TRIPOLI-4[®]. Subsequently, a core calculation is performed by TRIPOLI-4[®] instead of APOLLO3[®]. The TRIPOLI-4[®] calculation uses homogenized multigroup cross-section, contrary to the pointwise reference calculation of TRIPOLI-4[®] (on the left side of Figure 5.23).

In case of TRIPOLI-4[®] core calculation, the complexity of calculation is less limited than in APOLLO3[®] where the calculation time and memory usage increases significantly with the number of finite elements and energy groups. This fact allows us to perform finer calculation within feasible amount of time. In each case the cross-sections library is created in APOLLO3[®] lattice calculation by a standard flux-volumes homogenization/condensation procedure, and is therefore influenced by the bias of lattice calculation (fundamental mode approximation, limited flux and cross-section anisotropy, multigroup approximation, bias of P_{ij} and MOC solver). However, the TRIPOLI-4[®] core calculation does not require homogenization and condensation to make calculation feasible. We can thus try different approaches to homogenization and condensation and quantify the bias introduced in each case.

More specifically, by using this method in TRIPOLI-4[®], we were able to employ three different spatial homogenization patterns (Figure 5.24) in the full scale 3D core calculation. Moreover, the method allows us to perform calculations with both 33 energy groups as well as very expensive 1760 groups, i.e., without condensing cross-section after lattice calculation. Additionally, the core calculation is free of biases coming from deterministic core solver; the accuracy is limited only by the statistical convergence of results.

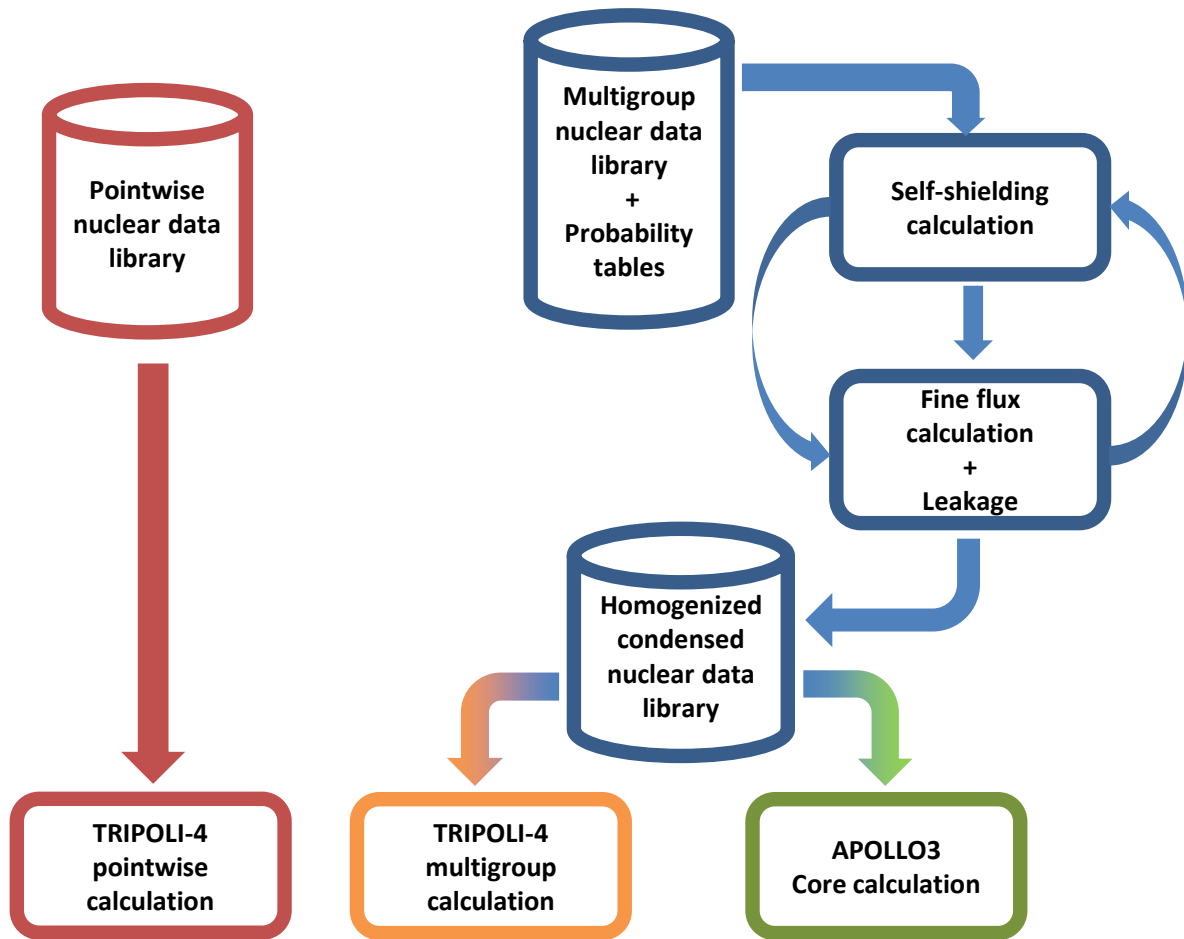


Figure 5.23: Depiction of two-step deterministic-Monte Carlo calculation scheme alongside fully deterministic APOLLO3[®] scheme and reference Monte Carlo scheme.

5.6.1 Global bias on core reactivity

The global biases calculated with A3-T4 calculation scheme with respect to T4 reference calculation are presented in Figures 5.25a and 5.25b. Both the condensation and homogenization have a visible impact on the magnitude of global bias. To illustrate the decomposition of biases more clearly, a different interpretation of data from the previous figures was included in Figure 5.26.

For moderated cores the impact of homogenization was much higher than in case without moderator and it outweighs the impact of energy condensation. The impact of condensation was in fact more pronounced in case of standard SFR by roughly 80-100 pcm. This suggests that the 33 group mesh is at least as suitable for the CADOR core as for a standard SFR core and thus using any different mesh with similar number of groups is unlikely to bring a significant improvement. Regardless of moderator used we can see a visible trend of bias reduction with HOM as the worst case and the CYL as the best one. For 33 group mesh using CYL pattern in place of HOM led to an improvement of 277 pcm for ZrH₂-moderated

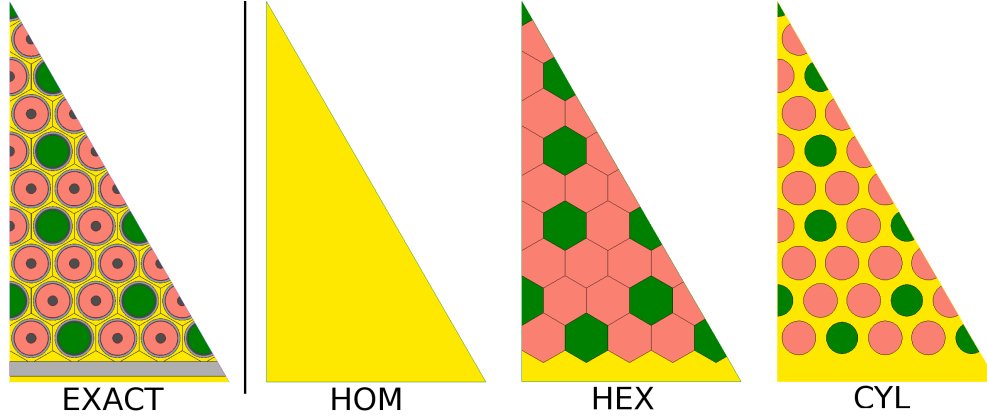


Figure 5.24: Exact geometry of 1/12th of fuel assembly and three homogenization patterns.

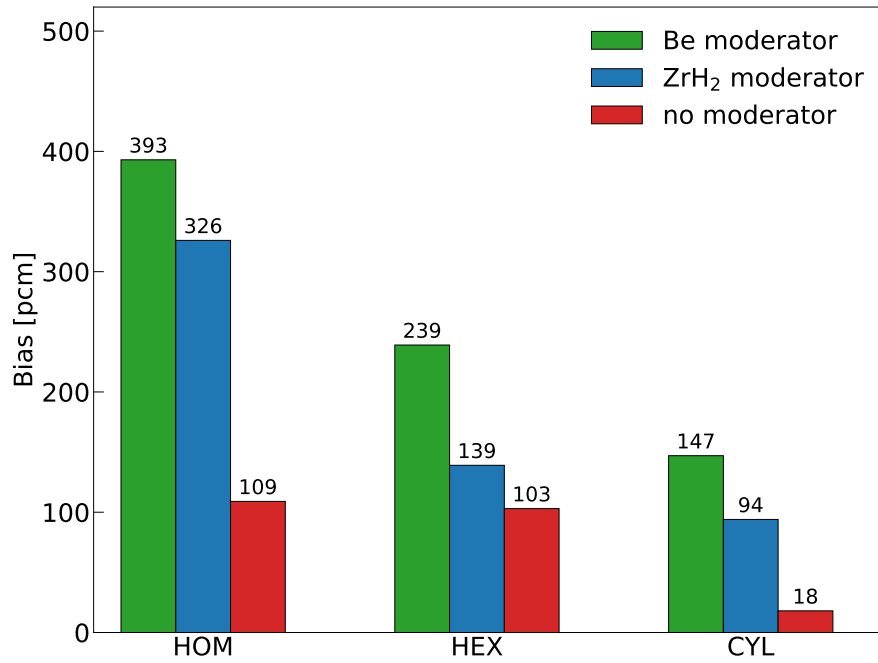
core and 225 pcm for Be-moderated core. Far lower bias reduction in case of standard SFR proves that CYL and HEX approaches are justified only if moderator is present. This fact combined with a higher bias due to condensation leads to global biases of standard SFR being of the same order as for CADOR assemblies in case of 33 energy groups and CYL or HEX homogenization. It is worth noting that the global bias in any of the cases was confined in a 500 pcm limit with possibility to consistently achieve biases below 400 pcm for HEX homogenization and 300 pcm for CYL homogenization even with 33 group energy mesh.

5.6.2 Bias on Doppler constant

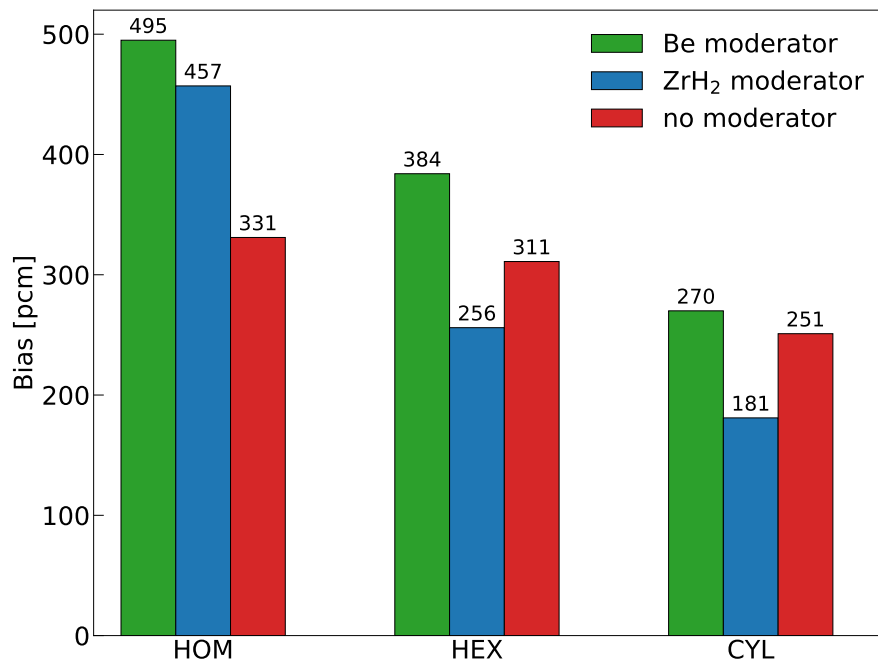
If we look at the bias of Doppler feedback (Table 5.23) we can notice that the values are very weakly dependent on the type of homogenization. The magnitude of Doppler effect was represented as a Doppler constant K_D , calculated for fuel temperatures of 900 °C and 2000 °C. Since both types of reactivity feedback require calculation of core in two different states, the biases of each individual calculation are compensated. The homogenization process does not affect the magnitude of Doppler effect. As a result the discrepancies from reference were very low and do not exceed 70 pcm.

Table 5.23: Bias of A3-T4 scheme on Doppler constant compared to T4 reference (in pcm). Absolute values of K_D are given in the column on the right.

	HOM	HEX	CYL	T4 reference, abs. values
Be moderator	-65 ± 10	-87 ± 10	-79 ± 10	-2417 ± 6
ZrH ₂ moderator	-49 ± 10	-89 ± 9	-107 ± 9	-2308 ± 6
no moderator	-46 ± 9	-28 ± 9	-50 ± 9	-855 ± 6

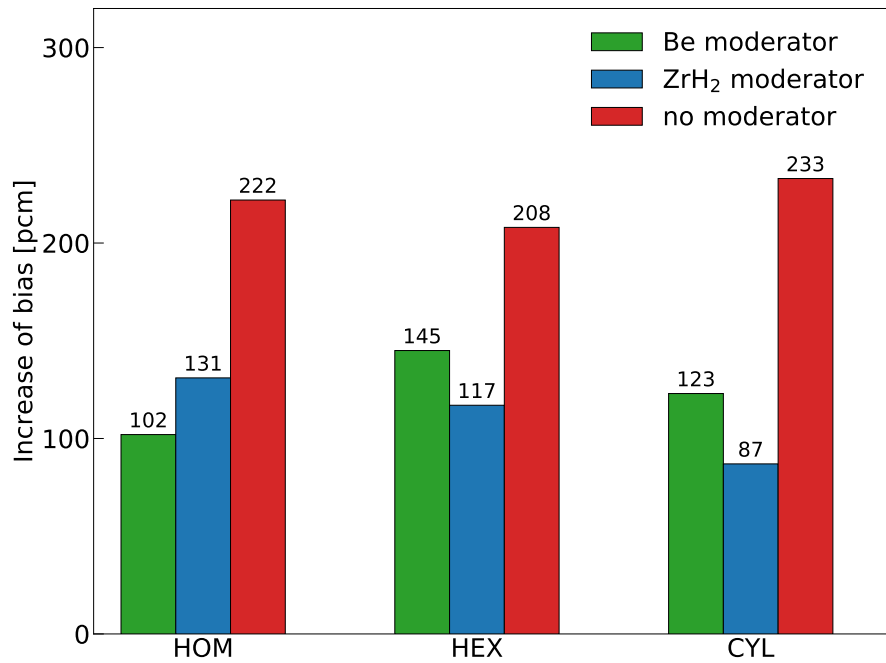


(a) 1760 energy groups (no condensation)

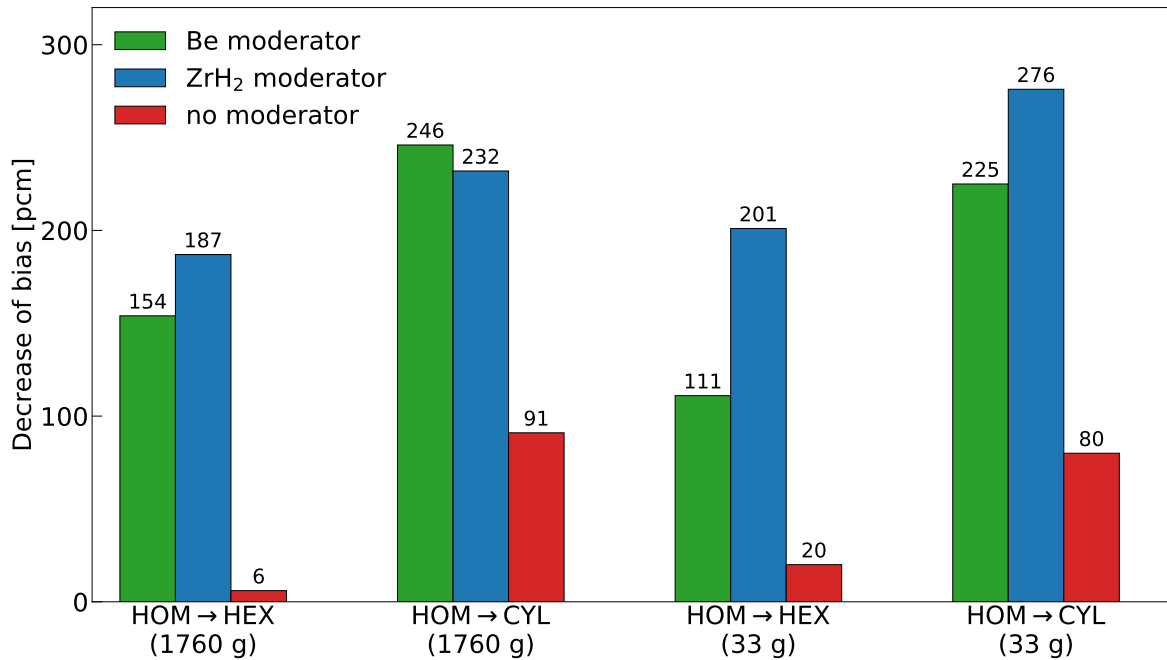


(b) 33 energy groups

Figure 5.25: Global core reactivity bias of A3-T4 scheme compared to T4 reference. Results for two energetic meshes.



(a) Increase of bias due to condensation from 1760 to 33 groups



(b) Decrease of bias due to using heterogeneous patterns instead of full assembly homogenisation

Figure 5.26: Evaluation of biases due to homogenization and condensation.

5.6.3 Bias on void coefficient

The void coefficient was calculated as a reactivity insertion caused by a decrease of sodium density to 1% of its original value in the entire fissile and fertile zone regions. The case of void coefficient was very similar to the one of Doppler constant. The data from Table 5.24 indicate that the biases were very low for each case that was studied, they do not cross the 100 pcm limit. In fact, the global bias on reactivity of APOLLO3[®] compared to reference TRIPOLI-4[®] was slightly lower for moderated assemblies. This can be attributed to higher mean neutron energy due to lower density of sodium that opposes the moderation effects in the assembly.

Table 5.24: Bias of A3-T4 scheme on void coefficient compared to T4 reference (in pcm). Absolute values of void effect are given in the column on the right.

	HOM	HEX	CYL	T4 reference, abs. values
Be moderator	58 ± 7	64 ± 7	22 ± 7	937 ± 4
ZrH ₂ moderator	78 ± 6	92 ± 6	41 ± 6	1070 ± 4
no moderator	94 ± 6	96 ± 6	55 ± 6	1737 ± 4

5.6.4 Bias on control rods worth

As in the study of control rod worth for APOLLO3[®] calculation scheme, the control rod worth in this study was defined as a reactivity difference between core with control rods fully extracted and core with DDC and DDA control rods inserted to the bottom of the fissile zone. The results were however calculated for the homogeneous model of CR assemblies in lattice calculation of APOLLO3[®] and in reference TRIPOLI-4[®]. The quantification of global bias on the rod worth is presented in Table 5.25.

Table 5.25: Biases of control rods worth in pcm compared to T4 reference. Results obtained by using homogeneous geometry of control rod assemblies in reference T4 and A3 lattice calculations. Absolute values of CR worth are given in the column on the right.

	HOM		HEX		CYL		T4 reference, abs. values
	P1	P3	P1	P3	P1	P3	
Be moderator	894 ± 6	492 ± 7	621 ± 7	520 ± 7	240 ± 7	262 ± 7	-8328 ± 4
ZrH ₂ moderator	606 ± 6	284 ± 6	393 ± 6	314 ± 6	130 ± 6	147 ± 6	-5838 ± 4
no moderator	226 ± 6	154 ± 6	202 ± 6	190 ± 6	15 ± 6	72 ± 6	-6830 ± 4

The bias on control rod worth for HOM patterns was much higher than what was previously presented for APOLLO3[®] calculation scheme using cross-sections derived from heterogeneous cluster in lattice calculation. In this case, a much higher bias on core reactivity after the insertion led to a high bias on control rods worth. The difference between CADOR cores

and standard SFR core was very pronounced here. Based on the results we can see two efficient ways of bias reduction. An improvement can be achieved by increasing scattering anisotropy by using Legendre polynomials of order up to P3. By doing so a visible improvement is achieved for moderated cores especially in case of Be moderator. The other way, as in the case of extracted rods, is to use the CYL and HEX homogenizations.

5.7 Semi-heterogeneous assemblies in MINARET

As seen in the previous section the homogenization patterns that preserve the partial heterogeneity of fuel assemblies can be a potential solution to limiting the global bias on reactivity of the APOLLO3[®] calculation scheme. However, this solution can become extremely inefficient in case of Finite Element Method where the entire geometry has to be covered with a mesh of triangles or prisms in a way that each finite element belongs to only one specific geometry cell. Because the HEX and CYL homogenization patterns increase the number of cells per assembly from one to almost 300, the efficient meshing with finite elements becomes difficult. To illustrate this point let's look at how MINARET meshing generating tool handles a single fuel assembly geometry. The visualization of mesh is presented in Figure 5.27. We see that in order to obey the rule described above the number of triangles per each assembly for HEX and CYL patterns goes beyond 1000 elements. Despite the equal number of cells per assembly, the CYL pattern requires almost six times more finite elements. The situation is caused by the small cylindrical shape of each discretized pellet that is an inconvenient shape to be represented by finite triangles. To give an estimate on the requirements of the core

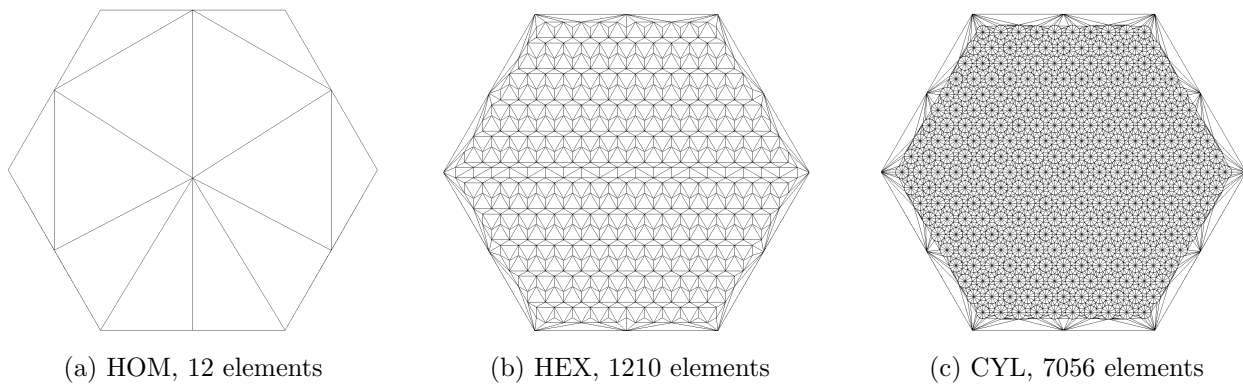


Figure 5.27: Finite element mesh generated with radial mesh size 10 cm MINARET option for different homogenization patterns.

calculation performed with such approach let's look at the number of finite elements needed for an entire core, as presented in Table 5.26. To perform a core calculation with the same MINARET options as before but with HEX pattern, 17 millions finite elements are needed. These number was found to be too high to perform the calculation on a computer used in this work due to excessive memory requirements. On the other hand the calculation for a “flat” 2D core with just one axial element, the number of finite elements required is very similar to the number of finite elements used in 3D core calculation with fully homogeneous

Table 5.26: Number of finite elements in a mesh generated with MINARET option radial mesh size 10 cm. The value for 3D core was calculated with assumption of an axial mesh size of 5 cm.

	HOM	HEX	CYL
single 2D assembly	12	1210	7056
1/3rd of 2D core	5.04×10^3	2.47×10^5	1.43×10^6
1/3rd of 3D core	3.53×10^5	1.73×10^7	1.00×10^8

assemblies therefore such a calculation can be performed in a similar time frame (around 3-5 hours calculation time with 32 processors depending on convergence criteria and maximum number of inner iterations). Results of such calculation are presented in Table 5.27.

Table 5.27: APOLLO3[®]/TRIPOLI-4[®] (reference) reactivity difference of MINARET core calculations with HOM and HEX patterns applied to 2D core (P3 Legendre expansion).

	2D core, HOM	2D core, HEX
Be moderator	308 ± 3	163 ± 3
ZrH ₂ moderator	320 ± 3	95 ± 3
no moderator	229 ± 3	211 ± 3

As for calculations with A3-T4 hybrid scheme, we notice a large improvement of accuracy when using HEX pattern instead of HOM for cores with moderator, and almost no effect for core without moderator. It is worth noting that for the flat 2D cores the APOLLO3[®]/TRIPOLI[®] discrepancies were smaller than for 3D cores studied previously; the difference between moderated and not moderated cores is also smaller. Another benefit of using HEX pattern is a better spatial resolution of reaction rate distribution. Because each assembly contains almost 300 separate regions the local variation of reaction rates discussed in Chapter 4 can be reproduced in core calculation to a much better degree than with fully homogeneous assemblies. An example of power peaks identified after core calculation with HEX pattern is shown in Figure 5.28. Such 2D core calculation can serve as a highly accurate reference in validation of less demanding deterministic calculation schemes.

5.8 Conclusions: core calculations

The global bias on reactivity of the entire APOLLO3[®] calculation scheme established in this chapter was found to be equal to around 450–500 pcm for moderated CADOR cores and 350 pcm for the core without additional moderation. Despite our efforts to diminish the bias, higher anisotropy order or homogenization/condensation by flux moments did not result in a consistent improvement in each case. Although a visible difference between moderated and not moderated cores was obtained, the MINARET settings that allow for sufficient convergence were found to be the same for each core type.

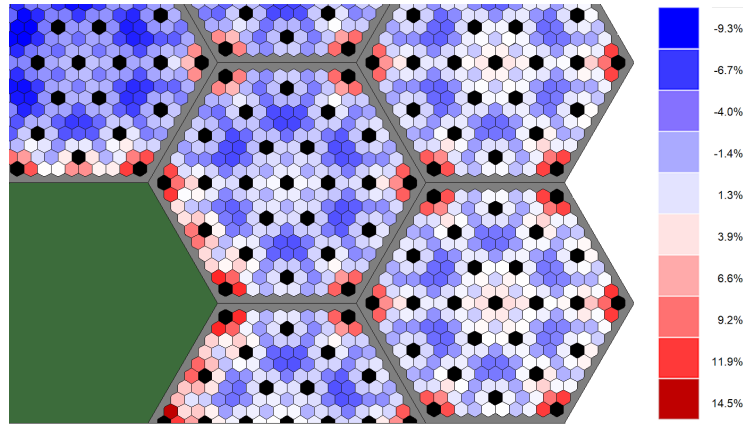


Figure 5.28: Example of average power distribution in several fuel assemblies in ZrH_2 -moderated CADOR core modeled with HEX pattern. Black hexagons denotes homogenized pin-cells containing ZrH_2 . Green hexagon is a homogeneous material made in 92 % of sodium. The values deviation from average power of all assemblies visible.

The impact of resonance upscattering at the core level was found to be very similar to the results obtained for a single assembly. In TRIPOLI-4[®] the impact of using exact free gas scattering model (instead of simplified “constant cross-section” approach) on the magnitude of Doppler effect was equal to 3.5 % and 5.2 % for Be and ZrH_2 moderators respectively. For this reason the usage of “ups” multigroup libraries in APOLLO3, that take into account the free gas scattering, is highly recommended in APOLLO3 calculations.

By establishing a A3-T4 hybrid calculation scheme we attempted to decompose some of the biases and find a way to improve the performance of the calculation scheme. We found that heterogeneous assembly models in core calculation can bring a significant improvements of accuracy, much higher in case of moderate cores. Interestingly, the results suggest that the bias related to condensation from 1760 to 33 energy groups is higher in case of standard core without moderator.

This result, combined with the study of APOLLO3[®] core calculation 24-group energy mesh, suggests that 33 energy groups are enough to represent the CADOR core with sufficient accuracy in the core calculation.

Even when we account for the larger APOLLO3[®]/TRIPOLI-4[®] discrepancies for moderated cores, the design of the calculation scheme proved to be robust. We have shown that a generic fast reactor calculation scheme with a few small changes is able to account for phenomena induced by atypical spectrum of CADOR without losing much of its accuracy.

Chapter 6

Quantification of the impact of nuclear data uncertainties

6.1 Introduction

This chapter aims to quantify another sources of uncertainty of neutron transport calculations, which is the statistical uncertainties related to nuclear data. Unlike the biases of the calculation scheme, the uncertainties discussed in this chapter are classified as statistical (or random) uncertainties that are related to our ignorance with respect to the input parameters used in the computation. In other words, the uncertainty of nuclear data emerges from a finite accuracy of evaluations of cross-sections via physical experiments.

To quantify the extent to which the results are influenced by the uncertainties of input parameters, it is necessary to see how these uncertainties propagate through the calculation. A convenient way is to link the inputs and outputs of the calculation through a sensitivity analysis. Sensitivity of output Y to variations in parameter p is defined as

$$S(Y, p) = \frac{dY/Y}{dp/p} \quad (6.1)$$

Parameter p can stand for, e.g., a cross section for particular reaction and isotope, whereas Y can represent multiplication factor, reactivity difference, reaction rate, etc.

The analysis could be performed manually by comparing results obtained with varying input parameters. However, this approach would be extremely cumbersome given how many different multigroup cross-sections there are to consider. A much more efficient method is to use the perturbation theory [98], a mathematical tool designed for estimating a response to variations of parameters.

6.2 Perturbation calculation

First, let us start by defining two important notions:

1. An inner product of two functions f and g of variables $(\vec{r}, E, \vec{\Omega})$ is defined as

$$\langle f, g \rangle = \int_D d^3r \int_0^\infty dE \int_{4\pi} d^2\Omega f(\vec{r}, E, \vec{\Omega}) g(\vec{r}, E, \vec{\Omega}) \quad (6.2)$$

2. If an operator \mathcal{M}^\dagger is an adjoint operator of an arbitrary linear operator \mathcal{M} , it must satisfy the relation

$$\langle \psi^\dagger, \mathcal{M}\psi \rangle = \langle \mathcal{M}^\dagger\psi^\dagger, \psi \rangle \quad (6.3)$$

To demonstrate the usefulness of the perturbation theory, we are going to look at the variation of multiplication factor. To calculate variations of k as a result of small perturbation of parameters it is sufficient to use Standard Perturbation Theory (SPT). Let us consider an infinitesimal variation of neutron balance in a critical system. The transport equation for such system can be written as $(\mathcal{A} - \frac{1}{k}\mathcal{F})\psi = 0$ where operator $\mathcal{A} = \mathcal{L} - \mathcal{H}$. Then, a small variation can be expressed as

$$d \left[\left(\mathcal{A} - \frac{1}{k}\mathcal{F} \right) \psi \right] = \left(d\mathcal{A} - \frac{1}{k}d\mathcal{F} \right) \psi + \left(\mathcal{A} - \frac{1}{k}\mathcal{F} \right) d\psi + \frac{dk}{k^2}\mathcal{F}\psi = 0 \quad (6.4)$$

where $dk/k^2 = d\rho$. By rearranging the terms we obtain

$$d\rho = \frac{(\mathcal{A} - \frac{1}{k}\mathcal{F})\psi + (d\mathcal{A} - \frac{1}{k}d\mathcal{F})\psi + (\mathcal{A} - \frac{1}{k}\mathcal{F})d\psi}{(\mathcal{F}\psi)} \quad (6.5)$$

After applying an inner product with an arbitrary function u to both sides we get

$$d\rho = \frac{\langle u, (d\mathcal{A} - \frac{1}{k}d\mathcal{F})\psi \rangle + \langle u, (\mathcal{A} - \frac{1}{k}\mathcal{F})d\psi \rangle}{\langle u, \mathcal{F}\psi \rangle} \quad (6.6)$$

Based on Eq. (6.3) we can see that if the function u is a solution of the adjoint transport equation¹

$$\left(\mathcal{A}^\dagger - \frac{1}{k}\mathcal{F}^\dagger \right) \psi^\dagger = 0 \quad (6.7)$$

than the term $\langle u, (\mathcal{A} - \frac{1}{k}\mathcal{F})d\psi \rangle$ will disappear completely. Such a function u is known as an adjoint flux ψ^\dagger . By substituting u for ψ^\dagger we get the final formula for variation of reactivity

$$d\rho = \frac{\langle \psi^\dagger, (d\mathcal{A} - \frac{1}{k}d\mathcal{F})\psi \rangle}{\langle \psi^\dagger, \mathcal{F}\psi \rangle} \quad (6.8)$$

The formula is a powerful tool as it allows studying small perturbations without calculating the deformation of flux shape $d\psi$ for each case. This means that we can study perturbation of

¹The superscript \dagger can be dropped for k in the adjoint transport equation as the multiplication factors k and k^\dagger are in fact equal [99].

concentrations and cross sections for each isotope and reaction without necessity of repeating the flux computation — we only need to calculate the ψ and ψ^\dagger once.

Starting from Eq. (6.8), it can be shown [100] that the sensitivity of multiplication factor to a parameter p can be expressed as

$$S(k, p) = \frac{dk/k}{dp/p} = k \frac{\langle \psi^\dagger, (\mathcal{A} - \frac{1}{k}\mathcal{F})_p \psi \rangle}{\langle \psi^\dagger, \mathcal{F}\psi \rangle} \quad (6.9)$$

where subscript p signifies operators with a perturbed value of parameter p . The formula is applicable only to parameters involved linearly in the operators, however, this assumption is satisfied for microscopic cross-sections.

6.2.1 Sensitivities

To calculate the sensitivities, the perturbation calculation module of APOLLO3[®] was used. Calculations were performed by MINARET solver using 3D core geometry. First, the direct flux was computed as in all previous calculations. Next, the adjoint neutron transport equation was solved with the same solver parameters to obtain the shape of adjoint flux. Finally, the integrals over angle, energy and space were performed to obtain the sensitivities, as described by equation (6.9).

Table 6.1 summarizes the values of sensitivities obtained for the 3D CADOR core with Be and ZrH₂ moderators and a standard core without moderator. The sensitivities for most records in the table are very similar for different core types. It is also worth noting that the sensitivities of moderator isotopes were very low in comparison with fuel isotopes. To better underline the differences between behavior of moderated and not moderated cores, Table 6.2 shows relative differences between sensitivities of the cores with moderators and the case without moderator, calculated as $(S_{\text{mod}}/S_{\text{nomod}} - 1) \cdot 100\%$.

We see lower sensitivity with respect to elastic, inelastic and n,xn scattering cross-sections. For most isotopes, the sensitivities for these reactions were lower than 0.5 pcm/%, hence the relative difference was negligible in absolute terms. An exception is a lower sensitivity related to inelastic scattering cross-section of ²³⁸U and elastic scattering cross-section of ¹⁶O, which can be explained by the softer spectrum of CADOR. An important part of the aforementioned reactions happens at high energies (resonances start above 300 keV for ¹⁶O and inelastic scattering for ²³⁸U does not occur below 45 keV as it is a threshold reaction), therefore, CADOR core was not as sensitive to variations of these cross-sections as standard SFR with higher fast neutron population. The moderated cores are also more sensitive to variation of capture cross-sections of all major isotopes excluding ¹⁶O, due to higher neutron flux in the resonance energy range. It is worth noting that the sensitivities for cores with Be and ZrH₂ behave very similarly (comparison can be seen in Table B.1 in the Appendix), their respective sensitivities are much closer than if we compare any of them with the core without moderator.

Table 6.1: Sensitivities of multiplication factor to variation of cross-sections of most important isotopes in CADOR core (in pcm/%)

(a) Be moderator

	Capture	Fission	Elastic	Inelastic	n,xn	ν	Fission spectrum	Total
Am241	-6	2	0	0	0	2	2	1
Be9	-9	-	-21	-	13	-	-	-50
Fe56	-16	-	7	-19	0	-	-	-42
Na23	-3	-	4	-6	0	-	-	-8
O16	-3	-	-13	0	0	-	-	-30
Pu238	-7	25	0	0	0	36	36	90
Pu239	-66	364	0	-2	0	518	518	1331
Pu240	-50	54	0	-2	0	78	78	157
Pu241	-15	168	0	-1	0	237	237	626
Pu242	-16	14	0	-1	0	20	20	37
U235	-1	7	0	0	0	11	11	27
U238	-258	58	7	-45	1	98	98	-81
Total	-473	692	-8	-85	14	1000	1000	2031

(b) ZrH₂ moderator

	Capture	Fission	Elastic	Inelastic	n,xn	ν	Fission spectrum	Total
Am241	-6	2	0	0	0	3	3	0
Fe56	-14	-	4	-16	0	-	-	-38
H1	0	-	-2	-	-	-	-	-5
Na23	-2	-	0	-6	0	-	-	-13
O16	-3	-	-17	0	0	-	-	-37
Pu238	-8	22	0	0	0	32	32	78
Pu239	-73	341	0	-2	0	509	509	1283
Pu240	-58	53	0	-2	0	80	80	152
Pu241	-18	161	0	-1	0	238	238	619
Pu242	-17	14	0	-1	0	22	22	39
U235	-1	6	0	0	0	10	10	25
U238	-227	60	7	-49	1	106	106	-40
Zr90	-1	-	0	-1	0	-	-	-2
Zr91	-2	-	0	0	0	-	-	-2
Zr92	-1	-	0	-1	0	-	-	-2
Zr94	0	-	0	-1	0	-	-	-1
Zr96	0	-	0	0	0	-	-	-1
Total	-450	658	-1	-89	1	1000	1000	2028

(c) no moderator

	Capture	Fission	Elastic	Inelastic	n,xn	ν	Fission spectrum	Total
Am241	-4	2	0	0	0	3	3	3
Fe56	-11	-	0	-19	0	-	-	-49
Na23	-2	-	-9	-7	0	-	-	-35
O16	-3	-	-56	0	0	-	-	-116
Pu238	-5	26	0	0	0	37	37	95
Pu239	-40	350	0	-3	0	501	501	1306
Pu240	-34	62	0	-3	0	96	96	214
Pu241	-11	152	0	-1	0	214	214	567
Pu242	-12	16	0	-1	0	25	25	51
U235	-1	6	0	0	0	10	10	24
U238	-223	63	8	-70	1	116	116	-55
Total	-362	677	-56	-116	1	1000	1000	1970

Table 6.2: Relative differences of sensitivities (in %)

(a) Be moderator vs no moderator

	Capture	Fission	Elastic	Inelastic	n,xn	ν	Fission spectrum	Total
Am241	28	-9	6	-48	-27	-14	-14	-74
Fe56	49	–	-6384	1	-10	–	–	-15
Na23	72	–	-142	-13	11	–	–	-76
O16	-21	–	-76	-10	-14	–	–	-74
Pu238	57	-1	10	-40	-30	-3	-3	-5
Pu239	66	4	10	-40	-28	3	3	2
Pu240	48	-14	10	-39	-30	-18	-18	-26
Pu241	33	11	4	-37	-29	11	11	10
Pu242	33	-13	9	-41	-28	-18	-18	-26
U235	40	12	-5	-43	-30	11	11	11
U238	16	-8	-4	-36	-30	-16	-16	47
Total	31	2	-85	-26	1533	0	0	3

(b) ZrH₂ moderator vs no moderator

	Capture	Fission	Elastic	Inelastic	n,xn	ν	Fission spectrum	Total
Am241	48	-7	3	-41	7	-8	-8	-93
Fe56	24	–	-4035	-14	16	–	–	-22
Na23	35	–	-103	-23	-4	–	–	-62
O16	-10	–	-70	-12	-9	–	–	-68
Pu238	68	-15	7	-34	2	-14	-14	-18
Pu239	81	-3	5	-32	8	2	2	-2
Pu240	72	-15	4	-33	3	-16	-16	-29
Pu241	60	6	4	-29	2	11	11	9
Pu242	46	-11	2	-35	8	-12	-12	-24
U235	55	0	-8	-37	2	6	6	3
U238	2	-5	-8	-30	2	-8	-8	-28
Total	-5	-5	-83	4	-94	0	0	0

6.3 Uncertainties of nuclear data

The information about the uncertainties related to the evaluated values of cross-sections is available in a form of covariance matrices. A covariance matrix D stores data on variances and covariances corresponding to cross sections for different reactions, isotopes, and energy groups. To calculate the uncertainties (standard deviations) for a given output parameter Y based on the sensitivities and covariance matrices, a well known propagation formula is used:

$$\sigma_Y = \sqrt{(S_Y)^T \times D \times S_Y} \quad (6.10)$$

where S_Y is a sensitivity vector containing arranged values of sensitivities of parameter Y to different perturbations of cross-sections (subscript T indicates a transposition of the vector).

In case of this study, the COMAC-V2.0 covariance matrix was used. COMAC-V2.0 is a covariance matrix created at CEA associated with the JEFF nuclear data library. Compared to its predecessor, COMAC-V2.0 involves integral data assimilation from a number of experiments (GODIVA, JEZEBEL and PROFIL).

6.3.1 Multiplication factor

Table 6.3 contains a breakdown of uncertainties of the multiplication factor. The data are presented for the most important isotopes in the core. The total uncertainty of k was estimated to be around 928, 899 and 929 pcm for Be, ZrH₂ and no moderator, respectively. All three values are in a similar range; furthermore, the values are in agreement with uncertainty analyses performed for the ASTRID reactor [101].

In all cases the biggest contribution to the uncertainty comes from the most abundant actinides: ²³⁸U, ²³⁹Pu and ²⁴⁰Pu. The presence of moderators did not result in a large change of uncertainty: 17 pcm for Be, 19 pcm for combined Zr isotopes and 23 pcm for ¹H.

6.3.2 Reactivity effects

To calculate the uncertainties of Doppler effect, void effect and control rod worth, it is first necessary to compute the corresponding sensitivities at nominal and perturbed states. The sensitivity of $\Delta\rho = \rho_1 - \rho_2$ can be then calculated as

$$S(\Delta\rho, p) = \frac{d(\Delta\rho)/\Delta\rho}{dp/p} = \frac{d(\rho_2 - \rho_1)/(\rho_2 - \rho_1)}{dp/p} \quad (6.11)$$

After calculating the differentials and using the definition of reactivity $\rho = (k - 1)/k$, a following formula is obtained:

$$S(\Delta\rho, p) = \frac{1}{\Delta\rho} \left(\frac{S(k_2, p)}{k_2} - \frac{S(k_1, p)}{k_1} \right) \quad (6.12)$$

The reactivity effects included in the study were:

Table 6.3: Uncertainties of multiplication factor (in pcm) for most important isotopes.

(a) Be moderator

	Capture	Fission	Elastic	Inelastic	n,xn	ν	Fission spectrum	Total
Am241	10	2	0	1	0	3	4	11
Be9	0	–	17	–	0	–	–	17
Fe56	118	–	34	54	0	–	–	134
Na23	31	–	12	16	1	–	–	37
O16	72	–	23	2	0	–	–	75
Pu238	48	10	1	1	0	100	52	122
Pu239	254	436	i9	30	i4	81	188	545
Pu240	i197	452	i7	i25	5	16	131	427
Pu241	144	116	1	8	1	130	280	360
Pu242	110	26	1	9	0	15	27	117
U235	17	4	1	0	0	2	3	18
U238	331	83	i38	272	i29	60	49	441
Total	441	645	26	278	i29	193	370	928

(b) ZrH₂ moderator

	Capture	Fission	Elastic	Inelastic	n,xn	ν	Fission spectrum	Total
Am241	10	2	0	1	0	3	3	12
Fe56	76	–	18	46	0	–	–	90
H1	0	–	23	0	0	–	–	23
Na23	25	–	5	14	0	–	–	29
O16	82	–	25	2	0	–	–	86
Pu238	51	9	1	2	0	87	28	105
Pu239	306	448	i9	29	-5	66	157	569
Pu240	i172	423	i7	i20	6	16	113	402
Pu241	168	124	1	9	1	131	222	332
Pu242	143	27	1	10	0	16	23	149
U235	13	3	0	1	0	2	2	14
U238	271	83	i32	272	-28	64	46	398
Zr90	7	–	1	–	–	–	–	7
Zr91	11	–	0	–	–	–	–	11
Zr92	5	–	1	–	–	–	–	5
Zr94	3	–	0	–	–	–	–	3
Zr96	12	–	0	–	–	–	–	12
Total	453	634	21	277	i27	183	300	899

(c) no moderator

	Capture	Fission	Elastic	Inelastic	n,xn	ν	Fission spectrum	Total
Am241	8	2	0	2	0	4	4	10
Fe56	84	–	17	54	0	–	–	101
Na23	22	–	26	17	i1	–	–	38
O16	91	–	59	3	0	–	–	109
Pu238	35	13	1	3	0	101	39	115
Pu239	149	259	i9	44	i6	87	172	358
Pu240	i255	526	i6	i48	7	20	144	480
Pu241	168	105	1	10	1	117	221	319
Pu242	54	30	1	14	0	19	29	72
U235	20	4	1	1	0	2	2	21
U238	401	65	i52	430	i40	70	55	595
Total	413	600	41	434	i40	192	323	927

- Doppler effect for fuel temperature increased from 900 °C to 2000 °C
- sodium void effect, from nominal conditions to 99 % void
- control rod worth, from full extraction to insertion of 10 cm

Because of the large quantity of data, the full breakdown of uncertainties can be found in Tables B.2, B.3 and B.4 in the Appendix. A concise summary of these tables is presented in Table 6.4.

Table 6.4: Summary of the uncertainties of reactivity effects (in %) for all isotopes combined.

	Capture	Fission	Elastic	Inelastic	n,xn	ν	Fission spectrum	Total
Doppler effect								
Be moderator	1.27	1.59	0.60	0.78	0.06	0.23	1.00	2.48
ZrH ₂ moderator	0.77	1.43	0.30	0.92	0.07	0.21	0.99	2.15
no moderator	1.37	1.99	1.28	1.52	0.11	0.24	1.06	3.32
Void effect								
Be moderator	6.38	7.75	0.81	2.49	0.13	0.98	1.14	10.48
ZrH ₂ moderator	3.07	3.58	0.65	1.51	-0.05	0.56	0.52	5.05
no moderator	2.17	2.54	1.19	0.97	-0.02	0.50	0.58	3.76
CR worth								
Be moderator	0.51	1.35	0.56	-0.18	0.02	0.20	0.71	1.71
ZrH ₂ moderator	0.50	1.36	0.48	-0.11	0.03	0.19	0.67	1.68
no moderator	0.72	1.51	0.52	-0.16	-0.04	0.20	0.79	1.93

The uncertainties of reactivity effects related to nuclear data are very similar for the moderated cores and the core without moderator. Both in case of the Doppler effect and the control rod worth, the uncertainties for Be and ZrH₂-moderated cores were in fact slightly smaller than in case of non-moderated core. The opposite is true when we look at the uncertainties of void effect, especially for core with Be where we observed uncertainty of more than 10%. The sensitivities of void effect are compared in Table 6.5.

The sensitivity to capture cross-section and fission cross-section for even-A actinides was much higher in case of Be moderator than when the moderator was not present, which is a possible source of higher uncertainty. In absolute terms, the uncertainties related to the value of void effect are equal to 99, 41 and 93 pcm for Be, ZrH₂ and no moderator, respectively. The absolute value was almost identical in case of Be moderator and no moderator, due to visibly higher reactivity effect of voiding for the latter.

6.3.3 Power ratio

To calculate the sensitivity of a ratio of any two reaction rates we can employ the General Perturbation Theory. The ratio R of two reaction rates can be expressed as:

$$S(R, p) = \frac{dR/R}{dp/p} = \frac{\langle (\sigma_n)_p, \psi \rangle}{\langle \sigma_n, \psi \rangle} - \frac{\langle (\sigma_d)_p, \psi \rangle}{\langle \sigma_d, \psi \rangle} - \left\langle \Psi^\dagger, \left(\mathcal{A} - \frac{1}{k} \mathcal{F} \right)_p \psi \right\rangle \quad (6.13)$$

Table 6.5: Sensitivities of void effect for cores with Be and without moderator.

(a) Be moderator [%/%]

	Capture	Fission	Elastic	Inelastic	n,xn	ν	Fission spectrum	Total
Am241	0.03	0.00	0.00	0.00	0.00	0.01	0.01	0.05
Be9	-0.06	-	-0.43	-	0.06	-	-	-0.97
O16	-0.01	-	-0.13	0.00	0.00	-	-	-0.28
Pu238	0.06	0.00	0.00	0.00	0.00	0.00	0.00	0.06
Pu239	0.53	-0.64	0.01	-0.01	0.00	-1.05	-1.05	-2.22
Pu240	0.42	0.20	0.01	-0.02	0.00	0.32	0.32	1.24
Pu241	0.09	-0.40	0.00	0.00	0.00	-0.64	-0.64	-1.60
Pu242	0.07	0.05	0.00	-0.01	0.00	0.08	0.08	0.29
U235	0.01	-0.01	0.00	0.00	0.00	-0.02	-0.02	-0.04
U238	0.59	0.13	0.14	-0.33	0.00	0.30	0.30	0.93
Total	2.15	-0.66	-0.34	-0.10	0.06	-1.00	-1.00	-1.48

(b) no moderator [%/%]

	Capture	Fission	Elastic	Inelastic	n,xn	ν	Fission spectrum	Total
Am241	0.02	0.00	0.00	0.00	0.00	0.00	0.00	0.02
O16	-0.01	-	-0.28	0.00	0.00	-	-	-0.57
Pu238	0.02	-0.03	0.00	0.00	0.00	-0.03	-0.03	-0.08
Pu239	0.24	-0.55	0.00	-0.01	0.00	-0.67	-0.67	-1.66
Pu240	0.16	0.05	0.00	-0.01	0.00	0.13	0.13	0.46
Pu241	0.04	-0.38	0.00	0.00	0.00	-0.50	-0.50	-1.35
Pu242	0.05	0.02	0.00	0.00	0.00	0.04	0.04	0.14
U235	0.00	-0.01	0.00	0.00	0.00	-0.02	-0.02	-0.05
U238	0.58	-0.02	0.08	-0.18	0.00	0.06	0.06	0.47
Total	2.35	-1.24	0.39	-0.12	0.00	-1.00	-1.00	-0.35

(c) $S_{Be}/S_{nomod} - 1$ [%]

	Capture	Fission	Elastic	Inelastic	ν	Fission spectrum	Total
Am241	84	482	108	-1	197	197	135
O16	105	-	-53	184	-	-	-51
Pu238	161	-100	103	47	-94	-94	-177
Pu239	118	16	117	32	56	56	33
Pu240	154	302	127	48	149	149	172
Pu241	102	6	96	52	27	27	19
Pu242	57	196	126	60	104	104	102
U235	95	-38	85	20	-8	-8	-25
U238	2	-771	83	87	424	424	97
Total	-9	-47	-189	-13	0	0	319

where n and d signify cross-section associated with reaction rate in the numerator and denominator of R , respectively, and Ψ^\dagger is a generalized importance function associated to the ratio of reaction rates — a solution of equation

$$\left(\mathcal{A}^\dagger - \frac{1}{k}\mathcal{F}^\dagger\right)\Psi^\dagger = \frac{\sigma_n}{\langle\sigma_n, \psi\rangle} - \frac{\sigma_d}{\langle\sigma_d, \psi\rangle} \quad (6.14)$$

Table 6.6 summarizes the results of the study. The full version of the result is shown in Table B.5 in the Appendix. The resulting uncertainties were very similar for all three core types. The total uncertainty did not exceed 2% for any core type.

Table 6.6: Summary of the uncertainties of power ratio (in %) for all types of reaction rates (all isotopes combined).

	Capture	Fission	Elastic	Inelastic	n,xn	ν	Fission spectrum	Total
Be moderator	1.03	0.57	0.90	0.27	0.05	0.13	0.30	1.54
ZrH ₂ moderator	1.18	1.04	1.00	0.44	0.05	0.12	0.32	1.94
no moderator	1.05	0.37	0.84	0.59	0.03	0.11	0.18	1.53

6.3.4 Summary

Table 6.7 contains a summary of all total uncertainties of nuclear data presented in this chapter. The uncertainties related exclusively to isotopes in Be and ZrH₂ moderators are summarized in Table 6.8.

Table 6.7: Total uncertainties for all five types of studies performed in this chapter.

	Be	ZrH ₂	no moderator
k	928 pcm	899 pcm	927 pcm
K_D	2.49 %	2.15 %	3.32 %
Voiding	10.48 %	5.05 %	5.76 %
CR worth	1.71 %	1.68 %	1.93 %
Power ratio	1.54 %	1.94 %	1.53 %

Table 6.8: Total uncertainties related to cross-sections of isotopes in moderators for all five types of studies performed in this chapter.

	${}^9\text{Be}$	${}^1\text{H}$	Zr (all isotopes)
k	17 pcm	23 pcm	19 pcm
K_D	0.36 %	0.16 %	0.04 %
Voiding	0.23 %	0.28 %	0.08 %
CR worth	0.23 %	0.12 %	0.04 %
Power ratio	0.06 %	0.15 %	0.04 %

6.4 Conclusions

The uncertainties of nuclear data for the CADOR core were found to be similar to typical values for standard SFR. For all three cores studied, the uncertainty of k was equal to around 900–950 pcm, a value 2-3 times higher than the systematic biases of the calculation scheme quantified in the previous chapter.

The largest uncertainty of reactivity effect found was the void effect of Be-moderated core — more than 10 %. However, because of lower absolute value of the void effect in the CADOR core compared to a standard SFR, the absolute uncertainty was around 100 pcm, similar as for the core without moderator. For the remaining reaction rates and power ratio only typical uncertainties of about 2-3 % were found.

The uncertainty related directly to the presence of Be or ZrH_2 where relatively low compared to fuel isotopes. Uncertainty of nuclear data for multiplication factor for Be and ZrH_2 17 pcm and 30 pcm respectively. This shows that the differences in uncertainties compared to non-moderated cores are mainly an indirect effect of moderation caused by softening of a neutron spectrum.

Chapter 7

Transient simulations with MACARENa code

After the quantification of epistemic biases and random uncertainties related to neutronic calculations, it is vital to evaluate their propagation during multiphysics simulations of transient scenarios. To simulate the transients, a one-way coupling was established with MACARENa code [102, 103], a transient simulation tool developed at CEA capable of simulating ULOF and global UTOP transients.

The aim of this last study was to investigate the differences in transient progression with the Doppler effect calculated with different neutron transport schemes: the standard SFR calculation scheme and the calculation scheme adapted to CADOR with “ups” multigroup library. The final goal was to see in what way the uncertainties of neutron calculation scheme influence the uncertainty of transient simulations and, by extension, the safety evaluation of the CADOR core. A study with similar goals was conducted in the past for sodium void effect in CFV core [91].

7.1 Principles of MACARENa calculations

The MACARENa code is a multiphysics tool created for simulation of behavior of an SFR core during transient, primarily ULOF. Models included in MACARENa allow simulation of thermohydraulics of two-phase sodium flow, fuel and cladding degradation and neutron kinetics in a form of a simple point (0D) model.

The core geometry in MACARENa is simulated as a bundle of vertical channels (Figure 7.1), representing the fuel assemblies, with a common sodium inlet at the bottom. At the top, the sodium from all channels is collected at the hot pool and redirected to the external part of the loop where the Intermediate Heat Exchanger is located. After transferring heat to the intermediate loop (not included in the schematic) the sodium is pumped through the cold pool back to the core.

The thermohydraulics of the core in MACARENa is governed by three principal models:

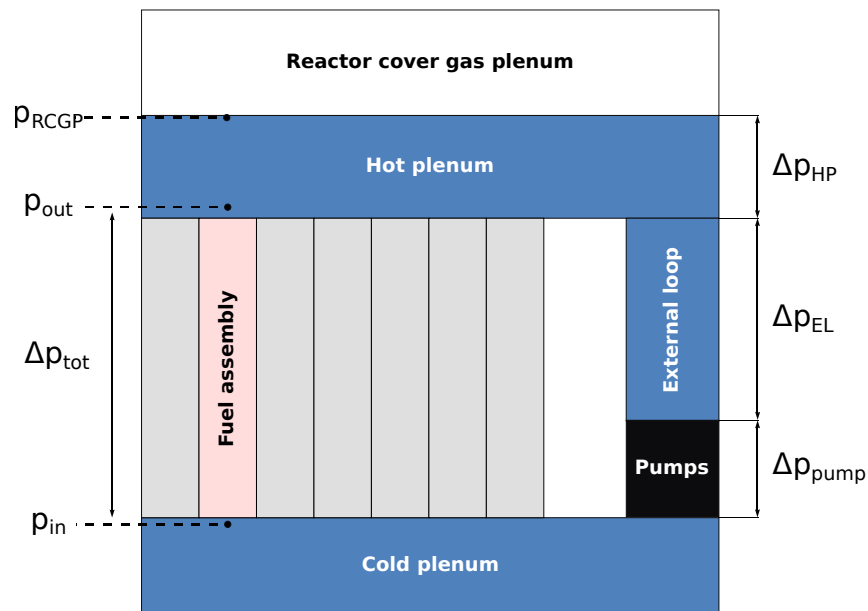


Figure 7.1: Model of primary loop used in MACARENa [102]. The indicated pressures p and pressure drops Δp are used to calculate sodium flow.

- a 0D model of momentum conservation used to calculate the time evolution of a mass flow in each channel
- a 2D (axial-radial) model of energy conservation, i.e., heat transfer between different materials of a fuel assembly and the resulting temperature evolution,
- a 1D (axial) model of sodium flow in the channel used for calculation of sodium heating and boiling.

The sodium flow is calculated separately in each channel and only along the vertical axis. The mass flow is calculated with 0D momentum conservation, based on the pressure difference generated by the pump Δp_{pump} and the pressure losses in the loop due to gravity, acceleration, friction and at singularities (disruptions of flow due to a change in channel geometry).

The heat transfer within each channel is realized by a radial-axial model. Fissile and fertile zones of assembly are represented by five radial media: fuel pellet, fuel-cladding gap, fuel cladding, sodium, wrapper tube and external sodium layer between assemblies. All fuel pins in the assembly are reduced to a single representative fuel pin (Figure 7.2). The heat is transferred between elements axially or radially. In addition to the aforementioned radial zones, each radial zone is divided into axial cells ($z - 1$, z , $z + 1$ in Figure 7.2). In each cell, local parameters such as temperature or density are considered constant. Moreover, every channel is treated separately, there is no evaluation of heat transfer across the channels.

Because simulating each fuel assembly as an individual channel would require an excessive computation time, MACARENa uses a notion of derivations. Derivation, in the context of MACARENa calculations, is a collective representation of a group of fuel assemblies as one

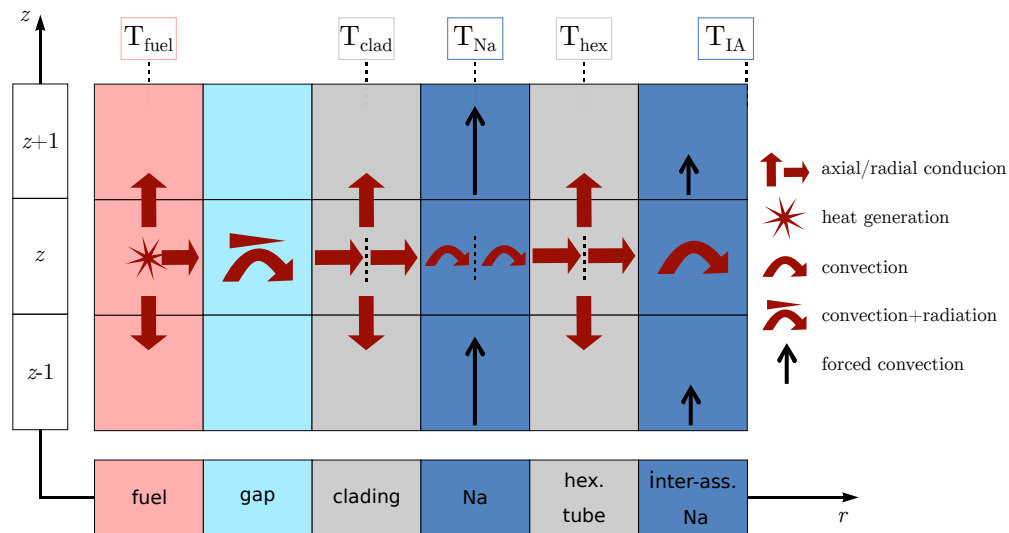


Figure 7.2: Schematics of heat transfer within assembly in MACARENa code [102].

assembly with averaged parameters (power, reactivity coefficients, heat transfer coefficient in pellet-cladding gap, etc.). In case of this study, the entire CADOR core was grouped into eight derivations, which means that only eight channels were actually simulated in MACARENA. The fuel assemblies were grouped according to similar power; the resulting derivations are shown in Figure 7.3.

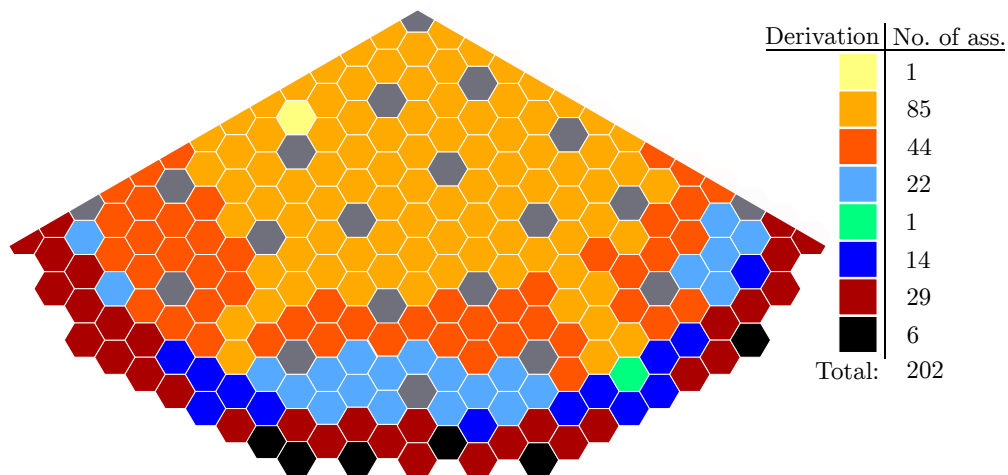


Figure 7.3: One third of the CADOR core divided into eight derivations, each represented by a different color. Gray color designates the subcritical assemblies.

7.2 APOLLO3[®]-MACARENa coupling

The coupling between MACARENa and APOLLO3[®] is a simple one-way coupling. The variation of power during transient is calculated directly by MACARENa via point kinetics model. The main assumption associated with the point kinetics model is the decomposition of a neutron flux into two separate factors

$$\phi(\vec{r}, t) = n(t) \cdot F(\vec{r}) \quad (7.1)$$

where $n(t)$ is the global neutron population in time t and $F(\vec{r})$ is a form factor depending solely on spatial variable. The $F(\vec{r})$ is assumed to be constant at all times; thus, the evolution of neutron population in time during transient is governed only by $n(t)$. The neutron balance in a multiplying medium in its entire volume can be then calculated with the point kinetics equations [33]

$$\begin{cases} \frac{dn(t)}{dt} = \frac{\rho - \beta_{\text{eff}}}{\Lambda} n(t) + \sum_i \lambda_i C_i \\ \frac{dC_i(t)}{dt} = \frac{\beta_{\text{eff},i}}{\Lambda} n(t) - \lambda_i C_i(t) \end{cases} \quad (7.2)$$

where

- Λ is the mean prompt neutron generation time
- λ_i is the decay constant for precursors in group i
- $\beta_{\text{eff},i}$ is the effective delayed neutron fraction in group i
- C_i is the number of precursors in group i

By solving Eq. (7.2) we obtain $n(t)$ which can be then used to calculate the proportional thermal power generated in the system. However, before attempting to solve the equations, the values of β_{eff} , Λ and ρ along with the power shape $F(\vec{r})$ have to be determined beforehand. Those coefficients cannot be computed directly in MACARENa and instead they are determined by the coupled neutron transport code, in our case APOLLO3[®].

7.2.1 Kinetic calculations

The kinetic parameters β_{eff} and Λ were calculated in an APOLLO3[®] module dedicated to kinetic calculations. For both parameters, the adjoint flux ψ^\dagger served as an importance function.

The β_{eff} was calculated as a ratio of importance of delayed neutrons to importance of all neutrons produced by fission [100]:

$$\beta_{\text{eff}} = \frac{\langle \psi^\dagger, \mathcal{F}_d \psi \rangle}{\langle \psi^\dagger, \mathcal{F} \psi \rangle} \quad (7.3)$$

where \mathcal{F}_D is an operator of delayed neutron production. The resulting values of β_{eff} is presented in Table C.1 in Appendix C.

Analogically, mean prompt neutron time Λ was computed as a ratio of static importance of neutron population to the importance creation rate by neutron produced via fission

$$\Lambda = \frac{\langle \psi^\dagger, \frac{1}{v}\psi \rangle}{\langle \psi^\dagger, \mathcal{F}\psi \rangle} \quad (7.4)$$

where $\frac{1}{v}\psi$ is equal to a neutron density n .

7.2.2 Calculation of the reactivity coefficients

MACARENa is able to take into account a variety of reactivity effects. The reactivity effect of each feedback f is calculated separately for each axial zone z in each channel c , then all contributions are summed into a global value of reactivity of the entire core

$$\rho = \rho_{\text{ext}} + \sum_f \sum_c \sum_z \rho_{f,c,z} \quad (7.5)$$

where ρ_{ext} is the external reactivity insertion that can be set manually by the user if UTOP transient is to be simulated.

As mentioned before, the necessary reactivity coefficients have to be calculated externally and provided to MACARENa as an input. In this study, the reactivity coefficients were computed only for the Doppler effect and the sodium expansion to simplify the necessary calculations, leaving the effects of expansion of solid materials equal to 0 at all times (studies such as [104] show, that Doppler effect and sodium expansion are the two most important effects during transients in CADOR core).

The reactivity coefficients depend on the neutron spectrum and, thus, their values are different in each zone of the core. To accurately represent the feedback of the entire core, the coefficients need to be calculated for each of the axial zones in each of eight derivations.

The reactivity differences between nominal state 0 and perturbed state p were calculated for each spatial cell i in the MINARET solver by using a general formula [100]

$$\Delta\rho_i = \frac{\langle \psi_0^\dagger, (\frac{1}{k}\Delta\mathcal{F} - \Delta\mathcal{A})\psi_p \rangle_i}{\langle \psi_0^\dagger, \mathcal{F}_p\psi_p \rangle} \quad (7.6)$$

where $\langle \rangle_i$ signifies an inner product with spatial integration limited to cell i . The reactivity coefficients per cell i were then calculated as follows:

$$\begin{aligned} \text{Doppler effect: } K_{D_i} &= \Delta\rho_{D_i} \frac{1}{\ln\left(\frac{T_p}{T_0}\right)} \\ \text{Na expansion: } \alpha_{\text{Na}_i} &= \frac{\Delta\rho_{\text{Na}_i}}{\Delta\rho_{\text{Na}}} \end{aligned} \quad (7.7)$$

where ρ_{Na} is the sodium density. The Doppler effect was calculated by perturbing fuel temperature from nominal $T_0 = 900$ °C to $T_p = 2000$ °C and the sodium expansion coefficient was obtained by lowering the ρ_{Na} to 1% of its nominal value.

Finally, the resulting coefficients of α_{Na_i} and K_{D_i} were radially reduced to form eight vectors of coefficients in each axial zone, one vector per each derivation c . For an arbitrary set of coefficients α such a vector in derivation c takes a form of

$$\vec{\alpha}_c = [\alpha_{c,z=1}, \alpha_{c,z=2}, \dots, \alpha_{c,z=N_z}] \quad (7.8)$$

Examples of axial distribution of reactivity coefficients can be found in Figures C.2 and C.1 in the Appendix.

7.3 ULOF and UTOP transients in MACARENa

In all studies in MACARENa conducted for this work, three different transient scenarios were simulated:

- ULOF with halving time $t_{1/2} = 10$ s, corresponding to a primary pump stop due to loss of offsite power
- UTOP constant: UTOP with 3\$ reactivity insertion in 0.01 s, staying constant after this point. The scenario corresponds to a simultaneous control rods withdrawal due to rupture of support plate
- UTOP peak: UTOP with reactivity insertion increasing linearly up to 3\$ in the first 0.05 s of the transient, then decreasing back to 0 over next 0.05 s. This scenario corresponds to a transient initiated by the worst case of a gas bubble passing through the core, i.e., complete sodium voiding in a brief period of time

Figure 7.4 presents graphically the principles of initiation for each of the studied scenarios.

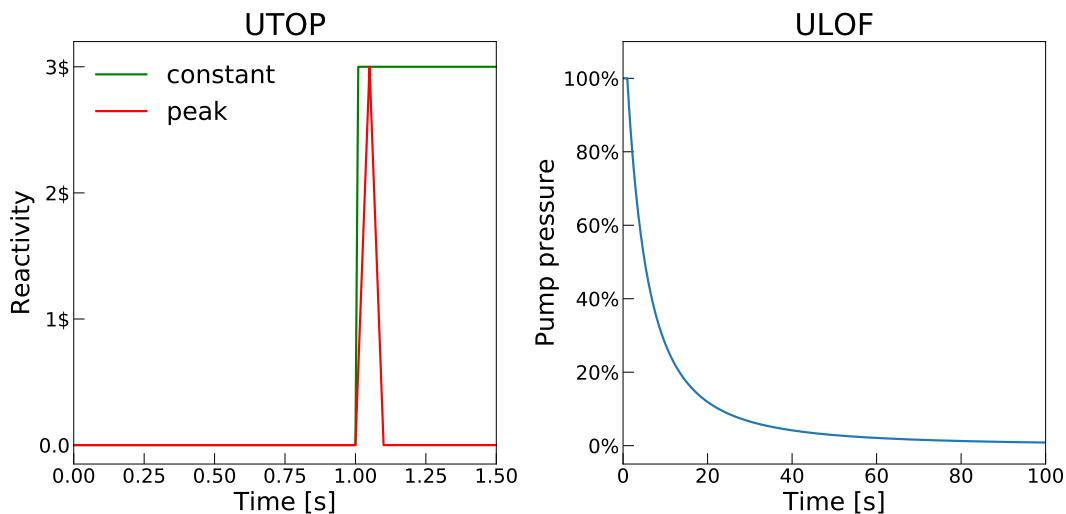


Figure 7.4: Demonstration of principles of the three transient scenarios simulated in MACARENa.

In case of ULOF in MACARENa, the pump pressure drops in time according to relation [102]

$$\Delta p_{\text{pump}}(t) = \frac{\Delta p_{\text{pump}}(t=0)}{\left(1 + \frac{t}{t_{1/2}}\right)^2} \quad (7.9)$$

The pumps reach 10 % of its initial pressure in around 22 s. At low pump pressure the coolant flow is still ongoing due to a natural convection induced by the temperature difference inside the loop, although the flow is much lower than during nominal forced convection (around 15.6 % of nominal mass flow).

7.4 Results of transient simulations

In the study we compared results from identical transient scenarios performed with different sets of reactivity coefficients for Doppler effect and void effect as well as power distribution. Initially, three sets of data were used:

A3 Up coefficients derived from APOLLO3[®] calculation with exact free gas scattering treatment

A3 coefficients derived from APOLLO3[®] calculation without exact treatment, “constant XS” assumption

T4 coefficients derived from A3 Up, but renormalized to the global values of K_D and void effect computed with TRIPOLI-4[®] reference

The differences between magnitude of Doppler effect are presented in Table 7.1

Table 7.1: Values of the Doppler constant K_D (900 °C → 2000 °C) for CADOR with Be moderator, calculated with different methods.

	K_D [pcm]		
	fissile zone	fertile zone	total
A3 Up	−2473	−39	−2512
A3	−2406	−37	−2443
T4 (reference)	−2438 ± 6	−40 ± 6	−2478 ± 6

In each case, the total core power was set to 1500 MW. The initial outlet temperature in each channel was set to be the same by adjusting the pressure drop at the inlets of assemblies, regulated by specific devices.

We begin with a comparison of maximum fuel temperatures during transients. The maximum temperature in this context is defined as an average temperature in the hottest mesh element of fuel material out of all axial meshes in all eight channels. The actual, physical highest temperature, located at the centerline of the fuel pin, would be in fact higher than the values calculated in this chapter. The plots in Figure 7.5 present the evolution of maximum

temperature for all three transient types and three sets of coefficients. A breakdown of reactivity effects throughout the transients can be found in Figure C.3 in the Appendix.

The differences in temperatures caused by different sets of reactivity coefficients were about an order of magnitude lower than the general trend of temperature increase observed during the transients. To make it easier to analyze, the highest fuel temperatures obtained in the study they are shown in Table 7.2.

Table 7.2: Maximum fuel temperatures [°C] during nominal operation and during transients simulated with different neutronic coefficients.

	A3 Up	A3	T4
ULOF			
fuel	937.0	938.3	937.6
sodium	891.4	892.1	891.6
cladding	891.7	892.0	892.0
UTOP constant			
fuel	1617.8	1640.9	1630.0
sodium	780.9	790.0	785.3
cladding	783.8	793.2	788.3
UTOP peak			
fuel	1363.0	1380.2	1371.5
sodium	650.5	654.3	652.3
cladding	655.4	659.4	657.3

Nominal T_{\max} : fuel=824 °C, sodium and clad.=554 °C

The differences between coefficient sets are higher for larger temperature jumps; however, even in case of “UTOP constant” only 22 °C difference between “A3 Up” and “A3” was observed during a temperature jump of around 800 °C (reached in 1 s after transient initiation). In case of ULOF transient, the maximum temperature increased gradually and stabilizes after less than 100 s at a value 110 degrees higher than nominal temperature. During the brief reactivity insertion in “UTOP peak” scenario the maximum temperature raised by around 550 °C in first milliseconds of the transient and comes back to nominal value in roughly 15 s. The highest temperature increase in all scenarios was obtained for “A3” set due to its lowest Doppler feedback. In all cases, the differences between sets were too small to raise safety concerns. For all three transients the margin to fusion was kept at a satisfying level of at least few hundred degrees. This further indicates that the CADOR core can safely withstand fast transients of the highest anticipated magnitudes.

7.4.1 Breakdown of CADOR design features

By modifying the simulation parameters we can demonstrate how the design principles of CADOR contribute to its robust passive protection. Results of such comparison are depicted

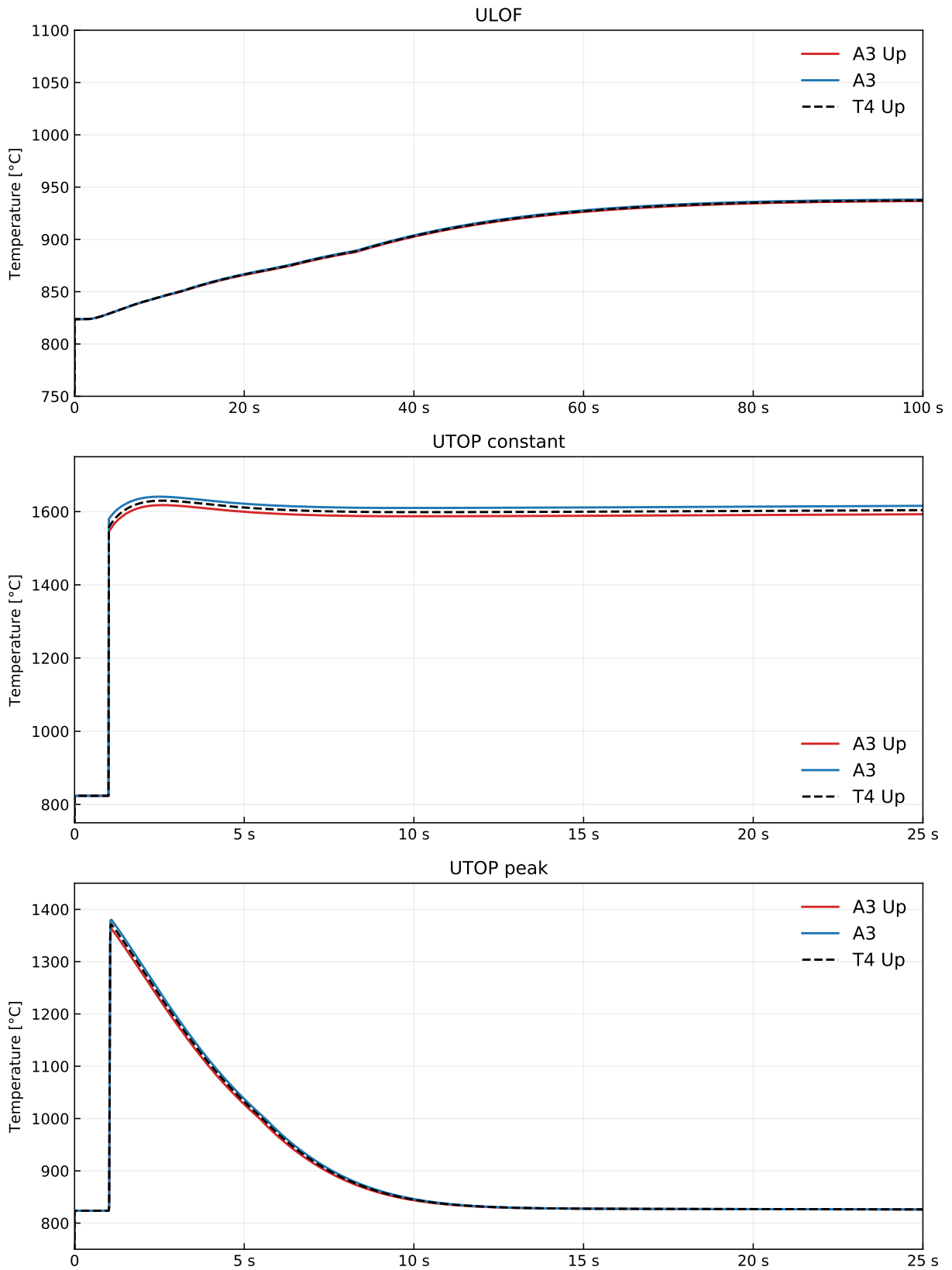


Figure 7.5: Maximum fuel temperatures during three types of transients.

in Figure 7.6 where, alongside “A3 Up” coefficients, a few modified sets were also used. Additional results (evolution of power and sodium flow) can be found in Figures C.6 and C.5 in Appendix C. Two sets of modified coefficients were obtained by increasing the core power by a factor of 1.5 and 2, to get closer to power of a conventional SFR design. Another two sets contained values of sodium expansion reactivity coefficients α_{Na} and K_D switched with values obtained for “no moderator” version of the core used in previous chapters.

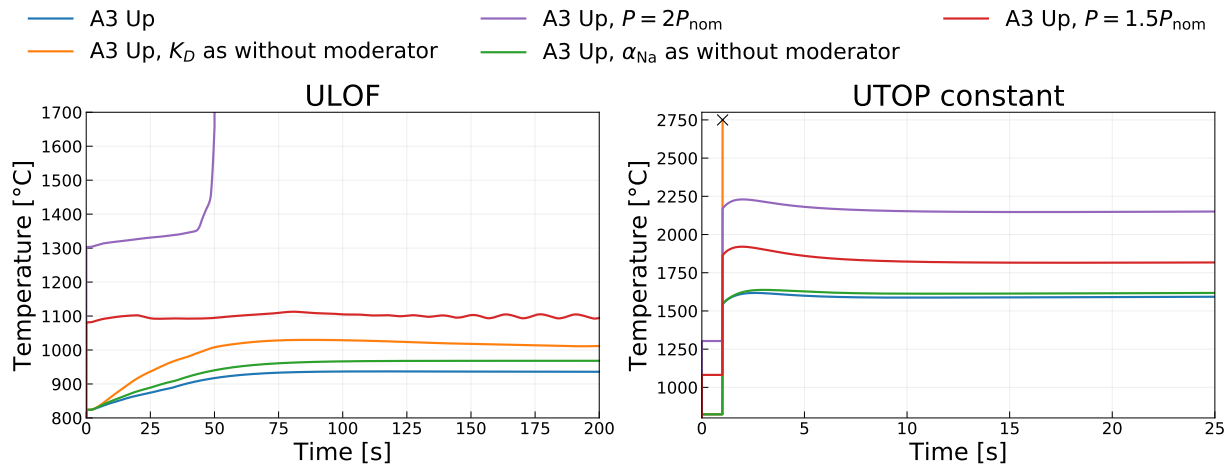


Figure 7.6: Comparison of the evolution of maximum fuel temperatures during two transient scenarios; “breakdown” of the CADOR design principles.

In case of ULOF, the highest fuel temperatures appeared in simulations with increased core power. At the power increased by a factor of 1.5, the boiling crisis took place almost immediately and continued through the duration of the transient causing the maximum temperature to visibly osculate after $t = 130$ s, however, the meltdown did not occur. In case of $P = 2P_{nom}$, the power started to rapidly increase at around $t=40$ s as a result of intense sodium boiling, which led to fuel meltdown shortly after at $t=50$ s. Compared to power increase, the degradation of Doppler constant to a value corresponding to lack of moderator had a lower importance: the boiling did not occur during entire transient and the maximum fuel temperature stabilized at a safe level of 1010 °C, less than 100 °C higher than CADOR with “A3 Up” coefficients. However, in this particular transient scenario, the higher temperature in “ K_D as without moderator” led to sodium boiling in the upper part of the fuel assembly, starting around $t = 90$ s, whereas no boiling was observed at nominal K_D of 2512 pcm (“A3 Up”).

While the increased Doppler effect made a visible improvement when it comes to the progression of the ULOF transient, it is clearly visible that the passive protection of CADOR relied more on lower nominal fuel temperature. This observation demonstrates that in CADOR both the limitation of linear power and the improvement of the Doppler constant are indispensable to provide a robust protection in case of unprotected transients.

In case of “UTOP constant” the temperature jumps at the beginning of transient were similar for all three values of power (from 780 °C for P_{nom} to 920 °C for $2P_{nom}$). The final

fuel temperature was much higher for $1.5P_{\text{nom}}$ and $2P_{\text{nom}}$ mainly as a result of higher initial fuel temperature and reached $1900\text{ }^{\circ}\text{C}$ and $2200\text{ }^{\circ}\text{C}$ respectively. Contrary to ULOF case, the sodium temperature was able to stabilize with no appearance of boiling despite high fuel temperatures, thanks to heat removal from the primary loop. For “ K_D as without moderator” the Doppler effect was too weak to prevent prompt supercriticality. As a result, the fuel meltdown occurred in less than 0.01 s after reactivity insertion. The breakdown for “UTOP peak” transient gave similar conclusions as “UTOP constant”. For both ULOF and UTOP the degradation of α_{Na} played a minor role during the course of transient.

7.4.2 Sensitivity of transient progression to variation of K_D

The sensitivity of transients with respect to the value of Doppler coefficients appears to be rather low: a 1% difference between K_D of “A3 Up” and “A3” results in a temperature peak different by only around $20\text{ }^{\circ}\text{C}$ in the worst case scenario. To further analyze the impact of different values of K_D a new set of calculations was conducted. This time, along with the base value of K_D for “A3 Up”, values of K_D ranging from 50% to 150% of the original value were also used. This way we studied the sensitivity of the system in a more general approach. The evolution of maximum fuel temperature obtained in this study is presented in Figure 7.7. The results are also summarized in the Table 7.3.

During ULOF transient we noticed a relatively low variation in maximum temperature. Even with K_D diminished by 50% the temperature stabilized in a similar time frame at a value higher by only $50\text{ }^{\circ}\text{C}$ compared to the original value of K_D . This further indicates that the magnitude of the Doppler effect is not a major effect in mitigation of loss of flow compared to other effects. By extension, we can conclude that even high uncertainty of K_D would not lead to large uncertainty of the outcome of the transient.

Much stronger differences were observed in simulations of UTOP transients. In all of the cases studied the meltdown did not appear immediately after reactivity insertion, as in “ K_D as without moderator” case from the previous study. For “UTOP constant” at K_D between $50\text{--}70\%$ of original value, the meltdown happened after a few seconds from the beginning of the transient and was preceded by additional reactivity jump caused by sodium boiling. All the other cases in the study did not lead to meltdown nor sodium boiling. Within $\pm 10\%$ of original K_D the maximum temperature during transient changed by around $100\text{ }^{\circ}\text{C}$ in the most sensitive case. The sensitivity was an order of magnitude higher than for ULOF, however, the results still indicate that the safety is ensured.

The uncertainties of nuclear data studied in the previous chapter combined with systematic biases of calculation scheme with “ups” library accumulate to only around 5% uncertainty of K_D . The 5% difference in K_D translate to only about $50\text{ }^{\circ}\text{C}$ difference in maximum fuel temperature in the “UTOP constant” transient. As demonstrated in the previous figures, it is a value significantly lower than what could be considered as a major safety concern.

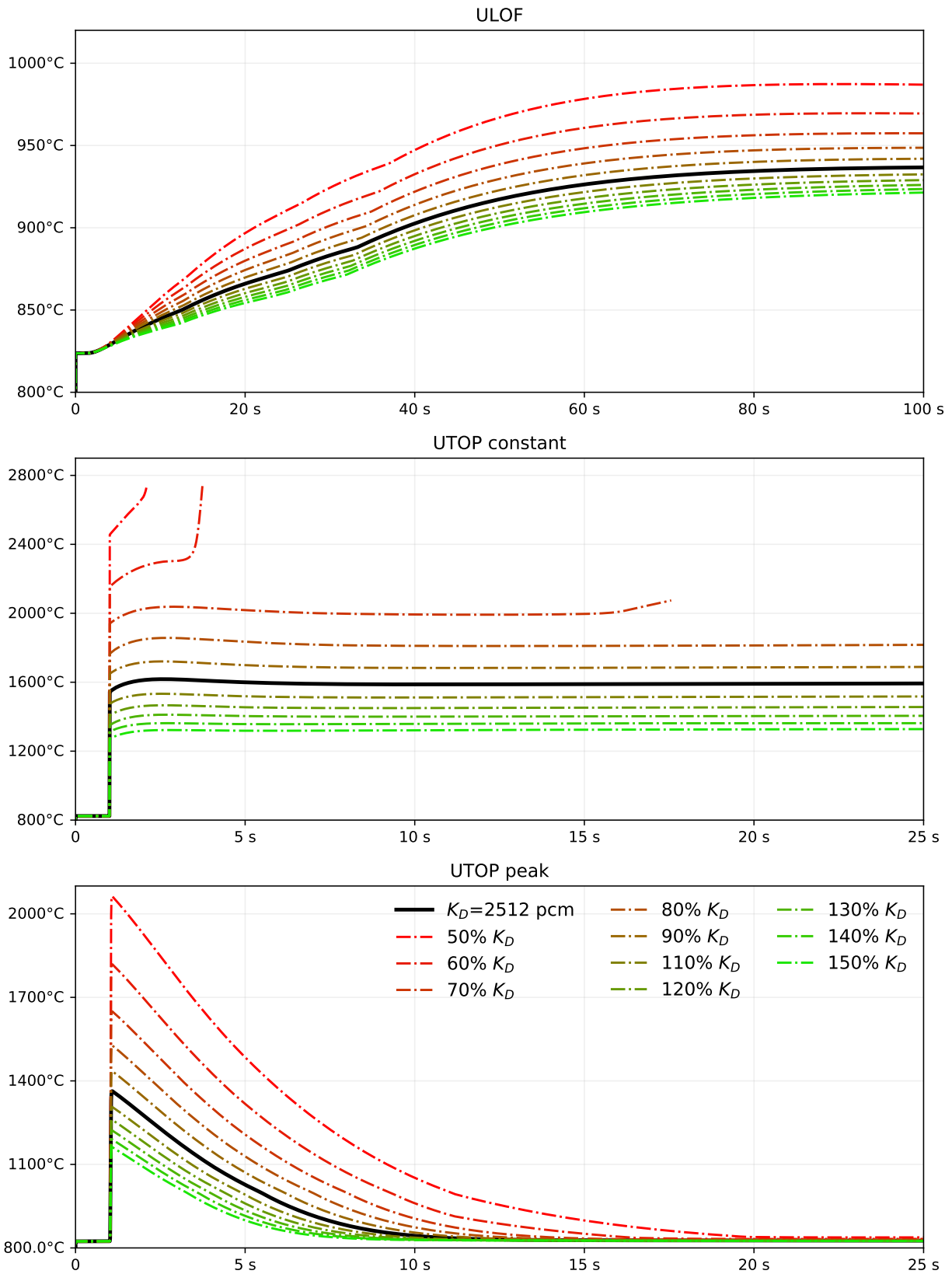


Figure 7.7: Evolution of maximum fuel temperatures during transients for different values of K_D .

Table 7.3: Maximum fuel temperatures that appeared during transient simulations for different values of K_D ; comparison with results obtained with base value of $K_D = 2512$ pcm.

fraction of K_D (A3 Up)	T_{\max} [°C]	ΔT [°C]	$\Delta T/\Delta K_D$ [°C/pcm]
ULOF			
50 %	987.3	50.3	-1.01
70 %	957.4	20.4	-0.68
90 %	942.0	5.0	-0.50
110 %	933.0	-4.0	-0.40
130 %	927.3	-9.7	-0.32
150 %	923.6	-13.4	-0.27
UTOP constant			
50 %	$> T_{\text{fusion}}$	-	-
70 %	$> T_{\text{fusion}}$	-	-
90 %	1720.8	103	-10.30
110 %	1533	-84.8	-8.48
130 %	1415.5	-202.3	-6.74
150 %	1336.4	-281.4	-5.63
UTOP peak			
50 %	2062.9	699.9	-14.00
70 %	1649.3	286.3	-9.54
90 %	1434.5	71.5	-7.15
110 %	1306.1	-56.9	-5.69
130 %	1221.6	-141.4	-4.71
150 %	1162.0	-201.0	-4.02

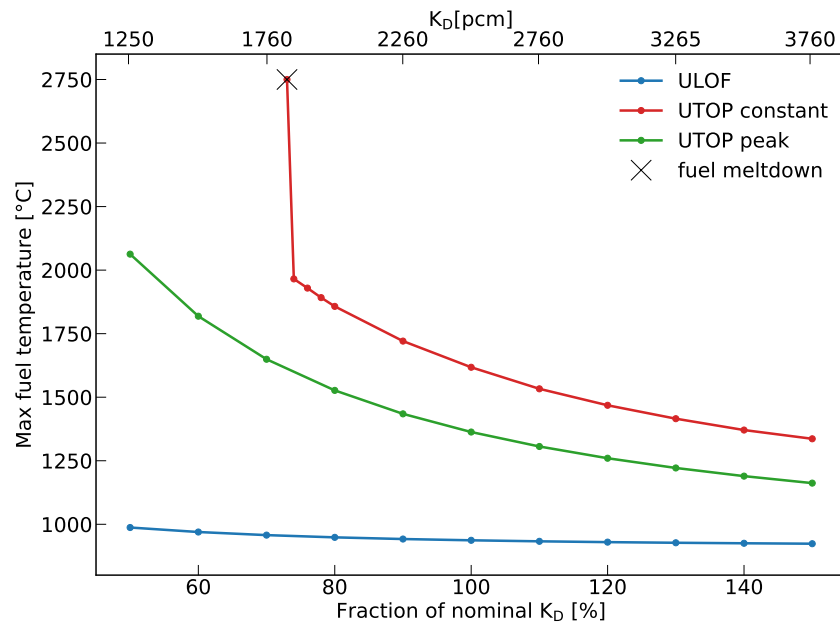


Figure 7.8: Maximum fuel temperature attained during transients for different values of K_D .

7.5 Remarks and conclusions

The approach used in this chapter was simplified in many ways. First, the reactivity coefficients were calculated with Beginning Of Life (BOL) core loaded only with fresh fuel. In an actual equilibrium cycle, where fresh fuel constitutes a minority of total fuel volume, the properties of core can differ significantly. The values of K_D and reactivity effect of total sodium voiding at the End of Cycle (EOC) were evaluated in internal studies to be 1968 pcm (around 22% lower than in this study) and 4.8\$ (78% higher), respectively. Moreover, the fuel melting point decreases with burnup and can drop to about 2600 °C at the most unfavorable conditions at the EOC, compared to 2750 °C for the fresh fuel used in this work. The study was limited to two types reactivity feedback, omitting five other types typically taken into account in such simulations: axial fuel expansion, axial and radial expansions of structure materials, expansion of the core support and core/control rod/vessel differential expansions.

For the reasons listed above, the results of this study should not be treated as a state-of-the-art analysis of physical phenomena during transient. The main purpose was to explore general trends and to give an estimation of how much the accuracy of neutron transport calculations can influence the accuracy of transient simulations. The data presented suggest with reasonable confidence, that the uncertainty related to reactivity coefficients calculated with APOLLO3[®] has a negligible impact on the progression of UTOP and ULOF transients. Even in the case of “UTOP constant”, the transient scenario with the strongest impact, the differences in maximum fuel temperatures between “A3” and “A3 Up” was only 22 °C.

The reactivity coefficients and the point-kinetics model that uses them are only a very small element of the entirety of equations solved by MACARENa. Therefore, the impact of varia-

tion in K_D between different calculations schemes in APOLLO3[®] was found to be relatively low from the point of view of MACARENa. As a general conclusion, the results show both the robustness of the passive safety approach of the CADOR design as well as robustness of the calculation scheme of APOLLO3[®] in the scope of multiphysics transient simulations.

An important category of transients, UTOP caused by a localized reactivity insertion, e.g., withdrawal of a single control rod cluster, was not included in the study. The scenario would require treatment of local reactivity changes, a feature that was not available in MACARENa at the time of this study.

Chapter 8

Conclusions

The goal of this thesis was to establish an accurate and efficient neutron transport deterministic calculation scheme applied to cores with softened fast spectrum. In particular, the motivation behind the thesis was the development of the CADOR core. The procedure included validation of a standard two-step calculation scheme used for fast reactor analysis in APOLLO3[®], with several proposals of improvements that can be considered as a best-estimate calculation scheme for this kind of moderated SFR. Moreover, in addition to quantification of epistemic biases related to models used in calculations, we were able to perform a sensitivity analysis to quantify the statistical uncertainties that derive from the nuclear data used. Finally, the calculation scheme was used to provide neutronic data for thermo-hydraulics code MACARENa in a one-way coupling. This last study allowed us to show that the biases identified in APOLLO3[®] calculations do not affect significantly the outcome of MACARENa transient simulations in case of UTOP and ULOF. The study can be also regarded as a first attempt to propagate the uncertainties of neutron transport calculations to multiphysics calculations.

8.1 Impact of moderation on the neutron physics

Our study began with identification of possible key points in which moderated SFR core differs from more conventional SFR designs in terms of neutron physics. The differences identified can be roughly divided into three distinct features and potential problems related to them.

First, the average neutron energy was significantly decreased and the fraction of neutrons in the resonance energy range was increased on the expense of neutrons in fast energy region. While this outcome is an intended choice, crucial for the CADOR reactor, it could have an impact on the performance of calculation scheme. As the slower neutrons are generally more likely to interact with the environment, the mean free path in both CADOR assemblies moderated by Be and ZrH₂ was shortened by approximately 7%. A natural implication of this fact is that the mesh size should be adapted by lowering its size. Different energy distribution of neutrons also puts into question the validity of standard energy mesh with group sizes

chosen to best accommodate a neutron energy distribution of standard fast reactors.

The second factor is the joint distribution of neutrons in space and energy. Because of the design choice made regarding the moderator placement, the effect of their presence is strongly localized, especially in case of a scarce lattice of ZrH_2 pins. Uneven spatial distribution of average neutron energy leads to uneven reaction rate in the assembly volume. We were able to show that the fuel zones in the direct vicinity of moderator experienced higher reaction rate — both fission and neutron capture. There are two primary problems related to that phenomenon. The locally increased fission rate implies formation of power peaks during reactor operation. After division of each fuel pin into 36 segments, the maximum power (fission rate) deviation from global average in any segment was found to be almost 3% for Be moderator and more than 10% for ZrH_2 moderator. Another important conclusion is that this localized effect is much less visible if the calculation is performed in accordance with conventional fast reactor approach where each fuel pellet is represented as a single cylindrical region without additional refinement.

The lowered average neutron energy has an additional consequence. As the average neutron speed decreases the scattering reactions at energies close to thermal equilibrium become more frequent. We demonstrated that in case of CADOR core the number of neutrons at energies of few to few hundred eV is large enough to call for improved scattering models. The impact of standard fast reactor approach, i.e., free gas model used only with assumption of constant scattering cross-section with respect to relative velocity, is particularly visible for higher fuel temperatures. CADOR core differs from thermal reactors where the impact of "constant XS" assumption is pronounced even at nominal temperature. The results obtained in TRIPOLI-4[®] show that for fuel temperature of 2000 °C the difference between exact scattering kernel (DBRC model) and the kernel that assumes constant cross-section (SVT model) reaches around 50 pcm and as much as 150 pcm in case of ZrH_2 . This deviation is primarily caused by resonance upscattering phenomenon, impossible to take into account correctly under the "constant XS" assumption. The effect is strongly related to the amount of plutonium in the fuel assembly. Lower Pu enrichment is linked to higher ²³⁸U content but also allows neutrons to reach the lower energies more frequently, thus increasing the importance of scatterings at these energies. Most importantly the choice of scattering kernel has a profound impact on the calculated value of Doppler effect. The value of Doppler constant based on flux calculations at 900 °C and 2000 °C suffers from a bias of around 2.2% and 6% for Be and ZrH_2 respectively, if the SVT model is used in place of DBRC. On the other hand the effect remains completely negligible if the moderator is not present in the core. In conclusion we demonstrated that the exact free gas kernel should be used when performing neutron transport calculation of fast reactor with moderating materials, particularly if the high fuel temperature is used.

8.2 Evaluation of the deterministic calculation scheme applied to moderated SFR

The calculation scheme in contemporary deterministic codes such as APOLLO3[®] is separated into two steps — the lattice calculation and the core calculations. Our evaluation

started at the lattice calculation of a 2D model of a single fuel assembly with reflective boundary conditions. We have shown that in terms of reactivity the agreement between APOLLO3[®] and the reference code TRIPOLI-4[®] was only slightly worse for moderated CADOR assemblies in comparison with assembly without moderator. The discrepancies at nominal fuel temperatures did not exceed 60 pcm for any assembly type used in the study. The APOLLO3[®]/TRIPOLI-4[®] discrepancy was higher for near-accidental fuel temperature and exceeded 100 pcm for inner core assembly with Be. The discrepancies were also generally higher for inner core assemblies, i.e., the ones with lower Pu enrichment and lower average neutron energy. According to our study, the difference between P1 and P3 Legendre expansion and Tone's and Sub-group self-shielding methods were small.

When compared to previous-generation transport code ECCO, the results of APOLLO3[®] appear to be much more consistent with TRIPOLI-4[®]. Bias on reactivity in case of ECCO calculations was especially high in case of moderated assemblies and in the worst case reached 900 pcm. The code seems to be unable to properly model the heterogeneous assembly design (two types of pins) due to two-step collision probability solver relying on assumptions about neutron current between cells. However, the differences between the codes were similar when estimating differential effects of Doppler feedback and voiding.

Applying the refined spatial mesh to better account for spatial self-shielding did not result in consistent improvement of the results. The differences for all cases did not exceed 30 pcm and in some cases the refinement lead to worse agreement with TRIPOLI-4[®].

A cell-by-cell analysis of reaction rates revealed higher APOLLO3[®]/TRIPOLI-4[®] discrepancies at the rim of fuel pins, most pronounced if the pin was neighboring moderator pin or was placed near the hexagonal wrapper tube. The highest relative difference in local absorption rate found was 2.4 % for Be moderator, 3.4 % for ZrH₂ moderator but only about 1.1 % in case of lack of moderator.

Motivated by our findings about accuracy of scattering models in TRIPOLI-4[®], we decided to improve the APOLLO3[®] calculation scheme by using a multigroup nuclear data library of 1760 group that was pre-processed to take into account the exact scattering kernel. When compared to TRIPOLI-4[®], the impact of exact kernel is slightly underestimated by APOLLO3[®], however the general trend in both codes was similar.

The bias on reactivity of the entire calculation scheme (lattice and core calculation) was found to be around 450-500 pcm in case of moderated cores and 350 pcm for standard core without additional moderation. Using higher anisotropy orders (P3) or flux moments homogenization were found to be a poor method of diminishing the bias. The differences between these options are not high and do not always lead to improvement at all. Despite higher bias associated with moderated cores, the recommended MINARET solver options were found to be the same for all three core types. 10 cm radial mesh size (12 triangles per assembly), 5 cm axial mesh size and S_n order 4 (36 directions) allowed for sufficient convergence.

The reactivity difference between the two scattering treatments was found to be almost at the same order as the one evaluated for a single assembly. The impact of exact scattering treatment on the magnitude of Doppler effect was 3.5 % and 5.2 % for Be and ZrH₂ moderators respectively (results of TRIPOLI-4[®]).

To find the source of the global bias of the calculation scheme we used a hybrid deterministic-Monte Carlo calculations, where APOLLO3[®] scheme was used until core calculation and the core calculations were performed by TRIPOLI-4[®]. By using this method we were able to conduct a deeper investigation at the homogenization/condensation process and test semi-heterogeneous approaches to homogenization that would be unfeasible to perform in MINARET solver. The results of such calculations show that the bias can be visibly reduced by preserving partial heterogeneity of fuel assemblies, essentially reaching similar deviation from TRIPOLI-4[®] reference calculation for moderated CADOR cores as for SFR core without moderator. We also show that the effect of condensation from 1760 to 33 energy groups is more visible in case of lack of moderator. Because of the number of finite elements required, the use of 3D core geometry with partially-heterogeneous assemblies is not feasible to be performed in MINARET. It can be however implemented to calculate a 2D "flat" core model that could be used as a reference for validation studies in the future.

Despite higher bias evaluated for moderated CADOR cores, the original calculation scheme of APOLLO3[®] was proven to be a robust tool, that requires only several small changes to become well adapted to significantly different operating conditions of CADOR core.

8.3 Uncertainties of nuclear data

To evaluate the uncertainty of nuclear data, a series of perturbation calculations was performed in APOLLO3[®] to determine the sensitivity coefficients. The uncertainty related to multiplication factor was found to be around 900 pcm regardless of the core version used. The uncertainties related to values of reactivity feedbacks, control rod worth and power ratio were also of a similar order of magnitude for all three cores. The only outlying value found was the uncertainty of void effect of more than 10%. This high uncertainty is caused by large difference of sensitivity between voided and nominal conditions for ²³⁹Pu isotope, for both capture and fission cross-section.

The statistical uncertainty originating from nuclear data is almost two times higher than the sum of epistemic bias of models used in the calculations scheme. The worse performance of the calculation scheme for the case of moderated cores is therefore partially overshadowed by much higher uncertainty of nuclear data. Unless the statistical bias is lowered, e.g., by assimilation of representative experimental data, the nuclear data remain the largest source of uncertainty identified.

8.4 Coupling with MACARENa code

The one-way coupling with MACARENa was used to investigate the sensitivity of transient progression to the value of Doppler constant calculated in APOLLO3[®]. The first goal was to compare ULOF and UTOP transients simulated with values of Doppler constant calculated with both exact and simplified scattering treatment. The relative difference between Doppler constant of a few percent was too low to have a non-negligible impact on the evolution of simulated transients. The maximum fuel temperature differed by only 20 °C in the worst case studied.

By performing a series of transient simulations for different values of Doppler constant we were able to estimate the sensitivity of the transient outcome on the Doppler constant. Even for K_D 10% lower than the APOLLO3[®] estimation, the progression of transient is very similar to the one obtained previously. Such lowering of the value of K_D can result in temperature jump during UTOP transient about 100 degrees higher, leaving the margin to meltdown still at around 1000 °C. Because the postulated 10% decrease of K_D is already larger than the combined uncertainty of the calculation scheme and the nuclear data, we can conclude that the accuracy of the Doppler effect is sufficient to be used in multiphysics transient simulations without risk of misrepresenting the core behavior in a way that would pose a safety concerns.

8.5 Future prospects

While the studies performed in this work were intended to highlight potential issues related to moderated fast reactors to establish a best-estimate neutron transport calculations scheme, it is inevitable that for some reactor concepts the conclusions included in this thesis may turn out to be at least partially false. Our work was limited to the use of only two different moderator types and only one way of including them in the core. There exist other ideas potentially worth investigating such as using dedicated moderator assemblies, doping already existing assembly elements with moderator or using moderator blankets placed in the fissile zone. All these solution were already proposed in several internal studies in CEA, however, the question of performance of neutron transport codes for such designs was not addressed in this thesis. The demonstrated robustness of the calculation scheme created in APOLLO3[®] suggests that the such different configurations should not have a major impact on the accuracy of neutron transport calculations performed with this scheme. It is however always of interest to try to expand the studies performed in this thesis to other design solutions in this category. Such additional studies, even in much more limited scope than in this thesis, could help to strengthen and generalize the conclusions of this thesis.

Another concept not mentioned in this work is a Small Modular Reactor (SMR) version of CADOR core, that is an active research subject within the project. From the point of view of validation of the calculation scheme, the smaller size of the core could on one hand highlight the importance of accurate modeling of the core-reflector boundary, and on the other hand could be used to evaluate some calculation approaches that are too expensive to be performed on a 1500 MW core used in this thesis, such as heterogeneous core calculations.

A topic not covered in the thesis is addition of the Super-Homogenization (SPH) equivalence [40] to the calculation scheme. The SPH is not a routine part of the fast reactor calculation schemes in APOLLO3[®]. However, it has been suggested that including the equivalence calculation to the homogenization/condensation procedure might solve some of the accuracy issues encountered, namely the cluster calculations and core calculations with semi-heterogeneous assemblies.

Lastly, the thesis contains no comparison with experimental data, that is typically an important part of the VVUQ process. Unfortunately, there exists only a rather limited amount of experiments that could provide data interesting from the point of view of the thesis. A

potential source of data can be provided by the measurements of Doppler effect conducted in SEFOR sodium-cooled fast experimental reactor in Arkansas, USA [81]. In particular, it is of interest to re-evaluate the results of experiments performed in SEFOR Core I which used an assembly made of six fuel pins tightened by a central pin made of BeO. However, despite the presence of moderator, the neutron spectrum of SEFOR Core I is quite far from the spectrum of CADOR due to extremely high ^{239}Pu enrichment; according to [105] the spectrum in Core I is in fact harder than in ASTRID core. Other examples of experiments combining moderation and fast neutron spectrum are ECRIX-B, ECRIX-H and DAC conducted in Phénix reactor [106] or COSMO experiment conducted in Masurca reactor [107].

Bibliography

- [1] International Energy Agency (IAEA) <https://www.iaea.org/data-and-statistics>. accessed 7 April 2020.
- [2] Power Reactor Information System (PRIS) <https://pris.iaea.org/pris/access07/04/2020>. accessed 7 April 2020.
- [3] World Nuclear Association, “Comparison of lifecycle greenhouse gas emissions of various electricity generation sources,” report, WNA, 2011.
- [4] M. Mirabile and J. Calder, “Clean power for a cool planet: Electricity infrastructure plans and the paris agreement – environment working paper no. 140,” OECD working paper, World Nuclear Association, November 2018.
- [5] IEA, “Nuclear power in a clean energy system,” tech. rep., IEA, Paris, 2010.
- [6] *Safety of Nuclear Power Plants: Design*. No. SSR-2/1 (Rev. 1) in Specific Safety Requirements, IAEA, 2016.
- [7] I. Charnley-Parry, J. Whitton, P. Cools, and A. Bergmans, “Integrated comparative report for in-depth understanding of the mechanisms for effective interaction with civil society, deliverable d.4.4. of history of nuclear energy and society,” report, Euratom, 2018.
- [8] *The Use of Scientific and Technical Results from Underground Research Laboratory Investigations for the Geological Disposal of Radioactive Waste*. No. 1243 in TECDOC Series, IAEA, 2001.
- [9] IRSN, “International panorama of research on alternatives to geological disposal of high-level waste and long-lived intermediate-level waste,” report/2019-00318, IRSN, 2019.
- [10] Nuclear Energy Agency, “Uranium 2018, resources, production and demand,” tech. rep., OECD, 2018.
- [11] Generation IV International Forum - official website <https://www.gen-4.org/>. accessed 7 April 2020.
- [12] Gen IV International Forum, “Technology roadmap update for Generation IV nuclear energy systems,” tech. rep., OECD Nuclear Energy Agency, January 2014.

- [13] A. E. Waltar and A. B. Reynolds, *Fast Breeder Reactors*. Pergamon Press, 1981.
- [14] A. E. Waltar, D. R. Todd, and P. V. Tsvetkov, *Fast Spectrum Reactors*. Springer US, 2012.
- [15] M. Salvatores, I. Slessarev, and M. Uematsu, “A global physics approach to transmutation of radioactive nuclei,” *Nuclear Science and Engineering*, vol. 116, no. 1, pp. 1–18, 1994.
- [16] Commissariat à l’énergie atomique et aux énergies alternatives, *Sodium-Cooled Nuclear Reactors*. CEA Saclay and Group Moniteur, 2016.
- [17] J.-F. Sauvage, *Phénix: 30 years of history: the heart of a reactor*. CEA and EDF, 2004.
- [18] AREVA NP and EFR SA, “Fundamental safety overview, volume 1: Head document, chapter A: EPR design description,” tech. rep., 2007.
- [19] V. Sobolev, “Database of thermophysical properties of liquid metal coolants for Gen-IV,” tech. rep., SCK-CEN, 2010.
- [20] J. Bussac and P. Reuss, *Traité de neutronique*. Hermann, 2nd ed., 1985.
- [21] AREVA NP and EFR SA, “The pre-construction safety report (PCSR) for UK EPR,” tech. rep., October 2012.
- [22] L. Buiron and L. DUJCIKOVA, “Low void effect (CFV) core concept flexibility: from self-breeder to burner core,” in *Proceedings of ICAPP 2015*, May 3-6 2015.
- [23] A. Zaetta *et al.*, “CADOR ”Core with Adding DOppleR effect” concept application to sodium fast reactors,” *EPJ Nuclear Sci. Technol.*, vol. 5, p. 1, 2019.
- [24] H. H. Hummel and D. Okrent, *Reactivity Coefficients in Large Fast Reactors*. American Nuclear Society, 1970.
- [25] *Status and Trends of Nuclear Fuels Technology for Sodium Cooled Fast Reactors*. No. NF-T-4.1 in Nuclear Energy Series, IAEA, 2011.
- [26] M. Adamson, E. Aitken, and R. Caputi, “Experimental and thermodynamic evaluation of the melting behavior of irradiated oxide fuels,” *Journal of Nuclear Materials*, vol. 130, pp. 349 – 365, 1985.
- [27] Schneider *et al.*, “APOLLO3[®]: CEA/DEN deterministic multi-purpose code for reactor physics analysis,” in *Proceedings of PHYSOR 2016, Unifying Theory and Experiments in the 21st Century*, May 1–5 2016.
- [28] R. Sanchez *et al.*, “APOLLO2 year 2010,” *Nuclear Engineering and Technology*, vol. 42, 10 2010.
- [29] J. Lautard, S. Loubiere, and C. Magnaud, “CRONOS, a modular computational system for neutronic core calculations,” in *IAEA Specialists Meeting on advanced calculational methods for power reactors*, 10-14 September 1990.

- [30] G. Rimpault *et al.*, “The ERANOS code and data system for fast reactor neutronic analyses,” in *Proceedings of PHYSOR 2002: International Conference on the New Frontiers of Nuclear Technology: Reactor Physics, Safety and High-Performance Computing*, October 7-10 2002.
- [31] ASN, “Qualification des outils de calcul scientifique utilisés dans la démonstration de sûreté nucléaire – 1re barrière,” guide no. 28, ASN, 2017.
- [32] G. Rimpault *et al.*, “The APOLLO3 scientific tool for SFR neutronic characterization current achievements and perspectives,” in *International conference on fast reactors and related fuel cycles: next generation nuclear systems for sustainable development (FR17)*, (Ekaterinaburg, Russia), IAEA, June 2017.
- [33] J. Duderstadt and L. Hamilton, *Nuclear Reactor Analysis*. John Wiley & Sons, Inc., 1976.
- [34] D. G. Cacuci, ed., *Handbook of Nuclear Engineering Vol. 1: Nuclear Engineering Fundamentals*. Springer US, 2010.
- [35] L. B. Levitt, “The probability table method for treating unresolved neutron resonances in Monte Carlo calculations,” *Nuclear Science and Engineering*, vol. 49, no. 4, pp. 450–457, 1972.
- [36] R. E. McFarlane and D. W. Muir, *The NJOY Nuclear Data Processing System Version 91*. Los Alamos National Laboratory, 1994.
- [37] JEFF-3.3 nuclear data library, accessed at <https://www.oecd-nea.org/janis/>.
- [38] Commissariat à l’énergie atomique et aux énergies alternatives, *Neutronics*. CEA Saclay and Group Moniteur, 2015.
- [39] C. Dean, C. Eaton, P. Ribon, and G. Rimpault, “Production of fine group data for the ECCO code,” in *International Conference on the Physics of Reactors: Operation, Design and Computation*, April 23-27 1990.
- [40] A. Hébert, *Applied Reactor Physics*. Presses Internationales Polytechnique, 2009.
- [41] P. Reuss, *Neutron Physics*. EDP Sciences, 2008.
- [42] G. I. Marchuk and V. I. Lebedev, *Numerical methods in the theory of neutron transport*. OPA (Amsterdam) B.V., 2nd ed., 1986.
- [43] R. Sanchez, “A transport multicell method for two-dimensional lattices of hexagonal cells,” *Nuclear Science and Engineering*, vol. 92, no. 2, pp. 247–254, 1986.
- [44] J. Askew, “A characteristics formulation of the neutron transport equation in complicated geometries,” report, United Kingdom Atomic Energy Authority, 1972.
- [45] F. Févotte, S. Santandrea, and R. Sanchez, “Tracking on periodic lattices for the method of characteristics,” in *Proceedings of International Conference on the Physics of Reactors 2008, PHYSOR’08*, September 14-19 2008.

- [46] D. Sciannandrone, *Acceleration and higher order schemes of a characteristic solver for the solution of the neutron transport equation in 3D axial geometries*. PhD thesis, Université Paris-Sud, September 2015.
- [47] W. H. Reed and T. R. Hill, “Triangular mesh methods for the neutron transport equation,” in *National topical meeting on mathematical models and computational techniques for analysis of nuclear systems*, April 8 1973.
- [48] N. Odry, *Méthode de décomposition de domaine avec parallélisme hybride et accélération non linéaire pour la résolution de l'équation du transport S_n en géométrie non-structurée*. PhD thesis, Aix-Marseille Université, October 2016.
- [49] J.-J. Lautard and J.-Y. Moller, “MINARET, a deterministic neutron transport solver for nuclear core calculations,” in *Proceedings of the International Conference on Mathematics and Computational Methods Applied to Nuclear Science and Engineering (M&C 2011)*, May 8-12 2011.
- [50] G. Rimpault *et al.*, “Validation of new sub-group algorithms for resonance self shielding in heterogeneous structures,” in *Proceedings of the Seminar on NJOY and THEMIS*, June 20-21 1989.
- [51] L. Mao, I. Zmijarevic, and R. Sanchez, “Resonance self-shielding methods for fast reactor calculations—comparison of a new Tone’s method with the Subgroup method in APOLLO3[®],” *Nuclear Science and Engineering*, vol. 188, no. 1, pp. 15–32, 2017.
- [52] T. Tone, “A numerical study of heterogeneity effects in fast reactor critical assemblies,” *Journal of Nuclear Science and Technology*, vol. 12, no. 8, pp. 467–481, 1975.
- [53] L. Mao and I. Zmijarevic, “A new tone’s method in APOLLO3[®] and its application to fast and thermal reactor calculations,” *Nuclear Engineering and Technology*, vol. 49, no. 6, pp. 1269 – 1286, 2017. Special Issue on International Conference on Mathematics and Computational Methods Applied to Nuclear Science and Engineering 2017 (M&C 2017).
- [54] F. Jeanpierre and M. Livolant, “Autoprotection des résonances dans les réacteurs nucléaires ; application aux isotopes lourds,” Report R-4533, CEA, 1974.
- [55] P. Ribon and J.-M. Maillard, “Les tables de probabilités. application au traitement des sections efficaces pour la neutronique,” Technical Report N-2485, CEA, 1986.
- [56] M. Coste-Delclaux, “GALILEE: A nuclear data processing system for transport, depletion and shielding codes,” in *Proceedings of PHYSOR 2008: Nuclear Power: A Sustainable Resource*, September 14-19 2008.
- [57] J.-F. Vidal *et al.*, “An improved energy-collapsing method for core-reflector modelization in sfr core calculations using the PARIS platform,” in *Proceedings of International Conference on the Physics of Reactors 2012, PHYSOR 2012: Advances in Reactor Physics*, April 15-20 2012.
- [58] I. Petrovic and P. Benoist, *B_N Theory: Advances and New Models for Neutron Leakage Calculation*, pp. 223–282. Springer US, 1997.

- [59] A. Plompen *et al.*, “The joint evaluated fission and fusion nuclear data library, JEFF-3.3,” *The European Physical Journal A*, vol. 56, no. 7, p. 181, 2020.
- [60] D. Brown *et al.*, “ENDF/B-VIII.0: The 8th major release of the nuclear reaction data library with CIELO-project cross sections, new standards and thermal scattering data,” *Nuclear Data Sheets*, vol. 148, pp. 1 – 142, 2018. Special Issue on Nuclear Reaction Data.
- [61] K. Shibata *et al.*, “JENDL-4.0: A new library for nuclear science and engineering,” *Journal of Nuclear Science and Technology*, vol. 48, no. 1, pp. 1–30, 2011.
- [62] N. Metropolis and S. Ulam, “The Monte Carlo method,” *Journal of the American Statistical Association*, vol. 44, no. 247, pp. 335–341, 1949.
- [63] S. A. Dupree and S. K. Fraley, *A Monte Carlo Primer: A Practical Approach to Radiation Transport*. Springer US, 2002.
- [64] I. Lux and L. Koblinger, *Monte Carlo Particle Transport Methods: Neutron and Photon Calculations*. CRC Press, 1991.
- [65] W. E. Lamb Jr., “Capture of neutrons by atoms in a crystal,” *Physical Review*, vol. 55, pp. 190 – 197, 1939.
- [66] G. Bell and S. Glasstone, *Nuclear Reactor Theory*. Litton Educational Publishing, Inc., 1970.
- [67] D. E. Cullen and C. R. Weisbin, “Exact Doppler broadening of tabulated cross sections,” *Nuclear Science and Engineering*, vol. 60, no. 3, pp. 199–229, 1976.
- [68] W. R. Martin, S. Wilderman, F. B. Brown, and G. Yesilyurt, “Implementation of on-the-fly Doppler broadening in MCNP,” in *Proceedings of International Conference on Mathematics and Computational Methods Applied to Nuclear Science and Engineering M&C 2013*, May 5-9 2013.
- [69] E. Brun, S. Chauveau, and F. Malvagi, “PATMOS: A prototype Monte Carlo transport code to test high performance architectures,” in *Proceedings of International Conference on Mathematics & Computational Methods Applied to Nuclear Science & Engineering M&C 2017*, April 16-20 2017.
- [70] C. Mounier and P. Mosca, “Resonant upscattering effects on ^{238}U absorption rates,” in *Proceedings of International Conference on Physics of Reactors PHYSOR 2014*, (Kyoto, Japan), Sept. 2014.
- [71] E. Wigner and J. Wilkins, “Effect of the temperature of the moderator on the velocity distribution of neutrons with numerical calculations for H as moderator,” technical report AECD-2275, IEA, Oak Ridge National Laboratory, Oak Ridge, TN, USA, September 1944.
- [72] M. Ouisloumen and R. Sanchez, “A model for neutron scattering off heavy isotopes that accounts for thermal agitation effects,” *Nuclear Science and Engineering*, vol. 107, no. 3, pp. 189–200, 1991.

- [73] D. Lee, K. Smith, and J. Rhodes, “The impact of ^{238}U resonance elastic scattering approximations on thermal reactor Doppler reactivity,” in *Proceedings of International Conference on the Physics of Reactors 2008, PHYSOR’08*, September 14-19 2008.
- [74] B. Becker, R. Dagan, and G. Lohnert, “Proof and implementation of the stochastic formula for ideal gas, energy dependent scattering kernel,” *Annals of Nuclear Energy*, vol. 36, no. 4, pp. 470 – 474, 2009.
- [75] R. Sanchez, C. Hewko, and S. Santandrea, “Numerical computation of Doppler-broadening in the resonance domain,” in *Proceedings of International Conference on Mathematics and Computational Methods Applied to Nuclear Science and Engineering M&C 2013*, May 5-9 2013.
- [76] *TRIPOLI-4 Version 10 user manual*, February 2017.
- [77] W. Rothenstein, “Effects of up scattering by heavy nuclides on Doppler changes of resonance adsorption,” in *International Conference on Reactor Physics and Reactor Computations*, January 23-26 1994.
- [78] T. Mori and Y. Nagaya, “Comparison of resonance elastic scattering models newly implemented in MVP continuous-energy monte carlo code,” *Journal of Nuclear Science and Technology*, vol. 46, pp. 793–798, 08 2009.
- [79] A. Zoia, E. Brun, C. Jouanne, and F. Malvagi, “Doppler broadening of neutron elastic scattering kernel in TRIPOLI-4[®],” *Annals of Nuclear Energy*, vol. 54, pp. 218 – 226, 2013.
- [80] L. Buiron *et al.*, “Innovative core design for Generation IV sodium-cooled fast reactors,” in *Proceedings of International congress on advances in nuclear power plants - ICAPP 2007*, (Nice, France), May 13-18 2007.
- [81] R. Meyer *et al.*, “Design and analysis of SEFOR Core 1,” AEC R&D report, General Electric Company, 1970.
- [82] H. S. Bailey and Y. S. Lu, “Nuclear performance of liquid-metal fast breeder reactors designed to preclude energetic hypothetical core disruptive accidents,” *Nuclear Technology*, vol. 44, no. 1, pp. 76–82, 1979.
- [83] A. G. Osborne and M. R. Deinert, “Reducing irradiation damage in a long-life fast reactor with spectral softening,” *Energies*, vol. 11, no. 6, p. 1507, 2018.
- [84] B. Merk and F.-P. Weiß, “Analysis of the influence of different arrangements for ZrH moderator material on the performance of a SFR core,” *Annals of Nuclear Energy*, vol. 38, no. 11, pp. 2374 – 2385, 2011.
- [85] A. Abou-Jaoude, N. Stauff, and A. Erickson, “Performance and safety evaluation of a mixed-spectrum reactor design,” *Annals of Nuclear Energy*, vol. 126, pp. 33 – 42, 2019.
- [86] Y. Oka and T. Jevremovic, “Negative coolant void reactivity in large fast breeder reactors with hydrogenous moderator layer,” *Annals of Nuclear Energy*, vol. 23, no. 14, pp. 1105 – 1115, 1996.

- [87] K. Tsujimoto *et al.*, “Improvement of reactivity coefficients of metallic fuel LMFBR by adding moderating material,” *Annals of Nuclear Energy*, vol. 28, no. 9, pp. 831 – 855, 2001.
- [88] S. Hong *et al.*, “Neutronic design of KALIMER-600 core with moderator rods,” in *Proceedings of the International Congress on Advances in Nuclear Power Plants, ICAPP’04*, June 13-17 2004.
- [89] B. Faure *et al.*, “A 2D/1D algorithm for effective cross-section generation in fast reactor neutronic transport calculations,” *Nuclear Science and Engineering*, vol. 192, no. 1, pp. 40–51, 2018.
- [90] S. Santandrea *et al.*, “A neutron transport characteristics method for 3D axially extruded geometries coupled with a fine group self-shielding environment,” *Nuclear Science and Engineering*, vol. 186, no. 3, pp. 239–276, 2017.
- [91] B. Faure, *Development of Neutronic Calculation Schemes for Heterogeneous Sodium-Cooled Nuclear Cores in the APOLLO3[®] Code*. PhD thesis, Aix-Marseille Université, September 2019.
- [92] P. Archier *et al.*, “New reference APOLLO3 calculation scheme for sodium cooled fast reactors: from sub-assembly to full-core calculations,” in *Proceedings of PHYSOR 2016: Unifying Theory and Experiments in the 21st Century*, May 1-5 2016.
- [93] G. Rimpault, “Algorithmic features of the ECCO cell code for treating heterogeneous fast reactor subassemblies,” in *Proceedings of International. Topical Meeting on Reactor Physics and Computations*, May 1-5 1995.
- [94] J. Ruggieri *et al.*, “ERANOS 2.1 : International code system for Gen IV fast reactor analysis,” in *Proceedings of International congress on advances in nuclear power plants - ICAPP’06*, June 4-8 2006.
- [95] P. Jacquet, *Nouvelles méthodes de modélisation neutronique des réacteurs rapides de quatrième génération*. PhD thesis, Université de Grenoble, May 2011.
- [96] V. Jouault, *Amélioration de la démarche de Vérification & Validation du nouveau code de Neutronique APOLLO3[®]*. PhD thesis, Aix-Marseille Université, September 2017.
- [97] C. B. Carrico, E. E. Lewis, and G. Palmiotti, “Three-dimensional variational nodal transport methods for cartesian, triangular, and hexagonal criticality calculations,” *Nuclear Science and Engineering*, vol. 111, no. 2, pp. 168–179, 1992.
- [98] A. Gandini, “A generalized perturbation method for bi-linear functionals of the real and adjoint neutron fluxes,” *Journal of Nuclear Energy*, vol. 21, pp. 755–765, 1967.
- [99] W. M. Stacey, *Nuclear Reactor Physics*. Wiley-VCH, 2nd ed., 2007.
- [100] J. Tomassi, “ERANOS user’s manual: application of perturbation theory with finite difference diffusion and transport flux solvers,” technical note, CEA, January 2008.

-
- [101] V. Huy, *Contribution to nuclear data improvement by assimilation of integral experiments for the ASTRID core neutronic characterization*. PhD thesis, Aix-Marseille Université, October 2018.
- [102] J.-B. Droin, *Modélisation d'un transitoire de perte de débit primaire non protégé dans un RNR-Na*. PhD thesis, Université Grenoble Alpes, September 2016.
- [103] J.-B. Droin *et al.*, “Design-oriented tool for Unprotected Loss Of Flow simulations in a sodium fast reactor: Validation and application to stability analyses,” *Nuclear Engineering and Design*, vol. 361, p. 110550, 2020.
- [104] P. Sciora *et al.*, “Importance of the Doppler constant and of the fuel temperature evaluation for the design of a ‘CADOR’ core,” in *Proceedings of ICAPP 2019*, May 12-15 2019.
- [105] M. Foissy, G. Rimpault, and L. Buiron, “Use of different libraries in the analysis of the Doppler measurements of the SEFOR reactor: assessment of the Doppler effect of the ASTRID core,” in *Proceeding of International Conference on Physics of Reactors PHYSOR 2020*, (Cambridge, United Kingdom), March 2020.
- [106] J. Guidez, *Phénix: Le retour d'expérience*. EDP sciences, 2013.
- [107] W. Assal, J. C. Bosq, and F. Mellier, “Experimental measurements at the MASURCA facility,” in *Proceedings of 1st International Conference on Advancements in Nuclear Instrumentation, Measurement Methods and their Applications*, June 7-10 2009.

Appendix A

Parameters of core geometries

This appendix contains some of the more detailed information about CADOR cores used in the thesis that were omitted in the main text for the sake of brevity and clarity. Core I is the preliminary CADOR core design that was used solely for single assembly calculations in Chapters 4 and single assembly calculations at the beginning of Chapter 5. Core II is the core design that was used in all later calculations: calculations of cluster, core etc.

Table A.1: Densities of all materials used in fuel assemblies of Core I.

Material	densities [g/cm ³]
Be	1.85
ZrH ₂	5.56
Fuel	11.08
Coolant	0.95
Structures	7.95

Table A.2: Volume fractions and densities of all materials used in fuel assemblies of Core I.

	10.5 % Be	3.5 % ZrH ₂	no moderator
Moderator	10.5 %	3.6 %	0.0 %
Fuel	27.6 %	34.6 %	38.1 %
Coolant	33.2 %	33.2 %	33.2 %
Structures	25.5 %	25.5 %	25.5 %
Void	3.2 %	3.2 %	3.2 %

Table A.3: Composition of EM10 ferritic steel used for wrapper in Core II.

density: 7.76 g/cm ³	
Element	Concentration
Fe	89 %
Cr	8.5 %
Mn	1 %
Mn	0.5 %
Ni	0.5 %
Si	0.3 %
Ti	0.02 %
He	0.08 %

Table A.4: Composition of AIM steel used for cladding in Core II.

density: 7.95 g/cm ³	
Element	Concentration
Fe	65.75 %
Ni	15.5 %
Cr	14.5 %
Mo	1.5 %
Mn	1.5 %
Si	0.85 %
Ti	0.4 %

Table A.5: Fuel composition in Core II.

Enrichment zones		Uranium composition		Other actinides composition	
C1	19.8 % Pu	²³⁸ U	99.8 %	²³⁸ Pu	4.02 %
				²³⁹ Pu	37.88 %
C2	22.0 % Pu	²³⁵ U	0.2 %	²⁴⁰ Pu	33.48 %
				²⁴¹ Pu	11.42 %
				²⁴² Pu	12.04 %
				²⁴¹ Am	1.16 %

Appendix B

Uncertainties of nuclear data

This part of appendix contains many detailed tables of sensitivities or uncertainties that were not included in the text due to their large size.

Table B.1: Relative differences of sensitivities (in %) between Be-moderated and ZrH₂-moderated CADOR core.

	Capture	Fission	Elastic	Inelastic	n,xn	v	Fission spectrum	Total
Am241	-13	-3	3	-11	-32	-6	-6	295
Fe56	20	-	60	17	-22	-	-	9
Na23	28	-	1375	13	16	-	-	-38
O16	-13	-	-21	2	-6	-	-	-20
Pu238	-6	17	3	-8	-31	13	13	16
Pu239	-8	7	5	-12	-33	2	2	4
Pu240	-14	2	6	-10	-32	-2	-2	4
Pu241	-17	4	1	-11	-31	-1	-1	1
Pu242	-9	-2	7	-9	-34	-6	-6	-3
U235	-10	11	3	-10	-31	6	6	8
U238	14	-3	4	-9	-31	-8	-8	103
Total	5	5	490	-4	1470	0	0	0

Table B.2: Uncertainties of Doppler effect (in %) for most important isotopes.

(a) Be moderator

	Capture	Fission	Elastic	Inelastic	n,xn	v	Fission spectrum	Total
Am241	0.03	0.01	0.00	0.00	0.00	0.01	0.01	0.04
Be9	0.00	0.00	0.36	0.00	0.00	0.00	0.00	0.36
Fe56	0.14	0.00	0.21	0.15	0.00	0.00	0.00	0.29
Na23	0.00	0.00	0.35	0.04	-0.01	0.00	0.00	0.35
O16	0.09	0.00	0.21	0.01	0.00	0.00	0.00	0.23
Pu238	0.18	0.03	0.00	0.01	0.00	0.12	0.22	0.31
Pu239	1.01	0.47	-0.03	0.07	0.01	0.14	0.51	1.23
Pu240	0.34	1.53	-0.02	-0.20	-0.01	0.03	0.46	1.62
Pu241	0.39	0.24	0.00	0.02	0.00	0.06	0.66	0.81
Pu242	0.31	0.07	0.00	0.03	0.00	0.03	0.10	0.34
U235	0.01	0.01	0.00	0.00	0.00	0.00	0.00	0.02
U238	0.40	-0.30	0.12	0.79	0.06	0.12	0.18	0.87
Total	1.27	1.59	0.60	0.78	0.06	0.23	1.00	2.48

(b) ZrH₂ moderator

	Capture	Fission	Elastic	Inelastic	n,xn	v	Fission spectrum	Total
Am241	0.03	0.00	0.00	0.00	0.00	0.01	0.01	0.04
Fe56	0.06	0.00	0.06	0.14	0.00	0.00	0.00	0.16
H1	0.00	0.00	0.16	0.00	0.00	0.00	0.00	0.16
Na23	0.01	0.00	0.16	0.04	0.00	0.00	0.00	0.17
O16	0.11	0.00	0.15	0.01	0.00	0.00	0.00	0.19
Pu238	0.15	0.02	0.00	0.01	0.00	0.12	0.20	0.28
Pu239	0.48	0.44	-0.01	0.07	0.01	0.11	0.53	0.85
Pu240	-0.14	1.39	0.01	-0.17	-0.01	0.03	0.45	1.45
Pu241	0.32	0.20	0.00	0.02	0.00	0.02	0.64	0.74
Pu242	0.06	0.07	0.00	0.03	0.00	0.03	0.10	0.15
U235	0.01	0.01	0.00	0.00	0.00	0.00	0.00	0.01
U238	0.48	-0.35	0.09	0.92	0.07	0.13	0.19	1.00
Zr90	0.00	0.00	0.01	0.00	0.00	0.00	0.00	0.01
Zr91	0.02	0.00	0.00	0.00	0.00	0.00	0.00	0.02
Zr92	0.00	0.00	0.00	0.00	0.00	0.00	0.00	0.00
Zr94	0.00	0.00	0.00	0.00	0.00	0.00	0.00	0.00
Zr96	0.03	0.00	0.00	0.00	0.00	0.00	0.00	0.03
Total	0.77	1.43	0.30	0.92	0.07	0.21	0.99	2.15

(c) no moderator

	Capture	Fission	Elastic	Inelastic	n,xn	v	Fission spectrum	Total
Am241	0.04	0.01	0.00	0.01	0.00	0.01	0.01	0.05
Fe56	0.34	0.00	0.51	0.17	0.00	0.00	0.00	0.64
Na23	-0.04	0.00	0.83	0.03	-0.01	0.00	0.00	0.83
Ni64	0.00	0.00	0.01	0.00	0.00	0.00	0.00	0.01
O16	0.12	0.00	0.67	0.01	0.00	0.00	0.00	0.68
Pu238	0.18	0.04	0.01	0.01	0.00	0.10	0.23	0.31
Pu239	0.93	0.67	0.02	0.09	0.01	0.17	0.57	1.29
Pu240	0.85	1.93	-0.05	-0.37	-0.02	0.04	0.55	2.14
Pu241	0.45	0.28	0.01	0.05	0.00	0.02	0.62	0.81
Pu242	0.43	0.08	0.01	0.06	0.00	0.04	0.13	0.46
U235	0.04	0.01	0.00	0.00	0.00	0.01	0.00	0.04
U238	-0.52	-0.54	0.40	1.55	0.11	0.14	0.22	1.45
Total	1.37	1.99	1.28	1.52	0.11	0.24	1.06	3.32

Table B.3: Uncertainties of void effect (in %) for most important isotopes.

(a) Be moderator

	Capture	Fission	Elastic	Inelastic	n,xn	v	Fission spectrum	Total
Am241	0.08	0.01	0.00	0.01	0.00	0.01	0.02	0.09
Be9	0.00	0.00	0.23	0.00	0.00	0.00	0.00	0.23
Fe56	1.18	0.00	0.47	0.47	0.00	0.00	0.00	1.35
Na23	2.37	0.00	0.75	1.36	0.07	0.00	0.00	2.83
O16	0.29	0.00	0.13	0.02	0.00	0.00	0.00	0.32
Pu238	0.58	0.04	0.01	0.01	0.00	0.06	0.34	0.68
Pu239	4.19	7.25	-0.13	0.25	0.03	0.88	0.27	8.42
Pu240	1.45	1.93	-0.06	-0.20	-0.02	0.07	0.92	2.58
Pu241	1.08	1.97	0.01	0.05	0.00	0.37	0.35	2.30
Pu242	1.19	0.15	0.02	0.06	0.00	0.07	0.21	1.22
U235	0.16	0.11	0.01	0.00	0.00	0.03	0.00	0.19
U238	3.28	-0.34	-0.44	2.03	0.11	0.18	0.30	3.84
Total	6.38	7.75	0.81	2.49	0.13	0.98	1.14	10.48

(b) ZrH₂ moderator

	Capture	Fission	Elastic	Inelastic	n,xn	v	Fission spectrum	Total
Am241	0.05	0.00	0.00	0.01	0.00	0.01	0.01	0.05
Be9	0.00	0.00	0.00	0.00	0.00	0.00	0.00	0.00
Fe56	0.84	0.00	0.30	0.23	0.00	0.00	0.00	0.92
H1	0.00	0.00	0.28	0.00	0.00	0.00	0.00	0.28
Na23	1.56	0.00	0.55	0.94	-0.01	0.00	0.00	1.90
O16	0.25	0.00	0.07	0.01	0.00	0.00	0.00	0.26
Pu238	0.23	0.03	0.01	0.01	0.00	0.04	0.10	0.26
Pu239	1.81	3.33	-0.07	0.13	0.00	0.42	0.07	3.81
Pu240	0.64	0.82	-0.05	0.11	-0.01	0.05	0.42	1.12
Pu241	0.61	1.05	0.01	0.04	0.00	0.34	0.22	1.28
Pu242	0.80	0.09	0.02	0.03	0.00	0.06	0.10	0.82
U235	0.07	0.05	0.00	0.00	0.00	0.01	0.00	0.09
U238	1.20	-0.19	-0.26	1.15	-0.04	0.12	0.15	1.64
Zr90	0.02	0.00	0.04	0.00	0.00	0.00	0.00	0.05
Zr91	0.03	0.00	0.01	0.00	0.00	0.00	0.00	0.03
Zr92	0.02	0.00	0.02	0.00	0.00	0.00	0.00	0.03
Zr94	0.01	0.00	0.02	0.00	0.00	0.00	0.00	0.02
Zr96	0.05	0.00	0.00	0.00	0.00	0.00	0.00	0.05
Total	3.07	3.58	0.65	1.51	-0.05	0.56	0.52	5.05

(c) no moderator

	Capture	Fission	Elastic	Inelastic	n,xn	v	Fission spectrum	Total
Am241	0.05	0.00	0.00	0.01	0.00	0.00	0.00	0.05
Fe56	0.66	0.00	0.25	0.13	0.00	0.00	0.00	0.71
Na23	0.74	0.00	1.13	0.65	-0.04	0.00	0.00	1.50
O16	0.14	0.00	0.30	0.01	0.00	0.00	0.00	0.33
Pu238	0.20	0.03	0.01	0.02	0.00	0.11	0.03	0.24
Pu239	1.09	2.42	-0.04	0.10	0.00	0.39	0.21	2.69
Pu240	0.53	0.34	0.02	-0.05	0.00	0.03	0.20	0.66
Pu241	0.56	0.70	0.01	0.11	0.00	0.28	0.50	1.07
Pu242	0.52	0.07	0.01	0.04	0.00	0.04	0.05	0.53
U235	0.03	0.03	0.00	0.00	0.00	0.01	0.00	0.04
U238	1.26	0.11	-0.12	0.69	0.03	0.03	0.04	1.44
Total	2.17	2.54	1.19	0.97	-0.02	0.50	0.58	3.76

Table B.4: Uncertainties of control rod worth (in %) for most important isotopes.

(a) Be moderator

	Capture	Fission	Elastic	Inelastic	n,xn	ν	Fission spectrum	Total
Am241	0.01	0.01	0.00	0.00	0.00	0.01	0.01	0.02
Be9	0.00	0.00	0.23	0.00	0.00	0.00	0.00	0.23
Fe56	0.10	0.00	0.36	0.05	0.00	0.00	0.00	0.38
Na23	0.06	0.00	0.12	-0.01	0.00	0.00	0.00	0.14
O16	0.10	0.00	0.17	0.00	0.00	0.00	0.00	0.20
Pu238	0.03	0.02	0.01	0.00	0.00	0.10	0.15	0.18
Pu239	0.24	0.33	-0.03	0.02	0.00	0.09	0.32	0.53
Pu240	-0.14	1.24	0.06	0.07	0.01	0.03	0.37	1.29
Pu241	0.09	0.14	0.02	0.03	0.00	0.08	0.47	0.50
Pu242	0.08	0.07	0.03	0.02	0.00	0.03	0.09	0.15
U235	0.01	0.00	0.00	0.00	0.00	0.00	0.00	0.01
U238	0.29	0.40	0.21	-0.20	0.02	0.11	0.13	0.53
Total	0.51	1.35	0.56	-0.18	0.02	0.20	0.71	1.71

(b) ZrH₂ moderator

	Capture	Fission	Elastic	Inelastic	n,xn	ν	Fission spectrum	Total
Am241	0.00	0.01	0.00	0.00	0.00	0.01	0.01	0.02
Fe56	0.07	0.00	0.30	0.04	0.00	0.00	0.00	0.31
H1	0.00	0.00	0.12	0.00	0.00	0.00	0.00	0.12
Na23	0.07	0.00	0.07	-0.01	0.00	0.00	0.00	0.09
O16	0.11	0.00	0.20	0.00	0.00	0.00	0.00	0.23
Pu238	0.03	0.02	0.01	0.00	0.00	0.10	0.13	0.17
Pu239	0.24	0.25	-0.02	0.01	-0.01	0.08	0.31	0.47
Pu240	-0.17	1.26	0.05	0.11	0.01	0.03	0.36	1.30
Pu241	0.10	0.12	0.02	0.03	0.00	0.07	0.44	0.48
Pu242	0.08	0.08	0.03	0.02	0.00	0.04	0.08	0.15
U235	0.01	0.00	0.00	0.00	0.00	0.00	0.00	0.01
U238	0.22	0.44	0.23	-0.17	0.03	0.11	0.12	0.54
Zr90	0.00	0.00	0.03	0.00	0.00	0.00	0.00	0.03
Zr91	0.01	0.00	0.01	0.00	0.00	0.00	0.00	0.01
Zr92	0.00	0.00	0.01	0.00	0.00	0.00	0.00	0.01
Zr94	0.00	0.00	0.01	0.00	0.00	0.00	0.00	0.01
Zr96	0.01	0.00	0.00	0.00	0.00	0.00	0.00	0.01
Total	0.50	1.36	0.48	-0.11	0.03	0.19	0.67	1.68

(c) no moderator

	Capture	Fission	Elastic	Inelastic	n,xn	ν	Fission spectrum	Total
Am241	0.01	0.01	0.00	0.00	0.00	0.01	0.01	0.02
Fe56	0.14	0.00	0.34	0.09	0.00	0.00	0.00	0.37
Na23	0.05	0.00	0.11	0.01	0.00	0.00	0.00	0.13
O16	0.10	0.00	0.23	0.01	0.00	0.00	0.00	0.25
Pu238	0.04	0.03	0.02	0.00	0.00	0.09	0.17	0.20
Pu239	0.11	0.34	-0.05	0.03	0.00	0.10	0.38	0.53
Pu240	0.36	1.42	0.09	0.09	0.01	0.04	0.44	1.54
Pu241	0.09	0.16	0.03	0.04	0.00	0.06	0.47	0.51
Pu242	0.08	0.08	0.04	0.02	0.00	0.04	0.10	0.17
U235	0.02	0.00	0.00	0.00	0.00	0.00	0.00	0.03
U238	0.40	0.37	0.25	-0.21	-0.04	0.12	0.16	0.59
Total	0.72	1.51	0.52	-0.16	-0.04	0.20	0.79	1.93

Table B.5: Uncertainties of power ratio between assembly in the center of the core and assembly in the outer core (in %) for most important isotopes.

(a) Be moderator

	Capture	Fission	Elastic	Inelastic	n,xn	v	Fission spectrum	Total
Am241	0.02	0.00	0.00	0.00	0.00	0.01	0.01	0.03
Be9	0.00	0.00	0.06	0.00	0.00	0.00	0.00	0.06
Fe56	0.37	0.00	0.40	0.18	0.00	0.00	0.00	0.58
Na23	0.07	0.00	0.08	0.06	0.01	0.00	0.00	0.12
O16	0.26	0.00	0.23	0.01	0.00	0.00	0.00	0.35
Pu238	0.06	0.01	0.00	0.00	0.00	0.07	0.06	0.11
Pu239	0.10	0.42	0.02	-0.01	0.01	0.10	0.07	0.44
Pu240	0.29	0.36	0.02	0.06	0.01	0.02	0.23	0.52
Pu241	0.12	0.12	0.01	0.04	0.00	0.03	0.14	0.23
Pu242	0.04	0.04	0.01	0.02	0.00	0.02	0.06	0.09
U235	0.04	0.01	0.00	0.00	0.00	0.01	0.00	0.05
U238	0.82	0.05	-0.10	0.18	0.05	0.04	0.05	0.84
Total	1.03	0.57	0.90	0.27	0.05	0.13	0.30	1.54

(b) ZrH₂ moderator

	Capture	Fission	Elastic	Inelastic	n,xn	v	Fission spectrum	Total
Am241	0.03	0.00	0.00	0.00	0.00	0.01	0.01	0.03
Be9	0.00	0.00	0.00	0.00	0.00	0.00	0.00	0.00
Fe56	0.33	0.00	0.39	0.19	0.00	0.00	0.00	0.54
H1	0.00	0.00	0.15	0.00	0.00	0.00	0.00	0.15
Na23	0.08	0.00	0.07	0.07	0.00	0.00	0.00	0.13
O16	0.26	0.00	0.32	0.01	0.00	0.00	0.00	0.41
Pu238	0.04	0.01	0.01	0.00	0.00	0.06	0.07	0.11
Pu239	0.63	0.92	-0.04	0.01	0.00	0.09	0.09	1.12
Pu240	0.39	0.45	-0.01	0.06	0.01	0.02	0.24	0.65
Pu241	0.10	0.11	0.01	0.04	0.00	0.04	0.16	0.23
Pu242	0.05	0.04	0.01	0.02	0.00	0.02	0.06	0.09
U235	0.04	0.01	0.00	0.00	0.00	0.01	0.00	0.04
U238	0.75	0.12	0.06	0.38	0.05	0.03	0.04	0.85
Zr90	0.02	0.00	0.01	0.00	0.00	0.00	0.00	0.03
Zr91	0.02	0.00	0.00	0.00	0.00	0.00	0.00	0.02
Zr92	0.02	0.00	0.01	0.00	0.00	0.00	0.00	0.02
Zr94	0.01	0.00	0.01	0.00	0.00	0.00	0.00	0.01
Zr96	0.01	0.00	0.00	0.00	0.00	0.00	0.00	0.01
Total	1.18	1.04	1.00	0.44	0.05	0.12	0.32	1.94

(c) no moderator

	Capture	Fission	Elastic	Inelastic	n,xn	v	Fission spectrum	Total
Am241	0.02	0.00	0.00	0.00	0.00	0.00	0.00	0.02
Fe56	0.27	0.00	0.40	0.17	0.00	0.00	0.00	0.52
Na23	0.07	0.00	0.07	0.06	0.00	0.00	0.00	0.12
O16	0.18	0.00	0.27	0.01	0.00	0.00	0.00	0.33
Pu238	0.08	0.01	-0.01	0.00	0.00	0.05	0.04	0.11
Pu239	0.44	0.32	0.04	0.01	0.01	0.09	0.05	0.55
Pu240	0.24	0.12	0.03	0.05	0.00	0.01	0.14	0.30
Pu241	0.21	0.16	0.01	0.04	0.00	0.01	0.08	0.28
Pu242	0.16	0.03	0.01	0.02	0.00	0.01	0.04	0.17
U235	0.05	0.01	0.00	0.00	0.00	0.00	0.00	0.05
U238	0.77	-0.03	-0.17	0.56	0.03	0.03	0.01	0.94
Total	1.05	0.37	0.84	0.59	0.03	0.11	0.18	1.53

Appendix C

Additional results of transient simulations in MACARENa

This section of Appendix contains a presentation of some additional results of transient simulations performed by MACARENa code.

Table C.1: Delayed neutron fraction and mean generation time used in MACARENa.

Group	β_{eff} [pcm]	λ [1/s]
1	6.2	0.012
2	62.7	0.028
3	23.0	0.043
4	56.2	0.133
5	117.9	0.292
6	51.3	0.666
7	44.0	1.635
8	18.8	3.555
Sum	380.0	

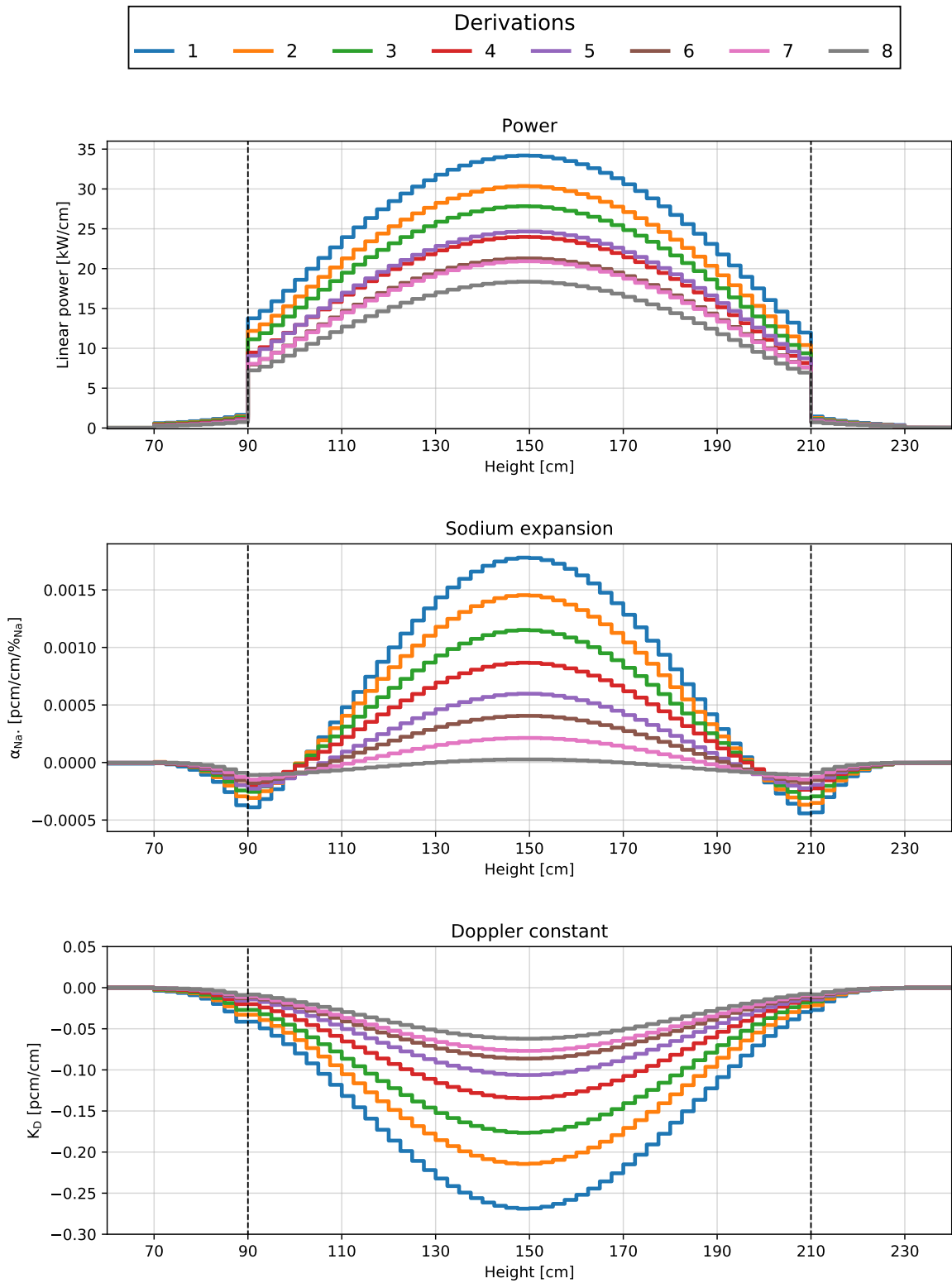


Figure C.1: Comparison of power profile and reactivity coefficients derived from APOLLO3 (“A3 Up” set of coefficients).

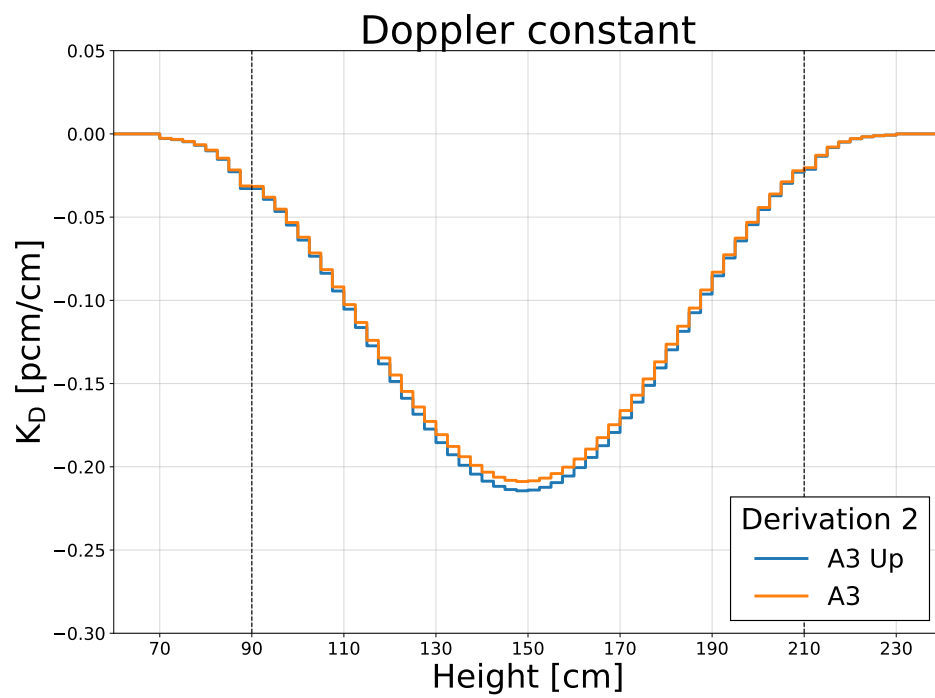


Figure C.2: Comparison of coefficients for Doppler constant from “A3” and “A3 Up” sets for the derivation 2.

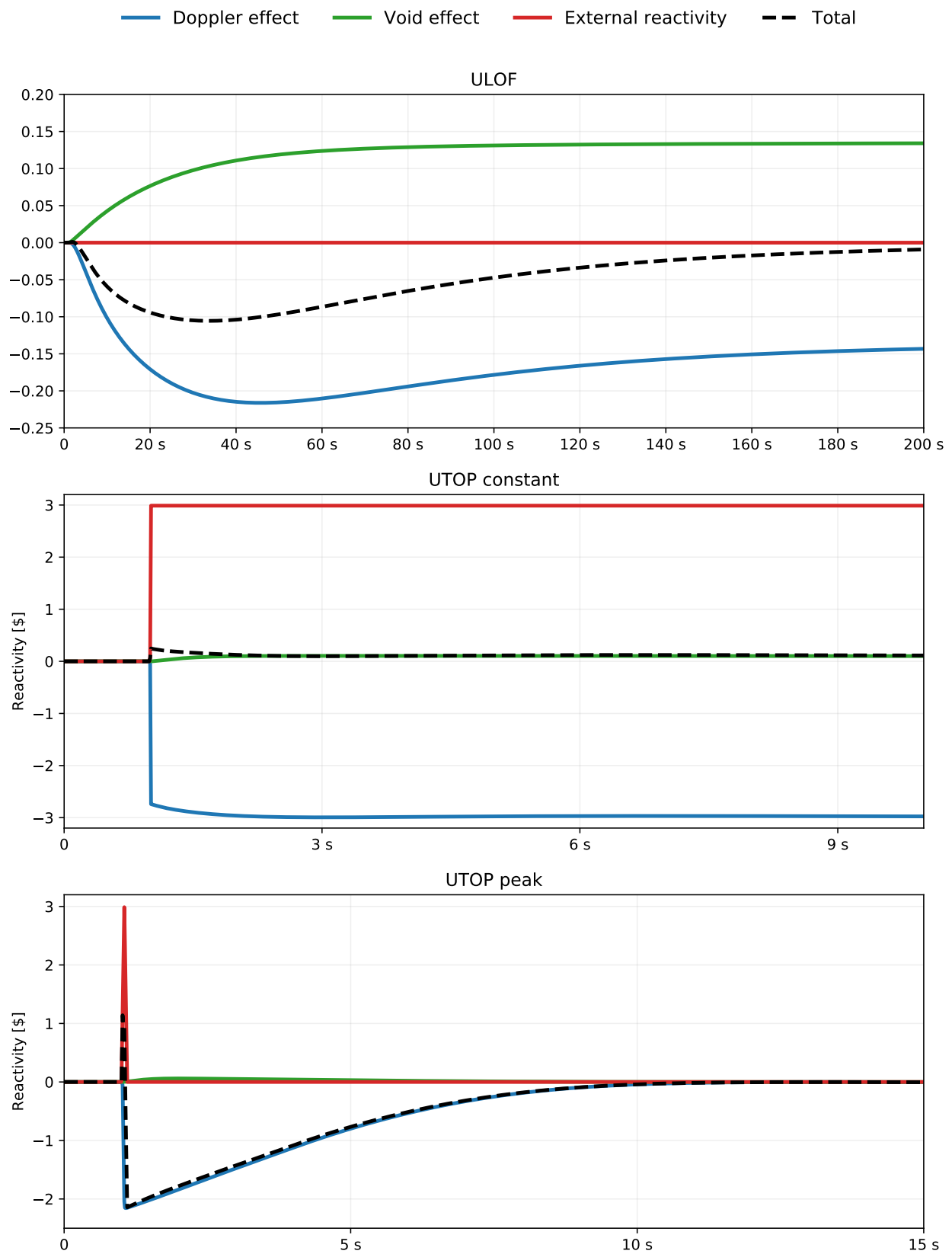


Figure C.3: Evolution of core reactivity during transients. Calculations performed with “A3 Up” reactivity coefficients.

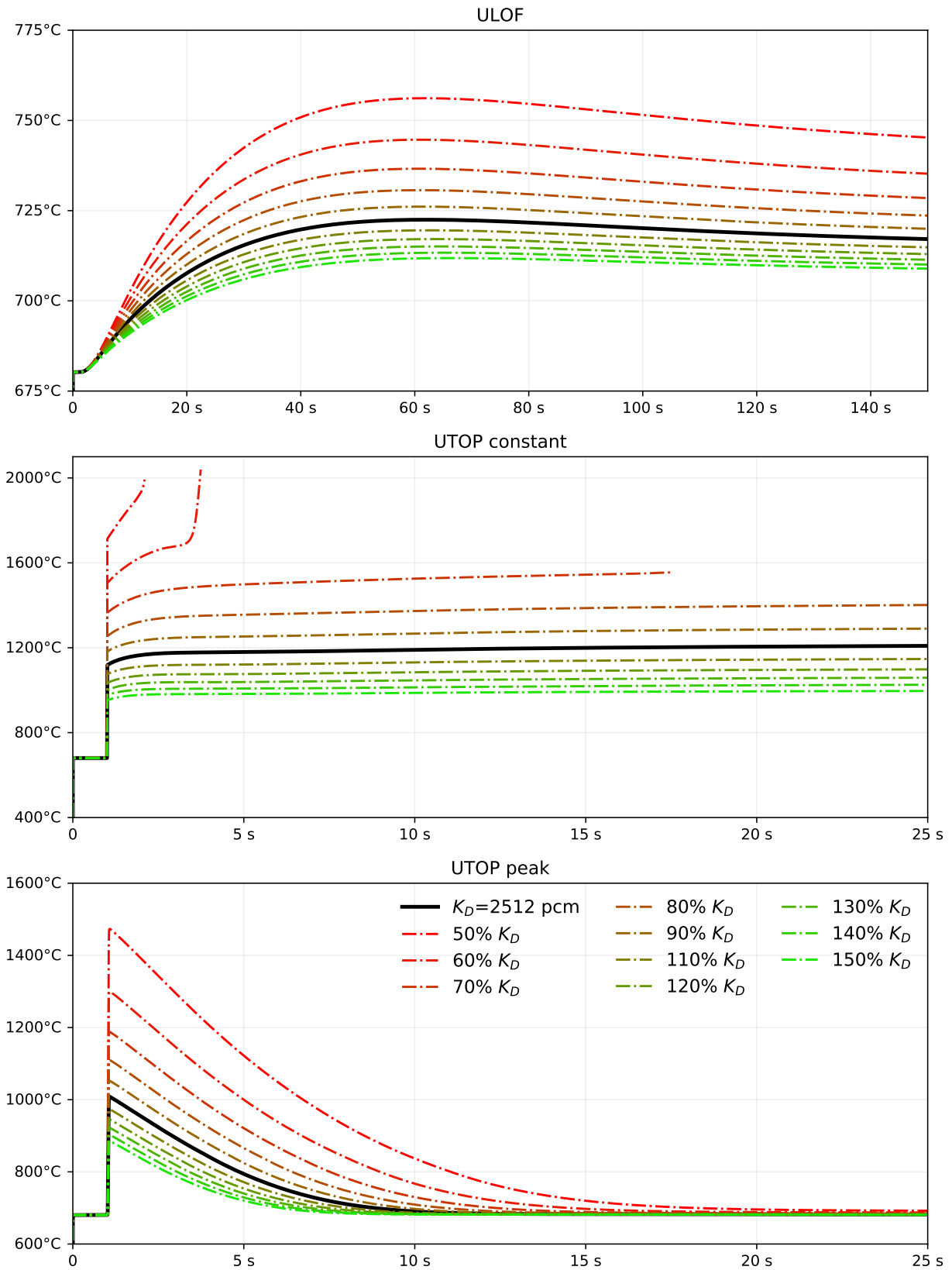


Figure C.4: Evolution of global average fuel temperatures during transients for different values of K_D .

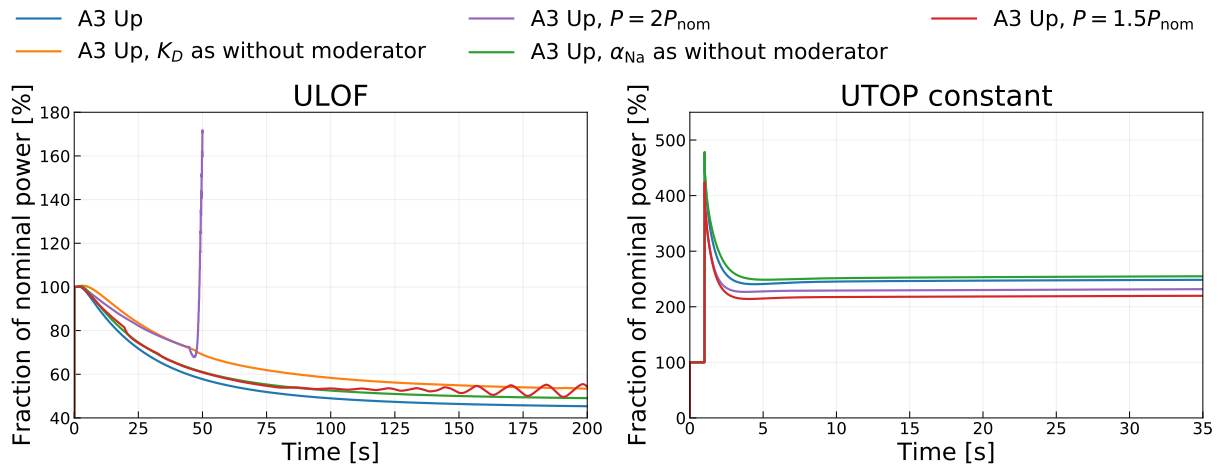


Figure C.5: Comparison of the evolution of thermal power of the core (as a percentage of nominal flow) during two transient scenarios.

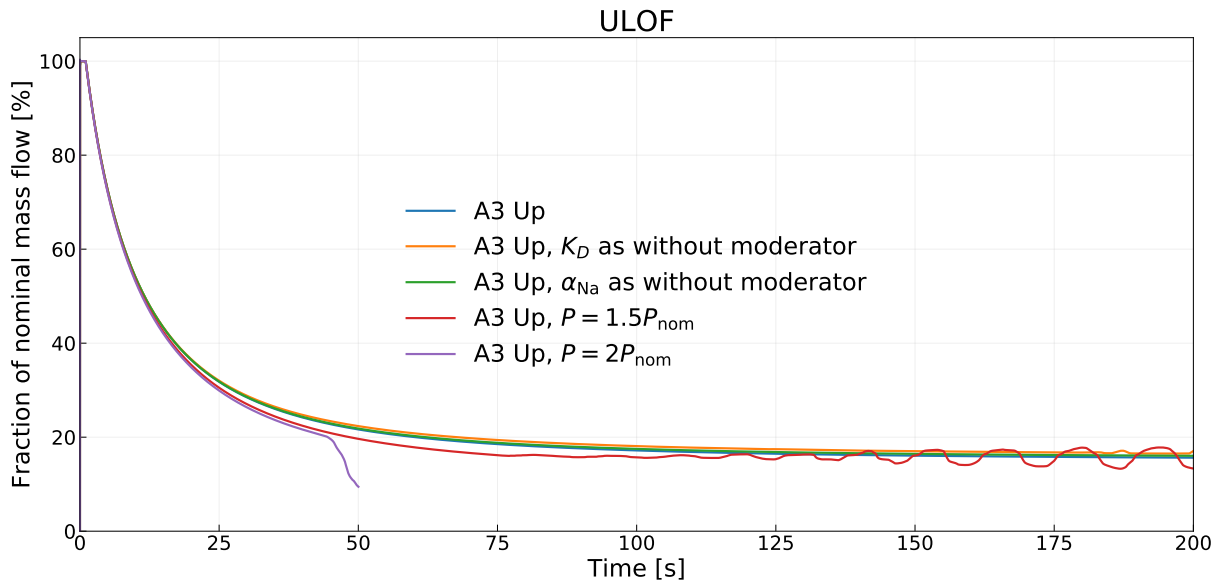


Figure C.6: Comparison of the evolution of sodium mass flow (as a percentage of nominal flow) during ULOF scenario.

Résumé Étendu

Afin d'améliorer la sûreté passive des réacteurs rapides refroidis au sodium (SFR) en cas de transitoires non protégés, tels que la perte de débit non protégée (ULOF) ou une insertion de réactivité (UTOP), le CEA a proposé le concept CADOR — une nouvelle conception du cœur SFR avec un effet Doppler renforcé. L'une des caractéristiques de conception la plus importante est l'introduction de modérateur dans chaque assemblage combustible pour diminuer l'énergie moyenne des neutrons d'environ 40 %. La solution conduit à un effet Doppler environ trois fois plus élevé en raison de l'augmentation de la population de neutrons dans les résonances. D'autre part, le spectre neutronique adouci modifie d'autres propriétés du cœur. Par exemple, le placement hétérogène du modérateur dans l'assemblage peut entraîner une distribution inégale de la vitesse de réaction et un risque de pics de puissance non observés dans les SFR standard. Pour démontrer la sûreté du concept CADOR, il est essentiel d'évaluer d'abord la fiabilité des outils de calcul, à la suite d'un processus de vérification, validation et quantification d'incertitude (VVQI). Les modifications du bilan neutronique remettent en question l'applicabilité des schémas de calcul standards du transport neutronique dans le cadre de ce concept CADOR. Par conséquent, le but de cette thèse est d'établir un schéma de calcul de neutronique précis, conforme aux principes de la VVQI, prenant en compte tous les phénomènes physiques pertinents liés aux propriétés atypiques de CADOR.

Un schéma de calcul du code neutronique déterministe APOLLO3[®] a été défini comme base de l'analyse. Les cœurs CADOR avec deux types de modérateurs différents, beryllium (Be) et hydrure de zirconium (ZrH_2), ont été utilisés. Les éléments du schéma et leurs améliorations possibles ont été étudiés par comparaison directe avec le code Monte Carlo de référence TRIPOLI-4[®]. Les biais systématiques des modèles numériques (différentes approches d'homogénéisation spatiale ou de traitement de upscattering résonant, différentes définitions d'énergie et de maillage spatial) ont été étudiés pour la précision de keff, l'effet Doppler et les taux de réactions. Les sources d'incertitudes les plus importantes ont été identifiées et quantifiées. Enfin, comme première estimation de la sensibilité du schéma de calcul multi-physique, l'impact des incertitudes sur les simulations des transitoires UTOP et ULOF a été évalué par couplage avec MACARENA, un code de calcul pour l'analyse transitoire en SFR.

Impact de la modération sur la neutronique

Notre étude a commencé par l'identification des points clés possibles dans lesquels le cœur SFR modéré diffère des conceptions SFR plus conventionnelles en termes de neutronique. Les différences identifiées peuvent être grossièrement divisées en trois caractéristiques distinctes et les problèmes potentiels qui y sont liés.

Premièrement, l'énergie moyenne des neutrons a été significativement diminuée et la fraction de neutrons dans la gamme d'énergie de résonance a été augmentée au détriment des neutrons dans la région d'énergie rapide. Si ce résultat est un choix intentionnel, crucial pour le réacteur CADOR, il pourrait avoir un impact sur les performances du schéma de calcul. Comme les neutrons plus lents sont généralement plus susceptibles d'interagir avec l'environnement, le libre parcours moyen dans les deux assemblages CADOR modérés par Be et ZrH_2 a été raccourci d'environ 7 %. Une implication naturelle de ce fait est que la taille du maillage doit être adaptée en diminuant sa taille. La distribution d'énergie différente des neutrons remet également en question

la validité du maillage énergétique standard avec des tailles de groupe choisies pour mieux s'adapter à une distribution d'énergie neutronique des réacteurs rapides standard.

Le deuxième facteur est la distribution conjointe des neutrons dans l'espace et l'énergie. En raison du choix de conception fait concernant le placement du modérateur, l'effet de leur présence est fortement localisé, en particulier dans le cas d'un maillage rare de crayons ZrH_2 . Une distribution spatiale inégale de l'énergie moyenne des neutrons conduit à une vitesse de réaction inégale dans le volume de l'assemblage. Nous avons pu montrer que les zones de combustible à proximité directe du modérateur ont connu une vitesse de réaction plus élevée — à la fois la fission et la capture de neutrons. Il y a deux problèmes principaux liés à ce phénomène. Le taux de fission localement accru implique la formation de pics de puissance pendant le fonctionnement du réacteur. Après division de chaque crayon de combustible en 36 segments, l'écart de puissance maximum (taux de fission) par rapport à la moyenne globale dans n'importe quel segment s'est avéré être presque 3% pour Be moderator et supérieur à 10% pour le modérateur ZrH_2 . Une autre conclusion importante est que cet effet localisé est beaucoup moins visible si le calcul est effectué selon l'approche conventionnelle du réacteur rapide où chaque pastille de combustible est représentée comme une seule région cylindrique sans raffinement supplémentaire.

L'énergie neutronique moyenne abaissée a une conséquence supplémentaire. Lorsque la vitesse moyenne des neutrons diminue, les réactions de diffusion à des énergies proches de l'équilibre thermique deviennent plus fréquentes. Nous avons démontré que dans le cas d'un cœur CADOR, le nombre de neutrons à des énergies de quelques à quelques centaines d'eV est suffisamment important pour exiger des modèles de diffusion améliorés. L'impact de l'approche standard du réacteur rapide, c'est-à-dire du modèle de gaz libre utilisé uniquement avec l'hypothèse d'une section efficace de diffusion constante par rapport à la vitesse relative, est particulièrement visible pour des températures de combustible plus élevées. Le cœur CADOR diffère des réacteurs thermiques où l'impact de l'hypothèse «constante XS» est prononcé même à température nominale. Les résultats obtenus dans TRIPOLI-4[®] montrent que pour une température de combustible de 2000 °C la différence entre le traitement de diffusion exact (modèle DBRC) et le modèle qui suppose une section efficace constante (modèle SVT) atteint autour de 50 pcm et autant que 150 pcm dans le cas de ZrH_2 . Cet écart est principalement provoqué par un phénomène de remontée de la résonance, impossible à prendre en compte correctement sous l'hypothèse «constante XS». L'effet est fortement lié à la quantité de plutonium dans l'assemblage combustible. Un enrichissement plus faible en Pu est lié à une teneur plus élevée en ^{238}U mais permet également aux neutrons d'atteindre plus fréquemment les énergies inférieures, augmentant ainsi l'importance des diffusions à ces énergies. Plus important encore, le choix du noyau de diffusion a un impact profond sur la valeur calculée de l'effet Doppler. La valeur de la constante Doppler basée sur les calculs de flux à 900 degreeCelsius et 2000 °C souffre d'un biais d'environ 2.2% et 6% pour Be et ZrH_2 respectivement, si le modèle SVT est utilisé à la place de DBRC. En revanche l'effet reste totalement négligeable si le modérateur n'est pas présent dans le cœur. En conclusion, nous avons démontré que le modèle de gaz libre exact doit être utilisé lors du calcul du transport de neutrons d'un réacteur rapide avec des matériaux modérateurs, en particulier si la température élevée du combustible est utilisée.

Evaluation du schéma de calcul déterministe appliqué au SFR modéré

Le schéma de calcul dans les codes déterministes contemporains tels que APOLLO3[®] est séparé en deux étapes — le calcul du réseau et les calculs de cœur. Notre évaluation a commencé par le calcul en réseau d'un modèle 2D d'un seul assemblage combustible avec des conditions aux limites réflecteur. Nous avons montré qu'en termes de réactivité, l'accord entre APOLLO3[®] et le code de référence TRIPOLI-4[®] n'était que légèrement moins bon pour les assemblages CADOR modérés par rapport à l'assemblage sans modérateur. Les écarts aux températures nominales du carburant ne dépassaient pas 60 pcm pour tout type d'assemblage utilisé dans l'étude. L'écart APOLLO3[®]/TRIPOLI-4[®] était plus élevé pour la température de carburant quasi-accidentelle et dépassait 100 pcm pour l'assemblage du cœur interne avec Be. Les écarts étaient également généralement plus élevés pour les assemblages de cœur interne, c'est-à-dire ceux avec un enrichissement en Pu plus faible et une énergie neutronique moyenne plus faible. Selon notre étude, la différence entre l'expansion de Legendre P1 et P3 et les méthodes d'auto-blindage de Tone et sous-groupe était faible.

Comparés au code de transport ECCO de la génération précédente, les résultats de APOLLO3[®] semblent être beaucoup plus cohérents avec TRIPOLI-4[®]. Le biais sur la réactivité dans le cas des calculs ECCO était particulièrement élevé dans le cas d'assemblages modérés et dans le pire des cas atteint 900 pcm. Le code semble incapable de modéliser correctement la conception d'assemblage hétérogène (deux types de crayons) en raison du solveur de probabilité de collision en deux étapes reposant sur des hypothèses sur le courant neutronique entre les cellules. Cependant, les différences entre les codes étaient similaires lors de l'estimation des effets différentiels de la rétroaction Doppler et de la miction.

L'application du maillage spatial raffiné pour mieux tenir compte de l'autoprotection spatial n'a pas abouti à une amélioration cohérente des résultats. Les différences pour tous les cas ne dépassaient pas 30 pcm et dans certains cas, le raffinement conduisait à un pire accord avec TRIPOLI-4[®].

Une analyse cellule par cellule des taux de réaction a révélé des écarts APOLLO3[®] / TRIPOLI-4[®] plus élevés au bord des crayons de combustible, plus prononcés si la broche était voisine de le crayon du modérateur ou était placée près du tube hexagonal. La différence relative la plus élevée dans le taux d'absorption locale trouvée était 2.4 % pour Be moderator, 3.4 % pour ZrH₂ moderator mais seulement environ 1.1 % en cas de manque de modérateur.

Motivés par nos résultats sur la précision des modèles de diffusion dans TRIPOLI-4[®], nous avons décidé d'améliorer le schéma de calcul APOLLO3[®] en utilisant une bibliothèque de données nucléaires multigroupe de 1760 groupes pré-traitée pour prendre en compte le traitement de diffusion exact. Par rapport à TRIPOLI-4[®], l'impact du modèle exact est légèrement sous-estimé par APOLLO3[®], cependant la tendance générale des deux codes était similaire.

Le biais sur la réactivité de l'ensemble du schéma de calcul (calcul du réseau et du cœur) s'est avéré être d'environ 450-500 pcm dans le cas de cœur modérés et 350 pcm pour le cœur standard sans modulation supplémentaire. L'utilisation d'ordres d'anisotropie plus élevés (P3) ou d'homogénéisation des moments de flux s'est avérée une mauvaise

méthode pour réduire le biais. Les différences entre ces options ne sont pas importantes et ne conduisent pas toujours du tout à une amélioration. Malgré un biais plus élevé associé aux cœurs modérés, les options de solveur MINARET recommandées se sont avérées les mêmes pour les trois types de cœurs. 10 cm maillage radial (12 triangles par assemblage), 5 cm maillage axial et S_n ordre 4 (36 directions) ont permis une convergence suffisante.

La différence de réactivité entre les deux traitements de diffusion s'est avérée être presque du même ordre que celle évaluée pour un seul assemblage. L'impact du traitement de diffusion exacte sur l'amplitude de l'effet Doppler était respectivement 3.5 % et 5.2 % pour les modérateurs Be et ZrH_2 (résultats de TRIPOLI-4[®]).

Pour trouver la source du biais global du schéma de calcul, nous avons utilisé un calcul hybride déterministe-Monte Carlo, où le schéma APOLLO3[®] a été utilisé jusqu'au calcul de base et les calculs de base ont été effectués par TRIPOLI-4[®]. En utilisant cette méthode, nous avons pu mener une enquête plus approfondie sur le processus d'homogénéisation/condensation et tester des approches semi-hétérogènes qui ne seraient pas réalisables dans le solveur MINARET.

Les résultats de ces calculs montrent que le biais peut être visiblement réduit en préservant l'hétérogénéité partielle des assemblages combustibles, atteignant essentiellement un écart similaire au calcul de référence TRIPOLI-4[®] pour les cœurs CADOR modérés comme pour les cœurs SFR sans modérateur. Nous montrons également que l'effet de condensation de 1760 à 33 groupes d'énergie est plus visible en cas de manque de modérateur. En raison du nombre d'éléments finis requis, l'utilisation de la géométrie de cœur 3D avec des assemblages partiellement hétérogènes n'est pas réalisable dans MINARET. Il peut cependant être mis en œuvre pour calculer un modèle de cœur 2D "plat" qui pourrait servir de référence pour des études de validation dans le futur.

Malgré un biais plus élevé évalué pour les cœurs CADOR modérés, le schéma de calcul original d'APOLLO3[®] s'est avéré être un outil robuste, qui ne nécessite que quelques petits changements pour devenir bien adapté aux conditions de fonctionnement significativement différentes du cœur CADOR.

Incertitudes sur les données nucléaires

Pour évaluer l'incertitude des données nucléaires, une série de calculs de perturbation a été effectuée dans APOLLO3[®] pour déterminer les coefficients de sensibilité. L'incertitude liée au facteur de multiplication s'est avérée être d'environ 900 pcm quelle que soit la version de cœur utilisée. Les incertitudes liées aux valeurs des rétroactions de réactivité, de la valeur des barres de contrôle et du rapport de puissance étaient également d'un ordre de grandeur similaire pour les trois cœurs. La seule valeur aberrante trouvée était l'incertitude de l'effet de vidange de plus de 10 %. Cette incertitude élevée est causée par une grande différence de sensibilité entre les conditions vides et nominales pour l'isotope ^{239}Pu , à la fois pour la section efficace de capture et de fission.

L'incertitude statistique provenant des données nucléaires est presque deux fois plus élevée que la somme des biais épistémiques des modèles utilisés dans le schéma de calcul. La pire performance du schéma de calcul pour le cas des modérés est donc partiellement éclipsée par une incertitude beaucoup plus élevée des données nucléaires.

À moins que le biais statistique ne soit réduit, par ex. par l'assimilation de données expérimentales représentatives, les données nucléaires restent la plus grande source d'incertitude identifiée.

Couplage avec le code MACARENa

Le couplage unidirectionnel avec MACARENa a été utilisé pour étudier la sensibilité de la progression transitoire à la valeur de la constante de Doppler calculée dans APOLLO3[®]. Le premier objectif était de comparer les transitoires ULOF et UTOP simulés avec des valeurs de constante Doppler calculées avec un traitement de diffusion exact et simplifié. La différence relative entre la constante de Doppler de quelques pour cent était trop faible pour avoir un impact non négligeable sur l'évolution des transitoires simulés. La température maximale du carburant ne différait que de 20 degreeCelsius dans le pire des cas étudiés.

En effectuant une série de simulations transitoires pour différentes valeurs de la constante Doppler, nous avons pu estimer la sensibilité du résultat transitoire sur la constante de Doppler. Même pour K_D 10% inférieur à l'estimation APOLLO3[®], la progression du transitoire est très similaire à celle obtenue précédemment. Une telle diminution de la valeur de K_D peut entraîner un saut de température pendant le transitoire UTOP d'environ 100 degrés plus haut, laissant la marge de fusion toujours autour de 1000 °C. Parce que la diminution de 10% de K_D postulée est déjà plus grande que l'incertitude combinée du schéma de calcul et des données nucléaires, nous pouvons conclure que la précision de l'effet Doppler est suffisante pour être utilisée dans des simulations transitoires multiphysiques sans risque de déformer le comportement du cœur d'une manière qui poserait des problèmes de sécurité.